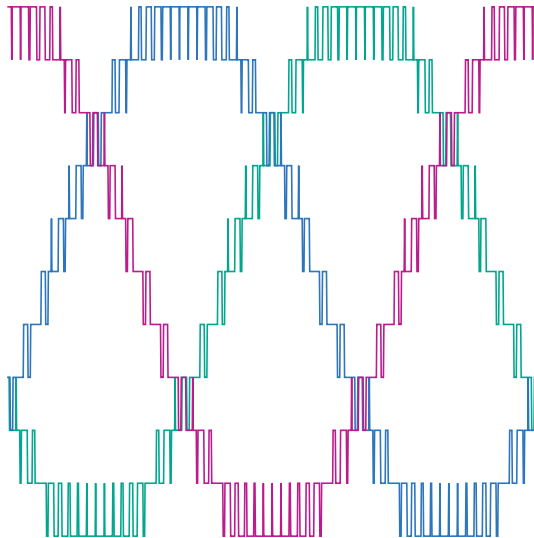


Dennis Bräcke

State Space Modelling and Control of the Modular Multilevel Converter



State Space Modelling and Control of the Modular Multilevel Converter

To obtain the academic degree of

**DOCTOR OF ENGINEERING SCIENCES
(Dr.-Ing.)**

by the KIT Department of
Electrical Engineering and Information Technology
of the Karlsruhe Institute of Technology (KIT)
accepted

DOCTORAL THESIS

of

M.Sc. Dennis Bräckle
born in Schorndorf

Date of the oral examination:

21. September 2021

PhD supervisor:

Prof. Dr.-Ing. Marc Hiller

Co-supervisor:

Prof. Dražen Dujčić

(Ecole Polytechnique Fédérale de Lausanne)

State Space Modelling and Control of the Modular Multilevel Converter

Zur Erlangung des akademischen Grades eines

**DOKTOR-INGENIEURS
(Dr.-Ing.)**

von der KIT-Fakultät für
Elektrotechnik und Informationstechnik
des Karlsruher Instituts für Technologie (KIT)
genehmigte

DISSERTATION

von
M.Sc. Dennis Bräckle
geb. in Schorndorf

Tag der mündlichen Prüfung:
Hauptreferent:
Koreferent:

21. September 2021
Prof. Dr.-Ing. Marc Hiller
Prof. Dražen Dujčić
(Ecole Polytechnique Fédérale de Lausanne)

Karlsruhe Institute of Technology (KIT)
Institute of Electrical Engineering (ETI)

To obtain the academic degree of Doctor of Engineering Sciences (Dr.-Ing.)
by the KIT Department of Electrical Engineering and Information Technology
of the Karlsruhe Institute of Technology (KIT) accepted PhD thesis
of Dennis Bräckle (M.Sc.)

Date of the oral examination: 21. September 2021
PhD supervisor: Prof. Dr.-Ing. Marc Hiller
Co-supervisor: Prof. Dražen Dujčić
(Ecole Polytechnique Fédérale de Lausanne)



This document - is licensed under a Creative Commons Attribution-ShareAlike
4.0 International License (CC BY-SA 4.0):

<https://creativecommons.org/licenses/by-sa/4.0/deed.en>

DOI: 10.5445/IR/1000138770

*”If you base medicine on science, you cure people.
If you base the design of planes on science, they fly.
If you base the design of rockets on science, they
reach the moon.
It works... bitches”*

Prof. Richard Dawkins, University of Oxford

Abstract

In der vorliegenden Arbeit wird ein neuer Ansatz zur Modellierung von Systemen basierend auf dem Modularen Multilevel Umrichter (MMC) vorgestellt. Mit Hilfe dieser Modellierung ist es möglich, neue, effiziente Regelungsalgorithmen für das System zu entwerfen. In Zukunft wird es für netzeinspeisende Umrichter immer wichtiger, nicht nur stabil, sondern auch netzverträglich operieren zu können.

Ausgehend von analytischen Differentialgleichungen wird ein Zustandsraummodell des MMC abgeleitet und eine Methode zur Entkopplung des Systems abgeleitet. Mathematische Werkzeuge erlauben eine systematische Analyse der auftretenden Steuer- und Ausgangsgrößen. Eine einfache Matrixdiagonalisierung erlaubt eine allgemeine Transformationsregel für MMC-basierte System zu formulieren.

Daraus resultieren einfache Möglichkeiten, Leistungsterme zu identifizieren, die die Zweigenergien des Systems im erlaubten Betriebsbereich halten können. Zusätzlich werden Freiheitsgrade der Kreisströme und der Nullspannung formuliert. Wie für MMC-basierte Topologien erwartet, können sie zur Reduzierung der Energiepulsationen der Zweige eingesetzt werden. Mit der vorgestellten Modellbeschreibung ist es möglich, neue Optimierungsverfahren unter Einbeziehung aller Freiheitsgrade durchzuführen, die eine Reduzierung der Energiepulsationen ermöglichen.

Die einfache Ableitung der Transformationsvorschrift bietet auch die Grundlage für den Entwurf komplexer Regelalgorithmen. Die Beschreibung in Matrixnotation erlaubt darüber hinaus eine einfache Implementierung einer modellbasierten, prädiktiven Regelung (MPC) der AC-Seite. Abschließend werden die entwickelte Energieregung, Energiehubreduktion, Entkopplung und Stromregelungen mit einem Laboraufbau validiert.

Acknowledgements

I would like to use this opportunity to thank all those involved in my private and professional environment, who have supported me during my doctoral studies. This was the only way to successfully complete my studies.

I express my sincere thanks to Prof. Dr.-Ing. Marc Hiller for his support and advice and for giving me the opportunity to work on this topic in a very free way. I thank Prof. Dražen Dujčić for his interest in my work and for being the co-examiner. I would also like to thank Prof. Dr.-Ing. Michael Braun, who first provided me with the opportunity to accept a position as a research assistant at the ETI.

The open, honest and constructive nature of the working environment at the ETI was definitely decisive for the success of my work. Therefore, I would like to express my heartfelt thanks to all ETI employees and friends for their constant support. Especially Patrick Himmelmann and Mathias Schnarrenberger had countless relevant and irrelevant discussions with me. Likewise, of course, Stefan Mersche, who first during his master thesis and later as a colleague always provided me with advice and support. And even when Matthias Brodatzki moved out, he was never gone. He provided additional motivation to finish my thesis. Our DnD party is waiting for us! A special thanks to Felix Kammerer and Johannes Kolb, who introduced me to modular multilevel converters. I would also like to thank Prof. Veit Hagenmeyer and Prof. Lutz Gröll from IAI for the numerous discussions on control engineering and optimization methods.

This work would not have been possible without my wonderful wife Rebecca. Thank you for the everlasting support and motivation. Even during a pandemic, we always had something to laugh about, together with our children Ragnar and Juna. This would not have been possible without all of you!

Dennis Bräckle, September 2021

Contents

1	Introduction	1
1.1	State of the Art	3
1.1.1	Approaches to Modelling the Overall System	4
1.1.2	Methods for the Reduction of Energy Pulsation	6
1.1.3	Requirements as Grid Connected Power Converter	9
1.2	Contribution of this Thesis to the Grid Connected MMC	10
1.2.1	Outline	12
2	Modelling of the Modular Multilevel Converter	15
2.1	Problem Description	16
2.2	System Equations	20
2.2.1	Physical Modelling	20
2.2.2	Control Engineering Modelling	23
2.3	System Analysis	30
2.3.1	Currents of the MMC	31
2.3.2	Energies of the MMC	33
2.4	Conclusion of this Chapter	35
3	Optimal Feed Forward Control for Reduction of Energy Pulsation	37
3.1	Power Feed Forward Control	39
3.1.1	Minimization of the RMS Value of the Arm Currents	41
3.1.2	Minimization of the Arm Current Under Consideration of the Average Energy Value	42
3.1.3	Analytical Compensation of the 2nd Harmonic	47
3.1.4	Disadvantages of the Analytical Compensation of the 2nd Harmonic	49
3.1.5	Parameter Optimization to Reduce the Energy Pulsation	51

3.1.6	Function Optimization	54
3.1.7	Results of the Function Optimization	56
3.2	Comparison of the Arm Currents With Different Compensation Methods	57
3.3	Reduction of the Energy Pulsation at Different Operating Points	62
3.4	Exemplary Calculations for an HVDC Converter	66
3.5	Conclusion of this Chapter	69
4	Energy and Current Feedback Control of the MMC	71
4.1	Energy control	73
4.1.1	Analysis of the Occurring Arm Powers	74
4.1.2	Energy Controller	80
4.2	Control of the DC Current and Internal Currents	83
4.2.1	Control of the DC current \tilde{x}_2	84
4.2.2	Control of the Internal Currents \tilde{x}_3 and \tilde{x}_4	86
4.2.3	Limitation of the Output Variables	88
4.3	Control of the AC grid side	91
4.3.1	Fundamentals of model-based control of the AC side	93
4.3.2	Optimal Output Trajectories by Solving the quadratic programming (QP)	104
4.3.3	Control Loop to Determine the Grid Angle	106
4.3.4	Simulation Results	110
4.4	Conclusion of this Chapter	118
5	Laboratory Setup for Validation of the Control Algorithms	121
5.1	Description of the power electronics	122
5.1.1	Laboratory Prototype of the MMC	124
5.2	Description of the Signal Processing Unit	126
5.2.1	Cell Control	128
5.2.2	Central field-programmable gate array (FPGA) of the Laboratory Setup	130
5.2.3	Timing of the System	131
6	Measurement Results	135
6.1	Quasi Stationary Operation of the System	135
6.1.1	Dynamic Load Step at the AC Side	138
6.1.2	Reduction of the Energy Pulsation	142
6.2	Response of the Converter in Case of a Grid Fault	148
6.2.1	Laboratory Setup for the Investigation of Grid Faults	148

6.2.2	Stable Operation During Grid Faults	149
6.2.3	Reduction of the Energy Pulsation During Grid Fault . . .	154
6.3	Conclusion of this Chapter	155
7	Conclusion	157
A	Appendix	161
A.1	System Matrices of the MMC with Uncoupled Arm Inductors . . .	161
A.2	System Matrices of the MMC with Coupled Arm Inductors . . .	163
A.3	Inverted System Matrices	166
A.4	Inverted and Transformed System Matrices	167
A.5	Calculation of Intrinsic Energy Pulsations	168
A.6	Power Transformation Matrices	171
A.7	Hesse-Matrix	172
A.8	Timevariant Vector $\underline{\Theta}_k$ of the Cost Function	174
A.9	Timevariant Scalar θ_k of the Cost Function	176
A.10	AC Current Trajectory in XY Representation	176
	List of Symbols	179
	List of Figures	183
	List of Tables	187
	Bibliography	189

Chapter 1

Introduction

Grid expansion is the backbone of the energy transition. Today, electricity is increasingly generated at decentralized locations. Especially in Germany, renewable electricity has to be transported from the sea and windy coasts to the consumption areas in the centre of the country. The energy grid and its components need to be improved, strengthened and expanded. Therefore, the growing task of future energy distribution is the focus of recent research. A key question to be answered is how to ensure grid stability and reliable supply of sustainable electrical energy to the public and industry in the coming years.

The grid of the future will fundamentally differ from today's energy grid. The steady increase of renewable energies in the gross energy generation in Germany will lead to more and more power electronics being used for feeding into the grid [1]. Today, synchronous machines, which still dominate power generation, bring large flywheel masses and thus stability to the grid. Converter-fed systems do not have these properties or only to a limited extent [2]. In consequence, it has to be assured that a grid dominated by power electronics does not lead to instabilities and unreliable energy supply. A variety of algorithms and methodologies exist to ensure system stability [3–8]. These methods require actuators, which in turn provide satisfactory control of the setpoint specifications of the higher-level grid control.

Additionally, inverters already need to be able to contribute to the support of the grid and fault-clearing in the event of a grid disturbance. Converters have to comply with the standards [D1–D4] for software and hardware design. One

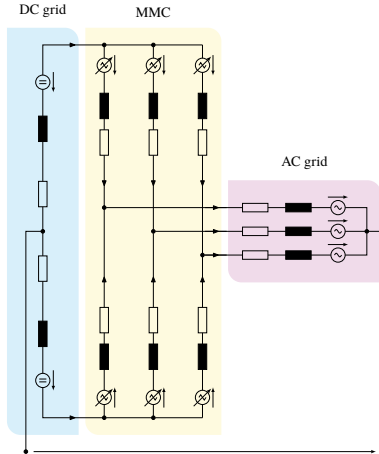


Figure 1.1: Schematic representation of the modular multilevel converter (MMC), that is the basis for the analysis and control design throughout the thesis at hand.

of the most important points is the supply of a sufficient amount of current in case of a short circuit. This is an unwanted and disadvantageous yet mandatory state of operation for the inverter and represents one of the greatest challenges for power electronics. The short-circuit current has to be taken into account when designing power semiconductors. They have to be thermally capable of carrying a required current. In addition, the semiconductor’s maximum current needs to remain within the safe operating area while providing sufficient margin to the device’s short-circuit detection. The control system has to have the necessary dynamics to ensure stable operation during grid fault.

The modular multilevel converter (MMC) as shown in Fig. 1.1 is a topology which was presented in 2002 [9, 10] and has since become established as the system of choice when it comes to the transmission of large amounts of power over long distances [11]. The development of multilevel converters enables the continuing development of larger high and extra-high voltage grids, both AC grids and DC grids [12–14]. In addition to transporting large amounts of electrical energy, modular multilevel converters are also used as components to improve the quality of the grid voltage. They support the grid as flexible AC transmission systems (FACTS) or static synchronous compensator (STATCOM) by making

use of the existing line capacities and by providing reactive power [15, 16]. The topology is also considered promising for use as DC breakers in extensive DC networks [17–20] or for use as galvanic isolation [21, 22]. The MMC is also becoming increasingly popular as drive converter [23–25].

The MMC control has to be designed to meet the requirements for grid connected power converters. Therefore, a high degree of model understanding of the converter, the controlled system and the electrical network is required. This enables control strategies to be developed, in order to support the network as well as ensure the safe operation of the converter.

For each system based on the MMC a specific approach is followed for energy control or voltage control [23, 26–34]. The thesis at hand develops a systematic control engineering derivation of the model equations and pursues a generalized description for MMC based systems. In contrast to the known methods, all MMC based systems can be described using the presented approach. This results in degrees of freedom for controlling and improving the inherent energy pulsations of the system [35, 36]. No additional investigation on power balancing terms needs to be performed. The presented description offers the possibility to calculate optimal current trajectories to reduce the energy pulsations in the system. Furthermore, a highly dynamic AC grid current control is designed for the MMC. An implementation on a laboratory scaled setup is presented to verify the superiority to state of the art grid control and reduction of energy pulsation approaches even during grid fault events.

1.1 State of the Art

Different approaches to modelling MMC topologies already exist as seen in Fig. 1.2. All approaches are designed to generate a model understanding in order to develop different approaches to control the system. All ideas have pros and cons, depending on what is to be investigated. Different approaches can be divided into switched models and averaging models as described below. From these system equations, rules for decoupling the system can be derived. The decoupling sets the basis for the approaches of current control and energy control in the system. Different mechanisms allow a reduction of the energy pulsation in the energy storages in certain operating points. With this understanding, a grid-compatible operation of the system is subsequently possible.

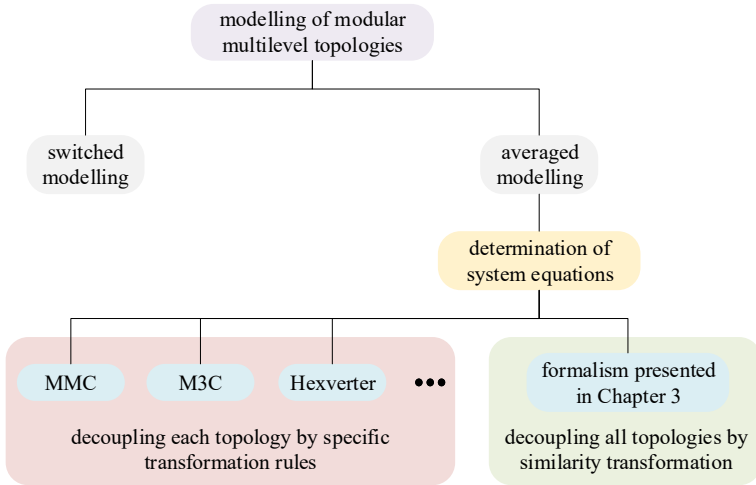


Figure 1.2: Visualization of different state of the art modelling approaches compared to the formalism presented in this thesis

1.1.1 Approaches to Modelling the Overall System

Switching and Averaging Models

The multilevel converter consists of a series connection of electrical two-poles with an energy storage device. For modelling purposes, each cell can be regarded as a switching component of the model. For modelling on the basis of switched components, each power semiconductor can be taken into account during modelling. If the individual cells are designed as full bridges, eight times as many power semiconductors have to be considered for the overall simulation with hundreds or thousands of cells. The level of detail ranges from simple ohmic representations of the switches to the non-linear characteristic curve for each semiconductor [37]. The results of the simulations are therefore more accurate. However, the effort and computing time involved in the development and design of the higher-level inverter control is not acceptable. Each additional cell, increases the simulation effort and expense unacceptably.

A significant reduction of the modeling effort is achieved by an average value analysis of the switched system. In order to simulate the behavior of the MMC, the series connections of the cells are solely modelled as adjustable voltage sources. It has already been shown that this type of modeling is sufficiently accurate with a small number of cells [37–41]. In order to be able to design and verify a draft of the voltage, energy and current controls without disproportionately high simulation effort, this type of modelling is the method of choice. It will be pursued further in this thesis.

Differential Equations of the System

The physical correlations in the system have to be described based on the approximation of the inverter arms as adjustable voltage sources. The 3AC-DC-MMC has already been modelled and the fundamental differential equations were set up to describe the physical relationships [23, 42, 43]. The procedures were further investigated and improved [44]. For the coupling of two or more DC or AC voltage systems, further topologies based on the MMC have been developed and investigated. These include the modular multilevel matrix converter [27, 45] and the hexverter [46]. Furthermore, galvanic isolating topologies and solid state transformers are more and more in the focus of scientific research [21, 22]. For the establishment of the system equations general approaches are pursued [31, 47].

The currents of a modular converter system for coupling two or more grids consist of a superposition of the currents at the terminals of the converter as well as circulating currents that do not affect the external terminals. For the control of the topologies based on the MMC, a decoupling of the system is desired. In particular, the decoupling for the MMC system by an amplitude-invariant Clarke transformation [48] with subsequent summation and difference calculation has become generally accepted. For other topologies [27, 45, 46] this procedure was extended according to [49]. For subsequent considerations, a decoupling based on an analysis of the systems according to Kirchhoff's laws [50] is assumed.

Others pursue a representation in the state space domain [51, 52]. In principle, this form of representation has the advantage that mathematical tools of control engineering can easily be applied with regard to the application and design of the control algorithms. However, the transformation rules need to be developed for each and every topology separately.

The thesis at hand presents a new formalism which allows a simple decoupling of any MMC based topology using mathematical methods. Therefore, topology specific decoupling rules do not have to be identified any more. The transformation matrices result from a simple similarity transformation of the system equations. In addition, the notation is transferred to the standard of common control engineering. Thus, an easy and fast interchange with other scientific fields is possible. This provides access to sophisticated design and optimization algorithms which allow a superior control of the system. The energy control is subsequently easily performed by analyzing the decoupled system equations.

1.1.2 Methods for the Reduction of Energy Pulsation

When designing MMC systems, many parameters and boundary conditions have to be considered. The total capacitance is of special importance [24, 53–55] for the use as drive converter and as grid converter in an high voltage direct current (HVDC) systems. Compared to conventional 2- or 3- level inverters, the required total capacitance of the MMC is much larger [56]. A reduction of the required converter capacitance is directly associated with a saving in costs and footprint. In addition, insulated gate bipolar transistor (IGBT) modules for low or medium voltage are becoming more and more performant [57, 58], while capacitors are improving less rapidly in terms of energy density, losses, load ratings and costs. All MMC topologies have in common that energy has to be stored periodically for stationary operation. This energy pulsation depends, among other things, on the operating point, phase angle and grid currents. For a given capacitor, the current and thus the power of the inverter is limited. When it becomes possible to drive more current with the same module size and the same cooling, the expansion of converter capacitance in the MMC is mandatory.

The converter has to be able to carry the fault current in the event of an AC or DC grid fault. The energy pulsations increase dramatically during the change of the operating point or under unbalanced load conditions. In general, those operating points are very decisive for the required maximum energy in the cell capacitors and are often the key factor when designing the system. In order to make the best possible use of the converter's capacitors, the focus is put on methods to reduce these energy pulsations utilizing circulating currents [59, 60].

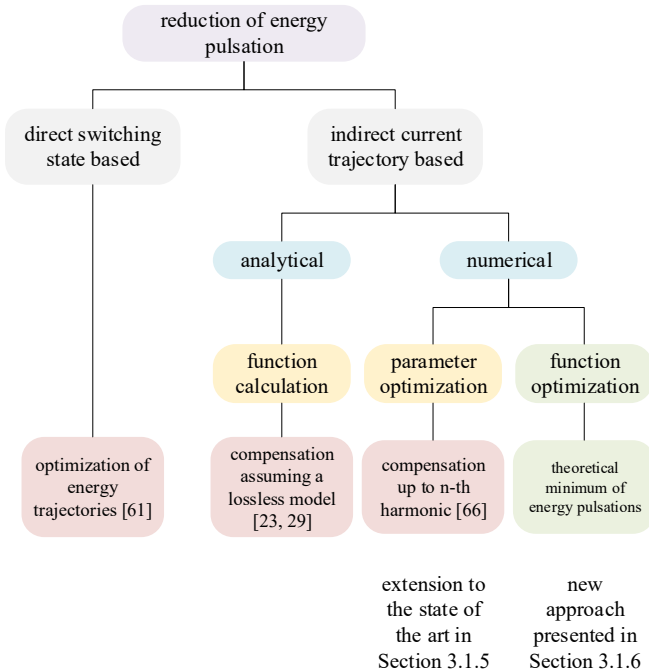


Figure 1.3: Classification of different approaches to the reduction of energy pulsation.

The different approaches for reduction of energy pulsation can be classified into analytical approaches and numerical approaches as presented in Fig. 1.3.

A distinction can be made between direct and indirect approaches to reducing the energy pulsations. The direct approach calculates the trajectory of the energies for each control interval depending on the switching states in the next control interval [61]. The optimal consecutive switching states are selected for each arm. This approach determines the local minimum in the next clock step. However, the calculation effort increases disproportionately with the number of possible switching states.

Using the indirect approach, current trajectories for reducing the pulsation of the energies are determined based on the operating point. The analytical approach is well known. It was already elaborated in [23, 33]. Assuming a lossless system, sinusoidal power terms, which eliminate the energy pulsations with the second and 4 harmonic of the grid frequency, can be calculated analytically. The terms can be calculated online or offline and stored in lookup tables for the entire operating range of the inverter [62]. These approaches are extended with regards to the total arm current [63, 64] and to other MMC based topologies [27, 45]. In addition, pulsations can be reduced during transient events at the terminals if an analytical description is available [26, 29]. The main advantage of those approaches is the straightforward calculation and implementation of the compensating terms. The disadvantage of this approach is the assumption of a lossless model with small arm inductances. Otherwise, a closed analytical solution cannot be given.

Numerical approaches have focused on the compensation of harmonic frequencies in the energy pulsation [65], as well. The approaches can be summarized as parameter optimization methods. The assumption of a lossless system is no longer required. The idea is to model the circulating currents as a superposition of sinusoidal waveforms of the second and fourth harmonics. Considering the limits of the system, the coefficients of the functions are calculated to minimize the energy pulsation [66].

In contrast to the known methods, the modelling of the system presented in this thesis opens up the possibility to formulate the energy pulsations of the system as an optimization problem. Building on the state of the art, a Fourier approach to the first n harmonics in the energy pulsation can be used to reduce the pulsations. In addition, a new procedure using function optimization is presented and provides the current trajectories that result in the minimum energy pulsation for any given operating point. The circulating currents are no longer required to be harmonics of the grid frequency. The optimization calculates current and voltage reference trajectories and not coefficients of given sinusoidal functions. By definition, this approach is the optimal solution with respect to the given constraints. In combination with a robust grid-side current control as well as a fast and accurate determination of the grid angle, the maximum energy pulsation is reduced, even in the event of a grid disturbance.

1.1.3 Requirements as Grid Connected Power Converter

The increasing share of renewable energies such as wind power or photovoltaics also requires an increasing share of power electronics in the grid. In order to continue to operate the grid in a stable condition, the active elements also have to be able to operate reliably under non-ideal grid conditions [1, 67]. This includes overvoltages as well as harmonics in the mains voltage and current or other transient events. At the minimum, however, they must provide support in case of a low voltage ride through (LVRT) and must not immediately disconnect from the grid. Different standards [D1–D4] define the requirements for the operation of power electronics for feeding into the electrical grid. In order to meet the requirements of the grid codes, the grid-side regulation of the active feed-in systems must be closely examined. This applies not only to MMC systems, but to all topologies connected to the public grid.

One of the central issues is the correct and fast determination of the phase angle of the mains voltage. Phase angle and frequency are determined via phase locked loop (PLL) or frequency locked loop (FLL) [68–71]. This enables a phase-correct adjustment of the mains current and thus the active and reactive power. Even in the event of a fault, it has to be possible to reliably determine the grid angle in order to meet the requirements of the feed-in standards. A double synchronous reference frame (DSRF)-PLL [68] provides a good tradeoff between complexity, dynamics and stability to determine the mains angle and forms the basis for the AC-side control of the MMC of this work.

For the current control of the AC side, proportional-integral (PI) controllers with feed forward control in the rotating reference frame or proportional-resonant (PR) controllers [72] in the stationary reference frame are often used in conventional inverters. A disadvantage of the control structures is that they must be set and track frequency-selectively. They precisely regulate the current sinusoidally and stationarily. The complexity is increased by additional LCL filters. By using active or MMC based filters, the passive components become smaller and the grid side control can be designed straightforward [73]. When controlling current harmonics, additional controllers need to be implemented for each frequency separately [68, 71].

To even reduce the effort with higher harmonics, trajectory-based controls can be used. Model-based predictive approaches allow easy implementation of the control. These controls can be designed and implemented in a simple and fast

way with a mathematical description of the system. For grid and drive applications, these approaches are increasingly becoming the focus of research [74–77]. However, direct optimization of the switching times is less suitable for the control of the MMC, since the number of possible switching states rises sharply with an increasing number of cells.

As a result, optimization at high switching frequencies is no longer possible while meeting the real-time requirement. An indirect model-based predictive control (MPC) is an alternative capable of generating optimal setpoints. These are subsequently processed by a subordinate modulator into switching signals for the semiconductors [78]. This method is independent of the number of possible switching states and thus also suitable for use in MMC. The approach of an MPC for the overall control of the system is the subject of current research [79–81]. The solution of the optimization problem under compliance with the real-time condition is essential for the use of MPC in grid-supported converters. In this thesis an indirect approach and implementation for the control of AC currents which can be solved online meeting the real-time requirements at high control frequencies is presented.

1.2 Contribution of this Thesis to the Grid Connected Modular Multilevel Converter

Considering the state of the art, this thesis presents further developments in the field of modelling and controlling the MMC. The differential equations of the system are formulated. The equations are then converted to matrix notation and interpreted as state space equations. This results in a coupled, non-linear set of equations to describe the MMC.

In contrast to the known approaches to decouple the system, a fast and simple method using a similarity transformation is introduced. Until now, the decoupling of each MMC based topology had to be considered separately. Using the mathematical formalism presented, a decoupling of any given topology results directly from the equations. An application of any Clarke transform and sum and difference calculation is no longer necessary. In addition, the formalism presents all possibilities for energy control in the system not depending on the specific topology. The new decoupling and energy control formalism can be applied to well known topologies like the MMC as well as to more complex topologies like

the Square-wave Powered Modular Multilevel Converter (SPMMC) [30] or the Modular Multilevel Solid State Transformer (MMSST) [22].

This methodical approach permits a simple identification of the degrees of freedom of the system. Based on this, new methods for reducing the energy pulsations of the system are introduced. The degrees of freedom are determined based on the model equations by means of heuristic or deterministic optimization in such a way that the energy pulsation is minimized. This leads to optimal current and voltage trajectories. From the optimal feed forward control for energy deviation reduction and the decoupled system a regulation for the control of the energies can be derived. Due to the decoupling, the corresponding energy and current controllers can be easily designed.

In this thesis, the MMC in inverter operation is investigated. The DC voltage of the system is assumed as the disturbance vector and the DC current is set according to the AC power, losses and the total energy of the system.

In order to be able to operate the inverter as a grid-connected system, a trajectory-based, predictive controller for the AC side is presented. The current control is attributed to a quadratic programming (QP) problem. A real time capable solution of the problem with state variable limitation and control variable limitation is presented. The AC current control is performed in real time with the control frequency of the converter setup. In addition, a simple implementation of a double synchronous reference frame (DSRF)-phase locked loop (PLL) on an field-programmable gate array (FPGA) is given in order to be able to operate the system in a stable manner, even in case of a failure.

The realization on a low voltage prototype allows a final validation of the developed methods. The modelling provides the basis for the optimal reduction of energy pulsation of the system while meeting the confinements. With the model-based current control on the AC side, the MMC can also be operated with a lower energy deviation in the event of a fault and thus make better use of the installed hardware.

1.2.1 Outline

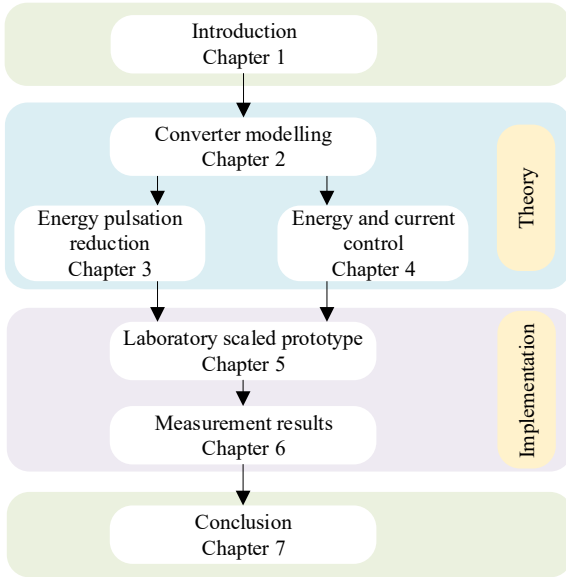


Figure 1.4: Outline of this thesis

The work is divided into 7 chapters

Chapter 2 The differential equations of the system are formulated. Through an interpretation as state variables a non-linear state space model of the MMC is established. Mathematical mechanisms are used to decouple the system and to identify the degrees of freedom which allow a control of the whole system.

Chapter 3 The control objectives are defined. The degrees of freedom in the system are identified and used in different methods of reduction of energy pulsation.

Chapter 4 The decoupled feedback control for the energies and currents of the system are introduced and designed. A highly dynamic AC-side control is designed and a grid angle identification is presented. Corresponding simulations validate the control.

Chapter 5 A laboratory setup used to verify the simulated algorithms is presented. A converter-based isolated grid allows the reliable reproducibility of critical grid states in order to be able to investigate the MMC also in case of grid failure. The control algorithms used are implemented on a low voltage prototype.

Chapter 6 Final measurement results of the described control algorithms are provided. Measurements on the laboratory grid as well as on the island grid are being presented to validate the modelling and control approach.

Chapter 7 The operation of the grid connected MMC is concluded. The results are summarized. Based on the new insights into MMC modelling and control provided, the feasibility as grid supporting converter is evaluated.

Chapter 2

Modelling of the Modular Multilevel Converter

The MMC topology has been known since the early 2000s [9] and has been used commercially since 2009 [82]. The converter is used mainly in high voltage direct current (HVDC) applications as well as in medium voltage drive applications. In addition to the MMC, various topologies such as the modular multilevel matrix converter (M3C) or the hexverter were presented and investigated [23, 27, 32]. To elaborate a suitable control structure of the converter, a mathematical model is necessary. There are many different starting points for modelling the system [12, 83]. The modelling can be carried out as averaged model or switched model.

For a new approach to modelling, a formalism is presented to describe and decouple topologies based on the MMC in a systematical manner. This formalism and decoupling was first presented in [E1] and ensures a uniform nomenclature throughout all MMC based topologies. In this context, the actual topology is not decisive. The formalism describes a general procedure to develop a model representation. Subsequently, it is easily possible to identify those degrees of freedom which allow the exchange of power between input and output side as well as the energy exchange between converter arms.

The control of the MMC has two objectives: First, the currents at the terminals to the connected grids need be controlled. Secondly, it has to be ensured that the stored energy is kept within a tolerance band. These control objectives are

generally pursued for all MMC topologies. Both aspects have been investigated with different emphases and approaches. They differ by focusing on switched or averaged models [38, 84], generalized approaches to determine the system equations [47, 85], straightforward Clarke transformation for decoupling [9, 12, 23, 83, 86] or deal directly with predictive control approaches [78].

The thesis at hand will focus on the averaged model for scalability and assurance of real-time capability of a digital signal processing system. Taking previous approaches into account, the system equations from the physical domain are derived. In contrast to the state of the art approaches for modelling, a generalized approach is presented that allows a fast and easy decoupling of any MMC topology. With the state space representation of the system and transition to control engineering notation, a simple similarity transform is applied. A decoupling of an MMC system is achieved without the application of Clarke transformations or sum and difference calculation of specific system equations. In addition, the energy control can be derived without additional calculations as in [23, 27, 30]. To be able to apply modern control algorithms like the MPC for grid current control, the systematic analytical state space model which can describe the converter comprehensively and mathematically correct is needed.

2.1 Problem Description

Figure 2.1 depicts the schematic of an MMC that couples a DC grid with a 3-phase AC grid. The MMC consists of the adjustable voltage sources v_{1-6} , the arm inductors L and the parasitic resistors R including the semiconductor losses. V_{dc} , R_{dc} and L_{dc} model the connected DC network. v_{s1-s3} , R_{ac} , and L_{ac} represent a three-phase grid. Each of the voltage sources v_{1-6} represent one arm of the MMC and consist of a series connection of cells.

Many different cell topologies have been proposed [87]. The most common topologies are the full bridge cell and the half bridge cell [12] shown in Figs. 2.2 (a) and 2.2 (b). Both topologies consist of a local energy storage capacitor C_{cell} and switches. From an electrical point of view, the cells are a two-pole circuit with no external power supply. The full bridge cell can provide the average cell voltage v_{cell} with $-v_C \leq v_{cell} \leq +v_C$. The half-bridge cell, on the other hand, can provide a voltage range of $0 \leq v_{cell} \leq +v_C$. The voltage of an arm results from the sum of all cell voltages.

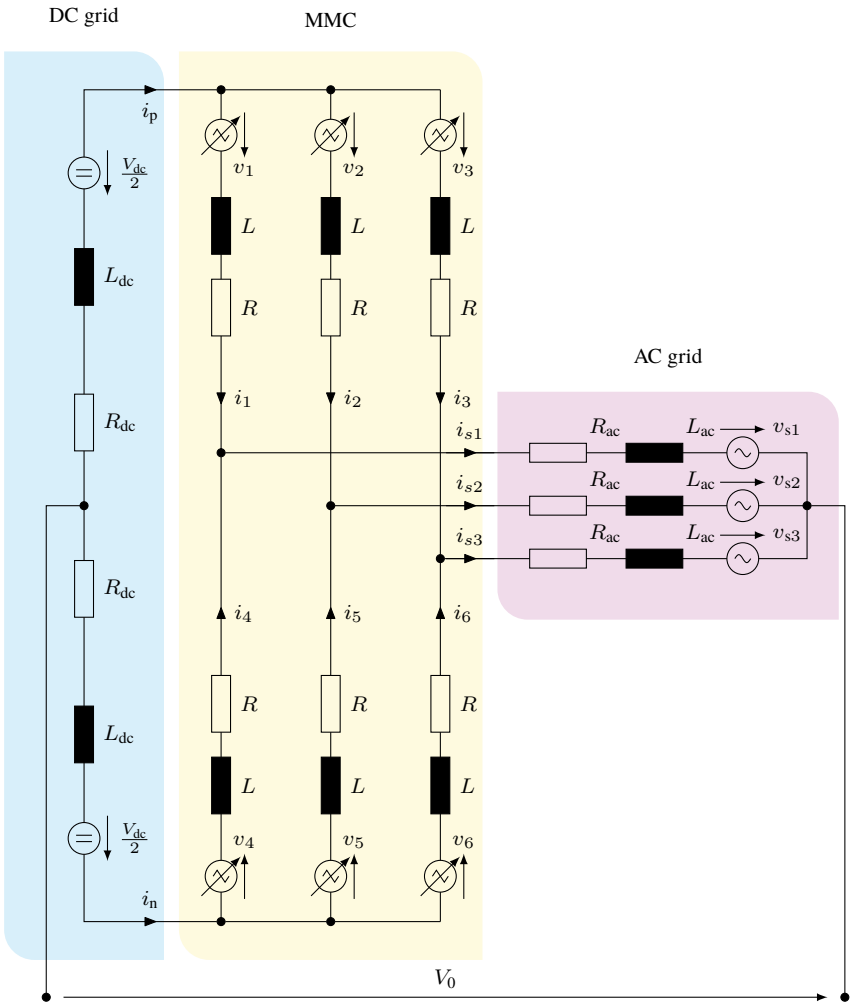


Figure 2.1: Circuit diagram of the MMC

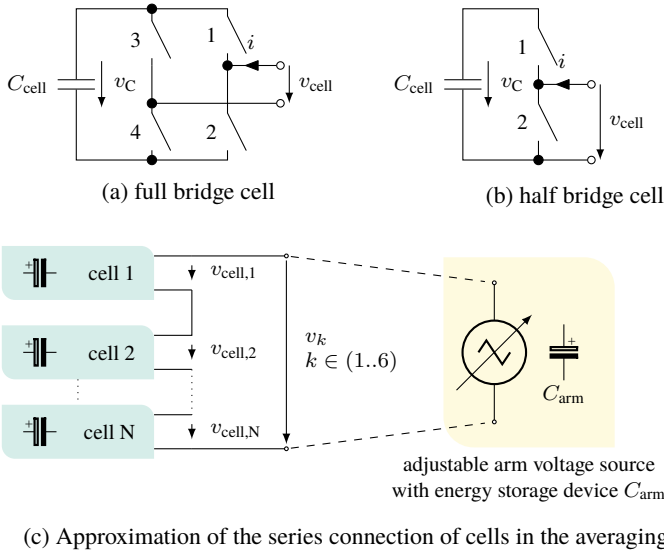


Figure 2.2: The two most common cell topologies and the series connection in the averaging model.

Figure 2.2 (c) illustrates the approximation of the series connection of N cells per arm. In the averaged model each series connection is assumed to be an adjustable equivalent voltage source $v_k, \in (1..6)$ with an equivalent capacitor C_{arm} . Assuming the same voltage for every arm capacitor, the arm capacitance is calculated on average by $C_{arm} = \frac{1}{N} C_{cell}$ [23]. With suitable modulation of the cells and with sufficiently large N the model errors for the analysis can be neglected [23, 27, 30] and an approximation as adjustable voltage sources is feasible.

Since each cell contains an energy storage device, it must be ensured that the energy is evenly distributed within an arm. There are different methods of balancing the energy among the cells in each arm [23]. The total arm voltage $v_{C,arm}$ is then equal to the sum of all cell voltages $v_{C,arm} = \sum_{m=1}^N v_{C,cell,m}$. Therefore the arm voltages v_{1-6} for the full-bridge MMC is given by $-N v_C \leq v_{1-6} \leq +N v_C$. The voltages v_{1-6} are used to control the arm currents i_{1-6} and in con-

sequence the grid currents. The possible voltage range at the terminals of an arm k is given by

$$-v_{C,\text{arm},k} \leq v_k \leq v_{C,\text{arm},k} \quad (2.1)$$

The average of the voltage v_k can be set precisely by suitable modulation of the cells of the arms. In order to be able to easily perform an analytical examination of the model, the switching operations of the individual cells are neglected and an adjustable voltage source within an arm is assumed. More cells within the arm reduce the model error. The laboratory setup in Chapter 5 illustrates that even with $N = 5$ cells the error is negligible. In that chapter a sorting method is presented, which was already used in [23, 27, 30]. It ensures that the assumption that all cells have the same voltage and same stored energy is valid under all operating conditions. The adjustable voltage sources are used to set the control variables v_k .

However, considering the stored energies instead of the capacitor voltages has been found beneficial in modeling and controlling the cell voltages of MMC based systems. The measured cell voltages v_{Ck} can be recalculated into arm energies w_k using

$$w_k = \sum_{n=1}^N \frac{1}{2} C_{\text{cell}} v_{C_{n,k}}^2 = \frac{1}{2} C_{\text{arm}} v_{C,\text{arm},k}^2; \quad k = 1, \dots, 6. \quad (2.2)$$

The arm capacitance results as a degree of freedom in hardware design when modelling the system with energies. The occurring energy pulsations only depend on the operating point. The average value of the stored energy is irrelevant in this context. Likewise, the absolute value of the pulsations is independent of the actual hardware of the system. Once the maximum pulsations occurring for a system have been elaborated, the capacitance can be chosen accordingly to ensure that the safe operating area of the capacitors and semiconductors is not exceeded at any given time. Therefore energy instead of capacitor voltage is considered for the energy control of the system within this thesis.

In order to meet the requirements of controlling the grid currents and keeping the energies within their permissible limits, a physical model is developed and subsequently transferred to the control engineering domain in the following sections.

2.2 System Equations

The modelling is carried out in two stages. First, a physical model for the arm currents and arm energies is established. In the second step, a control engineering model is determined on the basis of the physical equations. Based on this model, current and energy control of the system can be elaborated.

2.2.1 Physical Modelling

First the Kirchhoff's circuit laws [50] for the currents and voltages are applied and solved. Then, equations for the energy stored are set up and investigated. It is assumed that all arm inductances L and parasitic resistors R are the same throughout the whole converter. R includes the ohmic losses of the inductances as well as the approximated semiconductor losses.

Modelling of the arm Currents

For each inductor current $i_{1..6}$ an equation of the form

$$\begin{aligned}
 L \frac{d}{dt} i_k &= -v_k - R i_k + \frac{V_{dc}}{2} - R_{dc} i_p \\
 &\quad - L_{dc} \frac{d}{dt} i_p + V_0 - v_{sk} \\
 &\quad - L_{ac} \underbrace{\left(\frac{d}{dt} i_k + \frac{d}{dt} i_{k+3} \right)}_{i_{s,k}} - R_{ac} (i_k + i_{k+3}); k = 1, 2, 3 \quad (2.3)
 \end{aligned}$$

or

$$\begin{aligned}
 L \frac{d}{dt} i_k &= -v_k - R i_k - \frac{V_{dc}}{2} - R_{dc} i_n \\
 &\quad - L_{dc} \frac{d}{dt} i_n + V_0 - v_{sk-3} \\
 &\quad - L_{ac} \underbrace{\left(\frac{d}{dt} i_k + \frac{d}{dt} i_{k-3} \right)}_{i_{s,k-3}} - R_{ac} (i_k + i_{k-3}); k = 4, 5, 6 \quad (2.4)
 \end{aligned}$$

can be specified. Furthermore, the secondary condition that the sum of all currents must be 0 applies, since the star points of the AC side and DC side are not connected.

$$\sum_{k=1}^6 i_k = 0 \quad (2.5)$$

The Eqs. (2.3) to (2.5) can be transformed into a system of ordinary differential equations in matrix notation.

$$\begin{aligned} \underline{L} \frac{d}{dt} \underline{i} = & -L_{ac} \underline{M}_a \frac{d}{dt} \underline{i} - R_{ac} \underline{M}_a \underline{i} - L_{dc} \underline{M}_{dc} \frac{d}{dt} \underline{i} - R_{dc} \underline{M}_{dc} \underline{i} \\ & - \underline{M}_s \underline{v}_s - \underline{R} \underline{i} - \underline{v} \\ & + [1 \quad 1 \quad 1 \quad -1 \quad -1 \quad -1]^\top \frac{V_{dc}}{2} + V_0 \end{aligned} \quad (2.6a)$$

$$0 = [1 \quad 1 \quad 1 \quad 1 \quad 1 \quad 1] \underline{i} \quad (2.6b)$$

\underline{i} , \underline{v} and \underline{v}_s are vectors of the corresponding numbered values. \underline{R} is a diagonal matrix with the parasitic resistors R as entries.

$$\underline{R} = R \cdot \underline{I}_6 \quad (2.6c)$$

\underline{I}_6 describes the 6×6 identity matrix.

The inductance matrix \underline{L} describes the arm inductors. In Fig. 2.1 the arm inductors are not coupled. It follows that \underline{L} is also a diagonal matrix with the arm inductances L as entries.

$$\underline{L} = L \cdot \underline{I}_6 \quad (2.6d)$$

Additionally, the arm inductors might also be coupled [53]. This means that the upper and lower arm are inductively coupled with one core. As a result, only the leakage inductance of the coupled reactors is effective on the AC side which

will be shown by decoupling the system equations later. This leads to a further coupling of the system via the inductance matrix and the following applies

$$\underline{L} = \begin{bmatrix} L + L_\sigma & 0 & 0 & -L & 0 & 0 \\ 0 & L + L_\sigma & 0 & 0 & -L & 0 \\ 0 & 0 & L + L_\sigma & 0 & 0 & -L \\ -L & 0 & 0 & L + L_\sigma & 0 & 0 \\ 0 & -L & 0 & 0 & L + L_\sigma & 0 \\ 0 & 0 & -L & 0 & 0 & L + L_\sigma \end{bmatrix} \quad (2.6e)$$

L is the main inductance and L_σ the leakage inductance of the coupled arm inductors. For the basic consideration it is irrelevant whether coupled inductors are used in the actual system implementation or not. In the following, uncoupled inductors are assumed without restriction of the generality. The matrices \underline{M} are defined as

$$\underline{M}_a = \begin{bmatrix} \underline{I}_3 & \underline{I}_3 \\ \underline{I}_3 & \underline{I}_3 \end{bmatrix} \quad (2.7a)$$

$$\underline{M}_{dc} = \begin{bmatrix} 1_3 & 0_3 \\ 0_3 & 1_3 \end{bmatrix} \quad (2.7b)$$

$$\underline{M}_s = \begin{bmatrix} \underline{I}_3 \\ \underline{I}_3 \end{bmatrix}. \quad (2.7c)$$

Where \underline{I}_3 is the 3×3 identity matrix and 1_3 as well as 0_3 are 3×3 matrices filled with 1 or 0 respectively.

Modelling of the Arm Energies

The voltage sources v_k with $k = 1 \dots, 6$ are equipped with an energy storage device C_{arm} that holds the energy w_k $k = 1, \dots, 6$. For safe operation of the converter, these energies must remain within certain limits. Therefore, equations are required to describe the energy of the voltage sources. The arm energy w_k is calculated as an integral of the arm power p_k .

$$\frac{d}{dt} w_k = p_k = i_k \cdot v_k; \quad k = 1, \dots, 6 \quad (2.8)$$

The stored arm energies represent additional state variables which are included in the control and are kept within a tolerance band.

Table 2.1: Mapping of the physical quantities to control engineering quantities.

	physical	control
state space variable (i directly, w indirectly measurable)	i_{1-6} w_{1-6}	x_{1-6} x_{7-12}
input variable	v_{1-6}	u_{1-6}
disturbance variable (measurable)	v_{s1-3} V_{dc}	z_{1-3} z_4
output variable	$i_{s,k}$ $k = 1,2,3$	y_k
reference variable	$i_{sk,ref}$ $k = 1,2,3$	$y_{k,ref}$

2.2.2 Control Engineering Modelling

In order to establish a state space model of the converter, the physical quantities are mapped to control engineering quantities. In Table 2.1 the mapping of the variables is given. To establish a standard control structure, the system of equations Eqs. (2.6) and (2.8) is resolved to $\frac{d}{dt}i$ and mapped according to Table 2.1. Together with Eq. (2.8), a state space representation results, which reads in the control engineers notation according to Table 2.1 as

$$\dot{\underline{x}}_{1-6} = \underline{A} \underline{x}_{1-6} + \underline{B} \underline{u} + \underline{F} \underline{z} \quad (2.9a)$$

$$\dot{\underline{x}}_{7-12} = \underline{u} \odot \underline{x}_{1-6} \quad (2.9b)$$

$$\underline{y} = \underline{C} \underline{x}_{1-6} \quad (2.9c)$$

Here \odot denotes the Hadamard product - the component-wise multiplication of the vector entries. The matrices \underline{A} , \underline{B} , \underline{F} and \underline{C} are dense matrices and describe the MMC system. Equations (A.1a) to (A.1e), (A.2a) to (A.2e), (A.3a) to (A.3d) and (A.4a) represent the system matrices and are given in the appendix for reasons of clarity. Note that in addition to reformulation and variable renaming, a normalization based on the SI unit standard is carried out. Therefore, all matrices consist of unit-free numbers and the signals are unit-free, too.

The system matrix \underline{A} depends on the arm inductance L and the arm resistance R . In addition, the DC side inductance L_{dc} and resistance R_{dc} as well as the AC side parameters L_{ac} and R_{ac} influence the system matrix. The input matrices \underline{B} and \underline{F} only dependent on the inductances L , L_{dc} and L_{ac} . Since the output currents $\dot{i}_{s,1-3}$ are described by the arm currents \dot{i}_{1-6} , the output matrix \underline{C} is only filled with 1. The matrices shown describe the system with uncoupled arm inductors. In Sec. A.2 Eqs. (A.5a) to (A.5e), (A.6a) to (A.6e), (A.7a) to (A.7d) and (A.8a) are given for coupled arm inductors.

System Decoupling

The derived system matrices are dense and coupled. In order to control the currents and energies as easily as possible, the system has to be decoupled. There are different approaches for decoupling [42, 88, 89], all using basically the Clarke transformation of certain variables. In the following, a new approach to the mathematical derivation of decoupling is presented based on a similarity transformation. Since the matrices \underline{A} and \underline{B} are symmetrical, they both can be diagonalized with an orthogonal matrix. Furthermore, $\underline{A}\underline{B} = \underline{B}\underline{A}$ applies. Therefore a matrix \underline{T} exists, which diagonalizes both matrices equally [90, p. 172]. This transformation matrix \underline{T} is calculated with the eigenvectors λ_i of the system matrix \underline{A} . The eigenvalues of the system matrix are calculated as

$$eig(\underline{A}) = \begin{bmatrix} 0 \\ -\frac{-R+3R_{dc}}{L+3L_{dc}} \\ -\frac{R}{L} \\ -\frac{R}{L} \\ -\frac{R+2R_{ac}}{L+2L_{ac}} \end{bmatrix} \quad (2.10)$$

The matrix \underline{A} has the eigenvalue 0 as shown in Eq. (2.10), which means that the system is overdetermined. Physically, this leads to the fact that only 5 of the arm currents can be set freely using the 6 arm voltages. Only 5 of 6 currents may be chosen independently, since the neutral points are not connected and Eq. (2.5) must be satisfied.

The corresponding eigenvectors are chosen to form an orthogonal matrix. As a result the transformation matrix is

$$\underline{T} = \begin{bmatrix} \frac{1}{\sqrt{6}} & \frac{1}{\sqrt{6}} & \frac{1}{\sqrt{6}} & \frac{1}{\sqrt{6}} & \frac{1}{\sqrt{6}} & \frac{1}{\sqrt{6}} \\ -\frac{1}{\sqrt{6}} & -\frac{1}{\sqrt{6}} & -\frac{1}{\sqrt{6}} & \frac{1}{\sqrt{6}} & \frac{1}{\sqrt{6}} & \frac{1}{\sqrt{6}} \\ \frac{1}{2} & -\frac{1}{2} & 0 & -\frac{1}{2} & \frac{1}{2} & 0 \\ \frac{1}{\sqrt{12}} & \frac{1}{\sqrt{12}} & -\frac{1}{\sqrt{3}} & -\frac{1}{\sqrt{12}} & -\frac{1}{\sqrt{12}} & \frac{1}{\sqrt{3}} \\ -\frac{1}{2} & \frac{1}{2} & 0 & -\frac{1}{2} & \frac{1}{2} & 0 \\ -\frac{1}{\sqrt{12}} & -\frac{1}{\sqrt{12}} & \frac{1}{\sqrt{3}} & -\frac{1}{\sqrt{12}} & \frac{1}{\sqrt{12}} & \frac{1}{\sqrt{3}} \end{bmatrix} \quad (2.11)$$

The transformation matrix \underline{T} diagonalizes both the system matrix \underline{A} and the input matrix \underline{B} and thus decouples the system. This means that each transformed current can be set independently of the other currents. For the system with coupled inductors the same transformation matrix \underline{T} results. To decouple the system, a similarity transformation is performed and Eqs. (2.9a) to (2.9c) are multiplied by \underline{T} from the left

$$\underline{T} \dot{\underline{x}}_{1-6} = \underline{T} \underline{A} \underline{x}_{1-6} + \underline{T} \underline{B} \underline{u} + \underline{T} \underline{F} \underline{z} \quad (2.12)$$

For simplified notation, a tilde \sim denotes a variable in transformed coordinates. Thus

$$\tilde{\underline{x}}_{1-6} = \underline{T} \underline{x}_{1-6} \quad (2.13a)$$

$$\dot{\tilde{\underline{x}}}_{1-6} = \underline{T} \dot{\underline{x}}_{1-6} \quad (2.13b)$$

$$\tilde{\underline{u}} = \underline{T} \underline{u} \quad (2.13c)$$

respectively

$$\underline{x}_{1-6} = \underline{T}^{-1} \tilde{\underline{x}}_{1-6} \quad (2.13d)$$

$$\dot{\underline{x}}_{1-6} = \underline{T}^{-1} \dot{\tilde{\underline{x}}}_{1-6} \quad (2.13e)$$

$$\underline{u} = \underline{T}^{-1} \tilde{\underline{u}} \quad (2.13f)$$

are defined, keeping in mind that \underline{T} is an orthogonal matrix. Therefore $\underline{T}^{-1} = \underline{T}^\top$ applies. This will expand Eq. (2.12) to

$$\underline{T} \dot{\underline{x}}_{1-6} = \underline{T} \underline{A} \underline{x}_{1-6} + \underline{T} \underline{B} \underline{u} + \underline{T} \underline{F} \underline{z} \quad (2.14)$$

$$\dot{\tilde{\underline{x}}}_{1-6} = \underline{T} \underline{A} \underline{T}^\top \tilde{\underline{x}}_{1-6} + \underline{T} \underline{B} \underline{T}^\top \tilde{\underline{u}} + \underline{T} \underline{F} \underline{z} \quad (2.15)$$

The transformed system matrices are defined as

$$\tilde{\underline{A}} = \underline{T} \underline{A} \underline{T}^\top \quad (2.16)$$

$$\tilde{\underline{B}} = \underline{T} \underline{B} \underline{T}^\top \quad (2.17)$$

$$\tilde{\underline{F}} = \underline{T} \underline{F} \quad (2.18)$$

and inserted into Eq. (2.15). \underline{T} then diagonalizes the system matrices \underline{A} and \underline{B} .

To simplify the output equation as well, Eq. (2.9c) is multiplied by $\underline{T} \underline{C}^\top$. This is possible without loss of information, since \underline{C}^\top has more rows than columns and consists of invertible submatrices. It therefore follows that

$$\underline{T} \underline{C}^\top \underline{y} = \underline{T} \underline{C}^\top \underline{C} \underline{x}_{1-6} = \underline{T} \underline{C}^\top \underline{C} \underline{T}^\top \tilde{\underline{x}}_{1-6} \quad (2.19a)$$

$\underline{C}^\top \underline{C}$ is also diagonalized by \underline{T} . Further

$$\tilde{\underline{y}} = \underline{T} \underline{C}^\top \underline{y} \quad (2.19b)$$

$$\tilde{\underline{C}} = \underline{T} \underline{C}^\top \underline{C} \underline{T}^\top \quad (2.19c)$$

are defined. Used in Eqs. (2.9a) to (2.9c) the system can be finally described in transformed coordinates

$$\dot{\tilde{\underline{x}}}_{1-6} = \tilde{\underline{A}} \tilde{\underline{x}}_{1-6} + \tilde{\underline{B}} \tilde{\underline{u}} + \tilde{\underline{F}} \underline{z} \quad (2.19d)$$

$$\dot{\underline{x}}_{7-12} = \underline{T}^\top \tilde{\underline{u}} \odot \underline{T}^\top \tilde{\underline{x}}_{1-6} \quad (2.19e)$$

$$\tilde{\underline{y}} = \tilde{\underline{C}} \tilde{\underline{x}}_{1-6} \quad (2.19f)$$

The system matrices $\tilde{\underline{A}}$, $\tilde{\underline{B}}$, $\tilde{\underline{F}}$ and $\tilde{\underline{C}}$ describe the MMC in transformed coordinates. These matrices are diagonal matrices with the exception of $\tilde{\underline{F}}$. Therefore, the currents of the system are decoupled.

The matrices are calculated as follows

$$\underline{\tilde{A}} = \begin{bmatrix} 0 & 0 & 0 & 0 & 0 & 0 \\ 0 & -\frac{R+3R_{dc}}{L+3L_{dc}} & 0 & 0 & 0 & 0 \\ 0 & 0 & -\frac{R}{L} & 0 & 0 & 0 \\ 0 & 0 & 0 & -\frac{R}{L} & 0 & 0 \\ 0 & 0 & 0 & 0 & -\frac{R+2R_{ac}}{L+2L_{ac}} & 0 \\ 0 & 0 & 0 & 0 & 0 & -\frac{R+2R_{ac}}{L+2L_{ac}} \end{bmatrix} \quad (2.20a)$$

$$\underline{\tilde{B}} = \begin{bmatrix} 0 & 0 & 0 & 0 & 0 & 0 \\ 0 & -\frac{1}{L+3L_{dc}} & 0 & 0 & 0 & 0 \\ 0 & 0 & -\frac{1}{L} & 0 & 0 & 0 \\ 0 & 0 & 0 & -\frac{1}{L} & 0 & 0 \\ 0 & 0 & 0 & 0 & -\frac{1}{L+2L_{ac}} & 0 \\ 0 & 0 & 0 & 0 & 0 & -\frac{1}{L+2L_{ac}} \end{bmatrix} \quad (2.20b)$$

$$\underline{\tilde{F}} = \begin{bmatrix} 0 & 0 & 0 & 0 & 0 \\ 0 & 0 & 0 & 0 & -\frac{\sqrt{6}}{2L+6L_{dc}} \\ 0 & 0 & 0 & 0 & 0 \\ 0 & 0 & 0 & 0 & 0 \\ \frac{1}{L+2L_{ac}} & -\frac{1}{L+2L_{ac}} & 0 & 0 & 0 \\ \frac{\sqrt{3}}{3L+6L_{ac}} & \frac{\sqrt{3}}{3L+6L_{ac}} & -\frac{2\sqrt{3}}{3L+6L_{ac}} & 0 & 0 \end{bmatrix} \quad (2.20c)$$

$$\underline{\tilde{C}} = \begin{bmatrix} 2 & 0 & 0 & 0 & 0 & 0 \\ 0 & 0 & 0 & 0 & 0 & 0 \\ 0 & 0 & 0 & 0 & 0 & 0 \\ 0 & 0 & 0 & 0 & 0 & 0 \\ 0 & 0 & 0 & 0 & 2 & 0 \\ 0 & 0 & 0 & 0 & 0 & 2 \end{bmatrix} \quad (2.20d)$$

The equations of the MMC with coupled inductors are given in Eqs. (A.9a) to (A.9d) respectively.

A decoupling of the MMC system equations is also achieved by using the well known state of the art approaches including Clarke transformations and sum and difference calculation. However, each MMC based topology can be described, using this same formalism and similarity transformation. The approach is not only limited to the DC-3AC-MMC as shown. In addition, this kind of notation of the system equation allows a fast and simple development of an superimposed energy control. Degrees of freedom are easily identified to control the arm en-

ergies independently. Additionally, a notation based on Table 2.1 opens up the possibility to apply advanced optimization methods for reduction of energy pulsation.

Significance of the Decoupling

Equations (2.19d) to (2.19f) and (2.20a) to (2.20d) describe the decoupled system. As the system matrices are diagonal matrices, each of the the currents $\tilde{\underline{x}}$ can be set individually by the corresponding control variable $\tilde{\underline{u}}$ without affecting the remaining ones. The first line of Eq. (2.19d) is a zero line. This line describes the current between the neutral points which is equal to zero regardless of the voltage \tilde{u}_1 . The voltage between the two neutral points is referred to as zero sequence voltage. The $\tilde{\underline{L}}$ -matrix shows the influence of the grid variables on the system. Line 2 of Eq. (2.19d) describes the influence of the DC side. Rows 5 and 6 describe the influence of the AC side. Both sides can be adjusted independently of each other. Rows 3 and 4 have no influence on either of the two input sides. These are currents that can be set without regard to the terminal currents. Equations (2.19d) and (2.19f) can be displayed as physical equivalent circuit diagrams. Transformed physical parameters are introduced for simplification as a direct result of the transformed state space representation in Eq. (2.19d)

$$\tilde{\underline{L}} = \begin{bmatrix} \tilde{L}_1 \\ \tilde{L}_2 \\ \tilde{L}_3 \\ \tilde{L}_4 \\ \tilde{L}_5 \\ \tilde{L}_6 \end{bmatrix} = \begin{bmatrix} 0 \\ L + 3L_{dc} \\ L \\ L \\ L + 2L_{ac} \\ L + 2L_{ac} \end{bmatrix} \quad (2.21a)$$

$$\tilde{\underline{R}} = \begin{bmatrix} \tilde{R}_1 \\ \tilde{R}_2 \\ \tilde{R}_3 \\ \tilde{R}_4 \\ \tilde{R}_5 \\ \tilde{R}_6 \end{bmatrix} = \begin{bmatrix} 0 \\ R + 3R_{dc} \\ R \\ R \\ R + 2R_{ac} \\ R + 2R_{ac} \end{bmatrix} \quad (2.21b)$$

$$\tilde{\underline{v}}_s = \begin{bmatrix} \tilde{v}_{s,DC} \\ \tilde{v}_{s,\alpha} \\ \tilde{v}_{s,\beta} \end{bmatrix} = \begin{bmatrix} \frac{\sqrt{6}}{2} V_{dc} \\ -v_{s1} + v_{s2} \\ -\frac{1}{\sqrt{3}}v_{s1} - \frac{1}{\sqrt{3}}v_{s2} + \frac{2}{\sqrt{3}}v_{s3} \end{bmatrix} \quad (2.21c)$$

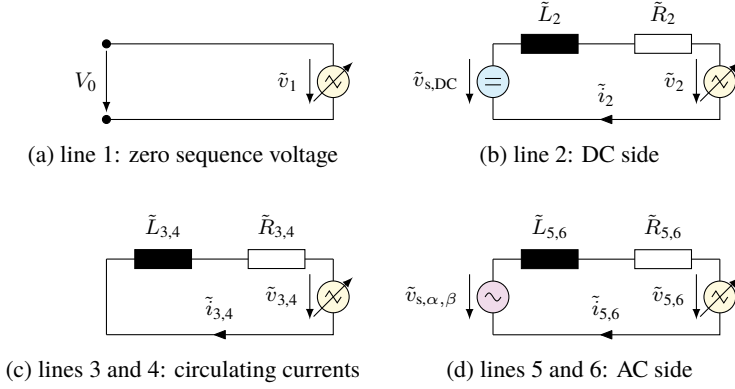


Figure 2.3: Decoupled representation of the MMC

The voltages from Eq. (2.21c) can be derived directly from Eqs. (2.19d), (2.20b) and (2.20c). Physically, the entire coupled MMC system can be represented as shown in Figs. 2.3 (a) to 2.3 (d). The line numbers refer to the lines from Eq. (2.19d). Figures 2.3 (a) to 2.3 (d) denote the MMC from Fig. 2.1 in transformed coordinates. Where Fig. 2.3 (a) is the zero voltage system. The set voltage \tilde{v}_1 has no effect on the currents in the system. Figure 2.3 (b) represents the second line from Eq. (2.19d). The set voltage \tilde{v}_2 only has an effect on the current \tilde{i}_2 , which corresponds to the transformed DC current. The AC side and circulating currents are not affected. The 3rd and 4th line of the equation are represented in Fig. 2.3 (c). The currents \tilde{i}_3 and \tilde{i}_4 can be adjusted using the voltages \tilde{v}_3 and \tilde{v}_4 . They have no influence on the DC side or the AC side. These currents and zero sequence voltage can later be used to distribute and balance energy within the converter. Figure 2.3 (d) represents lines 5 and 6. With the voltages \tilde{v}_5 and \tilde{v}_6 the AC currents \tilde{i}_5 and \tilde{i}_6 can be controlled. Since the star point of the AC side is not connected, the sum of all currents must also be zero. This means that only 2 of the 3 AC currents can be set independently. To transform the voltages at the terminals, Eq. (2.21c) is used. Lines 2 and 3 of Eq. (2.21c) describe the correlation between the transformed voltages \tilde{v}_5 and \tilde{v}_6 and the mains voltages $v_{s1,2,3}$.

To analyse the correlation between current \tilde{i}_5 and \tilde{i}_6 and the mains currents \underline{y} ($\underline{i}_{s1,2,3}$), Eq. (2.19b) can be recalculated.

$$\tilde{\underline{y}} = \underline{T} \underline{C}^\top \underline{y} \quad (2.22a)$$

$$\underline{y} = (\underline{C}^{\top+}) \underline{T}^\top \tilde{\underline{y}} \quad (2.22b)$$

$$= (\underline{C}^{\top+}) \underline{T}^\top \tilde{\underline{C}} \tilde{\underline{x}}_{1-6} \quad (2.22c)$$

$$= \begin{bmatrix} -\tilde{i}_5 - \frac{1}{\sqrt{3}}\tilde{i}_6 \\ \tilde{i}_5 - \frac{1}{\sqrt{3}}\tilde{i}_6 \\ \frac{2}{\sqrt{3}}\tilde{i}_6 \end{bmatrix} \quad (2.22d)$$

Equation (2.22d) shows that the mains currents are only composed of the transformed currents \tilde{i}_5 and \tilde{i}_6 under the assumption, that the zero sequence current \tilde{i}_1 is 0.

This shows, the transformation matrix \underline{T} from Eq. (2.11) enables a decoupling of the MMC. This allows DC and AC currents to be set independently of each other. In addition, the mathematical analysis provides further degrees of freedom in the form of $\tilde{i}_{3,4}$ and the zero voltage \tilde{v}_1 , which can be adjusted without affecting the AC side or the DC side. Based on these results, terms are identified in a simple way that used to adjust the energies of the system in a targeted manner.

In contrast to known approaches for decoupling the system equations, this is a purely mathematical method. Thus, even straightforward control engineering approaches and optimization for further control of the system can be quickly designed and implemented. Furthermore, the procedure is not limited to the MMC. The formalism also allows a simple analysis and decoupling of other topologies such as the M3C or the hexverter. Even new topologies like the MMSST or the parallel hybrid converter [91, 92] can be described in an easy, unified manner.

2.3 System Analysis

The objective of the MMC control is to control the grid currents while keeping the arm energies within a given tolerance band. Based on the state space equations Eqs. (2.9a) to (2.9c), the system is analyzed. All degrees of freedom are identified for current as well as for energy control.

2.3.1 Currents of the MMC

In steady state operation, the setpoints $\underline{y}_{\text{ref}}$ of the output variables limit the possible manipulated variables $\underline{u} = \underline{T}^\top \tilde{\underline{u}}$. The necessary input values $\tilde{\underline{u}}$ are calculated and reveal the remaining degrees of freedom.

First, the output equation Eq. (2.9c) of the system is recalculated. The nominal values $\underline{y}_{\text{ref}}$ are inserted for \underline{y} and therefore solved with respect to the state variables \underline{x}_{1-6} . To find the desired \underline{u} , the inverse of each of the system matrices must be calculated. Thereby, the advantage of the previous transformation is utilized. Since the system matrices in transformed coordinates are simple diagonal matrices, the inverses and the corresponding nullspaces can be determined significantly less complicated than with fully-occupied matrices.

For simplicity, all indices $k = 1, \dots, 6$ are omitted in this subsection since only the arm currents \underline{x}_{1-6} are considered.

$$\underline{y} = \underline{C} \underline{x} \quad (2.23a)$$

$$\tilde{\underline{y}} = \tilde{\underline{C}} \tilde{\underline{x}} \quad (2.23b)$$

$$\tilde{\underline{y}}_{\text{ref}} = \tilde{\underline{C}} \tilde{\underline{x}} \quad (2.23c)$$

$$\tilde{\underline{x}} = \tilde{\underline{C}}^+ \tilde{\underline{y}}_{\text{ref}} + \tilde{\underline{C}}_{\text{N}} \tilde{\underline{x}}_{\text{f}} \quad (2.23d)$$

Equation (2.23d) describes the relationship between the desired AC currents $\tilde{\underline{y}}_{\text{ref}}$ and the arm currents $\tilde{\underline{x}}$. However, the output matrix $\tilde{\underline{C}}$ cannot be inverted to be able to resolve according to the state variables. Therefore the pseudoinverse $\tilde{\underline{C}}^+$ is generated [93]. The identifier + indicates the pseudo inverse of $\tilde{\underline{C}}$. $\tilde{\underline{C}}_{\text{N}}$ is then a base of the nullspace of $\tilde{\underline{C}}$. This means that all vectors that are multiplied by $\tilde{\underline{C}}_{\text{N}}$ have no influence on the output variables $\tilde{\underline{y}}_{\text{ref}}$. $\tilde{\underline{x}}_{\text{f}}$ therefore denotes a vector with the remaining degrees of freedom in the system. \underline{C}^+ and \underline{C}_{N} are shown in Eqs. (A.11c) and (A.11d).

Due to the decoupling of the system, the currents \tilde{x}_5 and \tilde{x}_6 only depend on the setpoints \tilde{y}_{ref} , as can be seen in Eq. (A.11c). $\tilde{\underline{x}}_{\text{f}}$ is a vector with the degrees of freedom in the current. None of the three currents \tilde{x}_{1-3} has any influence on the AC currents of the system because of the definition of the nullspace.

To calculate the corresponding input variables $\tilde{\underline{u}}$, Eq. (2.19d) is solved with respect to the input variables.

$$\dot{\tilde{\underline{x}}} = \tilde{\underline{A}} \tilde{\underline{x}} + \tilde{\underline{B}} \tilde{\underline{u}} + \tilde{\underline{F}} z \quad (2.24a)$$

$$\tilde{\underline{B}} \tilde{\underline{u}} = \underline{\underline{A}} \tilde{\underline{x}} + \tilde{\underline{F}} z - \dot{\tilde{\underline{x}}} \quad (2.24b)$$

$$\tilde{\underline{u}} = \tilde{\underline{B}}^+ \left(\tilde{\underline{A}} \tilde{\underline{x}} + \tilde{\underline{F}} z - \dot{\tilde{\underline{x}}} \right) + \tilde{\underline{B}}_N \tilde{\underline{u}}_f \quad (2.24c)$$

Here, also the pseudoinverse of $\tilde{\underline{B}}$, and its nullspace matrix are calculated. $\tilde{\underline{u}}_f$ in Eq. (2.24c) represents a vector of the degrees of freedom in the control variables $\tilde{\underline{u}}$. $\tilde{\underline{B}}_N$ is a basis of the nullspace of $\tilde{\underline{B}}$. The corresponding matrices $\tilde{\underline{B}}^+$, $\tilde{\underline{B}}_N$ are shown in Eqs. (A.11a) and (A.11b) for overview reasons.

Equation (2.23d) inserted in Eq. (2.24c) results in

$$\begin{aligned} \tilde{\underline{u}} = & \tilde{\underline{B}}^+ \left(\left(\tilde{\underline{C}}^+ \dot{\tilde{\underline{y}}}_{\text{ref}} + \tilde{\underline{C}}_N \dot{\tilde{\underline{x}}}_f \right) - \tilde{\underline{A}} \left(\tilde{\underline{C}}^+ \tilde{\underline{y}}_{\text{ref}} + \tilde{\underline{C}}_N \tilde{\underline{x}}_f \right) - \tilde{\underline{F}} z \right) \\ & + \tilde{\underline{B}}_N \tilde{\underline{u}}_f \end{aligned} \quad (2.25)$$

This equation is divided into three different parts with respect to the control input $\tilde{\underline{u}}$ to simplify the analysis.

$$\begin{aligned} \tilde{\underline{u}} = & \underbrace{\tilde{\underline{B}}^+ \left(\tilde{\underline{C}}^+ \dot{\tilde{\underline{y}}}_{\text{ref}} - \tilde{\underline{A}} \tilde{\underline{C}}^+ \tilde{\underline{y}}_{\text{ref}} - \tilde{\underline{F}} z \right)}_{\tilde{\underline{u}}_{\text{ref}}} + \underbrace{\tilde{\underline{B}}^+ \left(\tilde{\underline{C}}_N \dot{\tilde{\underline{x}}}_f - \tilde{\underline{A}} \tilde{\underline{C}}_N \tilde{\underline{x}}_f \right)}_{\tilde{\underline{u}}_{\text{fx}}} \\ & + \underbrace{\tilde{\underline{B}}_N \tilde{\underline{u}}_f}_{\tilde{\underline{u}}_{\text{ff}}} \end{aligned} \quad (2.26)$$

Keeping in mind, that the designated grid currents $\tilde{\underline{y}}_{\text{ref}}$ are given, the necessary control inputs $\tilde{\underline{u}}$ were calculated by reforming the state space equation. As a result the remaining degrees of freedom of the control inputs $\tilde{\underline{u}}$ are obtained by dividing Eq. (2.26) into the three shown parts. The first part $\tilde{\underline{u}}_{\text{ref}}$ is calculated using the setpoints of the mains currents $\tilde{\underline{y}}_{\text{ref}}$ and the measured grid quantities z . These are the control variables which must be set to adjust the AC currents. $\tilde{\underline{u}}_{\text{fx}}$ is determined by choosing the degrees of freedom of $\tilde{\underline{x}}_f$ from Eq. (2.23d). The currents $\tilde{\underline{x}}_f$ can therefore be set as desired.

$\tilde{\underline{u}}_{\text{ff}}$ is determined directly by $\tilde{\underline{u}}_f$. This corresponds to the zero sequence voltage of the system. The control variables $\tilde{\underline{u}}$ can now be completely calculated and

are selected in such a way that the mains currents are set correctly. Thus, the first control objective - the correct value of the AC currents - is already achieved. The degrees of freedom in \tilde{x}_f and \tilde{u}_f are subsequently chosen in accordance with their ability to ensure stable operation of the system under given boundary conditions.

An analysis would have been possible even in untransformed coordinates. However, this would result in a multidimensional control problem due to the coupling. By decoupling the system beforehand, the formalism can be easily applied and simple control strategies for each component can be developed. In fact, the decoupling distantly corresponds to the already known approach using Clarke transformations. This has to hold true because the physical system is the same for all approaches.

2.3.2 Energies of the MMC

In Eq. (2.9b) the powers \dot{x}_{7-12} of each arm of the MMC are calculated. The stored energy of the system is the integral of this power according to Eqs. (2.2) and (2.8). The results from Sec. 2.3.1 are inserted into the energy state equation (Eq. (2.9b)). This yields the power terms that occur in the system for given quantities. Together with the knowledge about the degrees of freedom in the system, this enables conclusions to be made about which power terms are immanently given by the AC currents. In addition, power terms are obtained which can be specifically adjusted with the degrees of freedom. In preview, exactly these terms can be used to compensate the occurring power terms and thus reduce the energy pulsations of the energy storages.

The decoupling of the currents from Sec. 2.3.1 is also possible for energy control. This allows independent adjustment of the arm energies and therefore safe, stable operation. The power terms must be identified which can be used to adjust the energies independently. The direct decoupling of the arm energies of the MMC was already presented in [23, 30]. For other topologies based on the MMC approaches are also known [27, 46]. However, the approach to model the system presented here directly provides a guideline for transformation and decoupling of the power terms to balance the system. A transformation of the energies is not necessary. Only the power terms for setting the energies are transformed so that each term affects only one energy. In addition, this even allows a simple analysis for operation at low output frequencies, which can occur when using the MMC as a drive converter.

The arm energies from Eq. (2.27c) are generally expressed with transformed currents \tilde{x}_{1-6} and transformed voltages \tilde{u} . By utilizing the transformed coordinates, the inverses and nullspaces are calculated trivially. With Eqs. (2.9b), (2.13a), (2.13c) and (2.26) the result is

$$\dot{x}_{7-12} = \underline{u} \odot \underline{x}_{1-6} \quad (2.27a)$$

$$= \underline{T}^\top \tilde{u} \odot \underline{T}^\top \tilde{x}_{1-6} \quad (2.27b)$$

$$\begin{aligned} &= \underline{T}^\top (\tilde{u}_{\text{ref}} + \tilde{u}_{\text{fx}} + \tilde{u}_{\text{ff}}) \odot \underline{T}^\top \left(\tilde{C}^+ \tilde{y}_{\text{ref}} + \tilde{C}_N \tilde{x}_f \right) \\ &= \underline{T}^\top \tilde{B}^+ \left(\tilde{C}^+ \dot{\tilde{y}}_{\text{ref}} - \tilde{A} \tilde{C}^+ \tilde{y}_{\text{ref}} - \tilde{F} \underline{z} \right) \odot \underline{T}^\top \tilde{C}^+ \tilde{y}_{\text{ref}} \\ &\quad + \underline{T}^\top \tilde{B}^+ \left(\tilde{C}^+ \dot{\tilde{y}}_{\text{ref}} - \tilde{A} \tilde{C}^+ \tilde{y}_{\text{ref}} - \tilde{F} \underline{z} \right) \odot \underline{T}^\top \tilde{C}_N \tilde{x}_f \\ &\quad + \underline{T}^\top \tilde{B}^+ \left(\tilde{C}_N \dot{\tilde{x}}_f - \tilde{A} \tilde{C}_N \tilde{x}_f \right) \odot \underline{T}^\top \tilde{C}^+ \tilde{y}_{\text{ref}} \\ &\quad + \underline{T}^\top \tilde{B}^+ \left(\tilde{C}_N \dot{\tilde{x}}_f - \tilde{A} \tilde{C}_N \tilde{x}_f \right) \odot \underline{T}^\top \tilde{C}_N \tilde{x}_f \\ &\quad + \underline{T}^\top \tilde{B}_N \tilde{u}_f \odot \underline{T}^\top \tilde{C}^+ \tilde{y}_{\text{ref}} \\ &\quad + \underline{T}^\top \tilde{B}_N \tilde{u}_f \odot \underline{T}^\top \tilde{C}_N \tilde{x}_f \end{aligned} \quad (2.27c)$$

To enable stationary operation, the average value of the energy must be constant. So the power \dot{x}_{7-12} in each arm, i.e. the sum of the terms in Eq. (2.27c), must be 0 on average at all times.

$$\bar{x}_{7-12} = \int_t^{t+T} \dot{x}_{7-12} dt \stackrel{!}{=} \bar{W} \quad (2.28)$$

$\bar{W}_0 > 0$ is a constant offset of the arm energies in stationary operation and T is the period duration of the lowest frequency value, i.e. usually the grid voltage frequency. For simplicity, the offset is chosen to 0 J in the following chapters for the analysis of the energy pulsations.

An initial analysis of Eq. (2.27c) shows which power terms can be influenced at all. The first summand $\underline{T}^\top \tilde{B}^+ \left(\tilde{C}^+ \dot{\tilde{y}}_{\text{ref}} - \tilde{A} \tilde{C}^+ \tilde{y}_{\text{ref}} - \tilde{F} \underline{z} \right) \odot \underline{T}^\top \tilde{C}^+ \tilde{y}_{\text{ref}}$ from Eq. (2.27c) is only determined by the setpoints \tilde{y}_{ref} and disturbances \underline{z} . Therefore the summand cannot be influenced in any way. In steady-state operation, the reference values \tilde{y}_{ref} generally consist of pure sine values of the frequency ω_d and the phase shift φ_d . The disturbance variables z_{1-3} also correspond to a

sinusoidal, symmetrical three-phase voltage system of the frequency ω_d . z_4 is an ideal DC value.

The first summand hence contains terms of the frequencies 0 , $\pm\omega_d$ and $\pm 2\omega_d$. The detailed calculation is given in chapter Sec. A.5. The results are shown in Eqs. (A.12d) to (A.12i). Since the system matrices are constant, it can be concluded that the mean value of this term must be completely compensated by other terms in order to fulfill the condition from Eq. (2.28). An exact analysis of all the power terms and how the energy control can be developed is addressed in more detail in Sec. 4.1.

2.4 Conclusion of this Chapter

In this chapter the MMC was introduced and analyzed. With the help of Kirchhoff's circuit laws a set of equations was derived from the equivalent circuit diagram to describe the MMC. Subsequently, the physical quantities were mapped to control engineering quantities and the state space representation of the MMC was obtained. On the basis of this model the energies and their variation over time can be described.

The result is a mathematical consistent description that can be easily exchanged with other fields of research. A simple and easy to use mathematical formalism was presented, which enables the decoupling of the system. In contrast to state of the art methods, this description can be applied to other MMC based topologies as the M3C, the hexverter or even more complex topologies as the MMSST. Moreover, it provides an approach to control the currents and energies of those systems. Power terms are identified easily to control the arm energies independently without additional investigation of the system equations as in [23, 27, 30].

In the following, the model serves as a fundamental basis for a fast and simple control of the currents and energies of the MMC. The description additionally allows a straightforward implementation of advanced optimization methods for reduction of energy pulsation and current control algorithms.

Chapter 3

Optimal Feed Forward Control for Reduction of Energy Pulsation

The most important and simultaneously most expensive components of the converter are the power semiconductors and capacitors. This results in two optimization goals in the design of the control system besides the general and stable operation of the system. On the one hand, the arm current should be as low as possible for the entire operating range of the MMC to reduce the conduction and switching losses of the semiconductors. On the other hand, the stored energy should be minimized in order to use smaller cell capacitors. However, these two goals are in opposition to each other, because the easiest way to influence the energy is to add additional arm currents, as will be shown below.

In Chapter 2 the mathematical fundamentals of the MMC were derived. The results are now used to control the currents and energies of the system. By analyzing the power terms, conditions are identified which guarantee the stationary operation. In addition, there are terms that allow reductions of the inherent energy deviation. In parallel to the feed forward control of these terms, the degrees of freedom are used to keep the mean value of the arm energies steady.

Various methods for power feed forward control and reduction of the energy pulsation are already known. Accordingly, circulating currents and the zero se-

quence voltage [59, 60] or only circulating currents can be adjusted [62, 94]. The procedures can be divided into offline [62, 65], online [63, 64] and analytical [26, 56, 59, 95] approaches. The principles are based on different ways of modelling and assumptions. All procedures are based on the same physical system while addressing different aspects of energy control and reduction of the energy pulsation. These methods serve as a benchmark for the newly presented approaches.

There are different concepts for the feed forward control and the control of the energy pulsation in MMC systems. An analytical approach to compensate for the second harmonic in the energy pulsation of the arms was already presented in [23, 42]. Due to its simplicity, this method has been accepted so far and is applied in commercial projects. However, a significant reduction of the energy pulsation may only occur for small power factors $\cos(\varphi)$ on the AC side. If more reactive power is made available to the AC side or if the ratio of the DC voltage to the AC voltage changes, the analytical approach can even lead to an increase in the energy pulsation if the amplitude is not scaled properly [E2]. In addition, there are other approaches to reduce the energy pulsation, for example by filtering the 2nd harmonic and adjusting the mean value to zero e.g. [28]. Those procedures are extended to the effect that also higher harmonics are analytically calculated and compensated. A different approach is the direct control of the cell states (switching states) for a minimal energy deviation [96]. However the calculation effort increases with the number of cells which is a major disadvantage with regards to the real-time capability of the implementation. Approaches which reduce the energy pulsation via controllers lead to dynamic disadvantages when changing the operating point [97].

The new approach presented in this thesis allows a reduction of the energy pulsation over the entire working range by calculating optimal current trajectories beforehand. Even during grid faults, the reduction is superior to state of the art methods. The idea was presented in [E1] and is based on the modelling in Chapter 2. With the description a function optimization approach is possible. Consequently, the degrees of freedom x_f are optimized with respect to the energy pulsation in advance. By definition, the results are current trajectories that achieve optimal, i.e. minimal, energy pulsations for a given system.

Although the control of the energies is permissible via feed forward terms in simulation, in reality even small model errors lead to deviations which can lead to a violation of the maximum operating limits of the inverter (e.g. maximum arm currents). Consequently, feed forward control of certain power terms is a

good way to reduce the energy pulsation. In addition, the superimposed control loop only has to compensate for the model errors in order to achieve stationary accuracy.

This chapter first deals with the power feed forward control of the system. For steady state operation, requirements are specified for the currents. Additionally, the modelling of the system enables an easy approach for reducing the occurring energy pulsations with additional circulating currents.

Finally, the control algorithms are simulated and the results are presented in the last part of this chapter.

3.1 Power Feed Forward Control

In this section, power terms are identified, that allow a reduction of the energy pulsations in the system. Using the model equations, the trajectories of the arm energies are calculated. With the determined degrees of freedom, the energies are positively influenced in terms of deviation from their mean value. Different methods - online and offline - are presented and analyzed.

Prerequisites

In order to compare the different approaches to power feed forward control, the grid variables z_{1-3} are assumed to be an ideal, sinusoidal, symmetrical three-phase voltage system. z_4 is a constant DC voltage.

$$z_{1-3} = \hat{V} \cos \left(\omega_g t - \frac{2\pi(k-1)}{3} \right); k = 1,2,3 \quad (3.1a)$$

$$z_4 = V_{dc} \quad (3.1b)$$

The setpoints y_{ref} are also assumed to be a symmetrical three-phase system.

$$y_{k,ref} = \hat{I} \cos \left(\omega_g t - \frac{2\pi(k-1)}{3} - \varphi \right); k = 1,2,3 \quad (3.2)$$

The power feed forward is calculated for steady-state operation on the basis of the input and output currents and the operating state of the system.

In quasi-stationary operation Eq. (2.28) must be satisfied - i.e. the energy must be constant in average. Since the external voltages in Eq. (3.1a) are already defined as periodic with the frequency ω_g , a periodicity of the energies \underline{x}_{7-12} is also required. Thus, for the arm energies with a period T_g

$$\underline{x}_{7-12}(t) \stackrel{!}{=} \underline{x}_{7-12}(t + T_g) \quad (3.3)$$

For transient processes, a exclusively power feed forward is not sufficient and controller adjustments are absolutely necessary. Different optimization goals can be pursued when calculating the feed forward terms.

Optimization with regard to power semiconductors

The utilization of the semiconductors is essentially determined by the root mean square (RMS) value of the arm currents \underline{x}_{1-6} . Therefore, a lower RMS value of the current also means lower semiconductor losses.

Optimization regarding the installed capacitance

The dielectric strength of the capacitors is determined at an early stage of the inverter design. During stationary operation, energy pulsations occur within the converter's arms in correlation to the grid frequency. These energy deviations cause a voltage fluctuation depending on the installed capacitance.

To stay within the permissible operating range of the capacitors, the maximum voltage $V_{C,arm,max}$ might not be exceeded at any given time. Therefore the minimum installed capacitance is given by

$$C_{min} = \frac{2W_{arm,max}}{V_{C,arm,max}^2} \quad (3.4)$$

For a given $V_{C,arm,max}$ the capacitance is directly proportional to the stored energy. The energy is a composition of a constant mean energy and a zero-mean pulsation $W_{arm} = \bar{W} + \Delta W$. The ΔW is thereby not involved in the power transfer from the AC to the DC side and vice versa. It is rather a necessary characteristic of the system that occurs during operation.

The idea is to optimize the inverter operation with regard to the occurring ΔW over the whole operating range. By reducing the ΔW it is therefore possible to reduce the necessary minimum capacitance C_{\min} . In that way not only the required installation space is reduced but also in last consequence the costs are effectively reduced to build the converter for a given application.

3.1.1 Minimization of the RMS Value of the Arm Currents

When minimizing the RMS values of the arm currents, it is not appropriate to consider each arm current as an isolated entity. In principle, the reduction of one current is accompanied by the increase of another, so that the losses are not reduced but rather increased. Instead, the square of the sum of all RMS values of the arm currents is optimized. The overall losses is the sum of the losses per arm. Those losses themselves are directly proportional to the square of the RMS value of the respective arm currents. In the following $\underline{x}_{1-6}^\top \underline{x}_{1-6} = \|\underline{x}_{1-6}\|^2$ is considered.

$$\underline{x}_{1-6}^\top \underline{x}_{1-6} = \left(\underline{C}^+ \underline{y}_{\text{ref}} + \underline{C}_N \underline{x}_f \right)^\top \left(\underline{C}^+ \underline{y}_{\text{ref}} + \underline{C}_N \underline{x}_f \right) \quad (3.5)$$

The null space of both \underline{C} and $\underline{C}^{+\top}$ is identical. Hence \underline{C}_N is a base of null space for both matrices. Using Eq. (2.9c), Eq. (3.5) is thus simplified to

$$\underline{x}_{1-6}^\top \underline{x}_{1-6} = \left(\underline{C}^+ \underline{y}_{\text{ref}} + \underline{C}_N \underline{x}_f \right)^\top \left(\underline{C}^+ \underline{y}_{\text{ref}} + \underline{C}_N \underline{x}_f \right) \quad (3.6a)$$

$$\begin{aligned} &= \left\| \underline{C}^+ \underline{y}_{\text{ref}} \right\|^2 + \underbrace{\left(\underline{C}^+ \underline{y}_{\text{ref}} \right)^\top \left(\underline{C}_N \underline{x}_f \right)}_{=0 \text{ with } \underline{C}^{+\top} \underline{C}_N = 0} \\ &\quad + \underbrace{\left(\underline{C}_N \underline{x}_f \right)^\top \left(\underline{C}^+ \underline{y}_{\text{ref}} \right)}_{=0} + \left\| \underline{C}_N \underline{x}_f \right\|^2 \end{aligned} \quad (3.6b)$$

$$= \left\| \underline{C}^+ \underline{y}_{\text{ref}} \right\|^2 + \left\| \underline{C}_N \underline{x}_f \right\|^2 \quad (3.6c)$$

$\left\| \underline{C}^+ \underline{y}_{\text{ref}} \right\|^2$ describes the part of the arm currents caused by the AC reference values and cannot be changed. $\left\| \underline{C}_N \underline{x}_f \right\|^2$ are circulating currents that can be

adjusted without interfering with the reference values at the converter terminals. Equation (3.6c) shows that there is no value $\underline{x}_f \neq \underline{0}$ that would reduce the sum of the squares of the currents. Therefore it is shown that the smallest RMS value is obtained for $\underline{x}_f = \underline{0}$. This contrasts with the reduction of the energy pulsation, which is achieved by using $\underline{x}_f \neq \underline{0}$.

3.1.2 Minimization of the Arm Current Under Consideration of the Average Energy Value

To satisfy Eq. (2.28), the sum of the average power at the inverter terminals needs to be 0. In other words, the power on the AC side must be equal to the power on the DC side if losses are neglected. Looking at Eq. (A.9a), it is noticeable that the system matrix $\tilde{\underline{A}}$ is orders of magnitude smaller than $\tilde{\underline{B}}$ because it is multiplied by a matrix containing the small parasitic resistances. Starting from Eq. (2.27c) the terms with small coefficients can be neglected. This simplification omits the losses due to ohmic voltage drops in the system. In addition, the small inductive voltage drops are also omitted for simplification [23]. Assuming that the superimposed energy control compensates for these losses, the analysis is sufficiently accurate. Accordingly, $\tilde{\underline{A}} \approx 0$, and all time derivatives ≈ 0 follow directly. The zero sequence voltage is set to 0 as well, since it does not contribute to the power balance of the system at all. It has already been shown that the zero sequence voltage can be used to reduce the energy pulsation (e.g. [98]). There are different approaches how to choose the zero sequence voltage, but it is not always useful or possible to set such a voltage.

In order to compare the new optimization strategy presented here, the influence of circulating currents on the energy pulsation is examined below. After it is validated, that the optimization yields to good results, the zero sequence voltage is additionally included in the optimization as an optional degree of freedom. If the zero sequence voltage is not used to reduce the energy pulsation, overmodulation to the grid side, for example, can be performed.

To simplify the representation, the degrees of freedom are examined in transformed coordinates. From Eq. (2.19a) follows directly $\underline{C}_N x_f = \underline{T}^\top \tilde{\underline{C}}_N \tilde{x}_f$. Thus the arm powers under idealized conditions are denoted as

$$\dot{\underline{x}}_{7-12} = \dot{\underline{u}} = \underline{u} \odot \underline{x}_{1-6} \quad (3.7a)$$

$$\begin{aligned} &= -\underline{B}^+ \underline{F} \underline{z} \odot \underline{C}^+ \underline{y}_{\text{ref}} - \underline{B}^+ \underline{F} \underline{z} \odot \underline{C}_N \underline{x}_f \\ &\quad + \left(\underline{C}_N \underline{x}_f + \underline{C}^+ \underline{y}_{\text{ref}} \right) \underline{u}_f \end{aligned} \quad (3.7b)$$

$$\begin{aligned} &= -\underline{B}^+ \underline{F} \underline{z} \odot \underline{C}^+ \underline{y}_{\text{ref}} - \underline{B}^+ \underline{F} \underline{z} \odot \underline{T}^\top \tilde{\underline{C}}_N \tilde{x}_f \\ &\quad + \left(\underline{T}^\top \tilde{\underline{C}}_N \tilde{x}_f + \underline{C}^+ \underline{y}_{\text{ref}} \right) \odot \underline{u}_f \end{aligned} \quad (3.7c)$$

For analysis at the steady-state operating point, the disturbance variables are applied as ideal sine waves and DC quantity.

$$\underline{z} = \begin{bmatrix} v_{s1} \\ v_{s2} \\ v_{s3} \\ V_{\text{dc}} \end{bmatrix} = \begin{bmatrix} \hat{V} \cos(\omega_g t) \\ \hat{V} \cos\left(\omega_g t - \frac{2\pi}{3}\right) \\ \hat{V} \cos\left(\omega_g t - \frac{4\pi}{3}\right) \\ V_{\text{dc}} \end{bmatrix} \quad (3.8)$$

\hat{V} is the amplitude of the voltage with the frequency ω_g . V_{dc} describes the DC voltage of the system. Due to the periodic functions, the degrees of freedom \tilde{x}_f are also defined as general, sinusoidal quantities.

$$\tilde{x}_f = \begin{bmatrix} c_{10} + \sum_{i=1}^{\infty} a_{1i} \cos(i \cdot \omega_g t) + \sum_{i=1}^{\infty} b_{1i} \sin(i \cdot \omega_g t) \\ c_{20} + \sum_{i=1}^{\infty} a_{2i} \cos(i \cdot \omega_g t) + \sum_{i=1}^{\infty} b_{2i} \sin(i \cdot \omega_g t) \\ c_{30} + \sum_{i=1}^{\infty} a_{3i} \cos(i \cdot \omega_g t) + \sum_{i=1}^{\infty} b_{3i} \sin(i \cdot \omega_g t) \end{bmatrix} \quad (3.9)$$

Equations (3.8) and (3.9) are inserted into Eq. (3.7c). The power balance must be zero on average at least over the period $2\pi/\omega_g$. The degrees of freedom \tilde{x}_f must be chosen to satisfy this condition for all arm energies. This yields

$$\underline{w}(2\pi/\omega_g) - \underline{w}(0) = \int_0^{2\pi/\omega_g} \dot{\underline{w}}(\omega_g t) dt \stackrel{!}{=} 0 \quad (3.10a)$$

$$\begin{bmatrix} \frac{\pi}{6\omega_g} \left(V_{dc} (-\sqrt{6} c_{10} + 3 c_{20} + \sqrt{3} c_{30}) - 3\hat{I}\hat{V} \cos(\varphi) \right) \\ \frac{\pi}{6\omega_g} \left(V_{dc} (-\sqrt{6} c_{10} - 3 c_{20} + \sqrt{3} c_{30}) - 3\hat{I}\hat{V} \cos(\varphi) \right) \\ \frac{\pi}{6\omega_g} \left(V_{dc} (-\sqrt{6} c_{10} - 2\sqrt{3} c_{30}) - 3\hat{I}\hat{V} \cos(\varphi) \right) \\ \frac{\pi}{6\omega_g} \left(V_{dc} (-\sqrt{6} c_{10} + 3 c_{20} + \sqrt{3} c_{30}) - 3\hat{I}\hat{V} \cos(\varphi) \right) \\ \frac{\pi}{6\omega_g} \left(V_{dc} (-\sqrt{6} c_{10} - 3 c_{20} + \sqrt{3} c_{30}) - 3\hat{I}\hat{V} \cos(\varphi) \right) \\ \frac{\pi}{6\omega_g} \left(V_{dc} (-\sqrt{6} c_{10} - 2\sqrt{3} c_{30}) - 3\hat{I}\hat{V} \cos(\varphi) \right) \end{bmatrix} \stackrel{!}{=} 0 \quad (3.10b)$$

The integral of all occurring trigonometric terms in Eq. (3.9) are zero over a period and thus do not contribute to the total energy of the system. Note that there are three independent equation in the system Eq. (3.10b) and three variables c_{10}, c_{20} and c_{30} to solve for. To keep the energy constant during a grid period, the following must apply

$$c_{10} = \frac{\sqrt{6}}{2} \frac{\hat{V}}{V_{dc}} \hat{I} \cos(\varphi) \quad (3.11a)$$

$$c_{20} = 0 \quad (3.11b)$$

$$c_{30} = 0 \quad (3.11c)$$

This corresponds to a pure DC current for \tilde{x}_{f1} , which compensates the power of the AC side and keeps the total energy constant on average. In addition to the total energy of the system, the symmetrical distribution of energy between the arms is also required. However, symmetrization is not necessary under idealized consideration. With Eq. (2.26) the control variables \underline{u}_{1-6} can be calculated directly, which adjust the current trajectories.

Table 3.1: Normalized quantities for the comparison of different control strategies

electrical quantity	normalized value	description
V_{dc}	1.6 V	DC voltage
\hat{V}	1 V	AC voltage amplitude
\hat{I}	1 A	AC current amplitude
C	1 mF	arm capacitance
L	0.5 mH	arm inductance
L_{ac}	0.1 mH	AC side inductance
L_{dc}	0.1 mH	DC side inductance
R	1 m Ω	parasitic arm resistance
R_{ac}	1 m Ω	parasitic AC side resistance
R_{dc}	1 m Ω	parasitic DC side resistance
f	50 Hz	AC frequency
φ	0	current phase shift

Graphical Illustration of the Energy Trajectories

Equations (3.8) and (3.11a) are inserted into the ideal system equation Eq. (3.7c) from Sec. 3.1.2. To achieve easy comparability, all values are normalized to the AC side voltage of $\hat{V} = 1$ V and current of $\hat{I} = 1$ A. Table 3.1 lists the resulting values. The energy trajectories in the idealized system serve as a reference for all further considerations. The constant mean value \bar{W} is subtracted from all equations. Thereby the constant average value of the energy is set to 0. The energy pulsations are independent of this absolute value of the energy and can therefore be neglected for consideration without restriction of generality. This allows a simple comparison of the energy pulsations. The degree of freedom \tilde{x}_{f1}

is adjusted according to Eq. (3.11a) in a way that the DC power corresponds to the AC power. The resulting arm currents are

$$x_k = C^+ y_{\text{ref}} + T^T \tilde{C}_N \tilde{x}_f \quad (3.12a)$$

$$x_k = \frac{\hat{I}}{2} \cos\left(2\pi f t - \frac{2(k-1)\pi}{3} - \varphi\right) + \frac{\hat{I}\hat{V}}{2V_{\text{dc}}} \cos(\varphi); \quad (3.12b)$$

$$k = 1, 2, 3$$

$$x_k = \frac{\hat{I}}{2} \cos\left(2\pi f t - \frac{2(k-4)\pi}{3} - \varphi\right) - \frac{\hat{I}\hat{V}}{2V_{\text{dc}}} \cos(\varphi); \quad (3.12c)$$

$$k = 4, 5, 6.$$

Over a grid period of $T_g = 0.02$ ms, the mean energy in all arms is constant. This allows stationary operation of the converter.

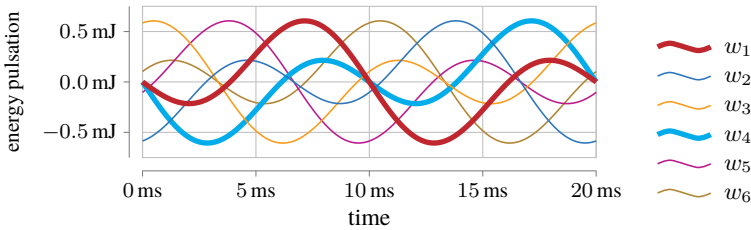


Figure 3.1: Normalized energy pulsations in the ideal system when the AC power is equal to the DC power. This also corresponds to an optimization with regard to the minimum RMS arm current for stable operation.

The energy trajectories shown in Fig. 3.1 serve as a reference for the evaluation of further methods for power feed forward control. W_{norm} describes the energy pulsation which results when the normalized values from Table 3.1 are inserted. The energy trajectories in all arms are congruent and phase shifted by 60° . Here the RMS value of the arm current has been minimized by setting the degrees of freedom to 0, because they do not contribute to the power exchange with the connected grids. In the following, different methods for reducing the energy pulsation, and thus the voltage ripple, in the arms are presented and finally compared.

3.1.3 Analytical Compensation of the 2nd Harmonic

The energy pulsations from Sec. 3.1.2 can be reduced during stationary operation. As already pointed out in [23] and pursued and extended in different approaches, terms from Eq. (3.7c) can be analytically calculated, compensated and the energy deviation thus reduced. Furthermore, the modelling from Chapter 2 allows a simple identification of those second harmonic terms. Analogous to Eq. (3.10b), the power equation Eq. (3.7c) is modulated with the double output frequency. As a result, the modulation products of the double frequency and the difference frequency are obtained. The difference terms then correspond to constant terms which can be compensated. From Eq. (3.11a) it follows for Eq. (3.9) that all a_{1i} , b_{1i} as well as c_{20} and c_{30} are set to 0. c_{10} will be set to $c_{10,id}$ according to Eq. (3.11a). To compensate for the second harmonic, all a_{2i} , b_{2i} , a_{3i} and b_{3i} are set to 0 for $i > 2$, which results in the approach for \tilde{x}_f :

$$\tilde{x}_f = \begin{bmatrix} c_{10,id} \\ a_{22} \cos(2 \cdot \omega_g t) + b_{22} \sin(2 \cdot \omega_g t) \\ a_{32} \cos(2 \cdot \omega_g t) + b_{32} \sin(2 \cdot \omega_g t) \end{bmatrix} \quad (3.13)$$

Solving the equation with respect to a_{22} , b_{22} , a_{32} and b_{32} is analogous to Eq. (3.10b) and provides the amplitudes for Eq. (3.13) which completely compensate the second harmonic in the energy under idealized considerations.

$$a_{22} = -b_{32} = \frac{\sqrt{3}}{2V_{dc}} \hat{V} \hat{I} \cos\left(\varphi + \frac{\pi}{6}\right) \quad (3.14a)$$

$$b_{22} = a_{32} = \frac{\sqrt{3}}{2V_{dc}} \hat{V} \hat{I} \sin\left(\varphi + \frac{\pi}{6}\right) \quad (3.14b)$$

The coefficients are directly inserted into Eq. (3.13):

$$\tilde{x}_f = \frac{\sqrt{3}}{2} \frac{\hat{V}}{V_{dc}} \hat{I} \begin{bmatrix} \sqrt{2} \cos(\varphi) \\ \cos\left(\frac{\pi}{6} - 2\omega_g t + \varphi\right) \\ \sin\left(\frac{\pi}{6} - 2\omega_g t + \varphi\right) \end{bmatrix} \quad (3.15a)$$

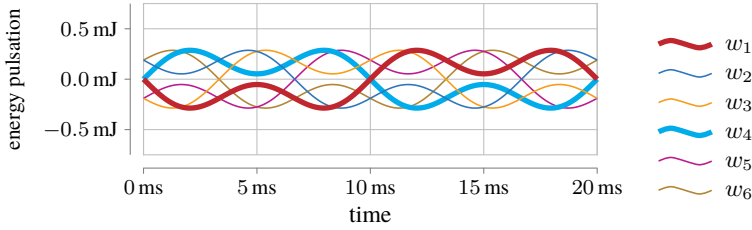


Figure 3.2: Normalized energy pulsations in the ideal system, with analytically calculated power feed forward for compensation of the 2nd harmonic.

and subsequently for the arm currents

$$\underline{x}_{1-6} = \begin{bmatrix} \frac{\hat{I}}{2} \cos(\omega_g t - \varphi) + \frac{\hat{V}}{2V_{dc}} \hat{I} (\cos(\varphi - 2\omega_g t) + \cos(\varphi)) \\ \frac{\hat{I}}{2} \cos(\omega_g t - \frac{2\pi}{3} - \varphi) - \frac{\hat{V}}{2V_{dc}} \hat{I} (\cos(\varphi - 2\omega_g t + \frac{\pi}{3}) - \cos(\varphi)) \\ \frac{\hat{I}}{2} \cos(\omega_g t - \frac{4\pi}{3} - \varphi) - \frac{\hat{V}}{2V_{dc}} \hat{I} (\cos(\varphi - 2\omega_g t - \frac{\pi}{3}) - \cos(\varphi)) \\ \frac{\hat{I}}{2} \cos(\omega_g t - \varphi) - \frac{\hat{V}}{2V_{dc}} \hat{I} (\cos(\varphi - 2\omega_g t) + \cos(\varphi)) \\ \frac{\hat{I}}{2} \cos(\omega_g t - \frac{2\pi}{3} - \varphi) + \frac{\hat{V}}{2V_{dc}} \hat{I} (\cos(\varphi - 2\omega_g t + \frac{\pi}{3}) - \cos(\varphi)) \\ \frac{\hat{I}}{2} \cos(\omega_g t - \frac{4\pi}{3} - \varphi) + \frac{\hat{V}}{2V_{dc}} \hat{I} (\cos(\varphi - 2\omega_g t - \frac{\pi}{3}) - \cos(\varphi)) \end{bmatrix}. \quad (3.15b)$$

The result of the compensation is shown in Fig. 3.2. Compared to the energy pulsation in Fig. 3.1 the energy pulsation $\Delta W = \max(w_{\text{norm}}) - \min(w_{\text{norm}})$ is reduced by 52.72%.

If the MMC operates in stationary mode, the designated currents $\underline{y}_{\text{ref}}$ can be set. In addition, the energy pulsations with the frequency of the second harmonics of the mains frequency can be compensated. The newly presented description of the system is used to determine the corresponding setpoints easily and quickly. The results are the arm currents from Eq. (3.13). The corresponding voltage setpoints \underline{u} can be calculated directly from Eq. (2.24c). Both, the determination of the DC current and the derivation for compensation of the 2nd harmonic are based on an ideal, lossless model.

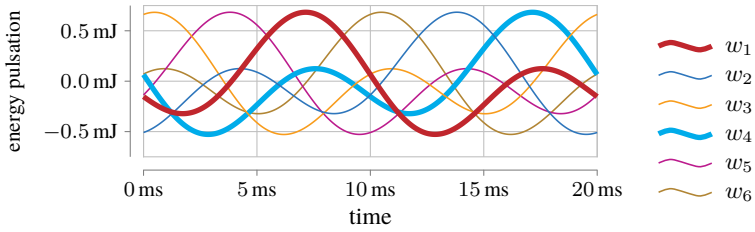
These calculations are analogous for different MMC based topologies. The necessary degrees of freedom in the circulating currents unfold themselves using

the presented formalism. A straightforward compensation is possible without further investigation of dedicated topology related energy pulsation terms.

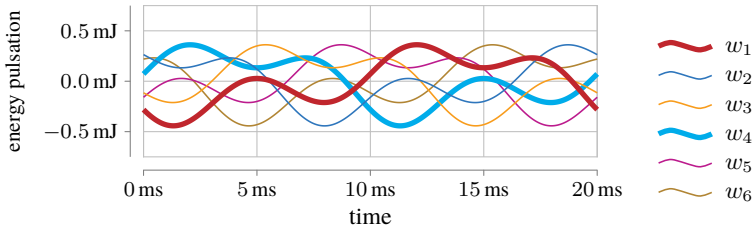
3.1.4 Disadvantages of the Analytical Compensation of the 2nd Harmonic

In Sec. 3.1.3 the analytical compensation of the 2nd harmonic in the energy pulsation was shown. This method is based on the approaches presented in [23, 95]. These approaches, however, assume a lossless system. In addition, they neglect all inductive voltage drops across the inductors L_x since $v_{Lx} = \frac{d}{dt} i_x L_x$. [E2] has already shown that the analytically calculated compensation depends not only on the inductors but also on the ratio of the DC and AC voltages. Furthermore, a reduction of the energy pulsation is only achieved if the power factor of the AC side is close to 1. In cases where the reactive power is increased, the compensation can achieve the exact opposite and the energy pulsation increase as can be seen later in Fig. 3.8. In this case this form of compensation must be omitted. If the inductive voltage drops are taken into account, the assumptions from Eq. (3.7c) are not valid. The inductances cannot be neglected and a closed solution of the currents for compensation cannot be given anymore. The simplest case is to determine the currents by the idealized system. However, the actual energy trajectories differ. Ohmic losses are still neglected.

Figure 3.3 (a) shows the energy trajectories considering the voltage drops across the inductors without compensation of the 2nd harmonic. Compensation after Eq. (3.15b) still results in a reduction of the total energy pulsation as can be seen in Fig. 3.3 (b). In contrast to Fig. 3.2, the reduction in a system with the properties from Table 3.1 is actually only 33.65 % compared to theoretical 52.72 % without consideration of the inductive voltage drops. There is a correlation between the size of the inductors and the degree of compensation effectively achievable. In addition, weighting the currents for compensation with a factor $k_{\text{komp}} \in (0; 1]$ can also have a positive effect on the energy deviation as already shown in [E2]. There are limits to the purely analytical calculation for compensation of the 2nd harmonic in the energy pulsation. At worst, the currents calculated according to Eq. (3.15b) can lead to an increase of the energy pulsation as also shown in [E2]. This break even point has to be calculated for each MMC setup and cannot be given in a general manner. However, since the calculation of the compensation currents is simple using the modelling in Chapter 2, this method can even be implemented in real time. Therefore, complex lookup tables are not necessary.



(a) without compensation



(b) with compensation

Figure 3.3: Normalized energy pulsation with consideration of inductive voltage drops.

3.1.5 Parameter Optimization to Reduce the Energy Pulsation

As discussed in Sec. 3.1.4, neglecting the inductive voltage drops in the system can lead to an unwanted increase of the energy pulsation. An extension of the approach is to compensate according to Eq. (3.9) not only the 2nd harmonic but to determine the coefficients of the first n terms which contribute to a reduction of the energy pulsation. Already in [26] the compensation up to the 4th harmonic was determined while neglecting the inductive voltage drops. With the help of the calculation of the higher harmonics, the energy pulsation can be reduced also under consideration of the inductive voltage drops.

While Secs. 3.1.2 and 3.1.3 aimed to calculate the DC current and compensation currents analytically to eliminate the 2nd harmonic, the parameter optimization targets the reduction of the energy pulsation directly. Without neglecting losses and inductive voltage drops, it is possible to reduce the energy pulsation over the entire operation range. However, a closed analytical solution is impossible. Therefore a numerical approach shall be considered. In order to determine the coefficients for reduction, a cost function is required. Normally, any arm energy of the converter pulsates around a constant mean value. With a symmetric built MMC all mean values are set to the same constant \bar{W} . Then, a minimizing of the energy pulsation is equal to minimizing the amplitude around the point of operation. This results in the optimization function

$$J = \left\| \underline{x}_{7-12}(t) - \bar{W} \underline{1}_6 \right\|_{L^\infty([0, T_g])} \quad (3.16a)$$

$$= \max_{t \in [0, T_g]} \left\| \underline{x}_{7-12}(t) - \bar{W} \underline{1}_6 \right\|_\infty. \quad (3.16b)$$

A satisfactory result is achieved when calculating the coefficients for the first 6 harmonics. For the currents in the transformed system, the following applies

$$\tilde{\underline{x}}_i = \left[\begin{array}{c} c_{10} \\ \sum_{i=2}^6 a_{2i} \cos(i \cdot \omega_g t) + \sum_{i=2}^6 b_{2i} \sin(i \cdot \omega_g t) \\ \sum_{i=2}^6 a_{3i} \cos(i \cdot \omega_g t) + \sum_{i=2}^6 b_{3i} \sin(i \cdot \omega_g t) \end{array} \right] \quad (3.16c)$$

After inserting the currents from Eq. (3.16c) into Eq. (2.27c), the optimization problem reads as follows

$$\text{minimize } J \quad (3.16d)$$

$$\text{subject to } c_{10}, a_{2i}, a_{3i}, b_{2i}, b_{3i}; \quad k = 2, \dots, 6, \quad (3.16e)$$

$$\text{and } \underline{0}_6 = \int_0^{T_g} \dot{x}_{7-12}(t) dt, \quad (3.16f)$$

$$\text{and } \int_0^{T_g} x_{7-12} dt = \bar{W} T_g \underline{1}_6. \quad (3.16g)$$

The zero sequence voltage is not included $\tilde{u}_f = 0$.

To perform the optimization efficiently, the Optimization Toolbox of the Math-Works' MATLAB is used. With the particle swarm optimization (PSO) algorithm [99] the best results in this case are achieved.

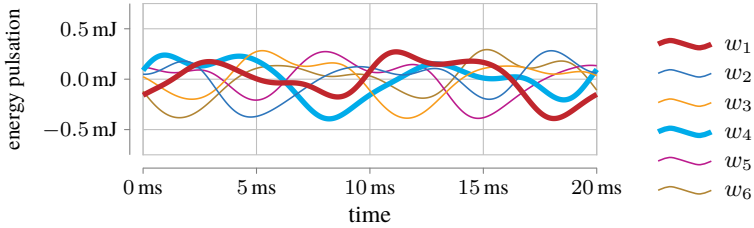


Figure 3.4: Normalized energy pulsations with PSO optimized coefficients for the circulating currents at $\varphi = 0^\circ$.

The particle swarm optimization (PSO) algorithm optimizes the coefficients from Eq. (3.16c) with respect to the minimum energy pulsation. Random initial conditions are chosen for this purpose. However, for the sake of comparability and reproducibility, this is omitted here and the default settings of Matlab are used. Slightly better results may be achieved with random selection for other points of operation. This must be examined separately for each implementation. With the system properties from Table 3.1, the coefficients a_{ik} and b_{ik} ; $i \in (2,3)$, $k \in (2,\dots,6)$ as well as c_{10} can be determined.

The coefficients have to be redetermined for all phase angles. This can be prepared offline by means of the entire operating range and stored in lookup tables.

The energy trajectories are shown in Fig. 3.4. Compared to the course without compensation but considering the inductive voltage drops (Fig. 3.3 (a)), the energy pulsation can be reduced by 43.37%. In contrast to the analytical calculation for compensating the 2nd harmonic (Fig. 3.3 (b)) a reduction by 14.64% is still possible in this operating point. A prerequisite for this procedure is that the converter is able to set currents with a frequency corresponding to 6 times the AC frequency.

3.1.6 Function Optimization

In contrast to the parameter optimization from Sec. 3.1.5, in this section an optimal periodic function rather than an approximation shall be determined. For function optimization, software packages exist that can directly process the equations of the state space representation of the system. The software package used here is a Python implementation of CasADi [100]. It can be used to calculate optimal solutions of differential equation systems. An advantage is that the equations from Eqs. (2.9a) to (2.9c) can be used directly. A core difficulty is the cost function.

The cost functional Eq. (3.16b) cannot be applied, since it is not continuously differentiable. However, the L^∞ -norm can be approximated by an L^{2p} -norm i.e. $\|\underline{x}_{7-12}(t) - \underline{1}_6 w \bar{W}_0\|_{L^\infty([0, T_g])} \approx \|\underline{x}_{7-12}(t) - \underline{1}_6 \bar{W}\|_{L^{2p}([0, T_g])}$, for sufficiently large p . Instead of the norm, the power of the norm is optimized to simplify the calculation. The minimizers remain the same. This results in the differentiable cost functional

$$\tilde{J} = \|\underline{x}_{7-12}(t) - \bar{W} \underline{1}_6\|_{L^{2p}([0, T_g])}^{2p} \quad (3.17)$$

$$= \int_0^{T_g} \sum_{k=7}^{12} (x_k(t) - \bar{W})^{2p} dt. \quad (3.18)$$

A satisfactory reduction of the energy pulsation is obtained for the choice $p = 5$. The optimization aims at an optimal solution for $\tilde{x}_f(t)$. If p is increased further, the computation time exceeds a feasible limit.

The optimization problem is formulated as

$$\text{minimize} \quad \tilde{J} \quad (3.19)$$

$$\begin{aligned} \text{subject to} \quad & \dot{\underline{x}}_{7-12}(t) = \underline{T}^\top \left(\tilde{\underline{C}}^+ \tilde{\underline{y}}_{\text{ref}}(t) + \tilde{\underline{C}}_{\text{N}} \tilde{\underline{x}}_f(t) \right) \\ & \odot T^\top \left(\tilde{\underline{B}}^+ \left(\tilde{\underline{C}}^+ \dot{\tilde{\underline{y}}}_{\text{ref}}(t) - \tilde{\underline{A}} \tilde{\underline{C}}^+ \tilde{\underline{y}}_{\text{ref}}(t) \right. \right. \\ & \quad \left. \left. - \tilde{\underline{F}} z(t) \right) + \tilde{\underline{B}}^+ \left(\tilde{\underline{C}}_{\text{N}} \dot{\tilde{\underline{x}}}_f(t) - \tilde{\underline{A}} \tilde{\underline{C}}_{\text{N}} \tilde{\underline{x}}_f(t) \right) \right), \end{aligned} \quad (3.20)$$

$$\text{and} \quad \underline{x}_{7-12}(t) = \underline{x}_{7-12}(t + T_g), \quad (3.21)$$

$$\text{and} \quad \int_0^{T_g} \underline{x}_{7-12} dt = \bar{W} T_g \underline{1}_6. \quad (3.22)$$

Applied Method The goal of function optimization is to calculate the voltage signals needed to make the criterion optimal, i.e. minimal. For this purpose, the system equations are first discretized. One grid period is divided into N equidistant time steps. For each time step, a decision variable for each arm voltage u_{1-6} is created which is assumed to be constant over a time step. This is permissible due to the discrete nature of the system.

Boundary Conditions Another significant advantage of optimization with CasADi is that boundary conditions can be defined and considered comparatively easy. The calculation in a Matlab environment produced no results, only runtime errors in the program. The calculation of optimal voltages is done for stationary operation. Therefore, all currents \underline{x}_{1-6} as well as all energies \underline{x}_{7-12} must be periodic within a grid period. The boundary conditions for the states reads as

$$\underline{x}(0) = \underline{x}(N) \quad (3.23)$$

The output currents are defined by the output equation Eq. (2.9c).

$$(\underline{C} \underline{x}_{1-6})_{1,2} = \underline{y}_{d1,2} \quad (3.24)$$

Only two of the three currents are specified, since the sum of all currents must be 0 via the condition Eq. (2.5). Compared to the methods already introduced, the zero voltage V_0 can be automatically taken into account for optimization. In order to achieve comparability, however, it is set to 0 in this case. This results in the further constraint $\sum_{i=1}^6 v_i = 0$

To obtain a plausible solution, maximum values for the arm currents are introduced. As per Eqs. (3.12b) and (3.12c) the minimum RMS value of the arm current is

$$I_{\text{arm,max}} = \left(\frac{1}{2 + \frac{\hat{V}}{2V_{\text{dc}}}} \right) \hat{I} = 0.8125 \text{ A} \quad (3.25)$$

According to Eq. (3.15b) the current with compensation of the second harmonic is 1.1250 A. In order that compensation is possible at all, a maximum current of $1.5 \text{ A} + \epsilon$ is permitted. Where $\epsilon > 0$ is a factor introduced for numerical stability. For solutions close to the maximum current, a soft limit can be defined by considering ϵ in the cost function, thus increasing the numerical stability. The software was written in Python and can be found at [E1].

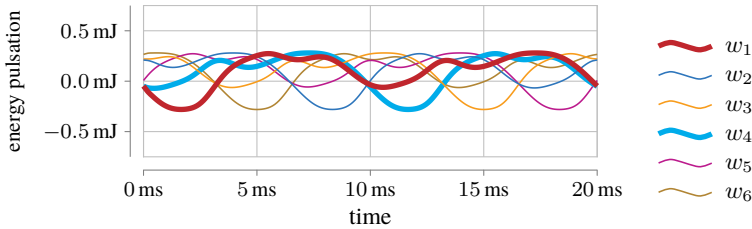


Figure 3.5: Normalized energy pulsation in the ideal system, with optimized trajectories of the circulating currents.

3.1.7 Results of the Function Optimization

The optimization of the circulating currents provides trajectories that will reduce the energy pulsation even further. In addition, the control variables \underline{u}_{1-6} are calculated and can be set as a current feed forward to dynamically improve the control of the system in Sec. 4.2. Figure 3.5 displays the energy trajectories of the arms under the influence of the calculated current trajectories. Here the zero voltage is chosen to $V_0 = 0$. Under these boundary conditions, the energy pulsation is reduced by 53.77% compared to operation without any compensation. In comparison to the analytical calculation of current trajectories with compensation of the 2nd harmonic, the energy pulsation is reduced by 30.32%. The parameter optimization provides good results, but can be reduced by 18.36% nevertheless.

3.2 Comparison of the Arm Currents With Different Compensation Methods

In order to be able to reduce the energy pulsation at all, however, additional arm currents must be injected. These additional currents cause additional ohmic losses. For each system and each operating point, it must be decided whether an additional current can be impressed, regardless of the type of compensation. If the energy pulsation is not reduced, the RMS values of arm currents according to Sec. 3.1.1 are minimal. In that case, the circulating currents are set to $x_{f,23} = \tilde{x}_{3,4} = 0$.

In contrast to the minimal RMS currents, the already known and new methods for reducing the energy pulsation were presented. To analyse the additional currents, the arm currents are calculated according to Eq. (2.23d) and converted into transformed quantities according to Eq. (2.13a). Physically \tilde{x}_1 represents the zero current between the neutral points of the system. \tilde{x}_2 is the DC current \tilde{i}_2 of the system. $\tilde{x}_{3,4}$ are the circulating currents $\tilde{i}_{3,4}$ which can be used to reduce the energy pulsation. $\tilde{x}_{5,6}$ are the corresponding AC currents $\tilde{i}_{5,6}$ to the grid. Since the transformation with \underline{T} corresponds to a power invariant transformation, the currents are scaled according to Eq. (2.11).

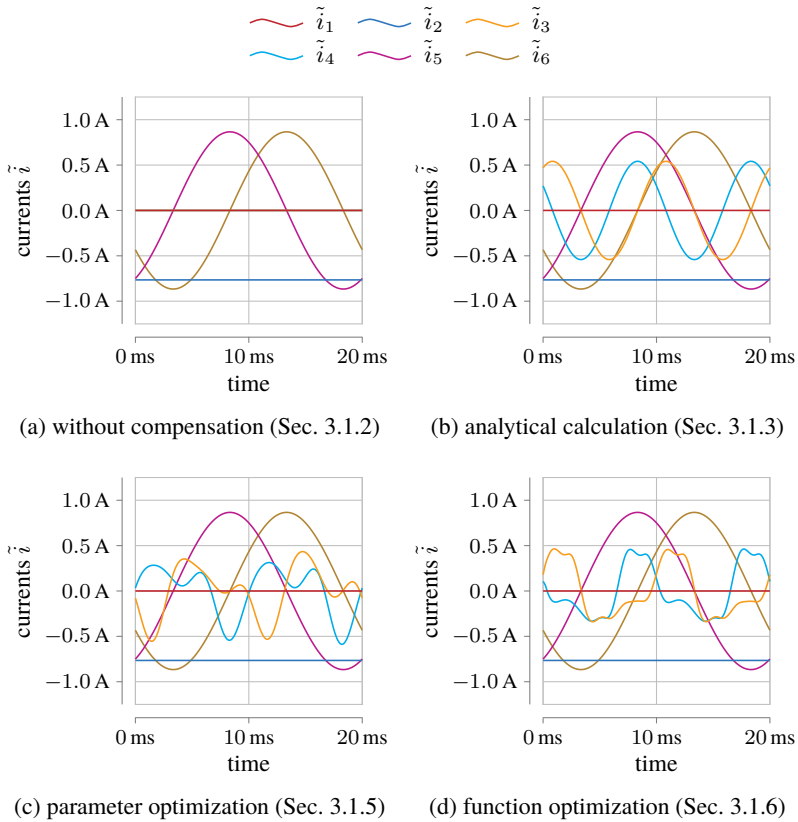


Figure 3.6: Comparison of the current trajectories in transformed coordinates.

Figures 3.6 (a) to 3.6 (d) show the current trajectories in transformed coordinates for all four presented compensation methods. The AC currents $\tilde{i}_{5,6}$ and the DC current \tilde{i}_2 are the same in all cases. The zero sequence current \tilde{i}_1 is 0. Thus the power exchange between the AC and DC side is the same in all cases. A difference can be found in the current trajectories of the circulating currents $\tilde{i}_{3,4}$, which have no influence on the power exchange due to the decoupling earlier.

In Fig. 3.6 (a) the currents are set to zero, which corresponds after Sec. 3.1.1 with the minimum RMS value of the arm currents. Figure 3.6 (b) shows the current trajectory for the reduction of the energy pulsation using the analytical calculation according to Sec. 3.1.3. If further harmonics are used for compensation, the current trajectories from Fig. 3.6 (c) are obtained with the newly presented procedure using the PSO algorithm. The deterministic optimal control inputs result in the current trajectories from Fig. 3.6 (d). To finally evaluate the methods, the RMS values of the resulting arm currents must be considered.

The RMS values are in initial estimation quadratically proportional to the additional ohmic losses. The frequency dependent losses of the additional currents can be neglected in first approximation. In the analytical calculation the maximum frequency of the circulating currents is $\omega_{\tilde{i},\max} = 2\omega_g$. The calculation provides the coefficients for sinusoidal currents up to the 6th harmonic $\omega_{\tilde{i},\max} = 6\omega_g$. The function optimization presented here uses $N = 100$ equidistant time steps. Thus, the maximum frequency at a network frequency of $f_{\text{grid}} = 50$ Hz is limited to a theoretical maximum of $f_{\tilde{i},\max} = 2.5$ kHz. However, the results show significant frequency components only up to $\omega_{\tilde{i},\max} \approx 20\omega_g$.

It was already shown in [23] that the switching frequency per cell is inversely proportional to the number of cells. Due to the sorting algorithm of the cells per arm, the number of switching events is distributed evenly across the cells' semiconductors. Therefore the switching losses are in first approximation decoupled from the current frequency. Thus it is assumed, that the conducting losses and therefore the RMS value of the arm currents is one benchmark criterion of the compensation methods.

The arm currents are calculated with Eq. (2.13a) and the RMS value is determined:

$$I = \sqrt{\frac{\omega_g}{2\pi} \int_0^{2\pi/\omega_g} \underline{T}^T \tilde{\underline{i}} dt} \quad (3.26)$$

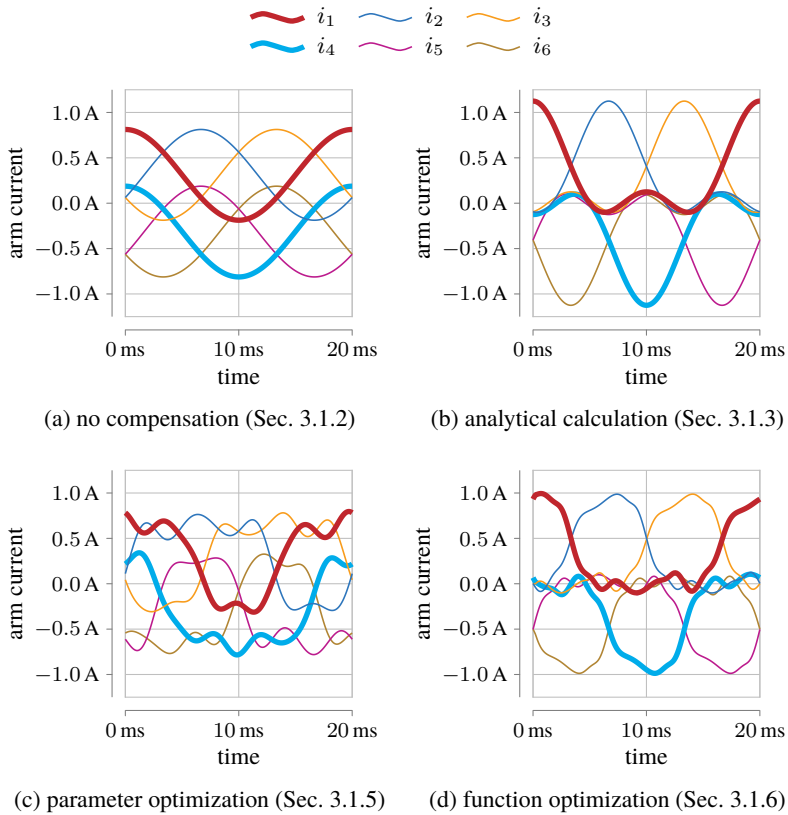


Figure 3.7: Comparison of the trajectories of the arm currents

Figures 3.7 (a) to 3.7 (d) show the trajectories of the arm currents resulting from the different feedforward methods. Figure 3.7 (a) thereby shows the arm currents without additional compensation of the energy pulsation and thus the minimum possible arm current according to Eqs. (3.12b) and (3.12c).

Table 3.2: Comparison of the different compensation methods depending on RMS arm current and energy deviation reduction at $\varphi = 0^\circ$

method	RMS-arm current	increase RMS	reduction energy pulsation
no compensation (Sec. 3.1.1)	0.4723 A	0 %	0 %
2nd harmonic analytically (Sec. 3.1.3)	0.5220 A	6.03 %	33.65 %
parameter up to 6th harmonic (Sec. 3.1.5)	0.5026 A	6.35 %	43.37 %
function optimization (Sec. 3.1.6)	0.5043 A	9.52 %	53.77 %

Table 3.2 is an overview that compares the reduction of the energy pulsation with the additional current. In contrast to the state of the art (analytical compensation of 2nd harmonics), significantly better degrees of reduction with up to 50 % can be achieved with the help of parameter compensation and function optimization. On the other hand, there are up to 10 % additional currents required for this. When designing a system, it must be examined for each operating point which type of compensation is permissible. The chosen method must be sensible within the scope of the load and cannot be answered in a generalized way. This work provides an overview of the possibilities to enable a quick and easy design of a system. Since the costs of a MMC are mainly determined by semiconductor costs and capacitor costs, these methods can already be taken into account in the initial design and contribute to the reduction of system costs.

3.3 Reduction of the Energy Pulsation at Different Operating Points

- no compensation (Sec. 3.1.2)
- analytical approach (Sec. 3.1.3)
- parameter optimization (Sec. 3.1.5)
- function optimization (Sec. 3.1.6)

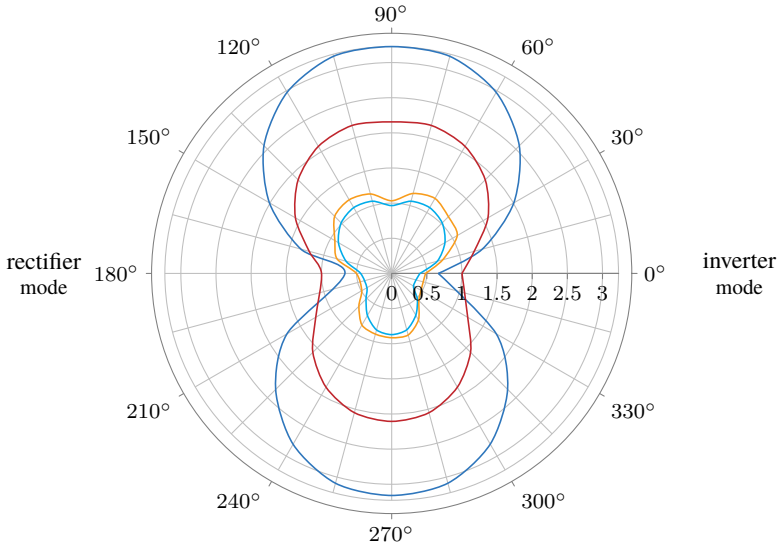


Figure 3.8: Comparison of the maximum energy pulsation of the different compensation methods over the entire phase angle φ of the AC side. The values are normalized to the maximum amplitude, without compensation at $\varphi = 0^\circ$

The magnitude of the energy pulsation is strongly dependent on the power factor of the AC side. For a phase angle $\varphi \neq 0$, the energy pulsation becomes larger for increasing φ until it reaches its maximum at $\varphi = \frac{\pi}{2}$. For the current trajectories of the analytical compensation, the phase angle is directly taken into account, as shown in Eq. (3.15a). The current trajectories of function and function optimization can be calculated separately for each operating point. In order to cover a continuous range of the phase angle φ in a later realization, interpolation is performed between the equidistant supporting points. The oper-

ation from Table 3.1 without additional reduction of the energy pulsation for a phase angle $0 \leq \varphi < 2\pi$ serves as reference. The maximum arm current is set to $i_{\text{arm,max}} = 1.5$ A. Figure 3.8 shows the comparison of the different compensation methods over the phase angle φ of the AC side. The energy pulsation without compensation at $\varphi = 0$ is used as baseline. All types of compensation allow a reduction of the energy pulsation. However, the energy pulsation increases significantly with an increasing proportion of reactive power transferred to the AC side. If the current trajectories of the circulating currents are now analytically determined and impressed according to Eq. (3.15a), the energy pulsation is even increased. This behavior is highly dependent on the system parameters and in particular on the inductors. The values from Table 3.1 are chosen in such a way that the effect of the increase of the energy pulsation is made particularly obvious. Already in [E2] further correlations between analytical compensation and energy pulsation were given. In contrast, the parameter optimized calculation of the current trajectories provides a reduction of the energy pulsation at every operating point of the system. The results are already very good, but can be further improved by function optimization. The function optimization, presented here, is the most effective method to reduce the energy pulsation in the entire working range of the system. As a trade-off, the additional current must be injected. This analysis must be carried out separately for each system. Using this thesis provides a fast method to set up the model equations and calculate the effects of each method.

Consideration of the Zero Sequence Voltage

In Sec. 3.1.2 was assumed, that the zero sequence voltage is chosen to 0 V. Since the function optimization gives the best results regarding the energy pulsation, the zero sequence voltage is additionally used for reduction using this method. When used on the grid, the zero sequence voltage cannot be chosen arbitrarily in all cases. A separate consideration must be made for each application. The function optimization is repeated under inclusion of the zero sequence voltage. For a phase angle of $\varphi = 0$ the energies and currents are shown in Figs. 3.9(a) and 3.9(c). The circulating currents \tilde{i}_3 and \tilde{i}_4 as well as the zero voltage \tilde{v}_0 are set in such a way that the optimal energy profile is shown in Fig. 3.9(c).

Compared to the function optimization without using the zero sequence voltage, the energy pulsation can be significantly reduced again in the entire range of the phase angle. Figure 3.9(d) shows the comparison with the two methods.

The maximum energy pulsation using function optimization without any zero sequence voltage from Fig. 3.8 is further improved by optimizing this voltage as well. The figure shows the maximum occurring energy pulsation normalized to the pulsation without any compensation as shown in Fig. 3.8.

Depending on the intended use of the system and restrictions on the use of zero voltage with regard to connection standards and insulation coordination, it must be weighed up against the use of zero voltage for energy swing reduction. In this case, the zero sequence voltage could not be used for overmodulation to the mains. In addition, Sec. 4.1.1 describes how the zero-sequence voltage can be used to balance the energies within the MMC. This option is not available when using the zero voltage for reduction of energy pulsation, since the required balancing power cannot be set independently at all times. Again this work presents an easy to use method to examine all possible modes of operation and the direct influence on the hardware.

In conclusion, the state of the art analytical consideration to compensate for the second harmonic for certain operating points, result in a reduction of the energy pulsation. However, by neglecting the inductive voltage drops in this method, it can lead to an unintentional increase in the energy pulsation. A current trajectory calculated offline for the circulating currents, on the other hand, can lead to a reduction at all operating points. The two new methods using parameter and function optimization based on the new type of modeling from Chapter 2 lead to significantly better results. The calculations provide the optimal current trajectories and the required setpoints for the adjustable voltage sources. By using the zero sequence voltage, the energy pulsations can be reduced even further in parameter and function approaches. If the model parameters are exactly known and no disturbances due to measurement noise or quantization occur, these methods are sufficient to be able to perform an MMC at any operating point. With Eq. (2.26) the control variables \underline{u}_{1-6} can be calculated directly from the current trajectories and disturbance variables. However, small model errors immediately lead to deviations in current and energy trajectories, so that energy and current controllers necessarily have to be designed and implemented for the realization. This will be described further in the following sections.

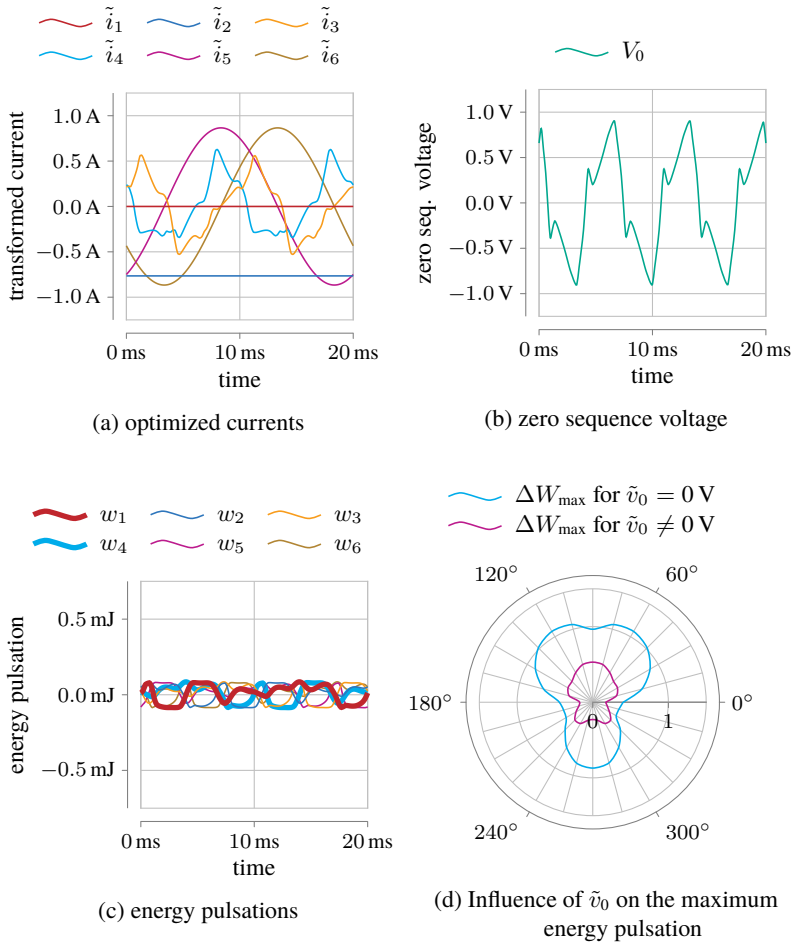


Figure 3.9: Influence of the zero sequence voltage \tilde{v}_0 on the maximum energy deviation and arm currents for function optimization.

Table 3.3: Technical specifications of an exemplary HVDC converter

Parameter	Value
Converter	
$P_{MMC,N}$	1000 MW
V_{dc}	700 kV
V_{ac}	400 kV
N_{cell} per arm	250
L_{arm}	90 mH
L_{ac}	120 mH
Cell	
half bridge semiconductors	FZ1200R45HL3 [D5]
C_{cell}	5 mF
$V_{C,mean}$	3 kV
$V_{C,max}$	3.75 kV
$I_{rms,max}$	1 kA
$f_{sw,mean}$	150 Hz
Module	
V_{CES}	4.5 kV
I_{CDC}	1.2 kA
I_{CRM}	2.4 kA

3.4 Exemplary Calculations for an HVDC Converter

The preceding analyses were performed with normalized quantities according to Table 3.1. To conclude, the fundamental findings of this chapter are applied to a sample configuration of an HVDC converter. The focus is on the reduction of the energy pulsation and the resulting increase of the arm current. Table 3.3 lists the parameter for a reasonable HVDC converter setup.

First, the system equations are calculated and parameterized according to Chapter 2. Secondly, the function optimization is performed according to Sec. 3.1.6. The cost function contains the energy pulsations. Using the parameters given in Table 3.3 the energies are recalculated into capacitor voltages. The result are

current and voltage trajectories for quasi-stationary operation at $\cos(\varphi) = 1$. Using a PLECS model provided by the manufacturer [D5], the semiconductor losses are calculated. Figures 3.10 (a) and 3.10 (b) show the voltage ripples of the converter in stationary operation. Using the new introduced function optimization, the voltage ripple can be reduced by approximately 30 %. The cell voltage ripple is reduced from 360 V down to 255 V. Besides the absolute reduction of the voltage ripple, the minimum voltage value increases. This also enlarges the safety margin towards the safe operating area of the converter since half bridges are assumed. Allowing a voltage ripple that is equivalent to the operation without additional circulating currents, the cell capacitance could be reduced by the same amount of approximately 30 % down to 3.5 mF. Moreover, the total stored energy in the system can be reduced.

The compensation using analytical compensation yields comparable results for this point of operation. However, with reference to Fig. 3.8, this is only valid around a narrow range with $\cos(\varphi) \approx 1$. The compensation becomes significantly worse than function optimization with decreasing power factors as already shown. For $\varphi = \frac{\pi}{3}$, the analytical approach reduces the pulsation by about 15 %. The function optimization still reduces the ripple down by approximately 26 %.

The arm currents of the HVDC application are shown in Figs. 3.10(c) and 3.10(d). The RMS value of the arm current increases due to the additional internal currents by about 5 % from 750 A to 790 A. A simulation using the calculated current and voltage trajectories show, that the semiconductor losses increase by about 9.8 % caused by increased arm currents and additional switching.

Overall, the calculations verify the results of Chapter 3. In addition to the state of the art approach of compensating the second harmonic, the function optimization approach allows a reduction of the voltage ripple over the entire operating range.

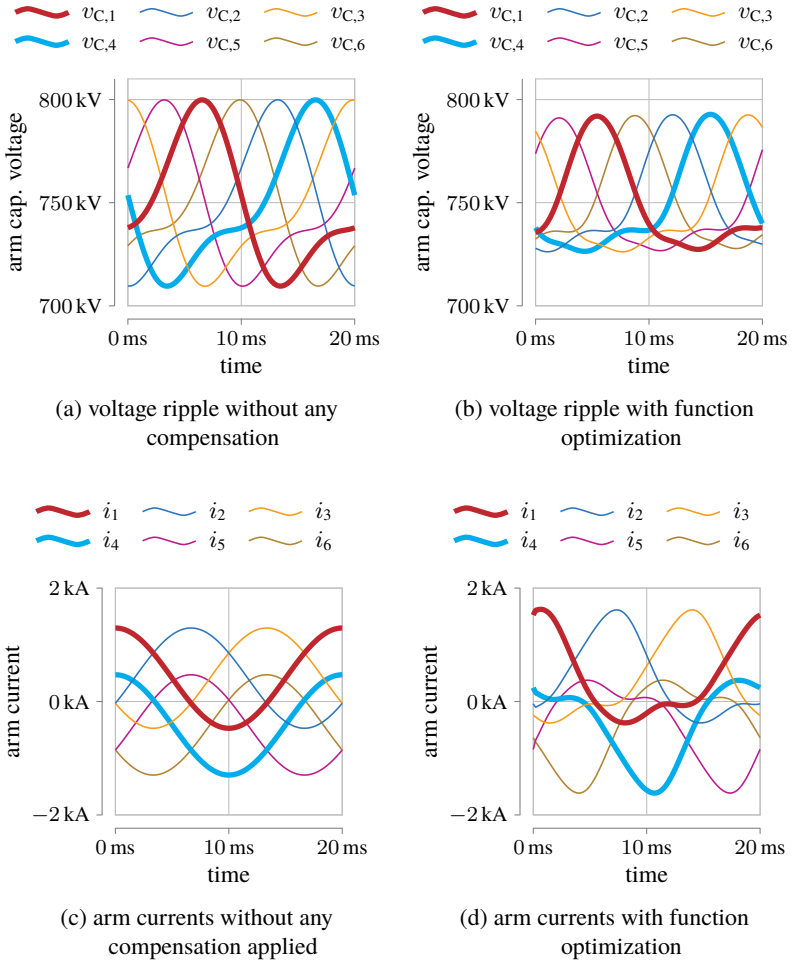


Figure 3.10: Comparison of voltage ripples and arm currents in an HVDC system using function optimization

3.5 Conclusion of this Chapter

In this chapter, a new feed forward control scheme of the MMC was derived and simulated on the basis of the system description in Chapter 2. The analysis provides degrees of freedom which can be used to reduce the energy pulsation over the entire operating range of the converter. The corresponding circulating currents can be calculated in advance.

The introduced formalism to describe MMC based topologies is well suited to calculate known approaches to reduction of energy pulsation like the analytical compensation of the second harmonic. Moreover, parameter optimization can be easily performed to reduce the energy pulsation over the entire operating range even under consideration of losses.

Additionally, a function optimization is introduced to determine the optimal current trajectories that result with the theoretical minimum of the energy pulsation for a given system. It was shown, that this approach is superior to the state of the art methods under all operation conditions. This even includes the pulsation during a grid fault which will be validated in Chapter 6. The zero sequence voltage can be included easily by adapting the optimization problem. The reduced energy pulsation can already be considered during the design of an MMC system reducing the need for installed capacitance. A calculation for an exemplary HVDC setup has proven the advantages of the function optimization over state of the art methods.

As shown, a reduction of the energy pulsation in an MMC based system comes always at the costs of increased arm currents. Regarding the future of energy generation and the increasing importance of power electronics, the efficiency of systems in use is becoming more and more important. With the function optimization shown, it is not only possible to reduce the required capacitance for MMC systems. The calculation allows the semiconductor losses to be included in the optimization as well. For this purpose, the cost function would only have to be extended by the semiconductor losses. Depending on the application, a cost-optimal design of the system can be achieved.

Chapter 4

Energy and Current Feedback Control of the MMC

In Chapter 3, optimal terms for current feed forward control were derived. These trajectories allow a stable operation of the system. Furthermore, the degrees of freedom in the current can be used to reduce the energy pulsations. Under ideal conditions, no further manipulation of the control variables is necessary. However, model errors, parameter deviations, approximations, quantization and measurement noise in the real system require a superimposed, feedback control structure to compensate for these inaccuracies.

To enable a stationary operation, the arm energies x_{7-12} must remain within defined limits. For the arm currents x_{1-6} setpoint trajectories are calculated which also have to be adjusted. The presented modelling allows an easy identification of the balancing power terms. There is no need for further investigation of those terms as in [23, 27]. The relations are inherently calculated. This applies to all MMC based topologies.

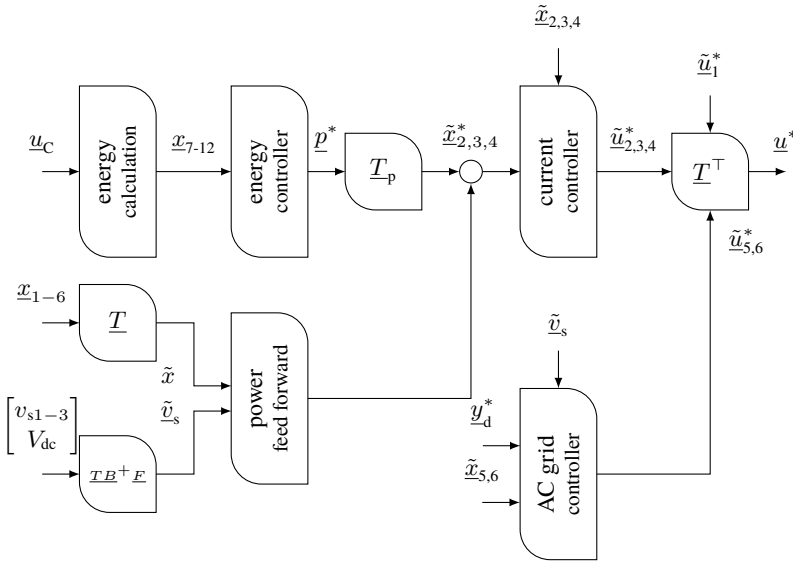


Figure 4.1: Overall control scheme of the MMC system

As a control approach, a cascaded scheme is built up, which can reduce the energy pulsation, adjust the average energy values and current trajectories. By modelling and decoupling through the transformation rule, it is possible to adjust the AC side independently of other control tasks. In order to be able to react as dynamically as possible to grid faults, the AC side is implemented using a model-predictive approach with high-frequency voltage feed forward. Due to the state space modelling, the design is straightforward.

Figure 4.1 shows an overview of the control of the MMC system. The following sections describe the depicted scheme in detail. The cascaded structure is based on the design of [23, 27, 30, 43]. However, the grid currents are examined separately in order to be able to inject accurate currents with the MMC even in the event of a grid fault. By decoupling the structure, the design and layout of the entire control system can be carried out in the transformed coordinates.

Particular attention is paid to AC side control, since the grid connected MMC is in the focus of this thesis. The AC side can be controlled independently of the

energy control. In addition, the AC voltage can be fed forward and the AC currents can therefore be adjusted highly dynamically. A model-predictive approach is chosen and verified on a real-time capable laboratory converter system for a high performance AC current control. In [78] the MPC for high power converters and industrial drives is derived and designed. Here, the MMC is treated as a representative of the modular converters. The grid control can be implemented independent of the actual topology.

In literature some further approaches to the MPC of the MMC have already been presented. However, those MPC of the overall system with hard and soft limitations of the state variables, control variables and setpoint variables requires a large computational effort with increasing number of cells. With the MPC approaches, all control and optimization goals of the system are often offset against each other in a cost function [101–104]. The optimal switching states of the individual semiconductors of the system are determined as output variables. The complexity of the optimization tasks can be further reduced [105], but the real-time calculation is still difficult. Optimization based on the mean value model using an underlying sorting algorithm for the capacitor voltages within an arm is more suitable for a real-time implementation [79, 106–108].

The control approach and implementation presented in [E3] and in this thesis focuses on the AC side current control in real time. According to the complexity of online optimization, the overall control structure is sufficient for a highly performant operation of the MMC even under faulty grid conditions.

First, the arm energy control is derived. The focus is on the decoupled control of each arm. The second part deals with the current control of the DC side and the internal currents. In addition, the AC side MPC based control approach is presented. Finally, the feedback control algorithms are simulated and the results are presented.

4.1 Energy control

In Chapter 3 and Sec. 3.1, optimal current trajectories were calculated with the modelling from Chapter 2 in order to keep the arm energies during steady state operation within the tolerance band. To be able to set the energies to their desired values, correlations must be found starting from the model with which all six energies can be set as independently of each other as possible.

Table 4.1: transformed quantities and their physical meaning

voltages		currents	
$\tilde{u}_1 = \tilde{u}_f$	zero sequence voltage	$\tilde{x}_1 = 0$	zero sequence current
\tilde{u}_2	DC voltage	$\tilde{x}_2 = \tilde{x}_{f,1}$	DC current
$\tilde{u}_{3,4}$	voltages across \tilde{L}	$\tilde{x}_{3,4} = \tilde{x}_{f,2,3}$	internal currents
$\tilde{u}_{5,6}$	AC voltages	$\tilde{x}_{5,6}$	AC currents

Analogous to the decoupling of the currents of the MMC, a decoupling of the energies is aimed at. If all model parameters are exactly known and no disturbing effects such as measurement noise occur, no feedback is necessary and the MMC can be operated directly controlled. In addition, all ohmic losses in the system have so far been neglected. To counteract these inaccuracies, a control of the energies and currents is mandatory.

4.1.1 Analysis of the Occurring Arm Powers

In Eq. (2.27c) the energies, respectively their derivatives are calculated as state variables $\underline{x}_{7-12} = \underline{u} \odot \underline{x}_{1-6}$ and their nonlinear relation is expressed. The control variable \underline{u} are expressed in Eq. (2.26) as a function of the setpoints $\underline{y}_{\text{ref}}$, the degrees of freedom \underline{x}_f and \underline{u}_f . With this approach, the degrees of freedom for adjusting the energies \underline{x}_{7-12} can be identified.

With respect to the power feed forward from Sec. 3.1, the degrees of freedom \underline{x}_f are expressed in transformed coordinates. Equation (2.27b) gives the arm powers in transformed currents and voltages. If this equation is multiplied out, all combinations $\tilde{u}_i \cdot \tilde{x}_j$, ($i, j \in 1, \dots, 6$) occur.

In principle, any current and voltage can be freely adjusted due to the decoupling. In the following, the power terms which must be set for stationary operation are identified. As a result, power terms remain which can be freely set and thus, in principle, balance the energy within the converter. These terms are examined to see whether they can influence the arm energies appropriately.

In Figs. 2.3 (a) to 2.3 (d) the physical relationship of the decoupled, transformed system to the MMC was already shown. Table 4.1 again shows these connections

in tabular form. The zero sequence current \tilde{x}_1 is always 0 A, because the neutral points are not connected to each other. The voltages $\tilde{u}_{3,4}$ describe the voltage drops across the arm inductors and parasitic resistances in the system.

Compared to the DC voltage and AC voltages that occur, the voltage drops across the arm inductors are small and can be neglected. For this reason, $\tilde{u}_{3,4} \approx 0$ V is assumed in the subsequent considerations.

Starting from a stationary operating point, the DC voltage, AC voltages, DC current and AC currents are defined to keep the average of the arm energies constant, as described in Sec. 3.1. It directly follows that further arm powers can only be freely set if the product is formed with \underline{u}_f or $\underline{x}_{f2,3}$. From Sec. 3.1, the AC side and DC side power must be equal to maintain steady state operation. However, since all losses have been neglected in feed forward control, the DC power $\tilde{u}_2 \cdot \tilde{x}_2$ must also be taken into account.

With Eqs. (2.27c), (2.28), (4.3e) and (4.4) the trajectories of arm powers and arm energies can be determined directly. To be able to influence these energies, power terms \tilde{p}_s are required, which are freely adjustable.

$$\tilde{p}_s = \begin{bmatrix} \tilde{p}_{s1} \\ \tilde{p}_{s2} \\ \tilde{p}_{s3} \\ \tilde{p}_{s4} \\ \tilde{p}_{s5} \\ \tilde{p}_{s6} \\ \tilde{p}_{s7} \\ \tilde{p}_{s8} \\ \tilde{p}_{s9} \end{bmatrix} = \begin{bmatrix} \tilde{u}_2 \cdot \tilde{x}_2 \\ \tilde{u}_1 \cdot \tilde{x}_3 \\ \tilde{u}_1 \cdot \tilde{x}_4 \\ \tilde{u}_2 \cdot \tilde{x}_3 \\ \tilde{u}_2 \cdot \tilde{x}_4 \\ \tilde{u}_5 \cdot \tilde{x}_3 \\ \tilde{u}_5 \cdot \tilde{x}_4 \\ \tilde{u}_6 \cdot \tilde{x}_3 \\ \tilde{u}_6 \cdot \tilde{x}_4 \end{bmatrix} \quad (4.1)$$

To determine the influence of the individual terms from Eq. (4.1) on the arm energies, Eq. (2.27b) $\dot{\underline{x}}_{7-12} = \underline{T}^\top \underline{\tilde{u}} \odot \underline{T}^\top \underline{\tilde{x}}_{1-6}$ is calculated and all other power terms are set to 0.

$$\dot{\underline{x}}_{7-12} = \underline{u} \odot \underline{x}_{1-6} \quad (4.2a)$$

$$= \underline{T}^\top \underline{\tilde{u}} \odot \underline{T}^\top \underline{\tilde{x}}_{1-6} \quad (4.2b)$$

inserting the boundary conditions and Eq. (4.1) yields

$$= \underline{T}_{\text{pn}}^\top + \tilde{p}_s \quad (4.2c)$$

Equation (4.2c) enables the arm energies \underline{x}_{7-12} to be influenced by means of the power terms \underline{p}_s . Since for the energy control the freely adjustable power terms $\tilde{\underline{p}}_s$ are required, the resulting matrix is defined as a pseudoinverse of the power transformation matrix. Equation Eq. (4.2c) can then be solved for $\tilde{\underline{p}}_s$.

$$\tilde{\underline{p}}_s = \underline{T}_{\text{pn}} \dot{x}_{7-12} \quad (4.2d)$$

The matrices $\underline{T}_{\text{pn}}$ and $\underline{T}_{\text{pn}}^+$ are given in Sec. A.6 in Eqs. (A.13a) and (A.13b).

Equation (4.2d) is the basis for the MMC energy control. An energy controller can be used to determine the power \dot{x}_{7-12} needed to keep the energies x_{7-12} within their tolerance band. The transformation matrix $\underline{T}_{\text{pn}}$ delivers the relation to the freely adjustable power terms $\tilde{\underline{p}}_s$. Thus, an energy control can be implemented, which is only realized by the previously determined degrees of freedom $\tilde{\underline{x}}_f$ and $\tilde{\underline{u}}_f$. The AC-side control is therefore decoupled from the energy control and the system can be operated stable and safe.

Example for Balancing Power Calculation

For stationary operation, the AC quantities are assumed to be a generic, symmetrical, sinusoidal system. The DC value is ideally smooth, with the DC current being selected to match the AC power. The circulating currents and the zero sequence voltage are freely adjustable. Assuming a constant DC voltage as well as a symmetrical, sinusoidal AC system, the approach for the voltages $\tilde{\underline{u}}$ is denoted as

$$\tilde{u}_1 = \underline{u}_{\text{ff}} = \hat{v}_0 \sin(\tilde{\gamma}_n) \quad (4.3a)$$

$$\tilde{u}_2 = \tilde{V}_{\text{dc}} \quad (4.3b)$$

$$\tilde{u}_3 = \tilde{u}_4 = 0 \quad (4.3c)$$

$$\tilde{u}_5 = \tilde{v}_{\text{ac}} \cos(\tilde{\gamma}_d) \quad (4.3d)$$

$$\tilde{u}_6 = \tilde{v}_{\text{ac}} \sin(\tilde{\gamma}_d) \quad (4.3e)$$

With respect to Eq. (2.21c) the DC voltage and AC voltages can be expressed in measured values as

$$\begin{bmatrix} \tilde{V}_{dc} \\ \tilde{v}_{ac} \cos(\tilde{\gamma}_d) \\ \tilde{v}_{ac} \sin(\tilde{\gamma}_d) \end{bmatrix} = \begin{bmatrix} \frac{\sqrt{6}}{2} V_{dc} \\ -v_{s1} + v_{s2} \\ -\frac{1}{\sqrt{3}} v_{s1} - \frac{1}{\sqrt{3}} v_{s2} + \frac{2}{\sqrt{3}} v_{s3} \end{bmatrix} \quad (4.3f)$$

The currents \tilde{x}_{1-6} result in

$$\tilde{x}_1 = 0 \quad (4.4a)$$

$$\tilde{x}_2 = \tilde{I}_{dc} = \tilde{x}_{f3} = \frac{\sqrt{6}}{2} \frac{\hat{V}}{V_{dc}} \hat{I} \cos(\varphi) \quad (4.4b)$$

$$\tilde{x}_3 = \tilde{x}_{f2} = \tilde{i}_{34} \cos(\tilde{\gamma}_{34}) \quad (4.4c)$$

$$\tilde{x}_4 = \tilde{x}_{f3} = \tilde{i}_{34} \sin(\tilde{\gamma}_{34}) \quad (4.4d)$$

$$\tilde{x}_5 = \tilde{i}_{ac} \cos(\tilde{\gamma}_d - \tilde{\varphi}) \quad (4.4e)$$

$$\tilde{x}_6 = \tilde{i}_{ac} \sin(\tilde{\gamma}_d - \tilde{\varphi}) \quad (4.4f)$$

where \tilde{v}_0 and \tilde{V}_{dc} are the transformed zero sequence voltage and DC voltage, respectively. The zero sequence voltage has a frequency ω_n with $\tilde{\gamma}_n = \omega_n t$. \tilde{v}_{ac} is the amplitude of the transformed AC voltages. \tilde{I}_{dc} is the DC current in transformed coordinates. \tilde{i}_{ac} is the amplitude of the transformed AC currents. $\tilde{\gamma}_d$ is the instantaneous value of the angle of the AC voltage system. For a sinusoidal movement of the voltage with the frequency ω_d , $\tilde{\gamma}_d = \omega_d t + \tilde{\varphi}_0$ applies with an offset angle $\tilde{\varphi}_0$ in the transformed system. The angle $\tilde{\varphi}$ is the phase angle of the currents in the transformed system. The degrees of freedom \tilde{x}_3 and \tilde{x}_4 are set as generic, sinusoidal, independent functions of amplitude \tilde{i}_{34} and the phase angle $\tilde{\gamma}_{34}$.

The setpoints of the DC current \tilde{x}_2 and the internal currents \tilde{x}_3 and \tilde{x}_4 are then composed of the superposition of all the partial terms from the energy control with respect to Eq. (4.2c). In addition, the AC power is fed forward analogous to Sec. 3.1.

In order to generate the required active power to balance the energies, the resulting power terms are divided and applied according to the absolute value and

phase of the currents and voltages. With DC quantities, there is no need to consider the phase, since only active power can be generated.

To be able to generate an averaged power, all sinusoidal terms from Eq. (4.1) must be examined. To ensure that the zero sequence voltage in combination with the AC currents does not produce unwanted active power, the zero sequence voltage and the AC side must have different frequencies, i.e. $\omega_d \neq \omega_n$.

Using the example of the balancing power \tilde{p}_{s6} the conditions of the frequencies are derived so that the energy can be influenced on average. The AC voltage \tilde{u}_5 is considered as given. The internal current \tilde{x}_3 can therefore be adjusted as required to balance the energies. For this part of the internal current $\tilde{\gamma}_{34} = \omega_{34,6}t + \tilde{\varphi}_{34,6}$ is applicable. For \tilde{w}_{s6} holds

$$w_{s6} = \int_0^t \tilde{p}_{s6} dt = \int_0^t \tilde{u}_5 \tilde{x}_3 dt \quad (4.5a)$$

$$= \int_0^t \tilde{v}_{ac} \tilde{i}_{34,6} \cos(\omega_d t) \cos(\omega_{34,6} t + \tilde{\varphi}_{34,6}) dt \quad (4.5b)$$

$$= \begin{cases} \tilde{i}_{34,6} \tilde{v}_{ac} \left(\frac{\sin(2\omega_{34,6}t + \tilde{\varphi}_{34,6})}{4\omega_{34,6}} + \frac{t \cos(\tilde{\varphi}_{34,6})}{2} \right) + \tilde{W}_0 & \omega_{34,6} = \mp \omega_d \\ \frac{\tilde{i}_{34,2} \tilde{v}_{ac}}{2(\omega_d + \omega_{34,1})} \sin(\tilde{\varphi}_{34,6} + (\omega_d + \omega_{34,6})t) \\ - \frac{\tilde{i}_{34,6} \tilde{v}_{ac}}{2(\omega_d - \omega_{34,6})} \sin(\tilde{\varphi}_{34,6} - (\omega_d - \omega_{34,6})t) + \tilde{W}_0 & \omega_{34,6} \neq \mp \omega_d \end{cases} \quad (4.5c)$$

Equations (4.5a) to (4.5c) show the concrete approach which influence the balancing power \tilde{p}_{s6} has on the energies. By integrating the balancing power, the frequencies are determined for which the mean value of the energy is manipulated. From [line 2 and 3](#) in Eq. (4.5c) it can be seen that for frequencies $\omega_{34,6} \neq \pm \omega_n$ exclusively periodic energy terms are formed. Thus, all power terms, which do not satisfy the requirement $\omega_{34,2} = \pm \omega_n$, are unsuitable and will not be considered anymore. For frequencies, which satisfy this equation ([line 1](#) in Eq. (4.5c)), two terms are decisive.

The [first term](#) is periodic with the double frequency of $\omega_{34,1}$ and thus does not contribute to the mean value of the energy. The [second term](#) can be unequal to 0 and thus changes the mean value of the energy over time. In order to obtain the maximum influence, $\tilde{\varphi}_{34,6}$ is set to $\tilde{\varphi}_{34,6} = 0$ without restriction of the generality.

Therefore, in order to be able to influence the mean value of the energy with the balancing power \tilde{p}_{s6} , a summand of the internal current \tilde{x}_3 must be added:

$$\tilde{x}_{3,6} = \frac{\tilde{p}_{s6}}{\tilde{v}_{ac}} \cos(\omega_d t) \quad (4.6)$$

The analysis of all further occurring symmetries from \tilde{p}_s is done in the same manner.

By selecting the orthogonal trigonometric functions and frequencies from Eqs. (4.1), (4.3e), (4.4) and (4.5) the total setpoint can be calculated from superposition of all individual setpoints. This leads to the following for the setpoints of the currents

$$\tilde{i}_2 = \tilde{x}_2 = \frac{1}{\tilde{u}_2} \left(\tilde{p}_{s1} - \underbrace{\tilde{u}_5 \tilde{x}_5 + \tilde{u}_6 \tilde{x}_6}_{P_{Ac}} \right) = \frac{1}{\tilde{V}_{dc}} \left(\tilde{p}_{s1} - \tilde{v}_{ac} \tilde{i}_{ac} \cos(\tilde{\varphi}) \right) \quad (4.7a)$$

$$\tilde{i}_3 = \tilde{x}_3 = \frac{\tilde{p}_{s2}}{\tilde{u}_1} + \frac{\tilde{p}_{s4}}{\tilde{u}_2} + \frac{\tilde{p}_{s6}}{\tilde{u}_5} + \frac{\tilde{p}_{s8}}{\tilde{u}_6} \quad (4.7b)$$

$$= -\frac{\tilde{p}_{s2}}{\tilde{v}_0} \sin(\omega_n t) + \frac{\tilde{p}_{s4}}{\tilde{V}_{dc}} + \frac{\tilde{p}_{s6}}{\tilde{v}_{ac}} \cos(\omega_d t) + \frac{\tilde{p}_{s8}}{\tilde{v}_{ac}} \sin(\omega_d t) \quad (4.7c)$$

$$\tilde{i}_4 = \tilde{x}_4 = \frac{\tilde{p}_{s3}}{\tilde{u}_1} + \frac{\tilde{p}_{s5}}{\tilde{u}_2} + \frac{\tilde{p}_{s7}}{\tilde{u}_5} + \frac{\tilde{p}_{s9}}{\tilde{u}_6} \quad (4.7d)$$

$$= -\frac{\tilde{p}_{s3}}{\tilde{v}_0} \sin(\omega_n t) + \frac{\tilde{p}_{s5}}{\tilde{V}_{dc}} + \frac{\tilde{p}_{s7}}{\tilde{v}_{ac}} \cos(\omega_d t) + \frac{\tilde{p}_{s9}}{\tilde{v}_{ac}} \sin(\omega_d t) \quad (4.7e)$$

The balancing powers \tilde{p}_{s1-9} can be calculated by the superimposed energy controllers, for example. In this way, it is possible to keep the arm energies on average at their setpoint value.

Balancing Without a Zero Sequence Voltage

Until now the balancing was shown using a zero sequence voltage. Using the MMC at low output frequencies, might make the usage of the zero sequence voltage necessary [23]. Depending on the operating point, however, this degree of freedom can be restricted or completely omitted. The power transformation matrix can be set up easily using the modelling approach by assuming $\tilde{u}_1 =$

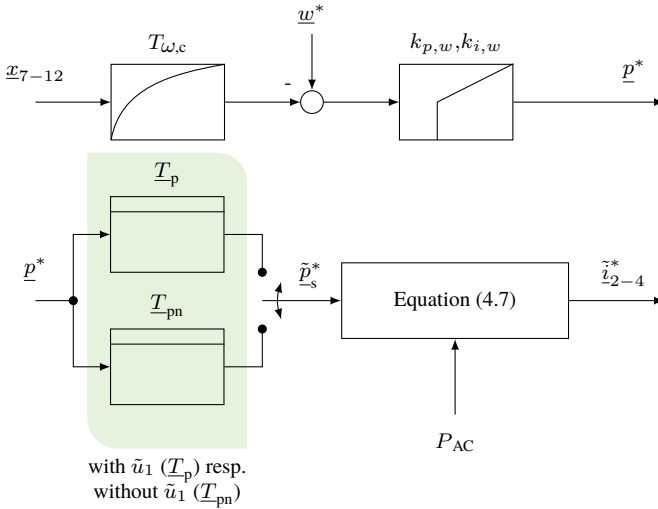


Figure 4.2: Control engineering schematic of the energy controllers

0. Thus, the balancing powers \tilde{p}_{s2} and \tilde{p}_{s3} in in Eq. (4.1) are 0. The resulting power transformation matrix T_p is specified in Chapter A in Eq. (A.13c). The setpoints of the balancing currents are calculated similar to Eqs. (4.2d) and (4.7). Depending on the operating point, it is possible to switch between T_p and T_{pn} to operate the converter safely.

4.1.2 Energy Controller

In Sec. 4.1.1 the correlation between the arm energies and balancing powers was shown. To determine the correct amount of balancing power, energy controllers are established. Each arm is adjusted by one controller. Since only the average values are controllable, the measured values are filtered in advance.

The calculated balancing powers are subsequently mapped to the balancing powers \underline{p}_s with respect to Eq. (4.2d) in transformed coordinates. The setpoints of the currents \tilde{x} calculated with Eq. (4.7) are then controlled by subordinate current controllers.

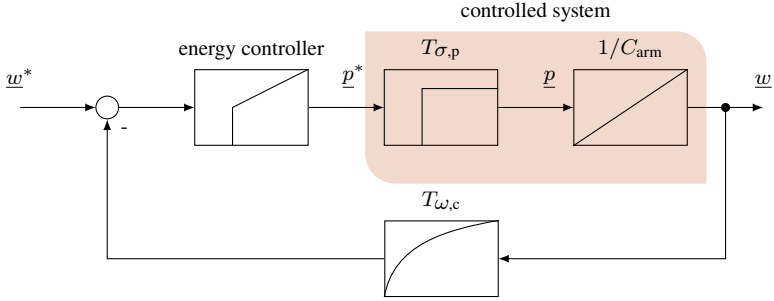


Figure 4.3: closed energy control loop

Figure 4.2 shows the control engineering equivalent diagram of the energy controllers. The measured quantities \underline{x}_{7-12} are each filtered with a 1st order low pass filter with the cutoff frequency ω_c . Since the implementation will later take place on a time-discrete system of the sampling time T_A , the controllers and filters are directly designed in the time-discrete domain. The transfer function $\underline{G}_f(z)$ of the filters are given by

$$\underline{G}_f(z) = \frac{1 - e^{-T_A \omega_c}}{z - e^{-T_A \omega_c}} \quad (4.8)$$

The mean values of the arm energies are entered as constants for the target values \underline{w}^* . The control deviations are fed to PI-controllers with the proportional amplification $k_{p,w}$ and the integral amplification $k_{i,w}$. The outputs of the controllers are those powers, which are necessary for adjusting the arm energies. The transfer function $\underline{G}_{\text{pi},w}(z)$ of the PI-controllers are given by

$$\underline{G}_{\text{pi},w}(z) = k_{p,w} + k_{i,w} \frac{z T_A}{z - 1} \quad (4.9)$$

The required powers are then converted with \underline{T}_p or $\underline{T}_{\text{pn}}$ to freely adjustable powers in transformed quantities. With the help of Eq. (4.7) the current setpoints are determined. These current setpoints are fed to the subordinate current controller, which determine the output variable for controlling the power.

Design of the Energy Controllers

Figure 4.3 shows the control engineering diagram of the closed energy control loop of the MMC. Due to the decoupling of the system the original multiple input multiple output (MIMO) problem is divided up into 6 single input single output (SISO) problems. Thus, the controllers are simple one dimensional, that can be designed fast and easily.

Besides the PI controllers with the gain factors $k_{p,w}$ and $k_{i,w}$ and the filters with the cutoff frequency ω_c in the feedback path from Sec. 4.1.2, the controlled system of the energy controller is shown. It consists of an ideal dead time representing the current control system and a following integrator for the arm capacitors.

The target powers \underline{p}^* are considered ideally set by the subordinate current control loop and the integrator after the dead time $T_{\sigma p}$. The integrator with gain 1 follows directly from Eq. (2.28). The smoothing time constant $T_{\omega,c}$ of the filter is derived from the inherent energy pulsations of the MMC.

To simplify the controller design, the underlying dead time $T_{\sigma p}$ is approximated by a first-order delay element according to [109, p.22]. The necessary time constant depends on the realization of the subordinated current controllers. Compared to the filter time constant, however, it is small and is chosen for all energy controllers as $T_{\sigma p} = 10 T_A$. With regard to the measurement results presented in Chapter 6, satisfactory results are achieved here. Depending on the application, the time constant can be adjusted.

To design the filters, the inherent energy pulsations are considered. After Sec. 3.1 the frequencies of the second harmonics appear dominant in the pulsations. These can be compensated and shifted to higher frequencies, but the filters are designed for operation with lowest arm current RMS value. This means that the filters have to damp these oscillation satisfactorily. A cutoff frequency of $\omega_c = \frac{\omega_d}{3}$ and thus a time constant $T_{\omega,c} = \frac{1}{2\pi\omega_c} = \frac{3}{2\pi\omega_d}$ provides very good results [23]. The dynamic requirements of the energy control loop are significantly determined by this time constant.

Consequently, the controllers are designed as PI controllers according to the symmetric optimum with the damping factor a_w [110, p.65]. The following applies

$$T_{\sigma,w} = T_{\sigma p} + T_{\omega,c} \quad (4.10a)$$

$$k_{p,w} = \frac{1}{a_w T_{\sigma,w}} \quad (4.10b)$$

$$k_{i,w} = \frac{1}{a_w^3 T_{\sigma,w}^2} \quad (4.10c)$$

Where $T_{\sigma,w}$ is the sum of the non-compensable time constants. The damping factor is chosen to $a_w = 2$. The design is the same for all 6 arm energy controllers. Thus, the closed control loops are stationary accurate and satisfy the dynamic requirements to be able to control the mean value of the arm energies to their setpoint value.

4.2 Control of the DC Current and Internal Currents

In Secs. 3.1 and 4.1 optimal current trajectories and current setpoints for balancing were calculated using the new modelling approach from Chapter 2. These currents are set with the control variables u . To overcome model errors and to achieve steady-state accuracy, current controllers are implemented. By decoupling the system according to Chapter 2 it is possible to set the DC current independently of the AC currents and independently of the internal currents. Figures 2.3 (a) to 2.3 (d) show the corresponding controlled systems and possibilities of influence. For each controlled system, corresponding controllers are designed and configured.

In order to investigate the potential of the MMC as a grid-side converter, the behavior towards the AC side is of special interest. The presented method for the modelling of the MMC allows a systematic design of powerful control algorithms to adjust the AC currents. Independent of this, the DC side and internal currents for power exchange and energy balancing must be tuned as dynamically as possible. The decoupling allows a separate consideration of the control tasks and a design of suitable controllers for these goals. It must also be possible to limit the

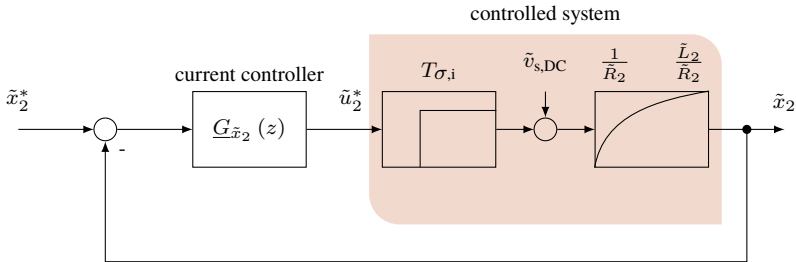


Figure 4.4: closed control loop of the DC current \tilde{x}_2

manipulated variables in order to set a stable operating point. In addition, a new approach for limitation of the output variables is described in Sec. 4.2.3.

By transformation and decoupling from Chapter 2, the control of all currents \tilde{x}_{1-6} is performed in the transformed domain. Equation (2.13c) provides, how the transformed setpoints $\tilde{\underline{u}}^*$ can be converted to control variables \underline{u}^*

$$\underline{u}^* = \underline{T}^\top \tilde{\underline{u}}^* \quad (4.11)$$

The regulation of the DC side and the internal currents has already been explained, discussed and verified in [23, 26, 30, 96]. Based on the modeling in Chapter 2 these can be realized and designed in a simple way according to those approaches. A new approach for a highly dynamic current control is considered and presented separately in Sec. 4.3.

4.2.1 Control of the DC current \tilde{x}_2

For the DC side, the transformed equivalent circuit diagram from Fig. 2.3 (b) is determining. The circuit time constant $\tau_{0,2}$ results directly from Fig. 2.3 (b) and can be calculated with Eqs. (2.21a) and (2.21b). Figure 4.4 shows the closed current control loop of the DC side. The corresponding system equation is given in line 2 Eq. (2.19d).

The system to be controlled is a first-order delay element with the gain $k_R = 1/\tilde{R}_2$ and the time constant $\tau_{0,2} = \tilde{L}_2/\tilde{R}_2$. The limited output of the current con-

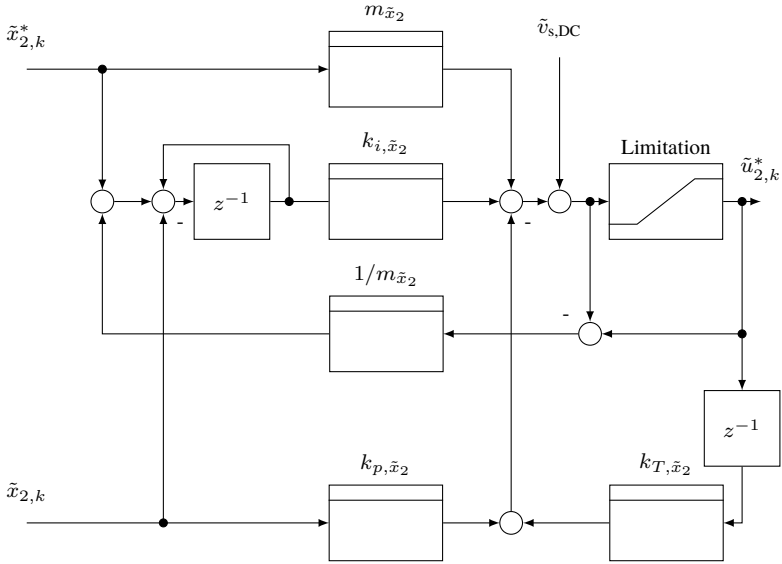


Figure 4.5: Time discrete current state controller with consideration of a computation dead time for \tilde{x}_2

troller is \tilde{u}_2^* . The maximum control voltage amplitude is calculated in Sec. 4.2.3. The DC voltage $\tilde{v}_{s,DC}$ appears as disturbance variable. The DC voltage is fed forward in Fig. 4.5. The digital implementation and modulation by the converter are modeled by a dead time $T_{\sigma,i} = T_A$.

In order to be able to precisely control the DC current \tilde{x}_2 dynamically and steady-state, a time-discrete current state controller with consideration of one computation dead time according to [111, 112] is established and designed.

Figure 4.5 shows the structure of the controller. It considers the digital implementation on the control system as well as the controlled system itself. With this controller structure, both, reference variable behavior and disturbance variable behavior can be configured separately by $\tau_{d,2}$ and $\tau_{i,2}$ respectively. The output variables can be easily limited.

For the calculation of the amplification factors the following applies

$$\tau_{d,2} = 10 T_A \quad (4.12a)$$

$$\tau_{i,2} = 15 T_A \quad (4.12b)$$

$$z_{d,2} = e^{-\frac{T_A}{\tau_{d,2}}} \quad (4.12c)$$

$$z_{i,2} = e^{-\frac{T_A}{\tau_{i,2}}} \quad (4.12d)$$

$$m_{\tilde{x}_2} = (1 - z_{d,2}) \frac{\tilde{R}_2}{1 - e^{-\frac{T_A}{\tau_{0,2}}}} \quad (4.12e)$$

$$k_{i,\tilde{x}_2} = (1 - z_{i,2}) m_{\tilde{x}_2} \quad (4.12f)$$

$$k_{T,\tilde{x}_2} = 1 - z_{d,2} - z_{i,2} + e^{-\frac{T_A}{\tau_{0,2}}} \quad (4.12g)$$

$$k_{p,\tilde{x}_2} = \left((1 - z_{d,2})(1 - z_{i,2}) + k_{T,\tilde{x}_2} e^{-\frac{T_A}{\tau_{0,2}}} \right) \frac{\tilde{R}_2}{1 - e^{-\frac{T_A}{\tau_{0,2}}}} \quad (4.12h)$$

The input time constant $\tau_{d,2}$ also takes into account the dynamics of the DC source. The integration time constant $\tau_{i,2}$ is chosen in order to ensure that model errors and other disturbance variables can be corrected satisfactorily in a stationary, precise and dynamic manner.

4.2.2 Control of the Internal Currents \tilde{x}_3 and \tilde{x}_4

The setpoints of the internal currents \tilde{x}_{3-4} are basically composed of two components. The first component are the setpoints, which are used to reduce the energy pulsation according to Sec. 3.1. The second component are the currents, which are determined by the superimposed energy controllers for balancing the energies. Different frequency components and phase positions occur. Thus, a control in a rotating reference system to ensure the stationary accuracy is not appropriate. Further smoothing filters would have to be implemented and thus dynamics would be sacrificed.

The dynamic requirements of the target values from the energy controllers are low compared to the requirement to reduce the energy pulsation. In the case of reduction by means of deterministic optimization, periodic current trajectories, which are dependent on the angle of the AC voltage, provide the required power.

This demands a highly dynamic, stationary precise adjustment of the internal currents in order to achieve the maximum reduction of the energy pulsation.

Already in [23, 27] simple proportional controllers were proposed to control the currents for balancing. The stationary deviations of the current control loops were compensated by the stationarily accurate, superimposed energy controller. However, this significantly reduces the effect of reducing the energy pulsations using optimized current trajectories.

One possible solution is a model-predictive approach for adjusting the optimal setpoint trajectories of the internal currents. This approach also requires a corresponding number of setpoints for prediction horizons $N > 1$. The reduction of energy pulsations is based on periodic signals and can therefore be predicted accordingly. For the setpoints of the energy symmetrization, however, a coupling to the energy controllers would be necessary. In addition, the solution of a multidimensional optimization problem with limited computing time in the microsecond range is not feasible. Since the focus is on the currents on the AC side, a prediction horizon of $N = 1$ is considered sufficient here. From this it follows that a current state controller as it is used for \tilde{x}_2^* in Sec. 4.2.1 is very well suited to adjust the current trajectories with the required dynamics and steady-state accuracy.

The system equations of the transformed internal system are given in lines 3 and 4 in Eq. (2.19d). The corresponding control systems for the design of the controllers are directly derived from Fig. 2.3 (c). Neither the controllers nor the controlled systems are coupled. The control structure in Fig. 4.6 is identical for \tilde{x}_3 and \tilde{x}_4 and is therefore shown here only once. The notation 3,4 describes the implementation for both components.

In contrast to the control circuit of the DC current, the disturbance for the internal currents is 0, since the voltage drop across the parasitic resistance is assumed to be negligible. The current controllers are designed and constructed analogous to Fig. 4.5. However, the system parameters and controller parameters differ from the design of the DC current controller. The system parameters \tilde{R}_3 , \tilde{R}_4 , \tilde{L}_3 and \tilde{L}_4 follow from lines 3 and 4 of the system equations from Eq. (2.19d).

The lead time constant and integration time constant are chosen to

$$\tau_{d,3,4} = 1 T_A \quad (4.13a)$$

$$\tau_{i,3,4} = 10 T_A \quad (4.13b)$$

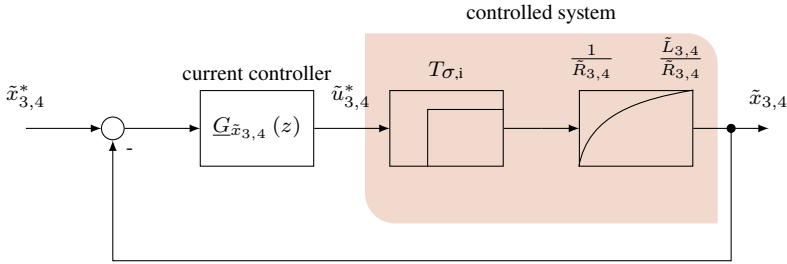


Figure 4.6: closed control loop of the internal currents \tilde{x}_3 and \tilde{x}_4

Thus, the internal currents are set within a sampling period T_A if the system parameters are known sufficiently accurate. Any current trajectories can be set reliably, the arm energies can be balanced and the energy pulsations can be reduced optimally.

4.2.3 Limitation of the Output Variables

To be able to control the system currents, the arm voltages must be set to Eq. (2.26). The maximum arm voltage is bound by the arm energies. In addition, the current and energy controllers from Secs. 4.1.2, 4.2.1 and 4.2.2 work with discrete integrators. To avoid a wind-up of the integrators when output variables are limited, a cascaded limitation structure is chosen.

In [23, 27, 30] the output variables were limited in the transformed system. However, by superimposing different phase positions and frequencies, the limitation in arm quantities presented here can have an advantage if the superposition of the quantities provides a lower, effective output variable. The maximum control voltage is given by the minimum of the arm capacitor voltages v_C in each sampling step by

$$u_{\max} = \min \{v_{C,k}\} = \min \left\{ \sqrt{\frac{2x_{k+6}}{C}} \right\}, k \in (1..6) \quad (4.14)$$

To enable the system to operate at all, the voltage on the DC side $v_{s,DC}$ must be fed forward as shown in Fig. 4.4. Since limiting is done in arm quantities, the corresponding setpoints are calculated. By using Eq. (2.21c) the feed forward term $\underline{u}_{2,ff}^*$ can be calculated from the system measurements.

$$\underline{u}_{2,ff}^* = \underline{T}^\top [2, :] \tilde{v}_{s,DC} \quad (4.15a)$$

$$= \underline{T}^\top [2, :] (\underline{T} \underline{B}^+ \underline{F} \underline{z}) [2] \quad (4.15b)$$

$$= \begin{bmatrix} -\frac{V_{dc}}{2} \\ -\frac{V_{dc}}{2} \\ -\frac{V_{dc}}{2} \\ \frac{V_{dc}}{2} \\ \frac{V_{dc}}{2} \\ \frac{V_{dc}}{2} \end{bmatrix} \quad (4.15c)$$

Here $\underline{T}^\top [2, :]$ denotes the second column of the back transformation matrix \underline{T}^\top . The addition $[2]$ in Eq. (4.15b) describes the second term of the resulting vector analogously. The result $\underline{u}_{2,ff}^*$ describes the 6 output variables of the 6 arms in order to be able to feed forward the DC voltage. This voltage is limited with u_{max} . If u_{max} is smaller than any of the adjustable voltages of the feed forward control, a reasonable operation is no longer possible. The control margin for the DC current control is calculated with Eqs. (4.14) and (4.15) to

$$u_{max,\tilde{x}_2} = u_{max} - \max \{ |u_{2,ff,k}^*| \}, k \in (1..6) \quad (4.16)$$

To avoid limiting each arm individually, the maximum of the absolute value of the voltage to be set is always subtracted from the control margin. The control voltage to be limited then results in

$$\underline{u}_{2,unltd}^* = \underline{u}_{2,ff}^* + \underline{T}^\top [2, :] \tilde{u}_{2,unltd}^* \quad (4.17)$$

$\tilde{u}_{2,unltd}^*$ is the unlimited output of the current controller for \tilde{x}_2 . The amplitude of the voltage to be controlled is linearly limited to the maximum control margin [113]. If the limit is exceeded, a limiting factor $l = \frac{u_{unltd}^*}{u_{max}}$ is calculated. The factor is needed to ensure that the integrators in the transformed reference system are also limited to prevent a wind-up.

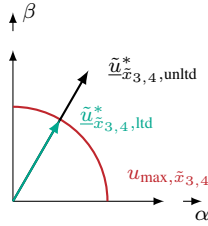


Figure 4.7: linear limitation of the control output space vector

Since the transformation is a linear operation, $\tilde{l} = l$ applies to the limiting factors. Thus, the control voltage for the current \tilde{x}_2 can be limited directly.

$$\tilde{u}_2^* = \tilde{u}_{2,\text{ltd}}^* = \tilde{l}_2 \tilde{u}_{2,\text{unltd}}^* \quad (4.18)$$

In the same way, the output signals of the internal balancing and reduction current controllers are limited. According to the approach from Eqs. (4.3e) and (4.4) the control voltages for the currents \tilde{x}_3 and \tilde{x}_4 form a voltage space vector whose amplitude can be limited as well. The following applies to the amplitude to be limited

$$\underline{u}_{\tilde{x}_{3,4},\text{unltd}}^* = \underline{u}_{2,\text{ff}}^* + \underline{u}_{2,\text{ltd}}^* + \underline{T}^\top [3 : 4, :] \begin{bmatrix} \tilde{u}_{3,\text{unltd}}^* \\ \tilde{u}_{4,\text{unltd}}^* \end{bmatrix} \quad (4.19)$$

The maximum amplitude is calculated as

$$u_{\max,\tilde{x}_{3,4}} = u_{\max} - \max \left\{ \left| u_{\tilde{x}_{3,4},\text{unltd},k}^* \right| \right\}, k \in (1, \dots, 6) \quad (4.20)$$

With the resulting factor $\tilde{l}_{3,4}$ the voltage space vector $\tilde{u}_{\tilde{x}_{3,4},\text{unltd}}^*$ is limited.

Figure 4.7 illustrates the limitation of the output variable to the maximum value using the factor $\tilde{l}_{3,4}$. This allows the integrators of the current controllers for the internal currents \tilde{x}_3 and \tilde{x}_4 to be bounded. The resulting output variables for the DC feed forward control, the DC currents and the internal currents $\underline{u}_{\text{dc,int,ltd}}^*$ are calculated as

$$\underline{u}_{\text{dc,int,ltd}}^* = \underline{u}_{2,\text{ff}}^* + \underline{u}_{2,\text{ltd}}^* + \underline{u}_{3,4,\text{ltd}}^* \quad (4.21)$$

and remaining control margin

$$u_{\max, \tilde{x}_{5,6}} = u_{\max} - \max \{ |u_{\text{dc,int},k}^*| \}, k \in (1..6) \quad (4.22)$$

can be provided for feed forward control of the AC side and for setting the AC currents. This limits all integrators of the current controls from Secs. 4.2.1 and 4.2.2 against overflow and the output variables \underline{u} do not exceed the maximum possible amplitude at any given time.

4.3 Control of the AC grid side

The presented control and balancing strategies from Secs. 3.1, 4.1 and 4.2 already allow a safe operation of the MMC. The AC side can be controlled or regulated at will. In Chapter 2 a symmetrical, sinusoidal current setpoint system was assumed. In principle, operation as motor converter [23] or emulation converter [30] would also be possible here. If the MMC is used as a grid-side power converter, the grid-side control in stationary operation and in case of a fault must be considered in detail. An approach for a MPC of the AC side is proposed, which in connection with the modeling also allows a safe operation in case of grid failure. Due to the highly accurate feed forward control of the AC voltage, the use of a PI current controller in rotating coordinates according to the state of the art is conceivable. However, it is not possible to control constant power or sinusoidal currents even in the event of a fault without considerable additional effort.

PR controllers are an extension and work in the stationary reference system. The controller is tuned to the mains frequency [68, 71]. However, [E4, E5] already investigated the MMC for inverter-based island grids and concluded that a simple PR-control is not viable, because the frequency is not necessarily constant in all operating points. Another good alternative, also in case of faults and asymmetrical current loads, is the MPC. It allows a trajectory-based control of the AC currents [78].

The MPC can be divided into two categories for power electronic systems. The direct predictive control directly optimizes the switching times of the power semiconductors under consideration of the boundary conditions [101–103]. It has the disadvantage, that the complexity of the calculation increases with the

number of switches or cells in the converter, since the switching times are calculated directly. For the later implementation a control frequency of at least $f = 8 \text{ kHz}$ is aimed at.

The indirect MPC optimizes the target voltage of the power unit and leaves the control of the semiconductors to the subordinate modulator [78, 104]. Together with the modeling from Chapter 2, which also assumed adjustable voltage sources as the actuator for the modeling, the indirect MPC is very well suited for controlling the AC currents in the MMC. The optimization associated with the MPC must also be calculated in the available control time to satisfy the real-time condition. Therefore, the MPC is used exclusively for the control of the AC currents \tilde{x}_5 and \tilde{x}_6 in the transformed system.

The solving of a constrained optimization problem is not easily possible on the used hardware in the given time. The approach presented here is based on the mean value representation of the system and manages to solve the constrained optimization in real time, taking into account the physical conditions of the system. Thus, arbitrary current trajectories can be adjusted, which can also be set correctly in the event of a fault by selective feed forward control. The conventional grid control in the rotating reference system with PI-controllers (e.g. [68, E5]) is not decoupled during transient processes. Thus, the decoupled SISO system becomes a coupled MIMO system. MIMO systems can be controlled comparatively well and dynamically with a model-based approach. The bandwidth is constrained by the approximation of the underlying system parts. For transient processes additional filters must be applied to ensure the safe operation of the system [78]. In the following the use on an MMC system is examined to increase the grid support of the converter.

The second point when considering AC control is the correct feed forward control of the AC voltage. The measured values must be fed forward in the correct phase. To set the power factor, the phase position of the voltage must also be known. This results in the requirement to implement the most accurate and fastest PLL as possible. For the operation of the converter for mains purposes, the phase angle and the mains frequency must be reliably detected. By decoupling the system, it is also possible to feed forward the mains voltage much faster than to execute the entire control algorithm. In the following both points are discussed. The calculations and implementation are first shown in [E3].

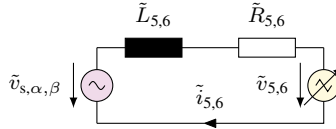


Figure 4.8: Transformed equivalent circuit diagram of the controlled system on the AC side (see Fig. 2.3 (d))

4.3.1 Fundamentals of model-based control of the AC side

A dynamic, state-space model of the system predicts its further development over a given prediction horizon. Boundary conditions are considered and the optimal trajectories of the output variables are determined by solving a mathematical optimization problem. In the next step, these are adapted taking into account new measured values. The formulation of a suitable optimization function is one of the biggest challenges in an MPC approach. In addition, the optimization has to take place in real time. This places demands on the complexity of the optimization equation as its solution must not be overly complicated.

The state space model is the basis of the MPC. The constraints of the input, output and state variables are directly considered in the controller design. The cost function describes the control objective. It includes, for example, deviations from the reference value or the effort to achieve the control objective. The optimization then minimizes the cost function taking into account the model and the constraints. The prediction horizon is recalculated for each time step but only the first step is realized. Thus, a feedback is obtained considering new measured values and hence robustness of the controller.

Dynamic State Space Model of the AC Side

Due to the decoupling from Chapter 2, a separate consideration of the AC side of the system is possible. The controlled system consists of the transformed quantities of the passive components $\tilde{L}_{5,6}$ and $\tilde{R}_{5,6}$ from Eqs. (2.21a) and (2.21b) as well as the counter voltages $\tilde{v}_{s,\alpha}$ and $\tilde{v}_{s,\beta}$ from Eq. (2.21c), which are calculated according to Eq. (2.21c). Figures 2.3 (d) and 4.8 respectively show the controlled

system in transformed coordinates, which is the basis for the design of the control of the AC side. The diagram is derived from the system state space equation Eqs. (2.19d) and (2.19f). More precisely it is about lines 5 and 6 of the system equations of the MMC in transformed coordinates.

$$\frac{d}{dt} \tilde{i}_5 = -\frac{\tilde{R}_5}{\tilde{L}_5} \tilde{i}_5 - \frac{1}{\tilde{L}_5} (\tilde{u}_5 - \tilde{v}_{s,\alpha}) \quad (4.23a)$$

$$\frac{d}{dt} \tilde{i}_6 = -\frac{\tilde{R}_6}{\tilde{L}_6} \tilde{i}_6 - \frac{1}{\tilde{L}_6} (\tilde{u}_6 - \tilde{v}_{s,\beta}) \quad (4.23b)$$

The whole AC side is represented with these equations due to the unconnected neutral points of the AC side and the DC side. By reshaping the state equations of the AC system the state space representation is found.

$$\dot{\tilde{x}}_{ac,t} = \tilde{A}_{ac,t} \tilde{x}_{ac,t} + \tilde{B}_{ac,t} (\tilde{u}_{ac,t} - \tilde{z}_{ac,t}) \quad (4.24a)$$

$$\begin{bmatrix} \dot{\tilde{x}}_5 \\ \dot{\tilde{x}}_6 \end{bmatrix} = \begin{bmatrix} -\frac{\tilde{R}_5}{\tilde{L}_5} & 0 \\ 0 & -\frac{\tilde{R}_6}{\tilde{L}_6} \end{bmatrix} \begin{bmatrix} \tilde{x}_5 \\ \tilde{x}_6 \end{bmatrix} + \begin{bmatrix} -\frac{1}{\tilde{L}_5} & 0 \\ 0 & -\frac{1}{\tilde{L}_6} \end{bmatrix} \left(\begin{bmatrix} \tilde{u}_5 \\ \tilde{u}_6 \end{bmatrix} - \begin{bmatrix} \tilde{v}_{s,\alpha} \\ \tilde{v}_{s,\beta} \end{bmatrix} \right) \quad (4.24b)$$

The output equation is

$$\tilde{y}_{ac,t} = \tilde{C}_{ac,t} \tilde{x}_{ac,t} \quad (4.24c)$$

$$\begin{bmatrix} \tilde{y}_5 \\ \tilde{y}_6 \end{bmatrix} = \begin{bmatrix} 2 & 0 \\ 0 & 2 \end{bmatrix} \begin{bmatrix} \tilde{x}_5 \\ \tilde{x}_6 \end{bmatrix} \quad (4.24d)$$

Equations (4.24c) and (4.24d) formulate the state space equations of the AC side. As a matter of fact those equations are a subset of the system equations derived in Chapter 2. The submatrices are provided with an additional index in the notation below for simplification.

Transition to Discrete Time Domain

Equations (4.24a) and (4.24c) are representations of the AC-side system in the time continuous domain. Since the MPC is computed in discrete time on a digital

signal processor (DSP), the system equations must be transformed using the z-transform.

$$\tilde{\underline{A}}_{ac} = e^{\tilde{\underline{A}}_{ac,t} \cdot T_A} \quad (4.25a)$$

$$\tilde{\underline{B}}_{ac} = \int_0^{T_A} e^{\tilde{\underline{A}}_{ac,t} \cdot \tau} \tilde{\underline{B}}_{ac,t} d\tau \quad (4.25b)$$

$$= \tilde{\underline{A}}_{ac,t}^{-1} \left(e^{\tilde{\underline{A}}_{ac,t} \cdot T_A} - \underline{I}_2 \right) \tilde{\underline{B}}_{ac,t} \quad (4.25c)$$

Equation (4.25c) results because $\left| \tilde{\underline{A}}_{ac,t} \right| \neq 0$ is true. Using the time-discrete state space matrices $\tilde{\underline{A}}_{ac}$ and $\tilde{\underline{B}}_{ac}$, the MPC can be implemented.

State Predictions

Based on the state equations Eq. (4.24a) the evolution of the states can be predicted. The MPC is based on a time-discrete implementation. All values are measured, calculated and set at equidistant times. Thus, the differential equations from Eq. (4.24a) are transformed into time-discrete difference equations.

Thereby, k denotes the current time instance. The AC voltages of the grid appear as disturbance quantities on the system. They are separately fed forward according to Sec. 4.3.3 and therefore do not have to be considered any further for the design of the current control system. For the design of the control system it is assumed that the AC voltages are ideally fed forward.

For the time $k + 1$ the states can be calculated directly

$$\tilde{\underline{x}}_{ac,k+1} = \tilde{\underline{A}}_{ac} \tilde{\underline{x}}_{ac,k} + \tilde{\underline{B}}_{ac} \tilde{\underline{u}}_{ac,k} \quad (4.26a)$$

For $k + 2$ results

$$\tilde{\underline{x}}_{ac,k+2} = \tilde{\underline{A}}_{ac} \tilde{\underline{x}}_{ac,k+1} + \tilde{\underline{B}}_{ac} \tilde{\underline{u}}_{ac,k+1} \quad (4.26b)$$

$$\tilde{\underline{x}}_{ac,k+2} = \tilde{\underline{A}}_{ac} \left(\tilde{\underline{A}}_{ac} \tilde{\underline{x}}_{ac,k} + \tilde{\underline{B}}_{ac} \tilde{\underline{u}}_{ac,k} \right) + \tilde{\underline{B}}_{ac} \tilde{\underline{u}}_{ac,k+1} \quad (4.26c)$$

$$\tilde{\underline{x}}_{ac,k+2} = \tilde{\underline{A}}_{ac}^2 \tilde{\underline{x}}_{ac,k} + \tilde{\underline{A}}_{ac} \tilde{\underline{B}}_{ac} \tilde{\underline{u}}_{ac,k} + \tilde{\underline{B}}_{ac} \tilde{\underline{u}}_{ac,k+1} \quad (4.26d)$$

and for any given time $k + 1$ accordingly

$$\tilde{x}_{ac,k+l} = \tilde{A}_{ac}^l \tilde{x}_{ac,k} + \sum_{i=1}^l \tilde{A}_{ac}^{(l-i)} \tilde{B}_{ac} \tilde{u}_{ac,(k+i-1)} \quad (4.26e)$$

For the output variables, the corresponding equations can be established as well. It holds for the points in time k and $k + 1$ up to the point in time $k + 1$ with Eqs. (4.26a), (4.26d) and (4.26e)

$$\tilde{y}_{ac,k} = \tilde{C}_{ac} \tilde{x}_{ac,k} \quad (4.26f)$$

$$\tilde{y}_{ac,k+1} = \tilde{C}_{ac} \tilde{x}_{ac,k+1} = \tilde{C}_{ac} \tilde{A}_{ac} \tilde{x}_{ac,k} + \tilde{C}_{ac} \tilde{B}_{ac} \tilde{u}_{ac,k} \quad (4.26g)$$

$$\tilde{y}_{ac,k+l} = \tilde{C}_{ac} \tilde{A}_{ac}^l \tilde{x}_{ac,k} + \tilde{C}_{ac} \sum_{i=1}^l \tilde{A}_{ac}^{(l-i)} \tilde{B}_{ac} \tilde{u}_{ac,(k+i-1)} \quad (4.26h)$$

Without restriction of the generality, the MPC is considered in this section with a prediction horizon of $N = 3$. The prediction horizon is one of the degrees of freedom in the design and performance of the MPC based approach. The chosen value shows very good control results of the AC currents when implemented on the test system from Chapter 5.

The vector $\tilde{X}(k)$ of the state variables at time k is calculated as follows

$$\tilde{X}(k) = \begin{bmatrix} \tilde{x}_{ac,k+1} \\ \tilde{x}_{ac,k+2} \\ \tilde{x}_{ac,k+3} \end{bmatrix} = \begin{bmatrix} \tilde{A}_{ac} \tilde{x}_{ac,k} + \tilde{B}_{ac} \tilde{u}_{ac,k} \\ \tilde{A}_{ac}^2 \tilde{x}_{ac,k} + \tilde{A}_{ac} \tilde{B}_{ac} \tilde{u}_{ac,k} + \tilde{B}_{ac} \tilde{u}_{ac,k+1} \\ \tilde{A}_{ac}^3 \tilde{x}_{ac,k} + \tilde{A}_{ac}^2 \tilde{B}_{ac} \tilde{u}_{ac,k} \\ + \tilde{A}_{ac} \tilde{B}_{ac} \tilde{u}_{ac,k+1} + \tilde{B}_{ac} \tilde{u}_{ac,k+2} \end{bmatrix} \quad (4.27a)$$

$$= \underline{\Gamma}' \tilde{x}_{ac,k} + \underline{\Upsilon}' \tilde{U}(k) \quad (4.27b)$$

with

$$\underline{\Gamma}' = \begin{bmatrix} \tilde{A}_{ac} \\ \tilde{A}_{ac}^2 \\ \tilde{A}_{ac}^3 \end{bmatrix} \quad (4.27c)$$

$$\underline{\Upsilon}' = \begin{bmatrix} \tilde{B}_{ac} & 0 & 0 \\ \tilde{A}_{ac}\tilde{B}_{ac} & \tilde{B}_{ac} & 0 \\ \tilde{A}_{ac}^2\tilde{B}_{ac} & \tilde{A}_{ac}\tilde{B}_{ac} & \tilde{B}_{ac} \end{bmatrix} \quad (4.27d)$$

Here $\tilde{\underline{U}}(k)$ describes the vector of the input variables within the prediction horizon.

$$\tilde{\underline{U}}(k) = \begin{bmatrix} \tilde{u}_{ac,k} \\ \tilde{u}_{ac,k+1} \\ \tilde{u}_{ac,k+2} \end{bmatrix} \quad (4.27e)$$

The goal of the MPC is to determine now the optimal $\tilde{\underline{U}}(k)$ with respect to the boundary conditions, which minimizes the cost function J that will be elaborated in the next section.

The output variables can be calculated in the same way.

$$\tilde{\underline{Y}}(k) = \begin{bmatrix} \tilde{y}_{ac,k+1} \\ \tilde{y}_{ac,k+2} \\ \tilde{y}_{ac,k+3} \end{bmatrix} = \begin{bmatrix} \tilde{C}_{ac}\tilde{A}_{ac}\tilde{x}_{ac,k} + \tilde{C}_{ac}\tilde{B}_{ac}\tilde{u}_{ac,k} \\ \tilde{C}_{ac}\tilde{A}_{ac}^2\tilde{x}_{ac,k} + \tilde{C}_{ac}\tilde{A}_{ac}\tilde{B}_{ac}\tilde{u}_{ac,k} \\ \quad + \tilde{C}_{ac}\tilde{B}_{ac}\tilde{u}_{ac,k+1} \\ \tilde{C}_{ac}\tilde{A}_{ac}^3\tilde{x}_{ac,k} + \tilde{C}_{ac}\tilde{A}_{ac}^2\tilde{B}_{ac}\tilde{u}_{ac,k} \\ \quad + \tilde{C}_{ac}\tilde{A}_{ac}\tilde{B}_{ac}\tilde{u}_{ac,k+1} + \tilde{C}_{ac}\tilde{B}_{ac}\tilde{u}_{ac,k+2} \end{bmatrix} \quad (4.27f)$$

$$= \underline{\Gamma}\tilde{x}_{ac,k} + \underline{\Upsilon}\tilde{\underline{U}}(k) \quad (4.27g)$$

with

$$\underline{\Gamma} = \begin{bmatrix} \tilde{C}_{ac} \tilde{A}_{ac} \\ \tilde{C}_{ac} \tilde{A}_{ac}^2 \\ \tilde{C}_{ac} \tilde{A}_{ac}^3 \end{bmatrix} \quad (4.27h)$$

$$\underline{\Upsilon} = \begin{bmatrix} \tilde{C}_{ac} \tilde{B}_{ac} & 0 & 0 \\ \tilde{C}_{ac} \tilde{A}_{ac} \tilde{B}_{ac} & \tilde{C}_{ac} \tilde{B}_{ac} & 0 \\ \tilde{C}_{ac} \tilde{A}_{ac}^2 \tilde{B}_{ac} & \tilde{C}_{ac} \tilde{A}_{ac} \tilde{B}_{ac} & \tilde{C}_{ac} \tilde{B}_{ac} \end{bmatrix} \quad (4.27i)$$

The system Eqs. (4.27b) and (4.27g) describe the dynamic system behavior for a given $\underline{\tilde{U}}(k)$ at a time k for the next $N = 3$ time steps. In general a short prediction horizon leads to a more aggressive controller behavior and vice versa.

Cost Function for Controlling the AC Currents

To calculate the optimal input $\underline{\tilde{U}}(k)$ for the next time steps, a cost function is required. The cost function must be optimized, i.e. minimized, within a control period of the system in order to satisfy the real-time condition.

The quadratic programming (QP) represents a special form of optimization and is a good compromise between control result and calculation complexity [114]. In the QP, the cost function J is a quadratic function with linear limiting functions. In the presented control approach, it is composed of a term J_1 and a term J_2 .

The first term formulates a quadratic quality measure for the deviation of the setpoint from the predicted value $\tilde{\xi}_{ac,k} = \tilde{y}_{ac,k}^* - \tilde{y}_{ac,k}$. Not only the actual error is included in the calculation, but also the predicted deviations based on the model

equations. At the sampling time k the following applies to the quadratic term with $N = 3$

$$J_1 = \sum_{l=k}^{k+2} \left\| \tilde{\xi}_{ac,l+1} \right\|_{\underline{Q}}^2 = \sum_{l=k}^{k+2} \tilde{\xi}_{ac,l+1}^{\top} \underline{Q} \tilde{\xi}_{ac,l+1} \quad (4.28a)$$

$$= \tilde{\xi}_{ac,k+1}^{\top} \underline{Q} \tilde{\xi}_{ac,k+1} + \tilde{\xi}_{ac,k+2}^{\top} \underline{Q} \tilde{\xi}_{ac,k+2} + \tilde{\xi}_{ac,k+3}^{\top} \underline{Q} \tilde{\xi}_{ac,k+3} \quad (4.28b)$$

$$= \begin{bmatrix} \tilde{\xi}_{ac,k+1}^{\top} & \tilde{\xi}_{ac,k+2}^{\top} & \tilde{\xi}_{ac,k+3}^{\top} \end{bmatrix} \begin{bmatrix} \underline{Q} & 0 & 0 \\ 0 & \underline{Q} & 0 \\ 0 & 0 & \underline{Q} \end{bmatrix} \begin{bmatrix} \tilde{\xi}_{ac,k+1} \\ \tilde{\xi}_{ac,k+2} \\ \tilde{\xi}_{ac,k+3} \end{bmatrix} \quad (4.28c)$$

$$= \tilde{\Xi}_{ac,k}^{\top} \tilde{\underline{Q}} \tilde{\Xi}_{ac,k} \quad (4.28d)$$

$$= \left\| \tilde{\Xi}_{ac,k} \right\|_{\tilde{\underline{Q}}}^2 \quad (4.28e)$$

In combination with Eq. (4.27g)

$$J_1 = \left\| \tilde{\Xi}_{ac,k} \right\|_{\tilde{\underline{Q}}}^2 \quad (4.28f)$$

$$= \left\| \tilde{\underline{Y}}(k)^* - \tilde{\underline{Y}}(k) \right\|_{\tilde{\underline{Q}}}^2 \quad (4.28g)$$

$$= \left\| \tilde{\underline{Y}}(k)^* - \underline{\Gamma} \tilde{x}_{ac,k} - \underline{\Upsilon} \tilde{\underline{U}}(k) \right\|_{\tilde{\underline{Q}}}^2 \quad (4.28h)$$

\underline{Q} is the weighting matrix for the tracking error. Here $\dim(\underline{Q}) = \dim(\tilde{y}_{ac,\cdot}) \times \dim(\tilde{y}_{ac,\cdot})$ applies. \underline{Q} is a 2×2 diagonal matrix in this specific implementation. To achieve a symmetrical weighting and thus symmetrical AC currents, the approach with the weighting factor q_{ac} is

$$\underline{Q} = q_{ac} \underline{I}_2 \quad (4.28i)$$

An increase of the weighting factor q_{ac} increases the cost of the term J_1 in the realization. Here, the tracking error is reduced as a consequence. By choosing a \underline{Q} with equal entries on the diagonal, in Eq. (4.28i) neither of the two currents is preferred in the control.

The second part of the cost function J formulates a quality measure for the control effort. This means that the difference of the output variables between the

time steps $\tilde{u}_{ac,k}$ and $\tilde{u}_{ac,k+1}$ is weighted and included in the total cost function. The weighting factor of the control effort is denoted by λ_u .

$$J_2 = \sum_{l=k}^{k+2} \lambda_u \|\Delta \tilde{u}_{ac,l}\|_2^2 = \lambda_u \sum_{l=k}^{k+2} (\tilde{u}_{ac,l} - \tilde{u}_{ac,l-1})^\top (\tilde{u}_{ac,l} - \tilde{u}_{ac,l-1}) \quad (4.29a)$$

$$= \lambda_u \begin{bmatrix} \tilde{u}_{ac,k}^\top - \tilde{u}_{ac,k-1}^\top & \tilde{u}_{ac,k+1}^\top - \tilde{u}_{ac,k}^\top & \tilde{u}_{ac,k+2}^\top - \tilde{u}_{ac,k-1}^\top \end{bmatrix} \begin{bmatrix} I_2 & 0 & 0 \\ 0 & I_2 & 0 \\ 0 & 0 & I_2 \end{bmatrix} \begin{bmatrix} \tilde{u}_{ac,k} - \tilde{u}_{ac,k-1} \\ \tilde{u}_{ac,k+1} - \tilde{u}_{ac,k} \\ \tilde{u}_{ac,k+2} - \tilde{u}_{ac,k-1} \end{bmatrix} \quad (4.29b)$$

$$= \lambda_u \left(\underline{S} \tilde{\underline{U}}(k) - \underline{E} \tilde{u}_{ac,k-1} \right)^\top \left(\underline{S} \tilde{\underline{U}}(k) - \underline{E} \tilde{u}_{ac,k-1} \right) \quad (4.29c)$$

$$= \lambda_u \left\| \underline{S} \tilde{\underline{U}}(k) - \underline{E} \tilde{u}_{ac,k-1} \right\|_2^2 \quad (4.29d)$$

with

$$\underline{S} = \begin{bmatrix} I_2 & 0 & 0 \\ -I_2 & I_2 & 0 \\ 0 & -I_2 & I_2 \end{bmatrix} \quad (4.29e)$$

$$\underline{E} = \begin{bmatrix} I_2 \\ 0 \\ 0 \end{bmatrix} \quad (4.29f)$$

$$\tilde{\underline{U}}(k) = \begin{bmatrix} \tilde{u}_{ac,k} \\ \tilde{u}_{ac,k+1} \\ \tilde{u}_{ac,k+2} \end{bmatrix} \quad (4.29g)$$

$\tilde{u}_{ac,k-1}$ are the actual output variables during the previous time instance. Here applies likewise, that an increase of the weighting factor λ_u leads to an increase of the costs of the control effort. From the ratio of q_{ac} and λ_u the dynamics of the controller can be adjusted. This presented design results in a compromise between tracking accuracy of the setpoint trajectory and the required effort in regards to the output variables.

Using Equations (4.28h) and (4.29d) the total cost function is calculated

$$J = J_1 + J_2 \quad (4.30a)$$

$$= \left\| \tilde{\underline{Y}}(k)^* - \underline{\Gamma} \tilde{\underline{x}}_{ac,k} - \underline{\Upsilon} \tilde{\underline{U}}(k) \right\|_{\tilde{\underline{Q}}}^2 + \lambda_u \left\| \underline{S} \tilde{\underline{U}}(k) - \underline{E} \tilde{\underline{u}}_{ac,k-1} \right\|_2^2 \quad (4.30b)$$

$$= \tilde{\underline{U}}(k)^\top \underline{H} \tilde{\underline{U}}(k) + 2\underline{\Theta}_k^\top \tilde{\underline{U}}(k) + \theta_k \quad (4.30c)$$

Equation (4.30c) describes the cost function of the control approach. This function has to be minimized by calculating the optimal input vector $\tilde{\underline{U}}(k)$ for the prediction horizon.

Equation (4.30c) is composed of several subterms. First important part is the Hessian matrix or Hessian \underline{H} . It is a square matrix of second-order partial derivatives of a function. In this case it is the second-order derivative of J with respect to $\tilde{\underline{U}}(k)$. Reshaping Eq. (4.30b) provides

$$\underline{H} = q_{ac} \underline{\Upsilon}^\top \underline{\Upsilon} + \lambda_u \underline{S}^\top \underline{S} \quad (4.30d)$$

It holds that

$$\underline{H} = \underline{H}^\top \text{ and } \underline{H} \succ 0 \text{ (positive definite) for } \lambda_u > 0 \quad (4.30e)$$

The matrix \underline{H} is a time invariant matrix, depending on $\tilde{\underline{A}}_{ac}$, $\tilde{\underline{B}}_{ac}$, $\tilde{\underline{C}}_{ac}$, q_{ac} and λ_u . The dimension of \underline{H} is given by $\underline{H} \in \mathbb{R}^{\dim(\tilde{\underline{u}}_{ac,k}) \cdot N \times \dim(\tilde{\underline{u}}_{ac,k}) \cdot N} = \mathbb{R}^{6 \times 6}$. The entire Hesse matrix of the AC current control for a prediction horizon of $N = 3$ is given in Sec. A.7 in Eq. (A.14).

$\underline{\Theta}_k$ is a time variant function of $\tilde{\underline{x}}_{ac,k}$, the input variable of the preceding sampling interval $\tilde{\underline{u}}_{ac,k-1}$, the setpoint trajectory $\tilde{\underline{Y}}(k)^*$ as well as the weighting factors λ_u and q_{ac} .

It follows

$$\underline{\Theta}_k = -\underline{\Upsilon}^\top \tilde{\underline{Q}} \left(\tilde{\underline{Y}}(k)^* - \underline{\Gamma} \tilde{\underline{x}}_{ac,k} \right) - \lambda_u \underline{S}^\top \underline{E} \tilde{\underline{u}}_{ac,k-1} \quad (4.30f)$$

with $\underline{\Theta}_k \in \mathbb{R}^{\dim(\tilde{\underline{x}}_{ac,k}) \cdot N} = \mathbb{R}^6$.

The entire time-variant vector for the AC current control is given in Sec. A.8 in Eq. (A.15). The term θ_k is a time variant scalar with $\theta_k \in \mathbb{R}$.

By recalculating Eq. (4.30c) results

$$\theta_k = \left\| \tilde{\underline{Y}}(k)^* - \underline{\Gamma} \tilde{\underline{x}}_{ac,k} \right\|_{\tilde{\underline{Q}}}^2 + \lambda_u \left\| \underline{E} \tilde{\underline{u}}_{ac,k-1} \right\|_2^2 \quad (4.30g)$$

with θ_k given in Sec. A.9 Eq. (A.16). Since θ_k does not depend on $\tilde{\underline{U}}(k)$, it will vanish for all derivatives of J with respect to $\tilde{\underline{U}}(k)$. Therefore this term has no further influence on the minimization of the cost function. The objective of the MPC is to find the minimum of the cost function J from Eq. (4.30c) in dependence of the output variables $\tilde{\underline{U}}(k)$ for each time step k .

State and Output Constraints

The minimum of the cost function must be determined considering boundary conditions. The maximum values of the currents must not be exceeded. The available control voltage is also limited by the energy stored in the arm capacitors. These considerations result in the limitations for the AC currents

$$\begin{bmatrix} -\tilde{x}_{AC,max} \\ -\tilde{x}_{AC,max} \end{bmatrix} \leq \begin{bmatrix} \tilde{x}_{AC,k,1} \\ \tilde{x}_{AC,k,2} \end{bmatrix} \leq \begin{bmatrix} \tilde{x}_{AC,max} \\ \tilde{x}_{AC,max} \end{bmatrix} \quad (4.31a)$$

Reshaping gives the form

$$\begin{bmatrix} 1 & 0 \\ 0 & 1 \\ -1 & 0 \\ 0 & -1 \end{bmatrix} \tilde{\underline{x}}_{ac,l} \leq \tilde{x}_{AC,max} \begin{bmatrix} 1 \\ 1 \\ 1 \\ 1 \end{bmatrix} \quad (4.31b)$$

$$\underline{G}_x \tilde{\underline{x}}_{ac,l} \leq \underline{g}_x; \quad l = k + 1, \dots, k + N \quad (4.31c)$$

Equation (4.31a) must be fulfilled at any time k over the entire prediction horizon. To limit the states depending on the output variables $\tilde{\underline{U}}(k)$, $\tilde{\underline{X}}(k)$ is expressed with Eq. (4.27b) by $\tilde{\underline{U}}(k)$.

$$\begin{bmatrix} \underline{G}_x & 0 & 0 \\ 0 & \underline{G}_x & 0 \\ 0 & 0 & \underline{G}_x \end{bmatrix} \tilde{\underline{X}}(k) \leq \begin{bmatrix} \underline{g}_x \\ \underline{g}_x \\ \underline{g}_x \end{bmatrix} \quad (4.31d)$$

$$\tilde{\underline{G}}_x \tilde{\underline{X}}(k) \leq \tilde{\underline{g}}_x \quad (4.31e)$$

$$\tilde{\underline{G}}_x \left(\underline{\Gamma}' \tilde{\underline{x}}_{ac,k} + \underline{\Upsilon}' \tilde{\underline{U}}(k) \right) \leq \tilde{\underline{g}}_x \quad (4.31f)$$

For the limitation of the output variables, the approach is analog

$$\begin{bmatrix} 1 & 0 \\ 0 & 1 \\ -1 & 0 \\ 0 & -1 \end{bmatrix} \tilde{\underline{u}}_{ac,l} \leq \tilde{u}_{AC,max} \begin{bmatrix} 1 \\ 1 \\ 1 \\ 1 \end{bmatrix} \quad (4.31g)$$

$$\underline{G}_u \tilde{\underline{u}}_{ac,l} \leq \underline{g}_u; \quad l = k, \dots, k + N - 1 \quad (4.31h)$$

$$\begin{bmatrix} \underline{G}_u & 0 & 0 \\ 0 & \underline{G}_u & 0 \\ 0 & 0 & \underline{G}_u \end{bmatrix} \tilde{\underline{U}}(k) \leq \begin{bmatrix} \underline{g}_u \\ \underline{g}_u \\ \underline{g}_u \end{bmatrix} \quad (4.31i)$$

$$\tilde{\underline{G}}_u \tilde{\underline{U}}(k) \leq \tilde{\underline{g}}_u \quad (4.31j)$$

Problem Definition

The fundamentals of MPC all together lead to a quadratic programming (QP). To obtain the optimal control variable trajectories under consideration of the costs and boundary conditions, the following problem must be solved.

$$\underset{\tilde{\underline{U}}(k)}{\text{minimize}} \quad J = \tilde{\underline{U}}(k)^\top \underline{H} \tilde{\underline{U}}(k) + 2\underline{\Theta}_k^\top \tilde{\underline{U}}(k) + \theta_k \quad (4.32a)$$

$$\text{subject to} \quad \tilde{\underline{G}}_x \left(\underline{\Gamma}' \tilde{\underline{x}}_{ac,k} + \underline{\Upsilon}' \tilde{\underline{U}}(k) \right) \leq \tilde{\underline{g}}_x \quad (4.32b)$$

$$\tilde{\underline{G}}_u \tilde{\underline{U}}(k) \leq \tilde{\underline{g}}_u \quad (4.32c)$$

J is a quadratic function. It applies to the Hesse matrix $\underline{H} = \underline{H}^\top$. J is convex and thus uniquely solvable, if $\underline{H} \succeq 0$, which is satisfied. The inequalities for limitation are affine functions.

4.3.2 Optimal Output Trajectories by Solving the QP

To calculate the optimal output variables, Eq. (4.32a) must be solved considering Eqs. (4.32b) and (4.32c). The solution of the unlimited problem can be calculated analytically. The limitation of the output variables can then be performed. But for limiting the state variables, a numerical optimization has to be performed if the problem is not modified further.

Analytical Solution of the Unconstrained Problem

The solution of Eq. (4.32a) is analytically determined

$$\underset{\underline{\tilde{U}}(k)}{\text{minimize}} \quad J = \underline{\tilde{U}}(k)^\top \underline{H} \underline{\tilde{U}}(k) + 2\underline{\Theta}_k^\top \underline{\tilde{U}}(k) + \theta_k \quad (4.33a)$$

$$\nabla J \left(\underline{\tilde{U}}(k) \right) = 2\underline{H} \underline{\tilde{U}}(k) + 2\underline{\Theta}_k \stackrel{!}{=} 0 \quad (4.33b)$$

$$\underline{\tilde{U}}(k)^* = -\underline{H}^{-1} \underline{\Theta}_k \quad (4.33c)$$

Subsequently, all elements from $\underline{\tilde{U}}(k)$ can be constrained to the maximum values so that the conditions from Eq. (4.32c) are satisfied. This provides a very good result and the real-time condition can be met. The calculated values for the first step $\underline{\tilde{u}}_{ac,k}$ are then realized. These are the optimal output variables to set the target currents $\underline{\tilde{Y}}(k)$ in the best possible way taking into account the cost function J . However, the states are not constrained in any way. If the result are currents exceeding the maximum, the solution is not optimal anymore.

Numerical Solution Considering the Limitation of State Variables

To constrain the AC currents, the state variables $\underline{\tilde{x}}_{ac,k}$ must be limited. Equation (4.32b) describes the inequalities that must be satisfied for each sampling step. Thus, an optimization in constrained conditions must be solved. The most

promising approach is the numerical optimization. With respect to the implementation on the test bench in Chapter 5 this optimization must be performed within one control period. The system is controlled by means of a DSP, which is programmed with C-code. To solve the QP, the First-Order Methods (FiOrdOs) Matlab Toolbox is used [115]. With the help of this toolbox, C code can be automatically generated using Matlab, which is able to solve the cost function taking into account the limitations. The boundary conditions are defined as a convex set Ξ . A solver for the given problem is generated, which can be directly embedded into the C-code. The disadvantage of this method is, that this solver is designed especially for this problem, but still requires so much computational effort, that the optimization cannot be completed within one controller period at $T_A = 125 \mu\text{s}$. On existing hardware, cycle times of up to $T_{\text{solve,max}} = 700 \mu\text{s}$ can occur. This justifies the fact that no other methods of MPC and optimization are investigated, since the computational effort is not reduced in every other case. If the computational performance of the laboratory setup is further increased or the control frequency is reduced, this method is a very good possibility to adjust the AC currents of the MMC. Another approach is necessary to realize the state limitation in real time.

Limitation of State Variables by System Analysis

The limitation of the state variables cannot be handled in real time with the available computing capacity. However, to satisfy the inequalities from Eq. (4.32b), the equation can be transformed. To get the needed inequalities, the maximum and minimum values are investigated separately. Therefore \tilde{G}_x is split up into \tilde{G}_{x+} and \tilde{G}_{x-} . In this way, the matrices are well suited for inversion. For simplicity, the index is omitted in the next equations, since the result is the same for both limits. For the maximum and minimum inequalities results

$$\tilde{G}_x \left(\Gamma' \tilde{x}_{\text{ac},k} + \Upsilon' \tilde{U}(k)^* \right) \leq \tilde{g}_x \quad (4.34a)$$

$$\tilde{G}_x \Upsilon' \tilde{U}(k)^* \leq \tilde{g}_x - \tilde{G}_x \Gamma' \tilde{x}_{\text{ac},k} \quad (4.34b)$$

$$\tilde{U}(k) \leq \left(\tilde{G}_x \Upsilon' \right)^{-1} \left(\tilde{g}_x - \tilde{G}_x \Gamma' \tilde{x}_{\text{ac},k} \right) \quad (4.34c)$$

Equation (4.34c) is only solvable, if the inverse $\left(\tilde{G}_x \Upsilon' \right)^{-1}$ exists. Thus, there has to be a unique assignment, which output variables result to which currents

over the prediction horizon. This is possible, if the 3-phase AC system is controlled in transformed quantities, as presented in this thesis. The zero sequence voltage, which is available as degree of freedom, is set decoupled from the AC current control and is not a parameter of the MPC. Thus also the limitation of state variables can be done analytically and the real time condition can be kept. A MPC control of the AC currents in real time and thereby all further advantages can be implemented on the MMC. The decoupling and separate feed forward control of the voltages enables the high-performance use of the system for grid service even in the event of faults. A control in untransformed variables would have had the difficulty that the state variables, i.e. the AC currents, could not be constrained. This would not have permitted a safe operation. By exploiting the decoupling and transformation, the use of the MPC in the laboratory setup is possible.

Compensation of a Calculating Time Delay

Due to the discrete implementation on a DSP and the realization by a real inverter setup, the system has a time delay of one control period. To increase the dynamics of the AC control, this time delay can be compensated. For this purpose, the states $\tilde{\mathbf{x}}_{ac,k}$ at time k are estimated from the measured values at time $k - 1$ and the optimal output variables $\tilde{\mathbf{u}}_{ac,k-1}$. With Eq. (4.24a) the states at time k result in

$$\tilde{\mathbf{x}}_{ac,k} = \tilde{\mathbf{A}}_{ac} \tilde{\mathbf{x}}_{ac,k-1} + \tilde{\mathbf{B}}_{ac} \tilde{\mathbf{u}}_{ac,k-1} \quad (4.35)$$

This information is already available at time k . The MPC is extended by this time delay compensation to obtain a reduced computational effort for the same prediction horizon, since time delay does not have to be considered.

4.3.3 Control Loop to Determine the Grid Angle

The AC voltage is assumed to be ideally fed forward. But to get information about the correct current grid angle, a PLL is necessary. This allows to control the active power P_{AC} and reactive power Q_{AC} exchanged with the grid. The setpoint trajectories of the current are then specified as a function of the grid angle γ_k and the desired power factor φ_k .

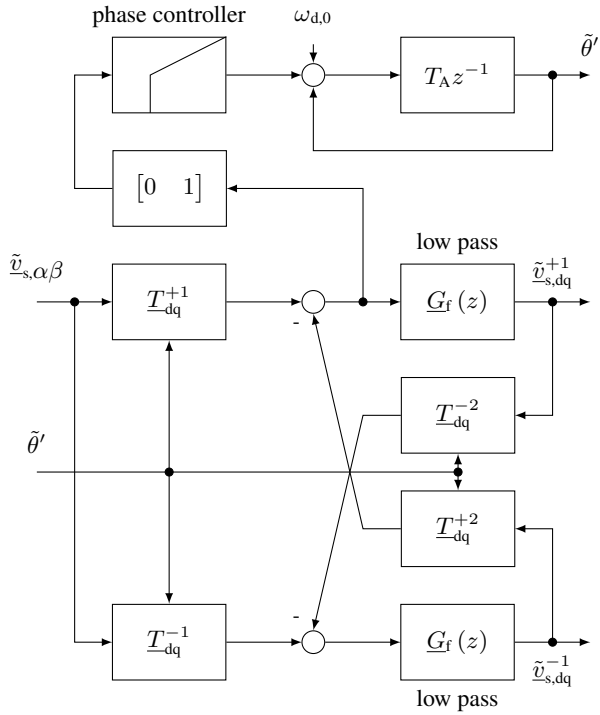


Figure 4.9: Phase-locked loop to determine the grid angle, the positive sequence and the negative sequence of the voltage.

Figure 4.9 shows the structure of the PLL. A DSRF PLL is used in the stationary reference system [68, 71, 116]. This structure is suitable to filter the fundamental frequency of the grid as well as the negative sequence and, if necessary, also higher harmonics. The rotation matrices \underline{T}_{dq}^{+1} and \underline{T}_{dq}^{-1} rotate the AC voltages into the synchronous reference system of the positive or the negative sequence. For decoupling, the sequences are rotated using the PLL angle $\tilde{\theta}'$, filtered and subtracted into the respective other reference system using the rotation matrices \underline{T}_{dq}^{+2} and \underline{T}_{dq}^{-2} . The following applies

$$\underline{T}_{dq}^{+1} = \underline{T}_{dq}^{-1\top} = \begin{bmatrix} \cos(\tilde{\theta}') & \sin(\tilde{\theta}') \\ -\sin(\tilde{\theta}') & \cos(\tilde{\theta}') \end{bmatrix} \quad (4.36a)$$

$$\underline{T}_{dq}^{+2} = \underline{T}_{dq}^{-2\top} = \begin{bmatrix} \cos(2\tilde{\theta}') & \sin(2\tilde{\theta}') \\ -\sin(2\tilde{\theta}') & \cos(2\tilde{\theta}') \end{bmatrix} \quad (4.36b)$$

The decoupled voltages are subsequently low pass filtered. The cut-off frequency of the low pass filters is selected to $\omega_c = \frac{\omega_g}{\sqrt{2}}$. This results in the transfer function of the filter

$$\underline{G}_f(z) = \begin{bmatrix} \frac{1-e^{-T_A \omega_c}}{z-e^{-T_A \omega_c}} & 0 \\ 0 & \frac{1-e^{-T_A \omega_c}}{z-e^{-T_A \omega_c}} \end{bmatrix} \quad (4.37)$$

The phase controller is implemented as PI controller. Its control objective is to bring the decoupled q-voltage of the positive sequence system to 0. The frequency determined in this way is offset by $\omega_{g,0} = \tilde{\omega}_g$ for better initial response. Subsequent integration results in the PLL angle $\tilde{\theta}'$, which also serves as input for the rotation matrices. The design of the PI controller is analogous to [71]. The assumption that the step response of a 2nd order system after a settling time $t_s = 4.6\tau$ is within a stationary accuracy of $\approx 1\%$ is used as a basis. The controller parameters are derived from this. The following applies

$$\omega_n = \sqrt{\frac{k_{p,PLL}}{T_{N,PLL}}} \quad (4.38a)$$

$$\xi_{PLL} = \frac{k_{p,PLL} T_{N,PLL}}{2} \quad (4.38b)$$

For the gain parameter $k_{p,PLL}$ and $k_{i,PLL} = k_{p,PLL}/T_{N,PLL}$ result with respect to the settling time t_s

$$k_{p,PLL} = 2 \xi_{PLL} \omega_n = \frac{9.2}{t_s} \quad (4.38c)$$

$$k_{i,PLL} = k_{p,PLL} \frac{\omega_n}{2 \xi_{PLL}} = \frac{2.3 k_{p,PLL}}{t_s \xi_{PLL}^2} \quad (4.38d)$$

Where ξ_{PLL} describes a damping factor of the PLL. For the operation of the PLL on the 50 Hz grid, the controller parameters are

$$t_s = 40 \text{ ms} \quad (4.38e)$$

$$\xi_{PLL} = \frac{1}{\sqrt{2}} \quad (4.38f)$$

These parameters provide a very good compromise between stability and dynamics of the PLL. For the overall transfer function of the PLL-PI controller, the following applies

$$\underline{G}_{PI,PLL}(z) = k_{p,PLL} + k_{i,PLL} \frac{z T_A}{z - 1} \quad (4.38g)$$

The controller parameters from Eqs. (4.38c) and (4.38d) are normalized to a voltage amplitude value of $|\tilde{v}_{s,\alpha\beta}| = 1$. In order to have the corresponding dynamics at the real grid, the controller parameters must be scaled accordingly. With the help of the determined grid angle, an AC current can be adjusted in phase using the MPC in the first step. This allows a direct specification of P_{AC} and Q_{AC} . This angle is determined so well even in the case of a negative sequence occurring, that operation of the MMC is still possible even in the event of a mains fault. Additionally, the information can also be used for better feed forward control of the AC voltages in order to be able to improve the control of the MMC in the event of a fault. The corresponding simulation results for AC side control are shown in Sec. 4.3.4.

Table 4.2: Circuit parameters for the simulation of the MPC and the PLL.

circuit parameter	numerical value
T_A	125 μs
ω_g	2π 50 Hz
$\tilde{\varphi}_0$	π
$\tilde{v}_{s,\alpha}$	1 V $\cos(\omega_g + \tilde{\varphi}_0)$
$\tilde{v}_{s,\beta}$	1 V $\sin(\omega_g + \tilde{\varphi}_0)$
$\tilde{R}_5 = \tilde{R}_6$	3 m Ω
$\tilde{L}_5 = \tilde{L}_6$	3.5 mH
t_s	50 ms
ξ_{PLL}	$\frac{1}{\sqrt{2}}$
q_{ac}	10
λ_u	1

4.3.4 Simulation Results

To verify the derivation of the MPC and the design of the PLL, a Matlab Simulink simulation is created. This is done directly in the decoupled system based on Fig. 2.3 (d). Table 3.1 and Eqs. (2.21a) to (2.21c) provide the basis for determining the system parameters.

Simulation of the PLL

Figures 4.10 (a) to 4.10 (d) show the transient response of the implemented PLL. In Fig. 4.10 (a) the mains voltages can be seen. The measured quantities of the mains voltage are superimposed with a normally distributed white noise to simulate the real measurement. To be able to evaluate the initial response, the mains voltage is given to the PLL with a phase offset of $\varphi_0 = \pi$. The reference system is stationary at this point.

Figure 4.10 (b) shows the determined grid frequency $f'_{g,\text{PLL}}$. After approximately 75 ms the PLL has settled and the determined frequency reaches its stationary final value.

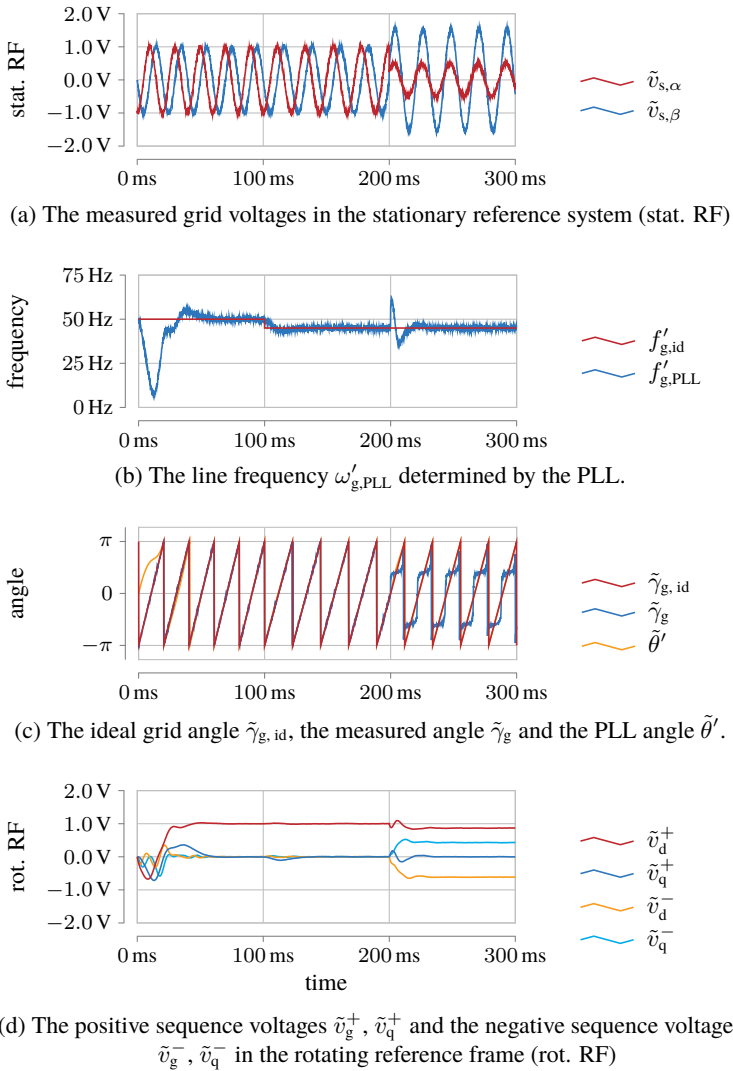


Figure 4.10: Settling process of the PLL at maximum phase difference at the beginning and response to occurring grid faults and disturbances.

In Fig. 4.10 (c) the ideal angle of the positive sequence $\tilde{\gamma}_{g,id}$, the grid angle $\tilde{\gamma}_g$, which results from the measured values of the grid voltage, as well as the angle $\tilde{\theta}'$ determined by the PLL are shown. At the beginning, the phase difference with $\Delta\varphi = \pi$ is at its maximum. After the transient process the angles match. If only a positive sequence occurs, the actual grid angle and the angle of the measured system match and a decoupling of the negative sequence is not necessary. The PLL angle can then be used for the orientation of the rotating reference system and for adjusting the phase angle between current and voltage.

Figure 4.10 (d) shows the mains voltages in the rotating reference system. The mains voltage consists of a positive sequence only. The d-component corresponds to the amplitude of the mains voltage in the stationary reference system. The q-component is thereby controlled by the PLL to 0 V. The simulation shows a very good transient response of the PLL. The disturbance behavior of the entire PLL is given by the settling time t_s and damping ζ_{PLL} specified in Table 4.2.

At the time $t_1 = 100$ ms a frequency jump of $\Delta\omega_g = -2\pi 5$ Hz is given. After the settling time of 50 ms the frequency is determined sufficiently exactly by the PLL. The angle of the positive sequence is identified very well.

At time $t_2 = 200$ ms a grid fault is simulated. The positive sequence is reduced in amplitude to 86.60 %. Additionally, a negative sequence with

$$\tilde{v}_{s,\alpha\beta}^- = 0.75 \text{ V} \begin{bmatrix} \cos\left(-\omega_g t - \frac{\pi}{2}\right) \\ \sin\left(-\omega_g t - \frac{\pi}{2}\right) \end{bmatrix} \quad (4.39)$$

occurs.

Figures 4.11 (a) to 4.11 (c) show the corresponding voltage vector trajectory of the AC voltage with the occurring grid fault. In Figs. 4.10 (b) to 4.10 (d) one can see how the correct voltages of both, the positive and negative sequence system, the correct angle of the positive sequence system and the correct frequency can be determined in spite of mains error after the settling time t_s .

This allows to feed a current matching the positive sequence into the grid even in case of a grid failure. Especially Fig. 4.10 (c) shows that the determined grid angle $\tilde{\gamma}_g$ would not be suitable for feeding a symmetrical, sinusoidal current system. Only the additional decoupling from the occurring negative sequence provides the resulting angle $\tilde{\theta}'$, which serves as a reference for the positive sequence. Additionally, the current angle of the negative sequence can be calculated by the relation $\tilde{\gamma}_g^- = \arctan\left(\frac{\tilde{v}_g^-}{\tilde{v}_q^-}\right)$.

Due to the MPC employed, other, generic curve shapes are also conceivable in principle. By feeding in the current in accordance with the positive and negative sequence, it is ensured that a constant active power exchange with the AC grid is maintained despite the grid fault that occurs. Additional currents could be used to increase the RMS value of the mains current to trigger corresponding mains protection elements and eliminate the mains error using the MMC.

Simulation of the MPC

In order to simulate the dynamics and performance of the presented MPC of the MMC, in the first step the AC voltage is no longer regarded as ideally feed forward controlled. Nevertheless, the AC voltage can be decoupled and fed forward according to Eq. (4.24a). It is assumed that the measurement, identification and calculation of the grid angle is performed at 5 times the control frequency of the MPC. With respect to the implementation on the test bench in Chapter 5 these are appropriate assumptions. The feed forward control will be implemented on a FPGA while the MPC will be programmed on a DSP.

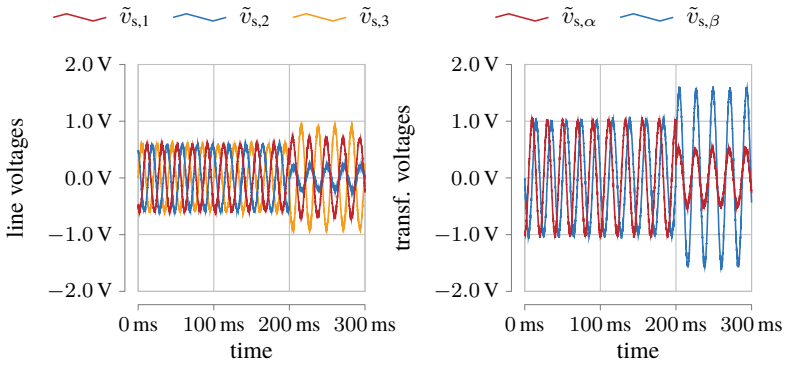
To simulate the MPC together with the PLL, another mains failure is simulated. To show the behavior more detailed, the grid fault is slightly changed in comparison to the previous one. The test starts with a step change of the setpoint, which adjusts the current taking into account the maximum control voltage. Then, from stationary operation, with pure active power injection, an additionally occurring negative sequence in the voltage is simulated. The setpoint trajectories of the current are not changed. Afterwards, the values determined by the PLL adjust the setpoints of the current in such a way that the power feed corresponds to that in undisturbed, stationary operation.

For the setpoint of the current, a symmetrical, sinusoidal current system without phase shift to the voltage is selected

$$\tilde{x}_{ac}^* = 1 \text{ A} \begin{bmatrix} \cos(\omega_g t) \\ \sin(\omega_g t) \end{bmatrix} \quad (4.40)$$

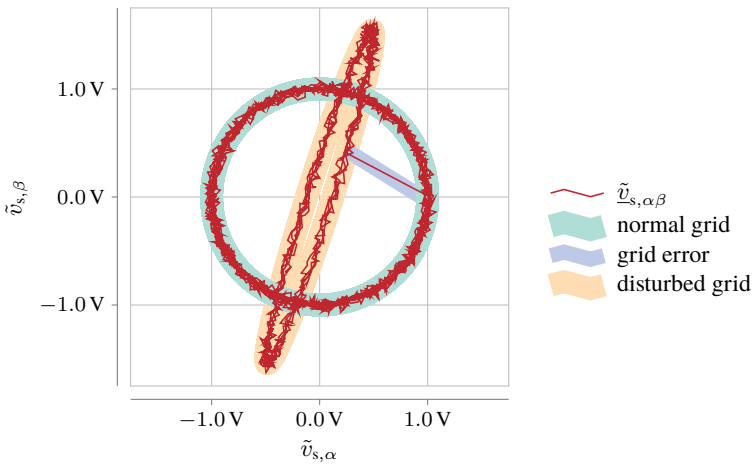
The output variables are constrained to the range $-1 \text{ V} \leq \tilde{u}_{AC} \leq 1 \text{ V}$.

Figures 4.12 (a) to 4.12 (d) show the behavior of the control loop in steady-state operation and in case of a grid fault. The grid voltage is shown in Fig. 4.12 (a).



(a) Line voltages

(b) Transformed voltages



(c) Voltage vector trajectory.

Figure 4.11: Simulated line voltages and corresponding transformed voltages during the grid fault.

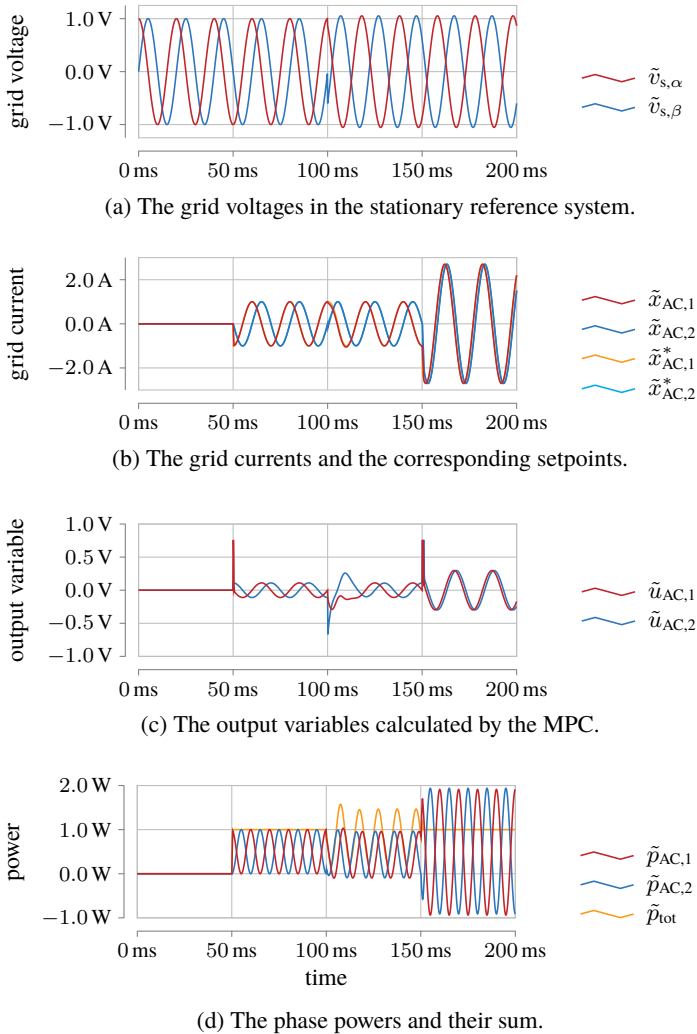


Figure 4.12: Reference and disturbance variable of the MPC with limits and influence of the PLL. At $t_1 = 50$ ms the current setpoint is applied. At $t_2 = 100$ ms the grid fault from Sec. 4.3.4 occurs. From $t_3 = 150$ ms the power delivered is constantly to the grid.

At $t_1 = 50$ ms the setpoint of the current trajectory is set to \tilde{x}_{ac}^* . The phase angle $\tilde{\theta}$ is determined by the subordinate PLL for the calculation of the setpoints. In Fig. 4.12 (b) the setpoints and actual values of the network current can be seen. The setpoint is precisely controlled in a stationary manner. The dynamics are limited by the limitation of the output variables. In Fig. 4.12 (c) the limited output variables can be seen. The power from Fig. 4.12 (d) is adjusted accordingly.

At $t_2 = 100$ ms the grid fault from Sec. 4.3.4 occurs. The setpoint of the grid current remains unchanged. Due to the collapsing mains voltage, it is incorrectly biased until the PLL has determined the correct phase angle. This error results in a current that has to be additionally controlled by the MPC. Despite the constrained output variables, the dynamics are sufficient to keep the currents within a safe operating range. As soon as the PLL has filtered the phase angle of the positive sequence and the system is in a quasi-stationary state, the current is also controlled in phase with the positive sequence. As a result, the power delivered to the grid is no longer constant, but is superimposed with a pulsation of twice the grid frequency.

At time $t_3 = 150$ ms the setpoint of the current trajectory is adjusted so that the power delivered to the grid corresponds to the power before the grid fault. Also in this case, the maximum dynamic is achieved under consideration of the limit values of the output variables. The MPC together with the PLL delivers highly dynamic and stationary accurate results in the quasi-stationary state as well as in transient processes, taking advantage of the maximum allowed output variables.

The selected parameters of the control loop offer a very good tradeoff between dynamics and stability and allow the adjustment of any current trajectories even under faulty network conditions. Thus, the MMC can be used not only for the transmission of high power but also for the support of grids.

Energy Pulsations During Grid Fault

The calculation of the optimal current trajectories from Sec. 3.1.6 can reduce the energy pulsation not only in stationary operation. It is also possible to reduce the energy pulsation in case of a failure. This gives a further degree of freedom for the design of the cell capacitors. To reduce the energy pulsation, lookup tables are stored for each operating point. Depending on the grid angle and the amplitudes of the positive and negative sequence, the optimal current trajectories

are selected. Using the new presented reduction method, the distance between the maximum arm energy and the switch-off threshold is increased. Therefore, a fundamental reduction of the arm capacitors is possible. To show the effect, the energy control from Sec. 4.1 is simulated. The setpoint trajectories of the AC currents are chosen so that the power exchanged with the grid is constant.

Figure 4.13 (a) shows the profile of the energy pulsation without compensation currents. At time $t_1 = 187.5$ ms a setpoint jump of the AC current amplitude is given. The arm energies are kept constant on average by the energy controllers.

At $t_2 = 375$ ms the grid fault from Sec. 4.3.4 occurs. A negative sequence voltage in addition with a positive sequence voltage sag is simulated. Due to the implemented PLL and the dynamics of the MPC it is possible to keep the AC power constant after a short transient response. The energy pulsation increases because the phased load within the system is no longer symmetrical. The presented control algorithm allows an operation of the MMC also in case of a mains failure.

If additional compensation currents are injected, the energy pulsation can be reduced. For clarity, the energy pulsation without compensation in steady-state operation is used as a reference value. Figure 4.13 (b) compares the energy pulsations without and with currents for reduction of energy pulsation. A significant reduction of the energy pulsation can already be seen at the setpoint jump.

If a grid fault occurs, with either method the energy pulsation increases. The arm capacitors must be designed for the maximum energy of the system. With internal currents for reduction, however, it is possible to reduce the maximum occurring energy pulsation by 24.91 %. Since the voltage occurring at the capacitor is related quadratically to the stored energy, a significant reduction of the maximum occurring voltage at the capacitor is achieved. Therefore, it is possible to use much less capacitance with the same voltage limitation.

4.4 Conclusion of this Chapter

In this chapter a feedback control scheme of the MMC was derived, designed and simulated on the basis of the system analysis in Chapters 2 and 3.

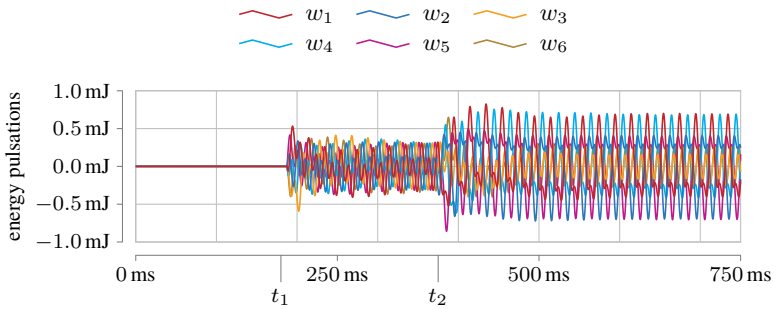
In addition to feed forward control for reduction of energy pulsation, the state variables need to be feedback controlled in order to be able to react to model errors and occurring disturbance variables. The derived equations of the system allow a direct transformation into decoupled subsystems. Thus, the average of the energies are controlled to their setpoints. The corresponding transformation rule allows a decoupling of the AC side and thus an independent control of the energies from the AC power supply.

Simple PI controllers are used to control the energies. The current trajectories for balancing and reduction of energy pulsation are set by subordinate current controllers. State controllers with finite response time are used.

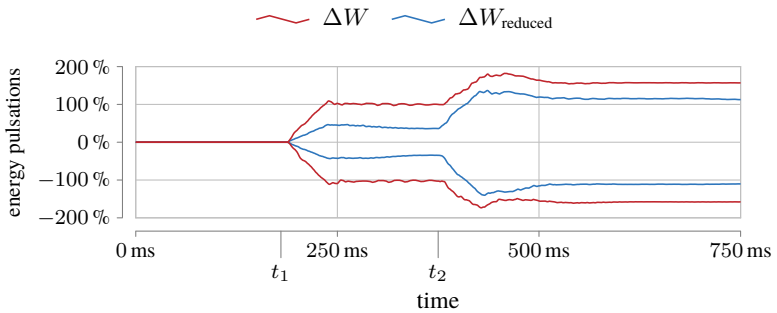
The control of the AC side is of special importance if the MMC is not only used for the transmission of large power but also for support of the connected grid. By using a DSRF PLL together with an MPC, it is possible to adjust the AC currents of the MMC dynamically and stationarily exact during steady-state operation and in case of a grid fault.

The modelling allows the reduction of the energy pulsation of the system depending on the operating point. The energy pulsation of the arms is also significantly reduced in the event of an AC grid fault. This allows a reduction of the installed arm capacitance or an increase of the arm current with the same limit values for the capacitor voltage.

By combining known grid control methods with the new approach to modelling, decoupling of the system and function optimization for reduction of energy pulsation, the MMC can be easily used for grid-related support tasks such as reactive current injection for voltage stabilization in the event of a grid fault. The formalism can be easily adapted for other MMC based topologies. In addition, there is no more need for balancing power term identification for each specific topology.



(a) Absolute energy pulsations in case of a grid fault at time $t_2 = 375$ ms without compensation currents.



(b) Comparison of the energy pulsations in case of a grid fault at time $t_2 = 375$ ms normalized to operation without compensation.

Figure 4.13: Comparison of the energy pulsations ΔW with a setpoint step and in case of a mains error without and with compensation currents in relation to the energy pulsation in the stationary case without compensation.

Chapter 5

Laboratory Setup for Validation of the Control Algorithms

The described control algorithms for the operation of the MMC as a grid serving converter were derived, designed and simulated in Chapters 2 and 3. For verification, the algorithms are implemented on a signal processing system and tested on a real grid using a laboratory prototype. In the following chapter, the concept of signal processing and the design of the prototype are presented. Sections 5.1 and 5.2 show the basic structure of the system consisting of a power section and a signal processing unit. The setup is based on a laboratory prototype from [27]. The power part was modified and the signal processing was made more powerful. The signal processing is based on a System-On-Chip platform [117] developed at the Elektrotechnisches Institut (ETI). To ensure that the grid connection conditions are reproducible, an inverter-based island grid was developed [E5]. This allows for the emulation of fixed grid conditions and the verification of control algorithms.

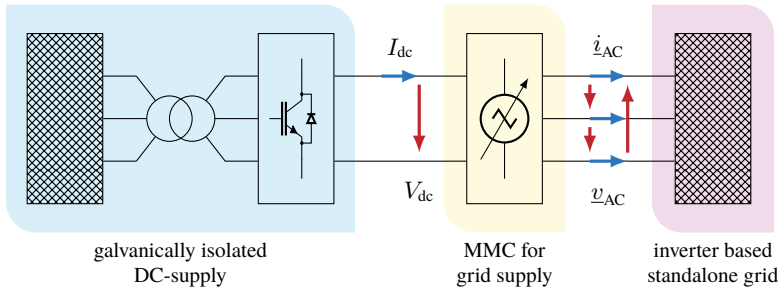


Figure 5.1: Overview of the power unit of the laboratory setup

5.1 Description of the power electronics

Figure 5.1 shows the schematic structure of the power electronics for validation of the described control algorithms. The central component is the MMC, which is fed on the DC side by an electrically isolated DC source. The power supply comes from the 400 V/50 Hz laboratory network. A transformer is used to supply a converter based on the single printed circuit board (PCB) converter system (EPSR) from [117]. The EPSR provides a stable DC link voltage for the MMC. The system of interconnected EPSR is designed for a power of $P_{\text{EPSR}} = 100 \text{ kW}$ and provides a maximum DC voltage of $V_{\text{dc,EPSR,max}} = 850 \text{ V}$. The EPSR is voltage controlled. Thus, the DC current is set by the MMC control.

In order to minimize the feedback effects of the voltage control on the MMC, the converter can optionally be fed by a machine set. In this case, the current-dependent voltage drop of the DC machine must be taken into account.

The MMC is connected to an inverter-based island grid [E5] or the laboratory supply grid on the AC side. This ensures that the control of the MMC can be investigated under reproducible grid conditions. The inverter supply allows all parameters of the AC grid to be set arbitrarily within the permissible limits.

Figure 5.2 shows the overview of the standalone network. The MMC is connected to the point of common coupling (PCC). The mains voltage itself is provided either by another MMC from [23] or by a two level converter with added LC filter. Additionally, different loads and sources of supply can be connected. These allow for realizing different operating points of the network, which

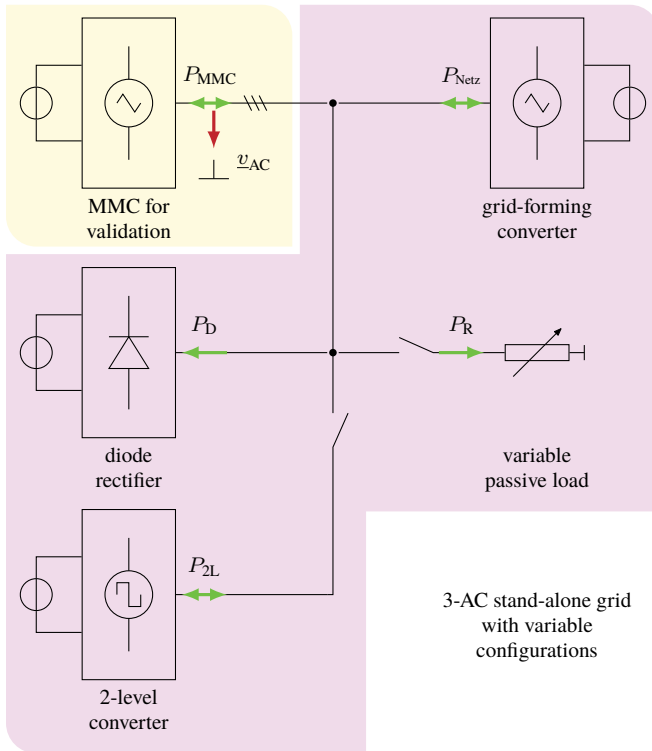


Figure 5.2: Overview of the stand-alone grid to create reproducible grid conditions.

can be approached reproducibly. The short-circuit power S_k at PCC is fixed by the converters to $S_k \approx 50$ kVA.

Due to the voltage-forming character of the grid-forming converter and its multi-level output voltage, a high dynamic, high quality stand-alone grid is provided.

Figure 5.3 shows the EPSR as it is deployed in different versions and configurations in the laboratory setup. Due to the variable application possibilities, the EPSR can be used both for the DC supply of the MMC and for the realization of loads in the island network.



Figure 5.3: The latest version of the utilized EPSR

The achievable output power can be increased by connecting the units in parallel. The diode rectifier in the island network is also realized with a EPSR based system. Here, only the free-wheeling diodes of the modules are used. The control of the converters is in all cases handled by the ETI-DSP system [117, 118].

Consequently, the island grid can be used not only for validating the MMC control algorithms but also to investigate new approaches to grid control in different configurations [E4, E5].

5.1.1 Laboratory Prototype of the MMC

Table 5.1 lists the parameters of the built prototype. The MMC has a nominal power of $P_{\text{MMC},N} = 10 \text{ kW}$. Each arm is a series circuit of $N = 5$ cells, with a maximum voltage of $v_C = 150 \text{ V}$. Coupled iron sheet arm inductors are used. Due to the very good coupling of the arm inductors, additional ferrite inductors are used as line inductors on the AC side. Figures 5.4 (a) to 5.4 (c) show the laboratory setup of the MMC with power terminals and signal processing. Each of the 6 converter arms is realized on a PCB shown in Fig. 5.4 (b). The power unit is adopted from [27]. Additionally, the signal processing has been modified and made more powerful. The semiconductors used are IPP110N20N3 from Infineon [D6].

The cell capacitance is realized from a parallel connection of 3 capacitors with 2.2 mF of the EETUQ series from Panasonic [D7]. For the power supply of the cell logic and gate drivers, a flyback converter is installed, which is locally

Table 5.1: Technical specifications of the MMC

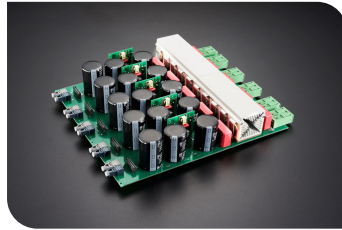
Parameter	Value
$P_{\text{MMC},N}$	10 kW
V_{dc}	650 V
V_{AC}	400 V
φ_d	0 to 2π
$I_{\text{arm,max}}$	40 A
N_{cell} per arm	5
full bridge semiconductors	IPP110N20N3
$R_{\text{ds,on}}$	10.7 m Ω [D6]
f_C	8 kHz
f_M	40 kHz
C_{cell}	6.6 mF
$L_{\text{h,arm}}$	241 μH
$L_{\sigma,\text{arm}}$	10.5 μH
L_{AC}	1.33 mH
L_{DC}	5.0 mH

fed from the intermediate circuit of the cells. The communication between the cells and the higher-level control system is realized galvanically isolated via fibre optic cable (FOC). The control of the full bridge and measurement of the DC link voltage of a cell is done with an FPGA 10M08SAE144 from Intel [D8]. Figure 5.4 (c) shows a close-up of the cell logic for an entire arm. The FPGAs are connected to the cells via a plug-in board.

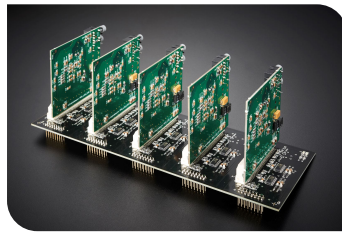
The laboratory setup of the stand alone network and the extensions of the MMC from [23, 27] was carried out and supervised in the context of several student projects [S1–S5].



(a) lab setup of the MMC



(b) arm PCB with 5 cells



(c) cell controller

Figure 5.4: Complete laboratory setup with power section and signal processing of the laboratory prototype.

5.2 Description of the Signal Processing Unit

Figure 5.5 shows a basic overview of the signal processing system of the MMC. In the next section, the individual components of the signal processing chain are elaborated further. The signal processing system is based on the DSP system developed at the ETI. It allows a fast implementation of control algorithms and control of the inverter periphery [113, 117, 118].

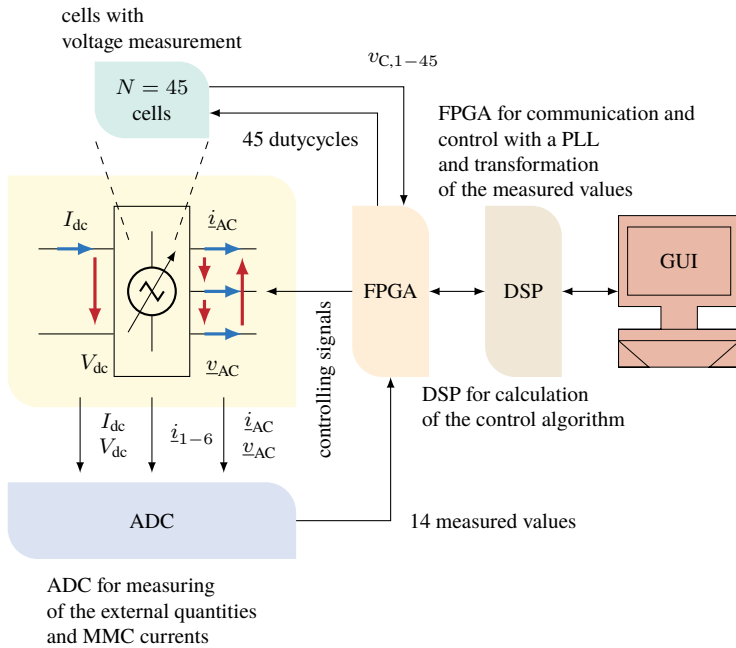


Figure 5.5: Overview of the signal processing unit of the MMC.

5.2.1 Cell Control

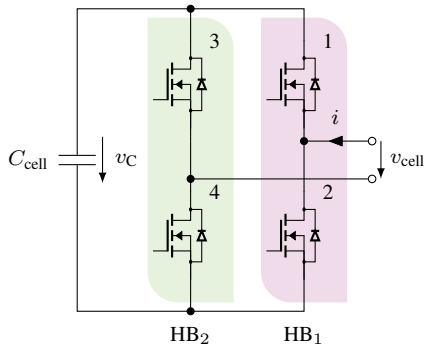
Each of the 45 cells of the converter contains a local unit to control the cell. The communication between the cell controller and the central logic unit is performed using a universal asynchronous receiver transmitter (UART) protocol via a FOC pair. At the same time, the DC link voltage of each cell is measured, limit values are monitored and the control signals of the full bridge are generated in order to realize the desired degree of modulation and therefore the output voltage. The cell-FPGA operates with a frequency of $f_{\text{cell,FPGA}} = 150 \text{ MHz}$. The DC link voltage is measured with the analog digital converter (ADC) of the MAX 10 with a resolution of 12 bit. From a maximum cell voltage of $V_{C,\text{max}} = 161.7 \text{ V}$ follows a resolution of 3.95 mV/bit . The sampling is always done in the middle of a modulation period. This ensures that the measurement is not influenced by switching operations of the semiconductors.

The full bridge is triggered with alternating switching using a carrier-based pulse width modulation (PWM) [110, 119]. Figure 5.6 (a) shows the schematic diagram of the metal–oxide–semiconductor field-effect transistor (MOSFET) full bridge as it is used in the laboratory setup. The output voltage v_{cell} can have the following values: $+v_C$, $-v_C$ and $\pm 0 \text{ V}$. $\pm 0 \text{ V}$ describes the states for an output voltage of 0 V if S_1 and S_3 (0_+) or S_2 and S_4 (0_-) are switched on. Depending on the output levels a_1 and a_2 of the two half bridges HB_1 and HB_2 the output voltage corresponds to the setpoint v_{cell}^* on average over a modulation period T_M . The following applies:

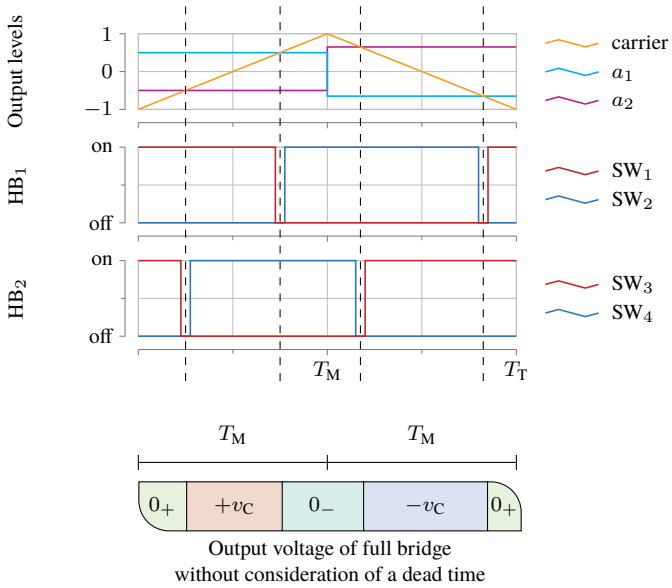
$$a_1 = \frac{v_{\text{cell}}^*}{v_C} \quad (5.1a)$$

$$a_2 = -\frac{v_{\text{cell}}^*}{v_C} = -a_1 \quad (5.1b)$$

The switching commands SW_{1-4} of the semiconductor switches are generated by comparing the output levels with the carrier signal. The triangular-shaped carrier has a period $T_T = 2T_M$, where T_M corresponds to a modulation period. The new modulation levels of the full bridge are always applied at the minimum and maximum of the carrier signal. The result is a center-symmetrical voltage signal at the center of a modulation period T_M . With a setpoint of $v_{\text{cell}}^* = 0 \text{ V}$ it is important to consider the switching state of the cell to avoid unnecessary switching during a period T_T between 0_+ and 0_- . This allows easy control of the full bridges.

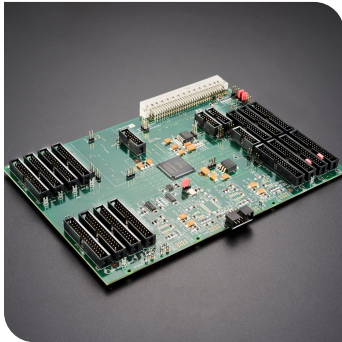


(a) Full bridge cell with MOSFET switches.

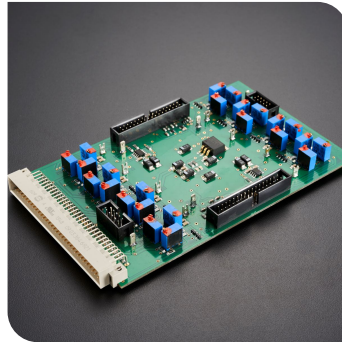


(b) Exemplary switching operation of a full bridge cell.

Figure 5.6: Modulation of a full bridge cell with MOSFET switches for two exemplary output levels.



(a) FPGA plug-in card



(b) 12 bit ADC

Figure 5.7: Main FPGA of the laboratory setup with mountable ADC for data acquisition.

The measured voltage values are transmitted to the higher-level control. The output levels are received accordingly before the start of each modulation period. The communication is established by FOC transmitter and receiver with a maximum transmission rate of 50 MBd [D9]. With a clock frequency of FPGA of 150 MHz the evaluation of the UART protocol takes place over at least 3 clock cycles. A majority decision shows a reliable function of the protocol during operation of the laboratory setup.

5.2.2 Central FPGA of the Laboratory Setup

Figures 5.7 (a) and 5.7 (b) are images of the central FPGA and ADC for data acquisition. The board carrying the FPGA was developed at the ETI under the name high power modulator board (HMK) as part of the ETI signal processing system. The central component is a Cyclone IV FPGA [D10] whose input/output (I/O) pins are connected to tub connectors. This allows the periphery of the converter to be controlled, semiconductor switching signals to be generated or data to be sent and received via FOC or cable-based bus systems.

The HMK generates the global counters for control, modulation and data acquisition. It is responsible for balancing the energy within the arms of the converter,

handles communication with the cells and controls the circuit breakers. Additionally, the ADC are directly connected to the HMK. Due to the direct value acquisition, it is possible to implement the PLL for the detection of the grid angle and for feed forward control of the grid voltage right on the FPGA. For this purpose, the transformation of the control and output variables must also be carried out on the FPGA. The communication with the superimposed DSP for the calculation of the control algorithm is realized simultaneously via a 16 bit parallel bus.

Data Acquisition and Evaluation

The ADC from Fig. 5.7 (b) are designed as a extension module for the HMK FPGA board. The ADC are 12 bit THS 1206 [D11] with 12 bit resolution, 4 channels and a sampling rate of 6 MS s^{-1} . Since the power semiconductors have a minimum on-time, the sampling of the signals to be measured can be done at the maximum and minimum of the modulation carrier signal. Thus, the disturbances, which can result from switching operations, are minimal. To further smooth possible interferences, the average of 8 samples around the sampling point is calculated.

The AC and DC voltages are mapped to the input range of the AD converter via a high-impedance voltage divider. This results in a resolution of 491.3 mV/bit . The 6 arm currents of the converter are measured with compensation current transformers LAH 50-P [D12]. The resolution of this measurement is 25.6 mA/bit .

5.2.3 Timing of the System

To ensure stable operation, special attention must be paid to the timing of the controls. At the beginning of each sampling period, the measured values for voltages and currents are determined and monitored for their limit values. Within one control sampling period, the algorithm for the calculation of output variables $\underline{u}_{\text{ref}}$ must be executed. The output variables must be transferred from DSP to FPGA and converted into modulation levels. At the same time, the DC link voltage of each cell is measured using the cell controllers and also transmitted to the FPGA. In order to ensure an equal distribution of energy within an arm, the cells are sorted for the next cycle period depending on the power sign of the

setpoints. At the end of the cycle period the output levels are transmitted to the respective cell controllers. In order to improve the voltage feed forward for the control of the AC side, the clock frequency is increased according to [30] with little effort by calculating the PLL directly on the FPGA. While the measurement of the AD channels, the sorting of the arm voltages, the calculation of the AC voltage feed forward and PLL as well as the evaluation of the modulation levels are calculated with a modulation period T_M , the control algorithm for current and energy control of the system is executed with a control period of $T_C = N_C T_M$.

In Fig. 5.8 an exemplary timing diagram for an increase of the modulation frequency by a factor of 2 is shown. ① describes the counter maximum and counter minimum of the global modulation period T_M . At this point the new modulation levels a are applied to the cells switches. The counter readings of the cells for determining the switching and measuring times are synchronized by UART transmission.

At the same time the ADC for voltage and current measurement are triggered and the averages of the last 4 and the upcoming 4 samples are calculated. The values are then available on the HMK for further processing.

The measured values of the grid voltage are fed to the PLL at the time ②. The PLL algorithm according to Sec. 4.3.3 is calculated within 18 FPGA clock cycles. The determined grid angle and frequency as well as the voltages of the positive and negative sequence are supplied to the DSP. At the same time, the setpoints $u_{1-6,AC,ff}^*$ are calculated directly on the FPGA for voltage feedforward control. This means that even in the event of a grid fault, the provided, incorrect voltage feed forward is still sufficiently accurate. This conditions, that the fault current of the system remains within its permissible limits.

At the time ③ the control algorithm is triggered on the DSP with the acquired values, when both periods have started. Otherwise, no trigger signal is generated in order to have sufficient computing time on the DSP for the more complex control algorithms.

The cell voltage measurements of the past modulation period are used for energy control. These are assumed to be constant within a control period T_C of the DSP. ④ is located in the middle of the period. The capacitor voltages are measured in the cells. By choosing the time of measurement, the effects of the switching operations on the sensors are minimized as described in Sec. 5.2.1.

At ⑤ the capacitor voltages are sorted. This is necessary to ensure that the voltage per arm is distributed equally among the cells on average. A sorting network

is used, which handles the sorting of the 5 arm cells. From an electrical point of view, the cells are bipoles, without energy supply. To balance the energy, the power sign will be used for assigning the switching states within the next modulation period in the arm. The sorting is described in detail in [23, 27, 30] and had only minor adjustments in this work.

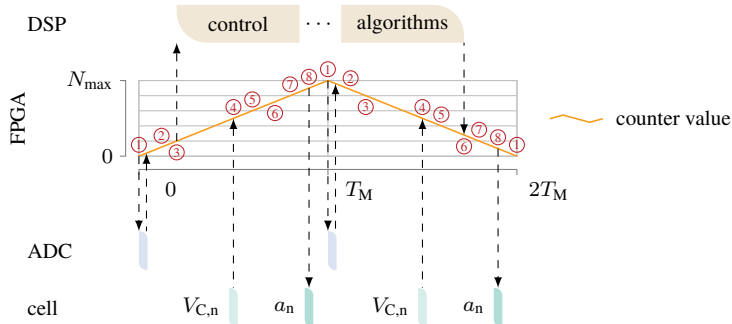
At the time ⑥ the calculated setpoints u_{1-6}^* of the control algorithm of the DSP must be available when the integer multiple $N_C = T_C/T_M$ is reached with respect to the start of the period. Otherwise, the setpoints of the previous control period T_C are used. In the event that the calculation is not completed, the converter is set to the error state and safely shut down, since the real-time condition is no longer satisfied and safe operation can no longer be guaranteed.

Afterwards, from ⑦ on, the output levels of all cells are calculated. Depending on the sort order it is decided which cells will be switched on completely during the next modulation period, which will be switched off completely and which cell will be switched on using the center-symmetric PWM. The aim is to approximate the arm voltage to be set as best as possible. To scale the PWM to the cell voltage of the switching cell, one division per arm, i.e. a total of 6 divisions, must be performed. Due to the high modulation frequency in comparison to the mains frequency, the assumption of the averaging model for the control of the system is justified.

Right before the beginning of the new modulation period, at the time ⑧ the new modulation levels are transmitted to the cells via UART. With ① the new modulation period starts and the new output levels are applied.

The timing of the system allows a highly dynamic feedforward control of the AC voltage even in the event of a grid failure. The used PLL identifies the positive sequence as well as the negative sequence. This also allows a correct rotation of the components to compensate for a sampling time. The different period length of modulation and control allows a decoupling of AC feedforward and control. This guarantees stable operation in case of a grid fault on the one hand and sufficient computing time in stationary operation on the other hand.

The presented system of power electronics, signal processing in the MMC and the inverter-based stand-alone grid are used in Chapter 6 to validate the modeling and control algorithms.



- ① Start of the modulation period and adoption of the output levels a on the cells, as well as triggering the ADC for voltage and current measurement.
- ② The PLL is calculated with the voltage measurements directly on the FPGA.
- ③ Once all values of the ADC have been transmitted, the control algorithm is triggered on the DSP each time a new DSP period T_c begins.
- ④ In the center of the modulation period, the capacitor voltages of the cells are measured and sent to the FPGA.
- ⑤ The cell voltages are calculated and sorted, depending on the power sign.
- ⑥ If the DSP has calculated new setpoints, the output levels are updated accordingly. Otherwise the new values of the PLL and the values of the previous control period are used.
- ⑦ The new output levels of the cells are calculated.
- ⑧ The output levels a_n are sent to the cells.

Figure 5.8: Exemplary timing diagram of the system with a ratio of the control period T_c and the modulation period T_M of 2.

Chapter 6

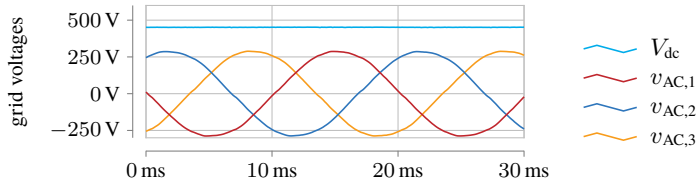
Measurement Results

In this chapter, measurement results obtained from the laboratory setup are presented. The modeling of the system presented in Chapter 2 and the derived control structures from Chapter 3 are verified and validated with the structure discussed in Chapter 5. Quasi-stationary and dynamic measurements at the laboratory grid and the inverter-based island grid are presented to demonstrate the basic functionality of the control. Finally, the performance in case of a grid failure is shown and the desired additional reduction of energy pulsation is validated.

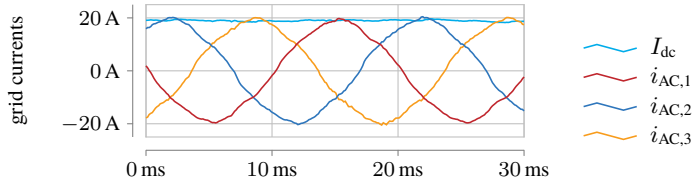
6.1 Quasi Stationary Operation of the System

The MMC is pre-charged and operated quasi-stationarily using the 400 V/50 Hz laboratory supply grid. The grid is connected via a Yz-transformer. Through this, the feeding network string voltage amplitude is $\hat{V}_{AC} = 400 \text{ V} / \sqrt{2} = 282 \text{ V}$. On the DC side, the MMC is controlled by a machine set with $V_{dc} = 450 \text{ V}$. The ratio is $V_{dc} / \hat{V}_{AC} \approx 1.6$. A power of $P = 8.5 \text{ kW}$ at a power factor of $\cos(\varphi_g) = 1$ is delivered to the AC grid.

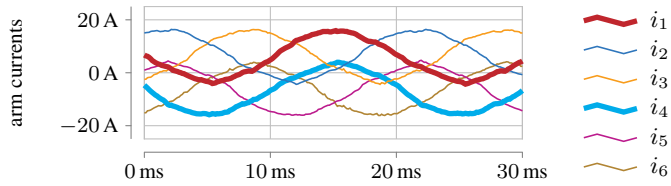
Figures 6.1 (a) and 6.1 (b) show measurements of the grid voltages and grid currents in this operating point. The values are recorded with the sampling period $T_C = 125 \mu\text{s}$. The voltage feed forward control and the PLL on the FPGA operate with factor five of the control frequency.



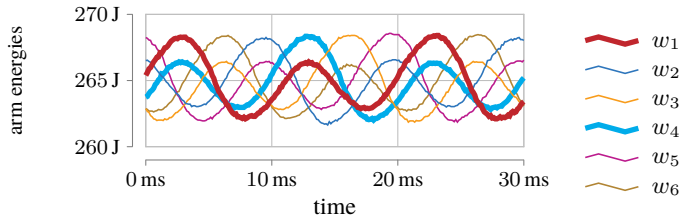
(a) measured AC voltages and DC voltage



(b) measured AC currents and DC current



(c) measured arm currents



(d) arm energies calculated from the measured arm voltages

Figure 6.1: Quasi-stationary operation at the 400 V/50 Hz-grid with $P = 8.5$ kW. The measured values are sampled with the control period $T_C = 125 \mu\text{s}$.

As can be seen, the grid currents are precisely controlled stationarily by the predictive approach of AC control as introduced in Sec. 4.3. Figure 6.1 (c) depicts the measured arm currents of all six inverter arms. As derived in Chapter 2, these are composed of a superposition of the AC currents and the DC current. In addition, currents are controlled to generate balancing power according to Sec. 4.1. With 0.5 A these currents are small compared to the total arm current. The energy control is steady-state accurate and ensures stable operation of the system.

Figure 6.1 (d) shows the arm energies calculated from the measured arm voltages v_{arm} according to Eq. (2.2). The occurring energy pulsation is $\Delta W = 8.567 \text{ J}$. On average all energies are constant around the mean value $W_{\text{mean}} = 264.92 \text{ J}$, which corresponds to an arm voltage of $V_{\text{mean}} \approx 650 \text{ V}$.

Oscillographed Voltages and Currents

The measurements performed with the DSP-system, are validated with oscilloscope measurements. To see the influence of the switching, the values must be oscillographed directly on the setup.

Figure 6.2 (a) shows the voltages of the first and fourth arm in steady state operation. The voltages were measured with Keysight N2790A 100 MHz differential probes [D13] directly at the hardware and evaluated with an Keysight MSOX3034T 350 MHz/5 GS s^{-1} oscilloscope [D14]. The individual voltage levels of the 5 cells can be seen very clearly. The voltage approximately corresponds MMC-typically to the superposition of the DC voltage and the AC voltage. The PWM is a very good approximation of the desired output variable. The modulation frequency is $T_M = 40 \text{ kHz}$.

Figure 6.2 (b) shows the voltages with higher temporal resolution. One level of the voltage depends on the energy of the arms and is approximately 140 V. The switching frequency of 40 kHz is clearly visible.

The measurements from Figs. 6.1 (a) to 6.1 (d) and 6.2 (a) show the basic functionality of the presented control algorithms, modulators and implementations on the hardware.

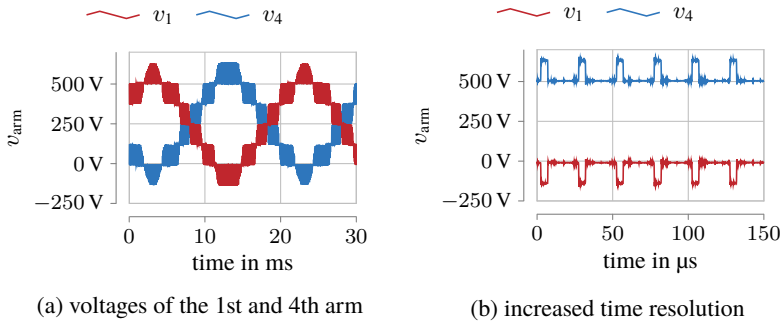


Figure 6.2: Oscillographed arm voltages of the 1st and 4th arm using differential probes and an increased time resolution.

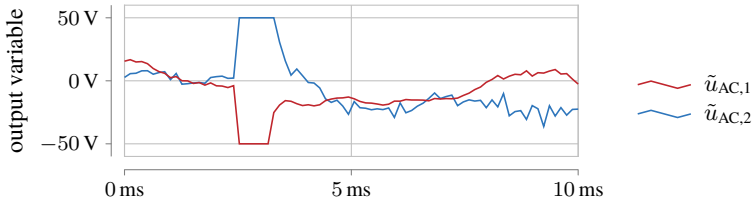
6.1.1 Dynamic Load Step at the AC Side

Due to the load step on the AC side, the AC currents must be controlled accordingly. The power factor of $\cos(\varphi_g) = 1$ means that the power must be adjusted on the DC side as well, to keep the energy within the converter constant. In addition, all energies must be kept constant around their mean value by the balancing control. In the following sections, the control objectives are analyzed and the performance of the control structure is shown.

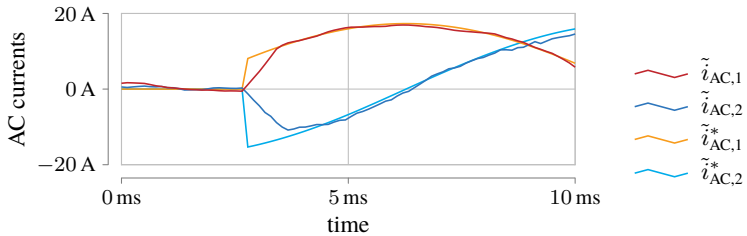
Control of the AC Currents

To reach the stationary operating point from Sec. 6.1, the AC current must be adjusted accordingly. The new approach of predictive AC control from Sec. 4.3 allows a current increase along the voltage limit, without overshoot and with stationary accuracy.

The examination takes place in the transformed system, since the currents and output variables can be considered decoupled for the AC side. The maximum output variable for the AC side can be freely adjusted by decoupling the controlled system. To demonstrate the performance at the voltage limit, the maximum control voltage is set to $\tilde{u}_{AC,max} = \pm 50 \text{ V}$.



(a) transformed output variables of predictive AC control



(b) transformed AC currents

Figure 6.3: transformed, constrained output variables and currents during a load step

Figure 6.3 (a) shows the transformed setpoints of the control variable to the time point of the load step. The limitation to ± 50 V is clearly visible.

Figure 6.3 (b) shows the transformed AC currents and their setpoints. By limiting the output variables, the current increases almost linearly until the setpoint is reached. Due to the modeling and the predictive approach the setpoint is reached with the greatest possible dynamics without overshoot and is precisely controlled in a steady-state manner.

The feed forward control of the measured AC voltage is performed directly on the FPGA with an increased modulation frequency of 40 kHz.

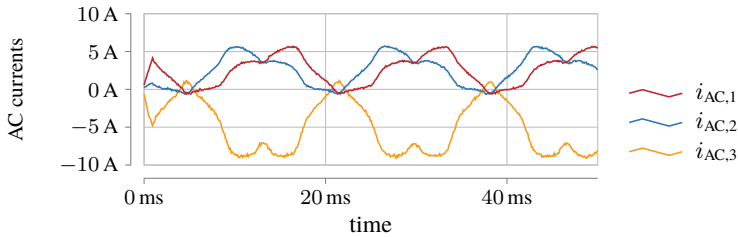


Figure 6.4: Non-sinusoidal current trajectories

Generic Current Trajectories to the AC Side

In addition to the symmetrical, sinusoidal current waveform, an arbitrary current trajectory can be injected by using the predictive approach. Since the neutral point of the AC side is not connected, $\sum i_{AC} \stackrel{!}{=} 0$ applies at all times.

Figure 6.4 shows a periodic current trajectory to the grid. The setpoints are stored and retrieved in lookup tables depending on the grid angle.

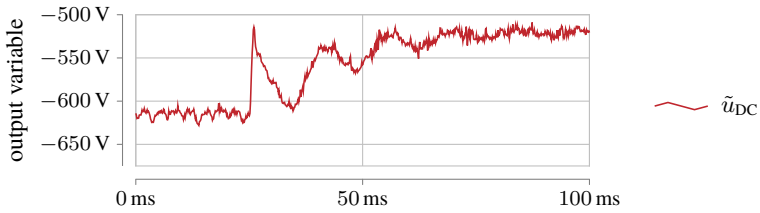
Figure A.1 shows the transformed AC currents in XY representation. The measurement demonstrates that the control structure can adjust not only symmetrical, sinusoidal variables. This allows asymmetrical setpoints to be set in the event of an fault.

Power Supply Tracking From the DC Side

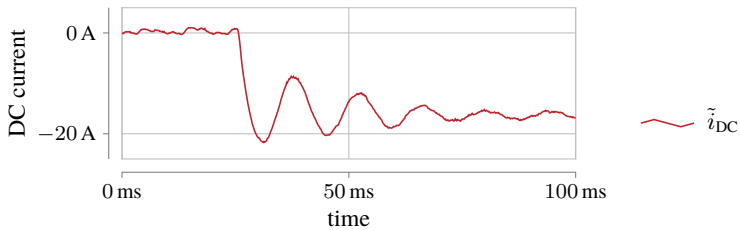
The active power, which is fed into the AC grid, must be tracked via the DC side. An additional dynamic results from the fact, that the DC voltage does not remain constant during the load step. The voltage of the feeding machine depends on the current load.

Figure 6.5 (a) shows the transformed output variable for feed forward control and regulation of the DC side. Before the load step, the DC voltage is fed forward. After the load step, the setpoint of the DC current increases.

To be able to control the current, the output variable is calculated by the DC current controller from Sec. 4.2.1. The actual value follows the setpoint with a delay



(a) transformed output variable of the DC control



(b) transformed DC current for power tracking

Figure 6.5: transformed output variable and current of the DC side during the AC load step

of one control period as in Fig. 6.5 (b). The DC current causes the voltage drop across the armature resistance of the supplying DC machine to increase. As a consequence, the DC voltage decreases in magnitude, which leads to oscillations in the controlled, feeding system.

However, the control structure of the MMC is able to compensate for this change in voltage. The oscillation could be damped by a reference variable filter. However, this would result in a more severe drop in the total energy of the system during the load step.

Balancing the Energies in the System

During the load step, the arms of the system are stressed differently depending on the phase angle and need to be symmetrized. The energy pulsation during the transient process can be reduced as described and shown in Sec. 4.3.4. Without compensation, it takes longer for the energies to reach their quasi-stationary final value.

Figure 6.6 (a) shows the currents for balancing the energies and Fig. 6.6 (b) shows the arm energies for the load step. In this operating point, the energies are balanced without using the zero sequence voltage.

The energy pulsation in steady-state operation after the jump is $\Delta W = 6.15 \text{ J}$. The maximum occurring energy pulsation during the load jump is $\Delta W_{\max} = 16.05 \text{ J}$.

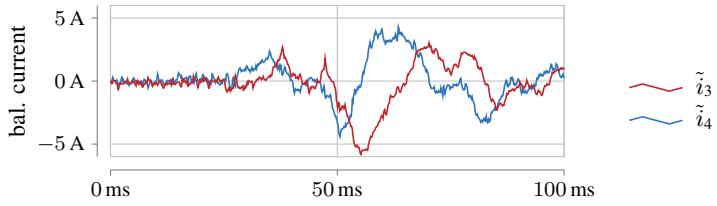
The energy control also symmetrizes the arm energies during the load jump and allows a stable operation of the MMC under dynamic conditions.

The measurement results from Figs. 6.1 (a) to 6.1 (d), 6.3 (a), 6.3 (b), 6.5 (a), 6.5 (b), 6.6 (a) and 6.6 (b) show that the presented control concept from Chapter 3 based on the modeling in Chapter 2 can operate the MMC stable, stationary and highly dynamic.

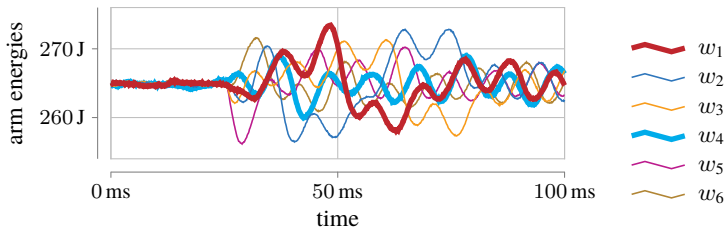
6.1.2 Reduction of the Energy Pulsation

In Chapter 3 new methods for reducing the energy pulsation were presented. Depending on the operating point, current trajectories for the internal currents are calculated in advance. Compared to the reduction of the second harmonic in the energy pulsation, the ΔW can be significantly reduced.

The feed forward control of the 2nd harmonic is used according to the state of the art to reduce the energy pulsation. The presented optimization methods allow a further reduction of the energy pulsation and a better utilization of the installed capacitors.

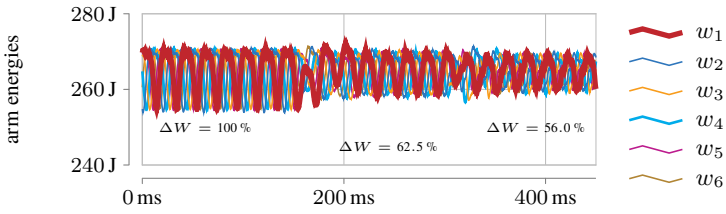


(a) transformed currents for balancing during the load step

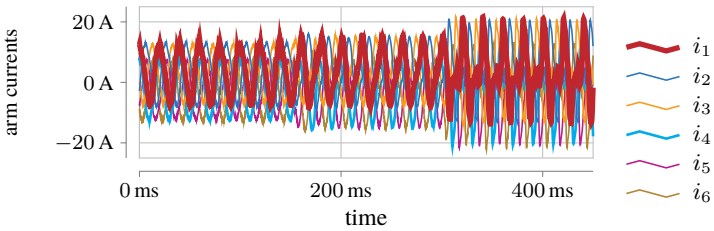


(b) arm energies during the load step

Figure 6.6: arm energies and transformed currents for balancing and the energies during the load step



(a) arm energies at different approaches to compensation



(b) arm currents at different approaches to compensation

Figure 6.7: Comparison of the measured arm energies and arm currents without compensation, with compensation of the 2nd harmonic and optimal current trajectories.

Comparison of Compensation Methods

To validate the statement of the performance from Sec. 3.1.6, the converter is operated in a stable operating point. A line current with an amplitude of $\hat{I}_{AC} = 20$ A is generated at a power factor of $\cos(\varphi_g) = 0.5_{\text{ind}}$. This corresponds to an apparent power of $S_{AC} = 8.5$ kVA. To show the effect of the reduction in the energy pulsation with the help of optimized current trajectories, both methods are applied successively and the energy trajectories are shown.

Figure 6.7 (a) shows the energy pulsation of the arms. Until the time $t_1 = 150$ ms no reduction is activated. The energy pulsation is $\Delta W_{\text{no}} = 16.07$ J.

In Fig. 6.7 (b) the corresponding arm currents are shown.

At time t_1 the reduction of the second harmonic is activated. After the transient process the energy pulsation is only 62.5 % of the original ΔW .

At time $t_2 = 300$ ms the optimized current trajectories are applied. The energy pulsation can thus be decreased by further 6.5 percentage points to 56.0 %. On the other hand, there are of course the higher currents in the converter, which cause additional losses. The maximum arm current of 40 A is never reached at any time. The RMS value of the arm currents increases from 7.1 A to 8.0 A and to 9.62 A.

The reduction of the energy pulsation using the optimized current trajectories is thus also proven and validated on the hardware design.

Additionally, the transient settling process can be further improved. Approaches to this are already shown in [26, 86]. Trajectories for the operating point change are predicted in order to reduce the energy pulsation. With the optimal current trajectories the results could be improved even further. This procedure can be applied to the operating point change as long as the stationary operating points are known.

Compensation for All Phase Angles

As already derived in Sec. 3.1 and shown in [E1] for the compensation of the 2nd harmonic, the degree of reduction depends on the phase angle of the AC side. For the hardware setup from Chapter 5 the energy pulsation can be calculated over the entire phase angle.

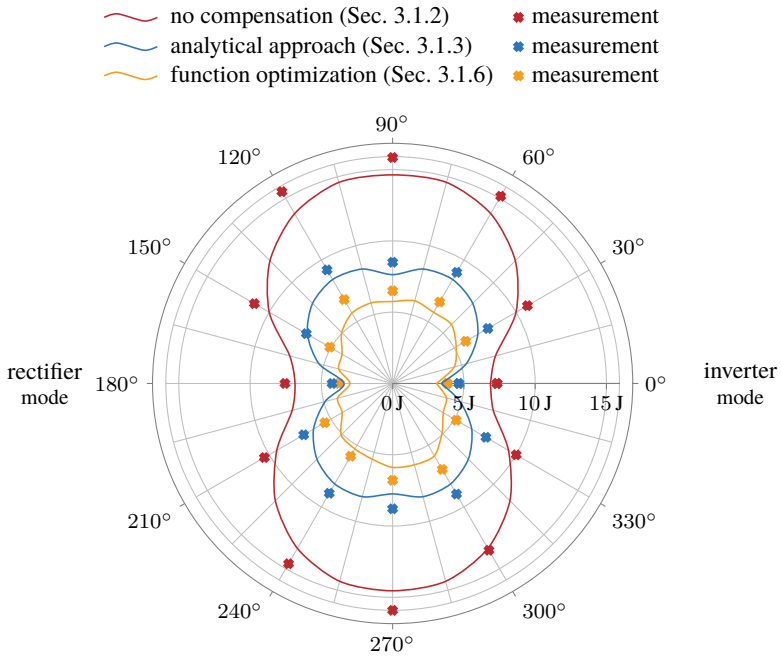


Figure 6.8: Theoretical and measured energy pulsation of the different methods for reduction of energy pulsation over the whole range of phase angle values

In addition, the theoretical values for the compensation of the 2nd harmonic are calculated. The theoretical values are then compared with the measured values. In parallel, the current trajectories for the optimal reduction of the energy pulsation are determined, tested in a simulation and validated by measurement on the setup.

Figure 6.8 shows the measured energy pulsation over the whole range of values of the phase angle φ_g .

In both cases the energy pulsations of the different methods, which theoretically according to Chapters 2 and 3, are shown. In contrast to the results from Fig. 3.8 the compensation of the 2nd harmonic at each operating point is more effective than no compensation at all. As already shown in [E2], this depends on the concrete realization of the hardware.

The reduction of the energy pulsation by using the optimal current trajectories leads to very good results in all operating points.

For all three approaches it can be seen that the measurement corresponds very well with the theoretical values. However, the measured pulsations tend to be higher than the theoretically calculated values. These deviations have two basic causes.

The theoretical values are calculated with a lossless model. The losses will be covered at constant AC power for $\varphi \leq \pm 90^\circ$ via the DC side. The DC current is thus greater than in the ideal case. For other phase angles the DC power is reduced accordingly. Due to the additional power, the energy pulsation is increased accordingly.

The second source of inaccuracies is the measurement value acquisition itself. Besides quantization errors and errors of the amplifications and offsets of the measuring device, the energies of the arms are only measured indirectly via the voltage of the capacitors. For the cell capacitance, the same nominal value is assumed for all cells. According to [D7] the nominal values of the electrolytic capacitors can deviate from the real values by up to $\pm 20\%$.

Nevertheless, the measurements show very good congruence between the theoretical and measured values. Furthermore, it is clear that the new function optimization method for reducing the energy pulsation is superior to the state of the art at any phase angle as long as the maximum allowed arm current is not exceeded.

6.2 Response of the Converter in Case of a Grid Fault

The modelling and design of the control from Chapters 2 and 3 achieves a reduction of the energy pulsation as verified in Sec. 6.1. In addition, the implementation of the PLL on the FPGA in connection with the low-effort increase of the modulation frequency by a factor of 5 according to [30], enables stable operation in case of grid faults. As described in Secs. 4.3 and 4.3.3, a negative sequence can be identified. This allows LVRT and high voltage ride through (HVRT) events to be passed through if the converter limits are not exceeded. The theory presented in this thesis enables to reduce the energy pulsation in the best possible way even in case of a grid fault.

To be permitted to connect a converter to the public grid, certain grid standards must be met in case of a fault [D1–D3]. In the occurrence of a negative sequence, the energy pulsation of the arms increases significantly [E6]. In order to ensure stable operation, the cell capacitance must be designed accordingly larger than necessary for stationary operation. If the energy pulsation is reduced even in case of failure, the cell capacitance can be designed smaller and thus effectively save costs.

6.2.1 Laboratory Setup for the Investigation of Grid Faults

In order to investigate the performance of the control system, it must be possible to set grid faults in a targeted and reproducible manner. Comparing the behavior of the compensation methods in a LVRT experiment requires that the mains voltage always drops by the same value at the same time.

The island grid presented in Fig. 5.2 and [E4, E5] provides the basis for the test setup. In purpose of minimizing feedback effects of switching converters, the island grid was provided by a 2-level converter with LC filter on the output side.

The maximum current amplitude of the grid feeding converter is $I_{\max} = 50$ A. The inductance of the filter was chosen to 1 mH and the capacitance to 160 μ F. The voltage amplitude is $\hat{V}_N = 150$ V at $\omega_g = 2\pi$ 50 Hz. The MMC is thereby fed by a machine set with $V_{\text{dc}} = 1.6 \hat{V}_N \approx 240$ V. In steady-state operation, the

MMC feeds a symmetrical current of $\hat{I} = 10$ A. The power factor is $\cos(\varphi_g) = 1$. This corresponds to an active power of $P \approx 2.25$ kW.

A grid fault is simulated and the behavior of the MMC is analyzed. For this purpose a LVRT event is triggered in the minimum of phase a of the supplying grid. The positive sequence is reduced by a factor of 0.87. At the same time, a negative sequence is triggered with

$$v_n = 0.75 \hat{V}_N e^{-j(\omega_g t + 55^\circ)} \quad (6.1)$$

This corresponds to a voltage drop to approximately 20 % of the nominal voltage of the second phase. The first and third phase rise of approximately 40 %. The LC filter of the supplying converter is only feed forward controlled. This causes transients to occur. Therefore, the power cannot be increased further. The presented control of the MMC is investigated on the laboratory setup under these conditions.

6.2.2 Stable Operation During Grid Faults

The MMC is in steady state operation at the time of the grid fault and feeds an active power into the AC grid.

Figure 6.9(a) shows the measured grid voltages. The grid fault occurs at $t = 20$ ms. In Fig. 6.9(b) the grid currents of the MMC can be seen.

Before the grid fault, the current is precisely controlled by the MPC. In case of a failure, the PLL on the FPGA has to determine the grid angle exactly. Additionally, the negative sequence needs be identified. This enables correct feed forward control of the voltage. During the transient compensation processes, the current in the line inductors increases because of the incorrect feed forward control. However, the MPC is able to keep the current within the limits of ± 50 A and thus avoid a fault state of the converters. Once the PLL correctly identifies all quantities, the currents are injected as a three-phase, symmetrical sinusoidal system despite an unbalanced voltage. Each phase is thereby stressed differently. This results in large energy pulsations in the MMC system.

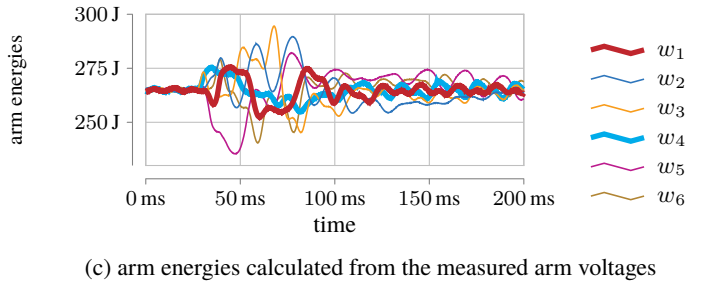
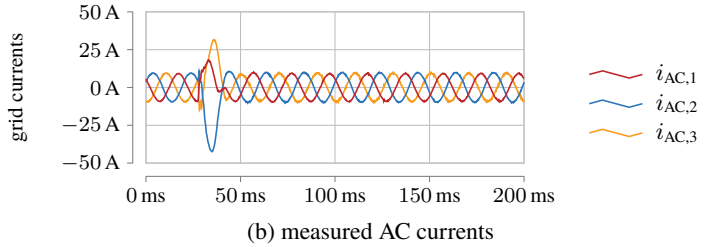
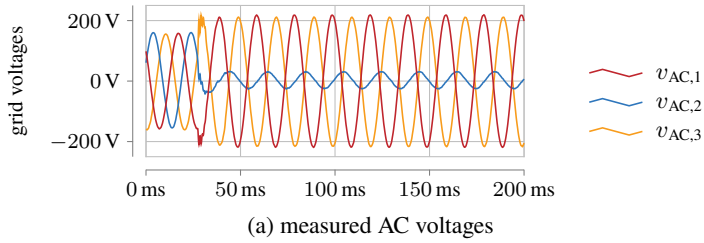


Figure 6.9: Directly measured and derived variables during the grid fault at constant AC current.

Figure 6.9 (c) shows the arm energies of the system. By means of the model and the energy control derived from it, the arm energies are also kept constant within their tolerance band and on average. Since the implemented PLL can identify and decouple the grid voltage in positive and negative sequences, the energies are balanced with the grid voltage in the positive sequence according to Eq. (4.1). There is no need to adapt the energy control scheme in case of an error.

The measurements from Figs. 6.9 (a) to 6.9 (c) show that the MPC from Chapter 3 together with the implementation of the PLL and the energy control derived from Chapter 2 are able to operate the MMC in a stable manner even in case of grid fault. However, the power delivered to the grid is not constant anymore.

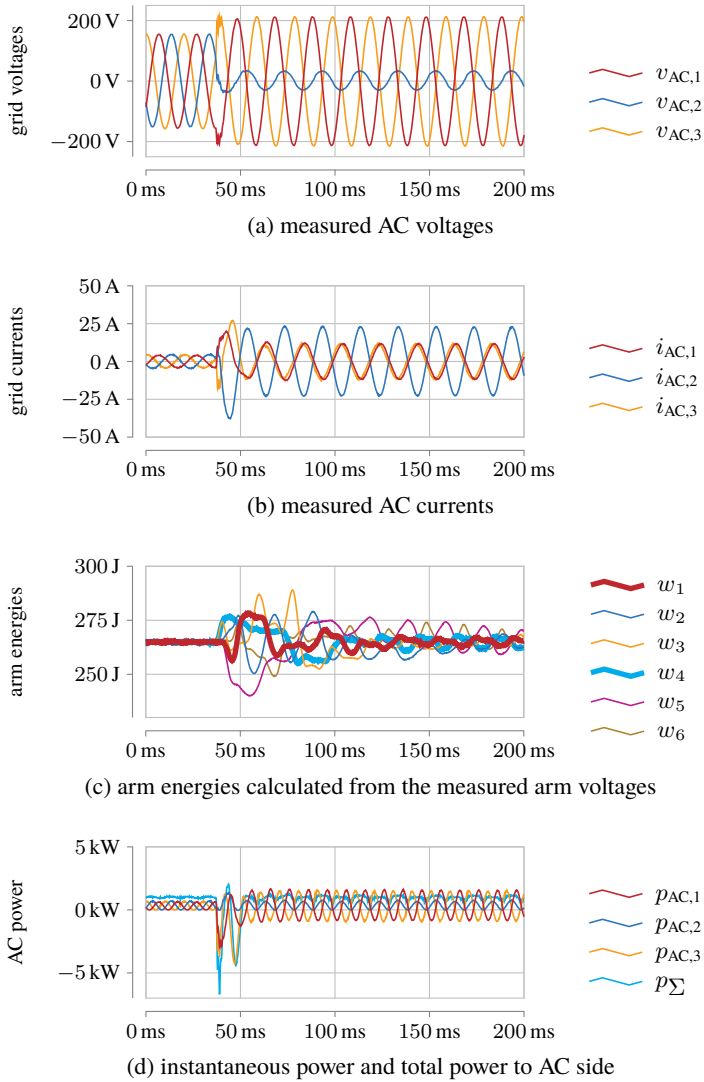


Figure 6.10: Directly measured and derived variables during grid fault

Another typical application of a MMC is the feeding of constant power from the DC side to the AC side. In the event of a grid fault, the power fed into the grid should be kept as constant as possible. In order to ensure a constant power supply, the control of the MMC must be able to quickly identify an occurring negative sequence and adjust the control voltage accordingly.

In order to demonstrate the performance of the PLL in combination with the MPC of the AC currents of the MMC, the power is fed constantly into the AC grid in case of grid fault.

Figures 6.10 (a) to 6.10 (d) show the measured values of the laboratory setup in case of grid fault. Before the grid fault, a constant AC power is delivered to the symmetrical, sinusoidal grid. At $t = 20$ ms the feeding converter emulates the grid fault and feeds the negative sequence of the voltage.

Figure 6.10(a) shows the measured grid voltages. The transient response of the LC filter is clearly visible. The PLL on the FPGA is designed according to Sec. 4.3.3 and identifies the positive sequence and the negative sequence as well as the corresponding grid angle and phase angle of the negative sequence. Based on this, the current trajectories of the AC currents can be calculated so that the active power fed into the AC grid remains constant, as can be seen in Figs. 6.10 (b) and 6.10 (d).

Due to the high repetition frequency of 40 kHz of the PLL and the associated voltage feed forward control, a stable operation of the converter is possible in case of a grid fault as well. The grid current is controlled correctly despite a voltage drop. In addition, it is possible to continue feeding the power constantly into the AC grid as before the grid fault. This means that the DC side does not have to be considered further or restricted if the limit values of the feeding converter are not exceeded.

The corresponding energy pulsation is shown in Fig. 6.10 (c). The arm energies are kept at their average value by the energy control. This is only possible if the positive sequence of the voltage is correctly identified, since this voltage is used to generate balancing power. Due to the unbalanced load of the output phases, the pendulum power must be temporarily stored in the capacitors. This increases the energy pulsation in stationary, unbalanced operation. In transient operation the energy pulsation is even further increased until the PLL has determined the corresponding quantities and a new operating point has been set.

The measurement results show that the modelling and control of the system allows a stable operation in case of an LVRT event.

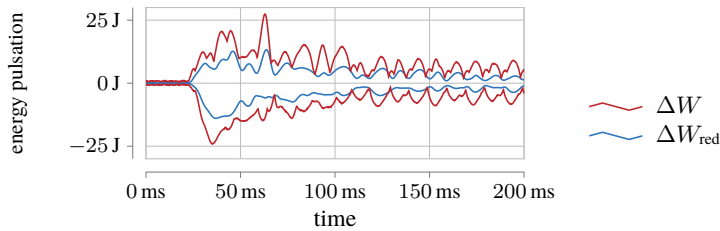


Figure 6.11: Comparison of the maximum energy pulsation in case of grid fault with (ΔW_{red}) and without compensation (ΔW) currents.

6.2.3 Reduction of the Energy Pulsation During Grid Fault

In the event of a fault, the arm energies experience a transient pulsation and even after the fault, the pulsations at constant power are still larger than in steady-state operation. In order to be able to utilize the capacitors further or to reduce the installed capacitance, the energy pulsation have to be reduced even in case of a fault. The transient range is of particular interest here. At this point, the maximum deviations from the mean value occur. In addition, this is the crucial operating point and essential for the cell capacitor design.

The new function optimization of the circulating currents optimizes the energy pulsations that arise in steady-state operation due to the positive sequence of current and voltage. The implemented PLL enables a fast identification of the positive sequence in amplitude and phase in case of a fault. Using this information, the optimal current trajectories are selected even in the event of a fault. Thus, the innovative type of feed forward control enables the reduction of energy pulsations even in the case of a grid fault.

Figure 6.11 shows a comparison of the envelopes of the arm energies in case of an error. If the grid voltage drops, the energy pulsation becomes significantly larger. In steady-state operation the energy pulsation was already reduced, so that overshoot is reduced, as well. After the voltage systems are identified by the PLL, the energies are transferred back to their stable operating point. The optimal current trajectories achieve a reduction of the energy pulsation during the grid fault and even with asymmetrical loading of the system.

6.3 Conclusion of this Chapter

Chapter 6 presented measurement results obtained at the laboratory setup in order to verify the model and the control structure derived from it.

Section 6.1 shows the performance of the control in steady-state operation. The modelling from Chapter 2 allows a quick and easy decoupling of the system. The analytical and systematical derivation of the transformation matrices allows a simple design of the energy and current controls. Due to the introduced straight-forward energy control, no adaptation of the chosen balancing terms has to be derived, even for faulty grid conditions. This even includes other MMC based topologies described and controlled in this manner.

During steady-state operation, the implemented and presented control of the AC side enables the required AC currents to be injected along the voltage limit without overshoot. In addition to symmetrical, sinusoidal current systems, any current trajectories can be specified. By modelling, the power terms are directly identified, which can be used for balancing the energy. The corresponding arm currents are calculated, impressed and enable a stable operation of the MMC.

It was proven that the optimal current trajectories reduce the energy pulsation significantly in contrast to the reduction using the state of the art analytical approach. This applies to the entire range of the power factor. With pure reactive power injection, the effect can even be observed considerably larger.

A widespread application of the MMC is the power exchange between DC systems and AC systems, resulting in the necessity to operate the MMC safely even during grid failures such as LVRT and HVRT.

To enable the comparison of control approaches in case of grid faults, a converter fed island grid is used. Due to the high switching frequency and the calculation of the PLL as well as the corresponding voltage feed forward, the currents can be fed in symmetrically in case of a grid fault. Therefore, a stable operation of the converter is possible even if the phase voltage drops to approximately 20 % within one sampling step.

The MPC based AC control also allows a constant AC power supply in case of a grid fault. The capacitors of the MMC are usually designed for the energy pulsation that occur during a transient event. The capacitance must be large enough so that the maximum arm voltage is not exceeded in the event of a grid failure. It is proven that the optimal current trajectories allow a reduction of

the maximum occurring energy pulsation even in the event of a harsh voltage sag. The quick identification of the symmetrical components of the feeding grid allows for the choice of optimal current trajectories. This reduces the maximum energy value and stable operation is quickly achieved.

The modelling from Chapter 2 and the design of the control from Chapter 3 are verified by means of the implementation in the MMC laboratory setup from Chapter 5.

Chapter 7

Conclusion

The thesis at hand introduced a new approach to modeling modular multilevel converter (MMC) based systems. With the help of this modelling it is possible to design new, efficient control algorithms for the system. In future, it will become more and more important for grid-feeding converters to be able to operate not only in a stable but also grid-compatible manner.

A state space model of the MMC was derived with analytically described differential equations. A method for decoupling the system was elaborated on, starting from the state of the art. Mathematical tools which enable a systematical analysis of the occurring control and output variables were used. A general transformation rule for MMC based systems has been developed by simple matrix diagonalization. It allows a decoupled consideration of those systems.

This directly resulted in simple possibilities to identify power terms which keep the arm energies of the system within their limits. Additionally, degrees of freedom of the circulating currents and the zero sequence voltage were formulated. As expected for MMC based topologies, they can be used to reduce the energy pulsation.

With the presented model description, it was possible to execute new optimization procedures including the degrees of freedom, which allow a reduction of the energy pulsation. According to the state of the art it was difficult to identify those power terms which allow a symmetrization of the system. With the state space description, the zero spaces of the system matrices allow a direct derivation of

those power terms. By superposing the balancing terms, an optimal feed forward control and simultaneous balancing of the whole system can be achieved.

The simple derivation of the transformation rule also provides the basis for the design of sophisticated control algorithms. This thesis explains how to design a closed-loop feed forward controller with finite response time for the DC side and the circulating currents. The description in matrix notation further allows a simple implementation of a model-based, predictive control of the AC side. It is not only possible to limit the output variables of the controller but also to limit the state variables. This calculation is generally complex and requires the solution of a constrained optimization problem.

The analysis of the MMC equations has shown that it is sufficient to solve an unlimited quadratic programming (QP) problem. This calculation can be done in real time and is therefore the basis of the implemented MPC approach. Thus, a current control to the AC side at the voltage limit of the converter is easily achieved.

In order to be able to set the current in the correct phase and to be able to precisely feed the voltage to the AC side, the phase locked loop (PLL) for grid identification is executed with increased clock frequency. The derived energy control, energy deviation reduction and decoupling is validated with a laboratory setup. It was demonstrated that the converter can be operated safely in case of a grid fault. Furthermore, it is possible to reduce the energy pulsation over the entire operating range in order to save costs in the design of the capacitors. In addition, power can constantly be fed into the faulty grid.

The new approach presented in this thesis to modelling and controlling MMCs has significant advantages over the state of the art methods including:

- An unified analytical formalism to describe MMC based systems. The similarity transform provides a decoupling of such systems independent of the specific topology.
- The energy control is derived based on the power terms. Additional topology related considerations are not necessary.
- The application of advanced optimization methods due to the control engineering notation.

-
- A reduction of the energy pulsation over the entire operating range of the MMC with function optimization. The circulating currents are determined and prepared in advance to achieve the theoretical minimum energy pulsation. An exemplary calculation shows that a reduction up to 30 % is possible.
 - Reduction of energy pulsation is achieved even during AC voltage sags.
 - Using cost functions to determine the control objective allow a simple extension. E.g. losses can be included to find the optimal control strategy for MMC based converters.
 - A straightforward and real-time capable implementation of model based control approaches for constrained grid side control is possible. Grid currents are fed into the grid along the voltage limit of the system.

Considering the fundamental results of this work with regards to the modelling and controlling of MMCs, further possibilities of research emerge. Due to the increasing complexity of power system equipment, stability considerations gain more and more importance. Questions arise on how to accurately calculate the harmonic impedance of an MMC system. No simple methods for impedance calculation are known so far when using nonlinear control concepts, like the ones implemented here for AC current control. Likewise, a general stability statement for model-based control approaches is not yet known. In the future, stability analysis will gain more importance for meshed, converter-fed grids in order to ensure a reliable supply of electrical energy to the public. In this context, the investigations are not limited to the AC side. DC systems will have a greater role to play in the supply as well. Behavior and response during grid faults will also play a central role. Using the fundamental description given in this thesis, other network control strategies can be developed and designed.

Furthermore, additional criteria can be included easily in the design of the control of MMC systems in the future. For example, by using optimization functions to formulate the control objectives, efficiency or harmonic impedance can also be taken into account during optimization. This is immediately followed by the question of whether optimization can also be calculated online as computing power continues to increase.

All this combined makes a dynamic, efficient and grid-compatible use of the MMC possible and enables it as tomorrow's backbone of the sustainable power supply.

Chapter A

Appendix

A.1 System Matrices of the MMC with Uncoupled Arm Inductors

$$\underline{A} = \frac{6}{L(L + 2L_{ac})(L + 3L_{dc})} \begin{bmatrix} a_3 & a_1 & a_1 & a_4 & a_2 & a_2 \\ a_1 & a_3 & a_1 & a_2 & a_4 & a_2 \\ a_1 & a_1 & a_3 & a_2 & a_2 & a_4 \\ a_4 & a_2 & a_2 & a_3 & a_1 & a_1 \\ a_2 & a_4 & a_2 & a_1 & a_3 & a_1 \\ a_2 & a_2 & a_4 & a_1 & a_1 & a_3 \end{bmatrix} \quad (\text{A.1a})$$

with

$$a_1 = L^2 R + 2L^2 R_{ac} - 3L^2 R_{dc} + 6LL_{dc}R - 6LL_{ac}R_{dc} + 6LL_{dc}R_{ac} + 6L_{ac}L_{dc}R \quad (\text{A.1b})$$

$$a_2 = L^2 R + 2L^2 R_{ac} + 3L^2 R_{dc} + 6LL_{ac}R_{dc} + 6LL_{dc}R_{ac} - 6L_{ac}L_{dc}R \quad (\text{A.1c})$$

$$a_3 = -5L^2 R - 4L^2 R_{ac} - 3L^2 R_{dc} - 6LL_{ac}R - 12LL_{dc}R - 6LL_{ac}R_{dc} - 12LL_{dc}R_{ac} - 12L_{ac}L_{dc}R \quad (\text{A.1d})$$

$$a_4 = L^2 R - 4L^2 R_{ac} + 3L^2 R_{dc} + 6LL_{ac}R + 6LL_{ac}R_{dc} - 12LL_{dc}R_{ac} + 12L_{ac}L_{dc}R \quad (\text{A.1e})$$

$$\underline{B} = \frac{6}{L(L + 2L_{ac})(L + 3L_{dc})} \begin{bmatrix} b_3 & b_1 & b_1 & b_4 & b_2 & b_2 \\ b_1 & b_3 & b_1 & b_2 & b_4 & b_2 \\ b_1 & b_1 & b_3 & b_2 & b_2 & b_4 \\ b_4 & b_2 & b_2 & b_3 & b_1 & b_1 \\ b_2 & b_4 & b_2 & b_1 & b_3 & b_1 \\ b_2 & b_2 & b_4 & b_1 & b_1 & b_3 \end{bmatrix} \quad (\text{A.2a})$$

with

$$b_1 = L^2 + L_{dc}L6 + 6L_{ac}L_{dc} \quad (\text{A.2b})$$

$$b_2 = L^2 - 6L_{ac}L_{dc} \quad (\text{A.2c})$$

$$b_3 = -5L^2 - 6LL_{ac} - 12LL_{dc} - 12L_{ac}L_{dc} \quad (\text{A.2d})$$

$$b_4 = L^2 + L_{ac}L6 + 12L_{ac}L_{dc} \quad (\text{A.2e})$$

$$\underline{F} = \begin{bmatrix} f_2 & f_1 & f_1 & f_3 \\ f_1 & f_2 & f_1 & f_3 \\ f_1 & f_1 & f_2 & f_3 \\ f_2 & f_1 & f_1 & -f_3 \\ f_1 & f_2 & f_1 & -f_3 \\ f_1 & f_1 & f_2 & -f_3 \end{bmatrix} \quad (\text{A.3a})$$

with

$$f_1 = \frac{1}{3L + 6L_{ac}} \quad (\text{A.3b})$$

$$f_2 = -\frac{2}{3L + 6L_{ac}} \quad (\text{A.3c})$$

$$f_3 = \frac{1}{2L + 6L_{dc}} \quad (\text{A.3d})$$

$$\underline{C} = \begin{bmatrix} 1 & 0 & 0 & 1 & 0 & 0 \\ 0 & 1 & 0 & 0 & 1 & 0 \\ 0 & 0 & 1 & 0 & 0 & 1 \end{bmatrix} \quad (\text{A.4a})$$

A.2 System Matrices of the MMC with Coupled Arm Inductors

$$\underline{A} = \frac{1}{(2L_{ac} + L_{\sigma})(12L + 6L_{\sigma})(2L + 3L_{dc} + L_{\sigma})} \begin{bmatrix} a_3 & a_1 & a_1 & a_4 & a_2 & a_2 \\ a_1 & a_3 & a_1 & a_2 & a_4 & a_2 \\ a_1 & a_1 & a_3 & a_2 & a_2 & a_4 \\ a_4 & a_2 & a_2 & a_3 & a_1 & a_1 \\ a_2 & a_4 & a_2 & a_1 & a_3 & a_1 \\ a_2 & a_2 & a_4 & a_1 & a_1 & a_3 \end{bmatrix} \quad (\text{A.5a})$$

with

$$\begin{aligned} a_1 = & 4L^2R + 8L^2R_{ac} + L_{\sigma}^2R + 2L_{\sigma}^2R_{ac} - 3L_{\sigma}^2R_{dc} + 6LL_{dc}R + 4LL_{\sigma}R \\ & - 12LL_{ac}R_{dc} + 12LL_{dc}R_{ac} + 6L_{ac}L_{dc}R + 8LL_{\sigma}R_{ac} - 6LL_{\sigma}R_{dc} \\ & + 6L_{dc}L_{\sigma}R - 6L_{ac}L_{\sigma}R_{dc} + 6L_{dc}L_{\sigma}R_{ac} \end{aligned} \quad (\text{A.5b})$$

$$\begin{aligned} a_2 = & 4L^2R + 8L^2R_{ac} + L_{\sigma}^2R + 2L_{\sigma}^2R_{ac} + 3L_{\sigma}^2R_{dc} + 6LL_{dc}R + 4LL_{\sigma}R \\ & + 12LL_{ac}R_{dc} + 12LL_{dc}R_{ac} - 6L_{ac}L_{dc}R + 8LL_{\sigma}R_{ac} + 6LL_{\sigma}R_{dc} \\ & + 6L_{ac}L_{\sigma}R_{dc} + 6L_{dc}L_{\sigma}R_{ac} \end{aligned} \quad (\text{A.5c})$$

$$\begin{aligned} a_3 = & -8L^2R - 16L^2R_{ac} - 5L_{\sigma}^2R - 4L_{\sigma}^2R_{ac} - 3L_{\sigma}^2R_{dc} \\ & - 12LL_{ac}R - 12LL_{dc}R - 14LL_{\sigma}R - 12LL_{ac}R_{dc} - 24LL_{dc}R_{ac} \\ & - 12L_{ac}L_{dc}R - 16LL_{\sigma}R_{ac} - 6L_{ac}L_{\sigma}R - 6LL_{\sigma}R_{dc} - 12L_{dc}L_{\sigma}R \\ & - 6L_{ac}L_{\sigma}R_{dc} - 12L_{dc}L_{\sigma}R_{ac} \end{aligned} \quad (\text{A.5d})$$

$$\begin{aligned} a_4 = & L_{\sigma}^2R - 16L^2R_{ac} - 8L^2R - 4L_{\sigma}^2R_{ac} + 3L_{\sigma}^2R_{dc} \\ & + 12LL_{ac}R - 12LL_{dc}R - 2LL_{\sigma}R + 12LL_{ac}R_{dc} - 24LL_{dc}R_{ac} \\ & + 12L_{ac}L_{dc}R - 16LL_{\sigma}R_{ac} + 6L_{ac}L_{\sigma}R + 6LL_{\sigma}R_{dc} + 6L_{ac}L_{\sigma}R_{dc} \\ & - 12L_{dc}L_{\sigma}R_{ac} \end{aligned} \quad (\text{A.5e})$$

$$\underline{B} = \frac{1}{6(2L + L\sigma)(2L_{ac} + L\sigma)(2L + 3L_{dc} + L\sigma)} \begin{bmatrix} b_3 & b_1 & b_1 & b_4 & b_2 & b_2 \\ b_1 & b_3 & b_1 & b_2 & b_4 & b_2 \\ b_1 & b_1 & b_3 & b_2 & b_2 & b_4 \\ b_4 & b_2 & b_2 & b_3 & b_1 & b_1 \\ b_2 & b_4 & b_2 & b_1 & b_3 & b_1 \\ b_2 & b_2 & b_4 & b_1 & b_1 & b_3 \end{bmatrix} \quad (\text{A.6a})$$

with

$$b_1 = 4L^2 + 4LL\sigma + 6L_{dc}L + L\sigma^2 + 6L_{dc}L\sigma + 6L_{ac}L_{dc} \quad (\text{A.6b})$$

$$b_2 = 4L^2 + 4LL\sigma + 6L_{dc}L + L\sigma^2 - 6L_{ac}L_{dc} \quad (\text{A.6c})$$

$$b_3 = -8L^2 - 5L\sigma^2 - 12LL_{ac} - 12LL_{dc} - 14LL\sigma - 12L_{ac}L_{dc} - 6L_{ac}L\sigma - 12L_{dc}L\sigma \quad (\text{A.6d})$$

$$b_4 = L\sigma^2 - 8L^2 + 12LL_{ac} - 12LL_{dc} - 2LL\sigma + 12L_{ac}L_{dc} + 6L_{ac}L\sigma \quad (\text{A.6e})$$

$$\underline{F} = \begin{bmatrix} f_2 & f_1 & f_1 & f_3 \\ f_1 & f_2 & f_1 & f_3 \\ f_1 & f_1 & f_2 & f_3 \\ f_2 & f_1 & f_1 & -f_3 \\ f_1 & f_2 & f_1 & -f_3 \\ f_1 & f_1 & f_2 & -f_3 \end{bmatrix} \quad (\text{A.7a})$$

with

$$f_1 = \frac{1}{6L_{ac} + 3L\sigma} \quad (\text{A.7b})$$

$$f_2 = -\frac{2}{6L_{ac} + 3L\sigma} \quad (\text{A.7c})$$

$$f_3 = \frac{1}{4L + 6L_{dc} + 2L\sigma} \quad (\text{A.7d})$$

$$\underline{C} = \begin{bmatrix} 1 & 0 & 0 & 1 & 0 & 0 \\ 0 & 1 & 0 & 0 & 1 & 0 \\ 0 & 0 & 1 & 0 & 0 & 1 \end{bmatrix} \quad (\text{A.8a})$$

$$\begin{aligned}
 \tilde{\underline{A}} &= \begin{bmatrix} 0 & 0 & 0 & 0 & 0 & 0 \\ 0 & -\frac{R+3R_{dc}}{2L+3L_{dc}+L\sigma} & 0 & 0 & 0 & 0 \\ 0 & 0 & -\frac{R}{2L+L\sigma} & 0 & 0 & 0 \\ 0 & 0 & 0 & -\frac{R}{2L+L\sigma} & 0 & 0 \\ 0 & 0 & 0 & 0 & -\frac{R+2R_{ac}}{2L_{ac}+L\sigma} & 0 \\ 0 & 0 & 0 & 0 & 0 & -\frac{R+2R_{ac}}{2L_{ac}+L\sigma} \end{bmatrix} \\
 &= \begin{bmatrix} 0 & 0 & 0 & 0 & 0 & 0 \\ 0 & R+3R_{dc} & 0 & 0 & 0 & 0 \\ 0 & 0 & R & 0 & 0 & 0 \\ 0 & 0 & 0 & R & 0 & 0 \\ 0 & 0 & 0 & 0 & R+2R_{ac} & 0 \\ 0 & 0 & 0 & 0 & 0 & R \end{bmatrix} \cdot \tilde{\underline{B}} \quad (\text{A.9a})
 \end{aligned}$$

$$\tilde{\underline{B}} = \begin{bmatrix} 0 & 0 & 0 & 0 & 0 & 0 \\ 0 & -\frac{1}{2L+3L_{dc}+L\sigma} & 0 & 0 & 0 & 0 \\ 0 & 0 & -\frac{1}{2L+L\sigma} & 0 & 0 & 0 \\ 0 & 0 & 0 & -\frac{1}{2L+L\sigma} & 0 & 0 \\ 0 & 0 & 0 & 0 & -\frac{1}{2L_{ac}+L\sigma} & 0 \\ 0 & 0 & 0 & 0 & 0 & -\frac{1}{2L_{ac}+L\sigma} \end{bmatrix} \quad (\text{A.9b})$$

$$\tilde{\underline{F}} = \begin{bmatrix} 0 & 0 & 0 & 0 \\ 0 & 0 & 0 & -\frac{\sqrt{6}}{4L+6L_{dc}+2L\sigma} \\ 0 & 0 & 0 & 0 \\ 0 & 0 & 0 & 0 \\ \frac{1}{2L_{ac}+L\sigma} & -\frac{1}{2L_{ac}+L\sigma} & 0 & 0 \\ \frac{\sqrt{3}}{6L_{ac}+3L\sigma} & -\frac{\sqrt{3}}{6L_{ac}+3L\sigma} & -\frac{2\sqrt{3}}{6L_{ac}+3L\sigma} & 0 \end{bmatrix} \quad (\text{A.9c})$$

$$\tilde{\underline{C}} = \begin{bmatrix} 2 & 0 & 0 & 0 & 0 & 0 \\ 0 & 0 & 0 & 0 & 0 & 0 \\ 0 & 0 & 0 & 0 & 0 & 0 \\ 0 & 0 & 0 & 0 & 0 & 0 \\ 0 & 0 & 0 & 0 & 2 & 0 \\ 0 & 0 & 0 & 0 & 0 & 2 \end{bmatrix} \quad (\text{A.9d})$$

A.3 Inverted System Matrices

$$\underline{B}^+ = \frac{1}{6} \begin{bmatrix} b_3 & b_1 & b_1 & b_4 & b_2 & b_2 \\ b_1 & b_3 & b_1 & b_2 & b_4 & b_2 \\ b_1 & b_1 & b_3 & b_2 & b_2 & b_4 \\ b_4 & b_2 & b_2 & b_3 & b_1 & b_1 \\ b_2 & b_4 & b_2 & b_1 & b_3 & b_1 \\ b_2 & b_2 & b_4 & b_1 & b_1 & b_3 \end{bmatrix} \quad (\text{A.10a})$$

with

$$b_1 = L + 2L_{ac} - 3L_{dc} \quad (\text{A.10b})$$

$$b_2 = L + 2L_{ac} + 3L_{dc} \quad (\text{A.10c})$$

$$b_3 = -5L - 4L_{ac} - 3L_{dc} \quad (\text{A.10d})$$

$$b_4 = L - 4L_{ac} + 3L_{dc} \quad (\text{A.10e})$$

$$\underline{B}_N = \begin{bmatrix} 1 \\ 1 \\ 1 \\ 1 \\ 1 \\ 1 \end{bmatrix} \quad (\text{A.10f})$$

$$\underline{C}^+ = \begin{bmatrix} \frac{1}{2} & 0 & 0 \\ 0 & \frac{1}{2} & 0 \\ 0 & 0 & \frac{1}{2} \\ \frac{1}{2} & 0 & 0 \\ 0 & \frac{1}{2} & 0 \\ 0 & 0 & \frac{1}{2} \end{bmatrix} \quad (\text{A.10g})$$

$$\underline{C}_N = \begin{bmatrix} \frac{-1}{\sqrt{2}} & 0 & 0 \\ 0 & \frac{-1}{\sqrt{2}} & 0 \\ 0 & 0 & \frac{-1}{\sqrt{2}} \\ \frac{1}{\sqrt{2}} & 0 & 0 \\ 0 & \frac{1}{\sqrt{2}} & 0 \\ 0 & 0 & \frac{1}{\sqrt{2}} \end{bmatrix} \quad (\text{A.10h})$$

A.4 Inverted and Transformed System Matrices

$$\underline{\tilde{B}}^+ = \begin{bmatrix} 0 & 0 & 0 & 0 & 0 & 0 \\ 0 & -L & 0 & 0 & 0 & 0 \\ 0 & 0 & -L & 0 & 0 & 0 \\ 0 & 0 & 0 & -L - 2L_{ac} & 0 & 0 \\ 0 & 0 & 0 & 0 & -L - 2L_{ac} & 0 \\ 0 & 0 & 0 & 0 & 0 & -L - 3L_{dc} \end{bmatrix} \quad (\text{A.11a})$$

$$\underline{\tilde{B}}_N = \begin{bmatrix} 1 \\ 0 \\ 0 \\ 0 \\ 0 \\ 0 \end{bmatrix} \quad (\text{A.11b})$$

$$\underline{\tilde{C}}^+ = \begin{bmatrix} \frac{1}{2} & 0 & 0 & 0 & 0 & 0 \\ 0 & 0 & 0 & 0 & 0 & 0 \\ 0 & 0 & 0 & 0 & 0 & 0 \\ 0 & 0 & 0 & \frac{1}{2} & 0 & 0 \\ 0 & 0 & 0 & 0 & \frac{1}{2} & 0 \\ 0 & 0 & 0 & 0 & 0 & 0 \end{bmatrix} \quad (\text{A.11c})$$

$$\underline{\tilde{C}}_N = \begin{bmatrix} 0 & 0 & 0 \\ 1 & 0 & 0 \\ 0 & 1 & 0 \\ 0 & 0 & 0 \\ 0 & 0 & 0 \\ 0 & 0 & 1 \end{bmatrix} \quad (\text{A.11d})$$

A.5 Calculation of Intrinsic Energy Pulsations

To calculate the intrinsic energy pulsations of the MMC the first summand of Eq. (2.27c) has to be analyzed. The equation represents a power term that occurs in each arm and cannot be influenced by any control variable.

$$\dot{\underline{x}}_{\text{int}} = \begin{bmatrix} \dot{x}_{7,i} \\ \dot{x}_{8,i} \\ \dot{x}_{9,i} \\ \dot{x}_{10,i} \\ \dot{x}_{11,i} \\ \dot{x}_{12,i} \end{bmatrix} = \underline{T}^\top \tilde{\underline{B}}^+ \left(\tilde{\underline{C}}^+ \dot{\underline{y}}_{\text{ref}} - \tilde{\underline{A}} \tilde{\underline{C}}^+ \tilde{\underline{y}}_{\text{ref}} - \tilde{\underline{F}} \underline{z} \right) \odot \underline{T}^\top \tilde{\underline{C}}^+ \tilde{\underline{y}}_{\text{ref}} \quad (\text{A.12a})$$

During stationary operation, the untransformed designated values $\underline{y}_{\text{ref}}$ are assumed to be a sinusoidal symmetrical three phase system. In transformed coordinates this results in

$$\tilde{\underline{y}}_{d,56} = \hat{y}_g \begin{bmatrix} \cos(\omega_g t + \tilde{\varphi}_g) \\ \sin(\omega_g t + \tilde{\varphi}_g) \end{bmatrix} \quad (\text{A.12b})$$

with an amplitude \hat{y}_g , the frequency ω_g and a phase shift $\tilde{\varphi}_g$. The disturbance variable \underline{z} is composed of the measured three phase voltage system and the DC side voltage. Assuming those values to be ideal results in

$$\underline{z} = \begin{bmatrix} \hat{z} \cos(\omega_g t) \\ \hat{z} \cos\left(\omega_g t - \frac{2\pi}{3}\right) \\ \hat{z} \cos\left(\omega_g t - \frac{4\pi}{3}\right) \\ z_{\text{DC}} \end{bmatrix} \quad (\text{A.12c})$$

Here \hat{z} denotes the voltage amplitude and z_{DC} is the constant DC voltage.

Inserting those assumptions into Eq. (A.12a) yields

$$\begin{aligned}
\dot{x}_{7,i} = & -\frac{1}{48\omega_g} \left(2\hat{y}_g^2 \omega_g (R + 2R_{ac}) - 2\hat{y}_g \hat{z} \omega_g \left(3\cos(\tilde{\varphi}_g) + \sqrt{3}\sin(\tilde{\varphi}_g) \right) \right. \\
& + 2\hat{y}_g z_{DC} \omega_g \left(3\cos(\omega_g t + \tilde{\varphi}_g) + \sqrt{3}\sin(\omega_g t + \tilde{\varphi}_g) \right) \\
& - 2\hat{y}_g \hat{z} \omega_g \left(3\cos(2\omega_g t + \tilde{\varphi}_g) + \sqrt{3}\sin(2\omega_g t + \tilde{\varphi}_g) \right) \\
& + \hat{y}_g^2 \left(\sqrt{3}(L + 2L_{ac}) + \omega_g (R + 2R_{ac}) \right) \cos(2\omega_g t + 2\tilde{\varphi}_g) \\
& \left. + \hat{y}_g^2 \left((-L - 2L_{ac}) + \sqrt{3}\omega_g (R + 2R_{ac}) \right) \sin(2\omega_g t + 2\tilde{\varphi}_g) \right) \quad (\text{A.12d})
\end{aligned}$$

$$\begin{aligned}
\dot{x}_{8,i} = & \frac{1}{48\omega_g} \left(2\hat{y}_g^2 \omega_g (-R - 2R_{ac}) + 2\hat{y}_g \hat{z} \omega_g \left(3\cos(\tilde{\varphi}_g) + \sqrt{3}\sin(\tilde{\varphi}_g) \right) \right. \\
& + 2\hat{y}_g z_{DC} \omega_g \left(3\cos(\omega_g t + \tilde{\varphi}_g) - \sqrt{3}\sin(\omega_g t + \tilde{\varphi}_g) \right) \\
& - 4\sqrt{3}\hat{y}_g \hat{z} \omega_g \sin(2\omega_g t + \tilde{\varphi}_g) \\
& + \hat{y}_g^2 \left(\sqrt{3}(L + 2L_{ac}) - \omega_g (R + 2R_{ac}) \right) \cos(2\omega_g t + 2\tilde{\varphi}_g) \\
& \left. + \hat{y}_g^2 \left((L + 2L_{ac}) + \sqrt{3}\omega_g (R + 2R_{ac}) \right) \sin(2\omega_g t + 2\tilde{\varphi}_g) \right) \quad (\text{A.12e})
\end{aligned}$$

$$\begin{aligned}
\dot{x}_{9,i} = & \frac{1}{24\omega_g} \left(\hat{y}_g^2 \omega_g (-R - 2R_{ac}) + \hat{y}_g \hat{z} \omega_g \left(3\cos(\tilde{\varphi}_g) + \sqrt{3}\sin(\tilde{\varphi}_g) \right) \right. \\
& + 2\sqrt{3}\hat{y}_g z_{DC} \omega_g \cos(\omega_g t + \tilde{\varphi}_g) \\
& - 2\hat{y}_g \hat{z} \omega_g \left(3\cos(2\omega_g t + \tilde{\varphi}_g) - \sqrt{3}\sin(2\omega_g t + \tilde{\varphi}_g) \right) \\
& + \hat{y}_g^2 \omega_g (R + 2R_{ac}) \cos(2\omega_g t + 2\tilde{\varphi}_g) \\
& \left. - \hat{y}_g^2 (L + 2L_{ac}) \sin(2\omega_g t + 2\tilde{\varphi}_g) \right) \quad (\text{A.12f})
\end{aligned}$$

$$\begin{aligned}
 \dot{x}_{10,i} = & \frac{1}{48 \omega_g} \left(2 \hat{y}_g^2 \omega_g (-R - 2R_{ac}) + 2 \hat{y}_g \hat{z} \omega_g \left(3 \cos(\tilde{\varphi}_g) + \sqrt{3} \sin(\tilde{\varphi}_g) \right) \right. \\
 & + 2 \hat{y}_g z_{DC} \omega_g \left(3 \cos(\omega_g t + \tilde{\varphi}_g) + \sqrt{3} \sin(\omega_g t + \tilde{\varphi}_g) \right) \\
 & + 2 \hat{y}_g \hat{z} \omega_g \left(3 \cos(2\omega_g t + \tilde{\varphi}_g) + \sqrt{3} \sin(2\omega_g t + \tilde{\varphi}_g) \right) \\
 & - \hat{y}_g^2 \left(\sqrt{3} (L + 2L_{ac}) + \omega_g (R + 2R_{ac}) \right) \cos(2\omega_g t + 2\tilde{\varphi}_g) \\
 & \left. + \hat{y}_g^2 \left((L + 2L_{ac}) + \sqrt{3} \omega_g (-R - 2R_{ac}) \right) \sin(2\omega_g t + 2\tilde{\varphi}_g) \right) \quad (\text{A.12g})
 \end{aligned}$$

$$\begin{aligned}
 \dot{x}_{11,i} = & \frac{1}{48 \omega_g} \left(2 \hat{y}_g^2 \omega_g (-R - 2R_{ac}) + 2 \hat{y}_g \hat{z} \omega_g \left(3 \cos(\tilde{\varphi}_g) + \sqrt{3} \sin(\tilde{\varphi}_g) \right) \right. \\
 & - 2 \hat{y}_g z_{DC} \omega_g \left(3 \cos(\omega_g t + \tilde{\varphi}_g) - \sqrt{3} \sin(\omega_g t + \tilde{\varphi}_g) \right) \\
 & - 4\sqrt{3} \hat{y}_g \hat{z} \omega_g \sin(2\omega_g t + \tilde{\varphi}_g) \\
 & + \hat{y}_g^2 \left(\sqrt{3} (L + 2L_{ac}) - \omega_g (R + 2R_{ac}) \right) \cos(2\omega_g t + 2\tilde{\varphi}_g) \\
 & \left. + \hat{y}_g^2 \left((L + 2L_{ac}) + \sqrt{3} \omega_g (R + 2R_{ac}) \right) \sin(2\omega_g t + 2\tilde{\varphi}_g) \right) \quad (\text{A.12h})
 \end{aligned}$$

$$\begin{aligned}
 \dot{x}_{12,i} = & -\frac{1}{24 \omega_g} \left(\hat{y}_g^2 \omega_g (R + 2R_{ac}) - \hat{y}_g \hat{z} \omega_g \left(3 \cos(\tilde{\varphi}_g) + \sqrt{3} \sin(\tilde{\varphi}_g) \right) \right. \\
 & + 2\sqrt{3} \hat{y}_g z_{DC} \omega_g \cos(\omega_g t + \tilde{\varphi}_g) \\
 & + 2 \hat{y}_g \hat{z} \omega_g \left(3 \cos(2\omega_g t + \tilde{\varphi}_g) - \sqrt{3} \sin(2\omega_g t + \tilde{\varphi}_g) \right) \\
 & - \hat{y}_g^2 \omega_g (R + 2R_{ac}) \cos(2\omega_g t + 2\tilde{\varphi}_g) \\
 & \left. + \hat{y}_g^2 (L + 2L_{ac}) \sin(2\omega_g t + 2\tilde{\varphi}_g) \right) \quad (\text{A.12i})
 \end{aligned}$$

Equations (A.12d) to (A.12i) show the expanded results. All powers consist only of terms with the frequencies 0, ω_g and $2\omega_g$. The converter arm powers only consists of these 3 frequencies.

A.6 Power Transformation Matrices

$$\underline{T}_{\text{pn}}^+ = \begin{bmatrix} \frac{1}{6} & \frac{1}{2\sqrt{6}} & \frac{1}{6\sqrt{2}} & -\frac{1}{2\sqrt{6}} & -\frac{1}{6\sqrt{2}} & -\frac{1}{4} & -\frac{1}{4\sqrt{3}} & -\frac{1}{4\sqrt{3}} & -\frac{1}{12} \\ \frac{1}{6} & -\frac{1}{2\sqrt{6}} & \frac{1}{6\sqrt{2}} & \frac{1}{2\sqrt{6}} & -\frac{1}{6\sqrt{2}} & -\frac{1}{4} & \frac{1}{4\sqrt{3}} & \frac{1}{4\sqrt{3}} & -\frac{1}{12} \\ \frac{1}{6} & 0 & -\frac{1}{3\sqrt{2}} & 0 & \frac{1}{3\sqrt{2}} & 0 & 0 & 0 & -\frac{1}{3} \\ \frac{1}{6} & -\frac{1}{2\sqrt{6}} & -\frac{1}{6\sqrt{2}} & -\frac{1}{2\sqrt{6}} & \frac{1}{6\sqrt{2}} & \frac{1}{4} & \frac{1}{4\sqrt{3}} & \frac{1}{4\sqrt{3}} & \frac{1}{12} \\ \frac{1}{6} & \frac{1}{2\sqrt{6}} & -\frac{1}{6\sqrt{2}} & \frac{1}{2\sqrt{6}} & -\frac{1}{6\sqrt{2}} & \frac{1}{4} & -\frac{1}{4\sqrt{3}} & -\frac{1}{4\sqrt{3}} & \frac{1}{12} \\ \frac{1}{6} & 0 & \frac{1}{3\sqrt{2}} & 0 & -\frac{1}{3\sqrt{2}} & 0 & 0 & 0 & -\frac{1}{3} \end{bmatrix}$$

(A.13a)

$$\underline{T}_{\text{pn}} = \begin{bmatrix} 1 & 1 & 1 & 1 & 1 & 1 \\ \frac{\sqrt{6}}{4} & -\frac{\sqrt{6}}{4} & 0 & -\frac{\sqrt{6}}{4} & \frac{\sqrt{6}}{4} & 0 \\ \frac{1}{2\sqrt{2}} & \frac{1}{2\sqrt{2}} & -\frac{1}{\sqrt{2}} & -\frac{1}{2\sqrt{2}} & -\frac{1}{2\sqrt{2}} & \frac{1}{\sqrt{2}} \\ -\frac{\sqrt{6}}{2} & \frac{\sqrt{6}}{2} & 0 & -\frac{\sqrt{6}}{2} & \frac{\sqrt{6}}{2} & 0 \\ -\frac{1}{\sqrt{2}} & -\frac{1}{\sqrt{2}} & \sqrt{2} & -\frac{1}{\sqrt{2}} & -\frac{1}{\sqrt{2}} & \sqrt{2} \\ -\frac{\sqrt{2}}{3} & -\frac{\sqrt{2}}{3} & 0 & \frac{\sqrt{2}}{3} & \frac{\sqrt{2}}{3} & 0 \\ -\frac{4}{\sqrt{3}} & \frac{4}{\sqrt{3}} & 0 & \frac{4}{\sqrt{3}} & -\frac{4}{\sqrt{3}} & 0 \\ -\frac{4}{\sqrt{3}} & \frac{4}{\sqrt{3}} & 0 & \frac{4}{\sqrt{3}} & -\frac{4}{\sqrt{3}} & 0 \\ -\frac{1}{4} & -\frac{1}{4} & -1 & \frac{1}{4} & \frac{1}{4} & 1 \end{bmatrix}$$

(A.13b)

$$\underline{T}_{\text{p}} = \begin{bmatrix} 1 & 1 & 1 & 1 & 1 & 1 \\ 0 & 0 & 0 & 0 & 0 & 0 \\ 0 & 0 & 0 & 0 & 0 & 0 \\ -\frac{\sqrt{6}}{2} & \frac{\sqrt{6}}{2} & 0 & -\frac{\sqrt{6}}{2} & \frac{\sqrt{6}}{2} & 0 \\ -\frac{1}{\sqrt{2}} & -\frac{1}{\sqrt{2}} & \sqrt{2} & -\frac{1}{\sqrt{2}} & -\frac{1}{\sqrt{2}} & \sqrt{2} \\ -1 & -1 & \frac{1}{2} & 1 & 1 & -\frac{1}{2} \\ -\frac{\sqrt{3}}{2} & \frac{\sqrt{3}}{2} & 0 & \frac{\sqrt{3}}{2} & -\frac{\sqrt{3}}{2} & 0 \\ -\frac{\sqrt{3}}{2} & \frac{\sqrt{3}}{2} & 0 & \frac{\sqrt{3}}{2} & -\frac{\sqrt{3}}{2} & 0 \\ 0 & 0 & -\frac{3}{2} & 0 & 0 & \frac{3}{2} \end{bmatrix}$$

(A.13c)

A.7 Hesse-Matrix

$$\underline{H} = \begin{bmatrix} h_1 & 0 & h_7 & 0 & h_8 & 0 \\ 0 & h_2 & 0 & h_9 & 0 & h_{10} \\ h_7 & 0 & h_3 & 0 & h_{11} & 0 \\ 0 & h_9 & 0 & h_4 & 0 & h_{12} \\ h_8 & 0 & h_{11} & 0 & h_5 & 0 \\ 0 & h_{10} & 0 & h_{12} & 0 & h_6 \end{bmatrix} \quad (\text{A.14a})$$

with

$$h_1 = \frac{2}{\tilde{L}_5^4} \left(\lambda_u \tilde{L}_5^4 + 2q_{ac} \tilde{L}_5^2 + 2q_{ac} \tilde{R}_5^4 + 2q_{ac} \tilde{R}_5^2 \right) \quad (\text{A.14b})$$

$$h_2 = \frac{2}{\tilde{L}_6^4} \left(\lambda_u \tilde{L}_6^4 + 2q_{ac} \tilde{L}_6^2 + 2q_{ac} \tilde{R}_6^4 + 2q_{ac} \tilde{R}_6^2 \right) \quad (\text{A.14c})$$

$$h_3 = \frac{2}{\tilde{L}_5^4} \left(\lambda_u \tilde{L}_5^4 + 2q_{ac} \tilde{L}_5^2 + 2q_{ac} \tilde{R}_5^2 \right) \quad (\text{A.14d})$$

$$h_4 = \frac{2}{\tilde{L}_6^4} \left(\lambda_u \tilde{L}_6^4 + 2q_{ac} \tilde{L}_6^2 + 2q_{ac} \tilde{R}_6^2 \right) \quad (\text{A.14e})$$

$$h_5 = \lambda_u + \frac{4q_{ac}}{\tilde{L}_5^2} \quad (\text{A.14f})$$

$$h_6 = \lambda_u + \frac{4q_{ac}}{\tilde{L}_6^2} \quad (\text{A.14g})$$

$$h_7 = -\frac{1}{\tilde{L}_5^4} \left(\lambda_u \tilde{L}_5^4 + 4q_{ac} \tilde{L}_5 \tilde{R}_5 - 4q_{ac} \tilde{R}_5^3 \right) \quad (\text{A.14h})$$

$$h_8 = -\frac{4q_{ac} \tilde{R}_5^2}{\tilde{L}_5^3} \quad (\text{A.14i})$$

$$h_9 = -\frac{1}{\tilde{L}_6^4} \left(\lambda_u \tilde{L}_6^4 + 4q_{ac} \tilde{L}_6 \tilde{R}_6 - 4q_{ac} \tilde{R}_6^3 \right) \quad (\text{A.14j})$$

$$h_{10} = -\frac{4q_{ac} \tilde{R}_6^2}{\tilde{L}_6^3} \quad (\text{A.14k})$$

$$h_{11} = -\lambda_u - \frac{4q_{ac} \tilde{R}_5}{\tilde{L}_5^3} \quad (\text{A.14l})$$

$$h_{12} = -\lambda_u - \frac{4q_{ac} \tilde{R}_6}{\tilde{L}_6^3} \quad (\text{A.14m})$$

A.8 Timevariant Vector $\underline{\Theta}_k$ of the Cost Function

$$\underline{\Theta}_k = \begin{bmatrix} \theta_1 \\ \theta_2 \\ \theta_3 \\ \theta_4 \\ \theta_5 \\ \theta_6 \end{bmatrix} \quad (\text{A.15a})$$

with

$$\begin{aligned}
\theta_1 = & -\lambda_u \tilde{u}_{AC,k-1,1} \\
& + \frac{2q_{ac}}{\tilde{L}_5} \left(\tilde{y}_{AC,k+1,1}^* + \frac{2\tilde{R}_5}{\tilde{L}_5} \tilde{x}_{AC,k,1} \right) \\
& - \frac{2q_{ac}\tilde{R}_5}{\tilde{L}_5^2} \left(\tilde{y}_{AC,k+2,1}^* - \frac{2\tilde{R}_5^2}{\tilde{L}_5^2} \tilde{x}_{AC,k,1} \right) \\
& - \frac{2q_{ac}\tilde{R}_5^2}{\tilde{L}_5^3} \left(\tilde{y}_{AC,k+3,1}^* + \frac{2\tilde{R}_5^3}{\tilde{L}_5^3} \tilde{x}_{AC,k,1} \right) \tag{A.15b}
\end{aligned}$$

$$\begin{aligned}
\theta_2 = & -\lambda_u \tilde{u}_{AC,k-1,2} \\
& + \frac{2q_{ac}}{\tilde{L}_6} \left(\tilde{y}_{AC,k+1,2}^* + \frac{2\tilde{R}_6}{\tilde{L}_6} \tilde{x}_{AC,k,2} \right) \\
& - \frac{2q_{ac}\tilde{R}_6}{\tilde{L}_6^2} \left(\tilde{y}_{AC,k+2,2}^* - \frac{2\tilde{R}_6^2}{\tilde{L}_6^2} \tilde{x}_{AC,k,2} \right) \\
& - \frac{2q_{ac}\tilde{R}_6^2}{\tilde{L}_6^3} \left(\tilde{y}_{AC,k+3,2}^* + \frac{2\tilde{R}_6^3}{\tilde{L}_6^3} \tilde{x}_{AC,k,2} \right) \tag{A.15c}
\end{aligned}$$

$$\begin{aligned}
\theta_3 = & -\frac{2q_{ac}}{\tilde{L}_5^5} \left(-\tilde{L}_5^4 \tilde{y}_{AC,k+2,1}^* + \tilde{L}_5^3 \tilde{R}_5 \tilde{y}_{AC,k+3,1}^* \right. \\
& \left. + 2\tilde{x}_{AC,k,1} \left(\tilde{L}_5^2 \tilde{R}_5^2 + \tilde{R}_5^4 \right) \right) \tag{A.15d}
\end{aligned}$$

$$\begin{aligned}
\theta_4 = & -\frac{2q_{ac}}{\tilde{L}_6^5} \left(-\tilde{L}_6^4 \tilde{y}_{AC,k+2,2}^* + \tilde{L}_6^3 \tilde{R}_6 \tilde{y}_{AC,k+3,2}^* \right. \\
& \left. + 2\tilde{x}_{AC,k,2} \left(\tilde{L}_6^2 \tilde{R}_6^2 + \tilde{R}_6^4 \right) \right) \tag{A.15e}
\end{aligned}$$

$$\theta_5 = \frac{2q_{ac}}{\tilde{L}_5^4} \left(\tilde{L}_5^3 \tilde{y}_{AC,k+3,1}^* + 2\tilde{R}_5^3 \tilde{x}_{AC,k,1} \right) \tag{A.15f}$$

$$\theta_6 = \frac{2q_{ac}}{\tilde{L}_6^4} \left(\tilde{L}_6^3 \tilde{y}_{AC,k+3,2}^* + 2\tilde{R}_6^3 \tilde{x}_{AC,k,2} \right) \tag{A.15g}$$

A.9 Timevariant Scalar θ_k of the Cost Function

$$\begin{aligned}
\theta_k = & \lambda_u (\tilde{u}_{AC,k-1,1}^2 + \tilde{u}_{AC,k-1,2}^2) \\
& + q_{ac} \left(\tilde{y}_{AC,k+1,1}^* + \frac{2\tilde{R}_5}{\tilde{L}_5} \tilde{x}_{AC,k,1} \right)^2 + q_{ac} \left(\tilde{y}_{AC,k+1,2}^* + \frac{2\tilde{R}_6}{\tilde{L}_6} \tilde{x}_{AC,k,2} \right)^2 \\
& + q_{ac} \left(\tilde{y}_{AC,k+2,1}^* - \frac{2\tilde{R}_5^2}{\tilde{L}_5^2} \tilde{x}_{AC,k,1} \right)^2 + q_{ac} \left(\tilde{y}_{AC,k+2,2}^* - \frac{2\tilde{R}_6^2}{\tilde{L}_6^2} \tilde{x}_{AC,k,2} \right)^2 \\
& + q_{ac} \left(\tilde{y}_{AC,k+3,1}^* + \frac{2\tilde{R}_5^3}{\tilde{L}_5^3} \tilde{x}_{AC,k,1} \right)^2 + q_{ac} \left(\tilde{y}_{AC,k+2,2}^* + \frac{2\tilde{R}_6^3}{\tilde{L}_6^3} \tilde{x}_{AC,k,2} \right)^2
\end{aligned} \tag{A.16}$$

A.10 AC Current Trajectory in XY Representation

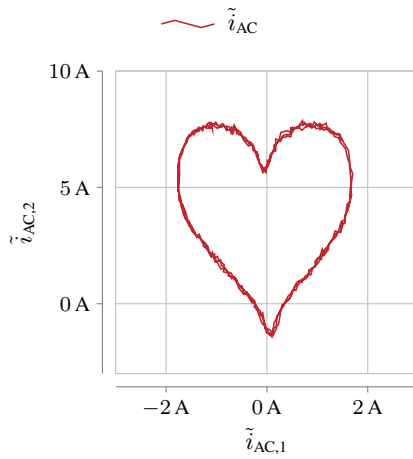


Figure A.1: XY representation of the measured, transformed AC currents from Sec. 6.1.1.

List of Symbols

Abbreviations

ADC	analog digital converter
DSP	digital signal processor
DSRF	double synchronous reference frame
EPSR	single PCB converter system
ETI	Elektrotechnisches Institut
FACTS	flexible AC transmission systems
FiOrdOs	First-Order Methods
FLL	frequency locked loop
FOC	fibre optic cable
FPGA	field-programmable gate array
HMK	high power modulator board
HVDC	high voltage direct current
HVDC	high voltage direct current
HVRT	high voltage ride through
I/O	input/output
IGBT	insulated gate bipolar transistor
LVRT	low voltage ride through
M3C	modular multilevel matrix converter
MIMO	multiple input multiple output
MMC	modular multilevel converter
MMSST	Modular Multilevel Solid State Transformer
MOSFET	metal-oxide-semiconductor field-effect transistor

MPC	model-based predictive control
PCB	printed circuit board
PCC	point of common coupling
PI	proportional-integral
PLL	phase locked loop
PR	proportional-resonant
PSO	particle swarm optimization
PWM	pulse width modulation
QP	quadratic programming
RMS	root mean square
SISO	single input single output
SPMMC	Square-wave Powered Modular Multilevel Converter
STAT-COM	static synchronous compensator
UART	universal asynchronous receiver transmitter

Formulars

Physical Variables

P	active power
Q	reactive power
S	apparent power
C_{cell}	cell capacitance
I_{dc}	DC current
i_{n}	negative dc current
i_{p}	positive dc current
\underline{i}	current vector
i	general current identifier
L_{ac}	ac side inductance
L_{dc}	dc side inductance
\underline{L}	inductance matrix
L_{σ}	stray inductance
L	arm inductance
ω	angular frequency

\underline{p}	power vecotr
p	general power identifier
R_{ac}	ac side resistance
R_{dc}	dc side resistance
\underline{R}	resistance matrix
R	parasitic arm resistance
v_C	cell capacitor voltage
v_{cell}	cell voltage
V_{dc}	DC voltage
V_0	zero sequence voltage
\underline{v}	voltage vector
v	general voltage identifier
\underline{w}	energy vector

Mathematical Expressions

\underline{A}	system matrix
\underline{B}	input matrix
\underline{C}	output matrix
$\frac{d}{dt}$	time derivative of a variable
\underline{F}	disturbance matrix
$\underline{\Gamma}$	predicted system matrix
\underline{G}	transfer function
\underline{I}	identity matrix
J	cost function for optimization
T_A	sampling time of the time-discrete system
$\underline{\Theta}$	time variant vector of the cost function
\underline{T}_{pn}	transformation matrix for powers with zero sequence voltage
\underline{T}_p	transformation matrix for powers
\underline{T}	transformation matrix
$\underline{\Xi}$	predicted tracking error
$\underline{\Upsilon}$	predicted input matrix
a	damping factor
k	gain factor
\underline{H}	Hessian

List of Symbols

λ	eigenvalue
\underline{G}	boundary matrix
\underline{g}	boundary vector
λ_u	weighting factor of the control effort
m	feedforward factor
θ	time variant scalar of the cost function
\sim	indicates a variable in transformed coordinates
\top	transpose of a matrix or a vector
u	input variable
\underline{E}	weighting matrix on the predicted output values
\underline{Q}	weighting matrix of the tracking error
\underline{S}	weighting matrix of the predicted output values
q	weighting factor of the tracking error
ξ	tracking error
x	state space variable
y	output variable
z	disturbance variable

List of Figures

1.1	Schematic representation of the MMC, that is the basis for the analysis and control design throughout the thesis at hand.	2
1.2	Visualization of different state of the art modelling approaches compared to the formalism presented in this thesis	4
1.3	Classification of different approaches to the reduction of energy pulsation.	7
1.4	Outline of this thesis	12
2.1	Circuit diagram of the MMC	17
2.2	The two most common cell topologies and the series connection in the averaging model.	18
2.3	Decoupled representation of the MMC	29
3.1	Normalized energy pulsations in the ideal system when the AC power is equal to the DC power. This also corresponds to an optimization with regard to the minimum RMS arm current for stable operation.	46
3.2	Normalized energy pulsations in the ideal system, with analytically calculated power feed forward for compensation of the 2nd harmonic.	48
3.3	Normalized energy pulsation with consideration of inductive voltage drops.	50
3.4	Normalized energy pulsations with PSO optimized coefficients for the circulating currents at $\varphi = 0^\circ$	53
3.5	Normalized energy pulsation in the ideal system, with optimized trajectories of the circulating currents.	56
3.6	Comparison of the current trajectories in transformed coordinates.	58
3.7	Comparison of the trajectories of the arm currents	60

3.8	Comparison of the maximum energy pulsation of the different compensation methods over the entire phase angle φ of the AC side. The values are normalized to the maximum amplitude, without compensation at $\varphi = 0^\circ$	62
3.9	Influence of the zero sequence voltage \tilde{v}_0 on the maximum energy deviation and arm currents for function optimization.	65
3.10	Comparison of voltage ripples and arm currents in an HVDC system using function optimization	68
4.1	Overall control scheme of the MMC system	72
4.2	Control engineering schematic of the energy controllers	80
4.3	closed energy control loop	81
4.4	closed control loop of the DC current \tilde{x}_2	84
4.5	Time discrete current state controller with consideration of a computation dead time for \tilde{x}_2	85
4.6	closed control loop of the internal currents \tilde{x}_3 and \tilde{x}_4	88
4.7	linear limitation of the control output space vector	90
4.8	Transformed equivalent circuit diagram of the controlled system on the AC side (see Fig. 2.3 (d))	93
4.9	Phase-locked loop to determine the grid angle, the positive sequence and the negative sequence of the voltage.	107
4.10	Settling process of the PLL at maximum phase difference at the beginning and response to occurring grid faults and disturbances.	111
4.11	Simulated line voltages and corresponding transformed voltages during the grid fault.	114
4.12	Reference and disturbance variable of the MPC with limits and influence of the PLL. At $t_1 = 50$ ms the current setpoint is applied. At $t_2 = 100$ ms the grid fault from Sec. 4.3.4 occurs. From $t_3 = 150$ ms the power delivered is constantly to the grid.	115
4.13	Comparison of the energy pulsations ΔW with a setpoint step and in case of a mains error without and with compensation currents in relation to the energy pulsation in the stationary case without compensation.	119
5.1	Overview of the power unit of the laboratory setup	122
5.2	Overview of the stand-alone grid to create reproducible grid conditions.	123
5.3	The latest version of the utilized EPSR	124

5.4	Complete laboratory setup with power section and signal processing of the laboratory prototype.	126
5.5	Overview of the signal processing unit of the MMC.	127
5.6	Modulation of a full bridge cell with MOSFET switches for two exemplary output levels.	129
5.7	Main FPGA of the laboratory setup with mountable ADC for data acquisition.	130
5.8	Exemplary timing diagram of the system with a ratio of the control period T_c and the modulation period T_M of 2.	134
6.1	Quasi-stationary operation at the 400 V/50 Hz-grid with $P = 8.5$ kW. The measured values are sampled with the control period $T_C = 125$ μ s.	136
6.2	Oscillographed arm voltages of the 1st and 4th arm using differential probes and an increased time resolution.	138
6.3	transformed, constrained output variables and currents during a load step	139
6.4	Non-sinusoidal current trajectories	140
6.5	transformed output variable and current of the DC side during the AC load step	141
6.6	arm energies and transformed currents for balancing and the energies during the load step	143
6.7	Comparison of the measured arm energies and arm currents without compensation, with compensation of the 2nd harmonic and optimal current trajectories.	144
6.8	Theoretical and measured energy pulsation of the different methods for reduction of energy pulsation over the whole range of phase angle values	146
6.9	Directly measured and derived variables during the grid fault at constant AC current.	150
6.10	Directly measured and derived variables during grid fault	152
6.11	Comparison of the maximum energy pulsation in case of grid fault with (ΔW_{red}) and without compensation (ΔW) currents. . .	154
A.1	XY representation of the measured, transformed AC currents from Sec. 6.1.1.	177

List of Tables

2.1	Mapping of the physical quantities to control engineering quantities.	23
3.1	Normalized quantities for the comparison of different control strategies	45
3.2	Comparison of the different compensation methods depending on RMS arm current and energy deviation reduction at $\varphi = 0^\circ$.	61
3.3	Technical specifications of an exemplary HVDC converter . . .	66
4.1	transformed quantities and their physical meaning	74
4.2	Circuit parameters for the simulation of the MPC and the PLL. .	110
5.1	Technical specifications of the MMC	125

Bibliography

List of Publications

- [E1] D. Braeckle, P. Himmelmann, L. Gröll, V. Hagenmeyer, and M. Hiller, “Energy pulsation reduction in modular multilevel converters using optimized current trajectories”, *IEEE Open Journal of Power Electronics*, vol. 2, pp. 171–186, 2021. doi: 10.1109/OJPEL.2021.3065115.
- [E2] D. Braeckle, P. Himmelmann, M. Hiller, and S. Nielebock, “Comparison of Modular Multilevel Topologies for AC to AC Applications”, in *2018 9th IEEE International Symposium on Power Electronics for Distributed Generation Systems (PEDG)*, IEEE, 2018, pp. 1–7. doi: 10.1109/PEDG.2018.8447711.
- [E3] D. Braeckle, P. Himmelmann, S. Mersche, L. Stefanski, and M. Hiller, “Highly Dynamic AC Current Control for Modular Multilevel Converters”, in *2021 23th European Conference on Power Electronics and Applications (EPE'21 ECCE Europe)*, 2021.
- [E4] D. Braeckle, B. Bohnet, M. Schnarrenberger, P. Himmelmann, M. Hiller, “A New control Approach for Modular Multilevel Converter Under Unbalanced Load Conditions”, in *The 9th IET International Conference on Power Electronics, Machines and Drives (PEMD 2018, Liverpool, UK)*.
- [E5] D. Braeckle, S. Mersche, M. Schnarrenberger, P. Himmelmann, and M. Hiller, “Modular Multilevel Converters as Active Filters to Mitigate Low Frequency Current Harmonics in Converter Fed Grid Applications”, Karlsruhe, 2018. doi: 10.5445/IR/1000084385.

- [E6] D. Braeckle, F. Kammerer, M. Schnarrenberger, M. Hiller, and M. Braun, “A Modular Multilevel Matrix Converter for High Speed Drive Applications”, in *PCIM Europe 2016; International Exhibition and Conference for Power Electronics, Intelligent Motion, Renewable Energy and Energy Management*, 2016, pp. 1–8.
- [E7] D. Braeckle, P. Himmelmann, M. Schnarrenberger, and M. Hiller, “Control strategy for modular multilevel matrix converters at high output frequencies”, in *2017 IEEE Energy Conversion Congress and Exposition (ECCE)*, IEEE, 2017, pp. 2137–2143. DOI: 10.1109/ECCE.2017.8096422.
- [E8] L. Stefanski, D. Bernet, D. Braeckle, A. Liske, B. Schmitz-Rode, R. Schwendemann, and M. Hiller, “A novel high dynamic six phase 120 kW Power Hardware in the Loop Emulation Test Bench for emulating of AC/DC Grids and Electrical Machines”, in *2021 23th European Conference on Power Electronics and Applications (EPE'21 ECCE Europe)*, 2021.
- [E9] M. Schnarrenberger, L. Stefanski, C. Rollbühler, D. Braeckle, and M. Braun, “A 50 kW power hardware-in-the-loop test bench for permanent magnet synchronous machines based on a modular multilevel converter”, 2018.
- [E10] M. Schnarrenberger, F. Kammerer, D. Braeckle, and M. Braun, “Cell Design of a Square-Wave Powered 1AC-3AC Modular Multilevel Converter Low Voltage Prototype”, in *2016 18th European Conference on Power Electronics and Applications (EPE'16 ECCE Europe)*, Messe Karlsruhe, 2016.
- [E11] F. Kammerer, D. Braeckle, M. Gommeringer, M. Schnarrenberger, and M. Braun, “Operating Performance of the Modular Multilevel Matrix Converter in Drive Applications”, in *PCIM Europe 2015 : International Exhibition and Conference for Power Electronics, Intelligent Motion, Renewable Energy and Energy Management*, 2015, pp. 549–556.

Supervised Student Thesis

- [S1] Calvin Laeske, “Untersuchung von Netzkupplungsstrategien”, bachelor thesis, Karlsruhe Institute of Technology (KIT), 2020.
- [S2] Joshua Schwarzmüller, “Design einer Netzkupplungseinheit für ein Inselnetz”, bachelor thesis, Karlsruhe Institute of Technology (KIT), 2017.
- [S3] Stefan Mersche, “Aufbau eines Inselnetzes auf Basis Modularer Multilevel Umrichter”, master thesis, Karlsruhe Institute of Technology (KIT), 2016.
- [S4] David Nass, “Erweiterung eines Modularen Multilevel Matrix Umrichters zum Betrieb als Modularer Multilevel Umrichter mit Vollbrücken”, master thesis, Karlsruhe Institute of Technology (KIT), 2016.
- [S5] Amine Ben Waddey, “Simulation von Modularen Multilevel Umrichtern im Netz-Fehlerfall und im Inselnetzbetrieb”, master thesis, Karlsruhe Institute of Technology (KIT), 2016.
- [S6] Patrick Gorski, “Aufbau von Vollbrückenmodulen zur Integration von Energiequellen und Energiesenken in Umrichter”, master thesis, Karlsruhe Institute of Technology (KIT), 2020.
- [S7] Fabian Zindorf, “Hochdynamische Stromregelung eines Modularen Multilevel Umrichters”, master thesis, Karlsruhe Institute of Technology (KIT), 2019.
- [S8] Patrick Gorski, “Konzeption und Realisierung eines Hörsaalversuchs zur selbstgeführten Drehstrombrücke”, bachelor thesis, Karlsruhe Institute of Technology (KIT), 2017.
- [S9] Felix Fürstenberger, “Simulation, Implementierung und Inbetriebnahme der Regelung für einen aktiven PV-Strangsammler”, master thesis, Karlsruhe Institute of Technology (KIT), 2016.
- [S10] Iteb Guenichi, “Neuentwicklung und Inbetriebnahme einer FPGA-basierten Inkrementalgeberauswertung”, master thesis, Karlsruhe Institute of Technology (KIT), 2015.

References

- [1] *Statistisches Jahrbuch Deutschland 2018*, 1., Auflage. Wiesbaden: Statistisches Bundesamt, 2018.
- [2] Y. Chen, R. Hesse, D. Turschner, and H. Beck, “Improving the grid power quality using virtual synchronous machines”, in *2011 International Conference on Power Engineering, Energy and Electrical Drives*, 2011, pp. 1–6. doi: 10.1109/PowerEng.2011.6036498.
- [3] N. Flourentzou, V. G. Agelidis, and G. D. Demetriades, “VSC-Based HVDC Power Transmission Systems: An Overview”, *IEEE Transactions on Power Electronics*, vol. 24, no. 3, pp. 592–602, 2009. doi: 10.1109/TPEL.2008.2008441.
- [4] J. M. Guerrero, M. Chandorkar, T.-L. Lee, and P. C. Loh, “Advanced Control Architectures for Intelligent Microgrids—Part I: Decentralized and Hierarchical Control”, *IEEE Transactions on Industrial Electronics*, vol. 60, no. 4, pp. 1254–1262, 2013. doi: 10.1109/TIE.2012.2194969.
- [5] M. Liserre, F. Blaabjerg, and S. Hansen, “Design and Control of an LCL-Filter-Based Three-Phase Active Rectifier”, *IEEE Transactions on Industry Applications*, vol. 41, no. 5, pp. 1281–1291, 2005. doi: 10.1109/TIA.2005.853373.
- [6] D. E. Olivares, A. Mehrizi-Sani, A. H. Etemadi, *et al.*, “Trends in Microgrid Control”, *IEEE Transactions on Smart Grid*, vol. 5, no. 4, pp. 1905–1919, 2014. doi: 10.1109/TSG.2013.2295514.
- [7] P. Rodriguez, J. Pou, J. Bergas, J. I. Candela, R. P. Burgos, and D. Boroyevich, “Decoupled Double Synchronous Reference Frame PLL for Power Converters Control”, *IEEE Transactions on Power Electronics*, vol. 22, no. 2, pp. 584–592, 2007. doi: 10.1109/TPEL.2006.890000.
- [8] J. Sun, “Impedance-Based Stability Criterion for Grid-Connected Inverters”, *IEEE Transactions on Power Electronics*, vol. 26, no. 11, pp. 3075–3078, 2011. doi: 10.1109/TPEL.2011.2136439.
- [9] R. Marquardt, A. Lesnicar, and J. Hildinger, “Modulares Stromrichterkonzept für Netzkupplungsanwendungen bei hohen Spannungen”, in *Bauelemente der Leistungselektronik und ihre Anwendungen*, ser. ETG-Fachbericht, vol. 88, Berlin: VDE-Verl., 2002, pp. 155–161.

-
- [10] A. Lesnicar and R. Marquardt, “An innovative modular multilevel converter topology suitable for a wide power range”, in *2003 IEEE Bologna PowerTech*, Piscataway, NJ: IEEE, 2003, pp. 272–277. doi: 10.1109/PTC.2003.1304403.
- [11] Y. Pipelzadeh, B. Chaudhuri, T. Green, Y. Wu, H. Pang, and J. Cao, “Modelling and dynamic operation of the zhoushan dc grid: Worlds first five-terminal vsc-hvdc project”, Oct. 2015. doi: 10.13140/RG.2.1.3449.3202.
- [12] M. A. Perez, S. Bernet, J. Rodriguez, S. Kouro, and R. Lizana, “Circuit Topologies, Modeling, Control Schemes, and Applications of Modular Multilevel Converters”, *IEEE Transactions on Power Electronics*, vol. 30, no. 1, pp. 4–17, 2015. doi: 10.1109/TPEL.2014.2310127.
- [13] S. Milovanovic, *MMC-based conversion for MVDC applications*, 2020. doi: 10.5075/EPFL-THESIS-8613.
- [14] S. Allebrod, R. Hamerski, and R. Marquardt, “New transformerless, scalable Modular Multilevel Converters for HVDC-transmission”, in *2008 IEEE Power Electronics Specialists Conference*, Piscataway, N.J.: IEEE, 2008, pp. 174–179. doi: 10.1109/PESC.2008.4591920.
- [15] M. Pereira, D. Retzmann, J. Lottes, M. Wiesinger, and G. Wong, “SVC PLUS: An MMC STATCOM for network and grid access applications”, in *2011 IEEE Trondheim PowerTech*, I. Staff, Ed., [Place of publication not identified]: IEEE, 2011, pp. 1–5. doi: 10.1109/PTC.2011.6019245.
- [16] “Proposed terms and definitions for flexible AC transmission system (FACTS)”, *IEEE Transactions on Power Delivery*, vol. 12, no. 4, pp. 1848–1853, 1997. doi: 10.1109/61.634216.
- [17] T. Nowak, M. Suriyah, and T. Leibfried, “Power tracking in a MMC-multi-terminal HVDC system with centralized and decentralized MPC using a black box modeling approach”, in *2017 52nd International Universities Power Engineering Conference (UPEC)*, I. U. P. E. Conference, Ed., [Piscataway, NJ]: IEEE, 2017, pp. 1–4. doi: 10.1109/UPEC.2017.8232017.
- [18] X. Jiang and M. M. Bakran, “Fault Current Behavior of MMC With the First Blocking Method”, *IEEE Transactions on Power Electronics*, vol. 34, no. 12, pp. 11 616–11 628, 2019. doi: 10.1109/TPEL.2019.2904549.

- [19] R. Sander, M. Suriyah, and T. Leibfried, “Characterization of a Counter-current Injection-Based HVDC Circuit Breaker”, *IEEE Transactions on Power Electronics*, vol. 33, no. 4, pp. 2948–2956, 2018. doi: 10.1109/TPEL.2017.2709785.
- [20] A. Schon and M.-M. Bakran, “Comparison of modular multilevel converter based HV DC-DC-converters”, in *2016 18th European Conference on Power Electronics and Applications (EPE'16 ECCE Europe)*, IEEE, 2016, pp. 1–10. doi: 10.1109/EPE.2016.7695259.
- [21] A. F. Christe, *Galvanically Isolated Modular Converter*, 2018. doi: 10.5075/EPFL-THESIS-8530.
- [22] P. Himmelmann and M. Hiller, “Solid-state transformer based on modular multilevel converters”, *The Journal of Engineering*, vol. 2019, no. 17, pp. 4490–4494, 2019. doi: 10.1049/joe.2018.8023.
- [23] J. Kolb, *Optimale Betriebsführung des Modularen Multilevel-Umrichters als Antriebsumrichter für Drehstrommaschinen*, 2014.
- [24] M. Hiller, D. Krug, R. Sommer, and S. Rohner, “A new highly modular medium voltage converter topology for industrial drive applications”, in *2009 13th European Conference on Power Electronics and Applications*, 2009, pp. 1–10.
- [25] P. Himmelmann, M. Hiller, D. Krug, and M. Beuermann, “A new modular multilevel converter for medium voltage high power oil & gas motor drive applications”, in *2016 18th European Conference on Power Electronics and Applications (EPE'16 ECCE Europe)*, IEEE, 2016, pp. 1–11. doi: 10.1109/EPE.2016.7695692.
- [26] H. Fehr and A. Gensior, “Model-Based Circulating Current References for MMC Cell Voltage Ripple Reduction and Loss-Equivalent Arm Current Assessment”, in *2019 21st European Conference*, 2019, pp. 1–10.
- [27] F. Kammerer, *Systemanalyse und Regelung des Modularen Multilevel Matrix Umrichters als Antriebsumrichter*, 2016.
- [28] A. Christe and D. Dujic, “Modular Multilevel Converter Control Methods Performance Benchmark for Medium Voltage Applications”, *IEEE Transactions on Power Electronics*, vol. 34, no. 5, pp. 4967–4980, 2019.

-
- [29] H. Fehr and A. Gensior, “Improved Energy Balancing of Grid-Side Modular Multilevel Converters by Optimized Feedforward Circulating Currents and Common-Mode Voltage”, *IEEE Transactions on Power Electronics*, vol. 33, no. 12, pp. 10 903–10 913, 2018. doi: 10 . 1109/TPEL . 2018 . 2805103.
- [30] M. Schnarrenberger, “Der Modulare Multilevel-Umrichter als dreiphasige Spannungsquelle”, PhD thesis, Karlsruhe Institute of Technology (KIT), 2019. doi: 10 . 5445/IR/1000096179.
- [31] P. Himmelmann and M. Hiller, “A Generalized Approach to the Analysis and Control of Modular Multilevel Converters”, in *PCIM Europe 2017; International Exhibition and Conference for Power Electronics, Intelligent Motion, Renewable Energy and Energy Management*, 2017, pp. 1–8.
- [32] L. Baruschka and A. Mertens, “A new 3-phase AC/AC modular multilevel converter with six branches in hexagonal configuration”, in *IEEE Energy Conversion Congress and Exposition (ECCE), 2011*, Piscataway, NJ: IEEE, 2011, pp. 4005–4012. doi: 10 . 1109/ECCE . 2011 . 6064314.
- [33] L. Angquist, A. Antonopoulos, D. Siemaszko, K. Ilves, M. Vasiladiotis, and H.-P. Nee, “Open-Loop Control of Modular Multilevel Converters Using Estimation of Stored Energy”, *IEEE Transactions on Industry Applications*, vol. 47, no. 6, pp. 2516–2524, 2011. doi: 10 . 1109/TIA . 2011 . 2168593.
- [34] S. Debnath, J. Qin, B. Bahrani, M. Saadedifard, and P. Barbosa, “Operation, Control, and Applications of the Modular Multilevel Converter: A Review”, *IEEE Transactions on Power Electronics*, vol. 30, no. 1, pp. 37–53, 2015. doi: 10 . 1109/TPEL . 2014 . 2309937.
- [35] A. Rasic, U. Krebs, H. Leu, and G. Herold, “Optimization of the modular multilevel converters performance using the second harmonic of the module current”, in *2009 13th European Conference on Power Electronics and Applications*, 2009, pp. 1–10.
- [36] M. Hagiwara and H. Akagi, “Control and Experiment of Pulsewidth-Modulated Modular Multilevel Converters”, *IEEE Transactions on Power Electronics*, vol. 24, no. 7, pp. 1737–1746, 2009. doi: 10 . 1109/TPEL . 2009 . 2014236.

- [37] H. Saad, J. Peralta, S. Denetière, *et al.*, “Dynamic Averaged and Simplified Models for MMC-Based HVDC Transmission Systems”, *IEEE Transactions on Power Delivery*, vol. 28, no. 3, pp. 1723–1730, 2013.
- [38] J. Peralta, H. Saad, S. Denetière, J. Mahseredjian, and S. Nguefeu, “Detailed and Averaged Models for a 401-Level MMC–HVDC System”, *IEEE Transactions on Power Delivery*, vol. 27, no. 3, pp. 1501–1508, 2012. DOI: 10.1109/TPWRD.2012.2188911.
- [39] A. Zama, S. Bacha, A. Benchaib, D. Frey, and S. Silvant, “Comparison and assessment of implementation techniques for dynamics MMC type models”, in *2019 21st European Conference on Power Electronics and Applications (EPE '19 ECCE Europe)*, [Piscataway, New Jersey]: IEEE, 2019, P.1–P.10. DOI: 10.23919/EPE.2019.8914946.
- [40] S. Rohner, J. Weber, and S. Bernet, “Continuous model of Modular Multilevel Converter with experimental verification”, in *IEEE Energy Conversion Congress and Exposition (ECCE), 2011*, Piscataway, NJ: IEEE, 2011, pp. 4021–4028. DOI: 10.1109/ECCE.2011.6064316.
- [41] H. Barnklau, A. Gensior, and S. Bernet, “Derivation of an equivalent submodule per arm for modular multilevel converters”, in *15th International Power Electronics and Motion Control Conference (EPE/PEMC), 2012*, Piscataway, NJ: IEEE, 2012, LS2a.2-1-LS2a.2-5. DOI: 10.1109/EPEPEMC.2012.6397407.
- [42] J. Kolb, F. Kammerer, and M. Braun, “Straight forward vector control of the Modular Multilevel Converter for feeding three-phase machines over their complete frequency range”, in *IECON 2011*, Piscataway, NJ: IEEE, 2011, pp. 1596–1601. DOI: 10.1109/IECON.2011.6119545.
- [43] M. Hagiwara and H. Akagi, “PWM control and experiment of modular multilevel converters”, in *2008 IEEE Power Electronics Specialists Conference*, Piscataway, N.J.: IEEE, 2008, pp. 154–161. DOI: 10.1109/PESC.2008.4591917.
- [44] A. Dekka, B. Wu, R. L. Fuentes, M. Perez, and N. R. Zargari, “Evolution of Topologies, Modeling, Control Schemes, and Applications of Modular Multilevel Converters”, *IEEE Journal of Emerging and Selected Topics in Power Electronics*, vol. 5, no. 4, pp. 1631–1656, 2017. DOI: 10.1109/JESTPE.2017.2742938.

- [45] W. Kawamura, K.-L. Chen, M. Hagiwara, and H. Akagi, “A Low-Speed, High-Torque Motor Drive Using a Modular Multilevel Cascade Converter Based on Triple-Star Bridge Cells (MMCC-TSBC)”, *IEEE Transactions on Industry Applications*, vol. 51, no. 5, pp. 3965–3974, 2015. doi: 10.1109/TIA.2015.2416130.
- [46] L. Baruschka, *Untersuchung des modularen Direktumrichters Hexverter*, 2013. doi: 10.15488/8010.
- [47] D. Karwatzki, L. Baruschka, M. Dokus, J. Kucka, and A. Mertens, “Branch energy balancing with a generalised control concept for modular multilevel topologies — Using the example of the modular multilevel converter”, in *2016 18th European Conference on Power Electronics and Applications (EPE'16 ECCE Europe)*, IEEE, 2016, pp. 1–10. doi: 10.1109/EPE.2016.7695619.
- [48] W. C. Dueterhoeft, M. W. Schulz, and E. Clarke, “Determination of Instantaneous Currents and Voltages by Means of Alpha, Beta, and Zero Components”, *Transactions of the American Institute of Electrical Engineers*, vol. 70, no. 2, pp. 1248–1255, 1951. doi: 10.1109/T-AIEE.1951.5060554.
- [49] H. Späth, *Leistungsbegriffe für Ein- und Mehrphasensysteme nach DIN 40110-1 und DIN 40110-2*, 2. Aufl., ser. VDE-Schriftenreihe 103. Berlin: VDE-Verl., 2012.
- [50] Gustav Robert Kirchhoff, “Ueber den Durchgang eines elektrischen Stromes durch eine Ebene, insbesondere durch eine kreisförmige”, *Annalen der Physik und Chemie*, vol. 140, no. 4, pp. 497–514, 1845. doi: 10.1002/andp.18451400402.
- [51] G. Bergna-Diaz, J. Freytes, X. Guillaud, S. D’Arco, and J. A. Suul, “Generalized Voltage-Based State-Space Modeling of Modular Multilevel Converters With Constant Equilibrium in Steady State”, *IEEE Journal of Emerging and Selected Topics in Power Electronics*, vol. 6, no. 2, pp. 707–725, 2018. doi: 10.1109/JESTPE.2018.2793159.
- [52] S. Liu, J. Jiang, and Y. Wan, “Generalised analytical methods and current-energy control design for modular multilevel cascade converter”, *IET Power Electronics*, vol. 6, no. 3, pp. 495–504, 2013. doi: 10.1049/iet-pe1.2012.0494.

- [53] J. Kolb, F. Kammerer, and M. Braun, “Dimensioning and design of a Modular Multilevel Converter for drive applications”, in *15th International Power Electronics and Motion Control Conference (EPE/PEMC), 2012*, Piscataway, NJ: IEEE, 2012, LS1a-1.1-1-LS1a-1.1-8. doi: 10.1109/EPEPEMC.2012.6397380.
- [54] K. Sharifabadi, H. P. Nee, L. Harnefors, R. Teodorescu, and S. Norga, *Design, control and application of modular multilevel converters for HVDC transmission systems*. Chichester, West Sussex, United Kingdom: John Wiley & Sons Inc, 2016.
- [55] G. T. Son, H.-J. Lee, T. S. Nam, Y.-H. Chung, U.-H. Lee, S.-T. Baek, K. Hur, and J.-W. Park, “Design and Control of a Modular Multilevel HVDC Converter With Redundant Power Modules for Noninterruptible Energy Transfer”, *IEEE Transactions on Power Delivery*, vol. 27, no. 3, pp. 1611–1619, 2012. doi: 10.1109/TPWRD.2012.2190530.
- [56] C. Zhao, Y. Li, Z. Li, P. Wang, X. Ma, and Y. Luo, “Optimized Design of Full-Bridge Modular Multilevel Converter With Low Energy Storage Requirements for HVdc Transmission System”, *IEEE Transactions on Power Electronics*, vol. 33, no. 1, pp. 97–109, 2018. doi: 10.1109/TPEL.2017.2660532.
- [57] S. Bernet, “Recent developments of high power converters for industry and traction applications”, *IEEE Transactions on Power Electronics*, vol. 15, no. 6, pp. 1102–1117, 2000. doi: 10.1109/63.892825.
- [58] N. Iwamuro and T. Laska, “IGBT History, State-of-the-Art, and Future Prospects”, *IEEE Transactions on Electron Devices*, vol. 64, no. 3, pp. 741–752, 2017. doi: 10.1109/TED.2017.2654599.
- [59] A. J. Korn, M. Winkelnkemper, and P. Steimer, “Low output frequency operation of the Modular Multi-Level Converter”, in *IEEE Energy Conversion Congress and Expo*, [Piscataway, N.J.]: IEEE, 2010, pp. 3993–3997. doi: 10.1109/ECCE.2010.5617802.
- [60] L. He, K. Zhang, J. Xiong, S. Fan, and Y. Xue, “Low-Frequency Ripple Suppression for Medium-Voltage Drives Using Modular Multilevel Converter With Full-Bridge Submodules”, *IEEE Journal of Emerging and Selected Topics in Power Electronics*, vol. 4, no. 2, pp. 657–667, 2016. doi: 10.1109/JESTPE.2015.2477433.

-
- [61] D. Dinkel, C. Hillermeier, and R. Marquardt, “Direct Multivariable Control for MMC: Digital Signal Processing and Experimental Results”, in *2020 22nd European Conference on Power Electronics and Applications (EPE'20 ECCE Europe)*, IEEE, pp. 1–11.
- [62] R. Picas, J. Pou, S. Ceballos, J. Zaragoza, G. Konstantinou, and V. G. Agelidis, “Optimal injection of harmonics in circulating currents of modular multilevel converters for capacitor voltage ripple minimization”, in *2013 IEEE ECCE Asia Downunder (ECCE Asia 2013)*, I. Staff, Ed., [Place of publication not identified]: IEEE, 2013, pp. 318–324. doi: 10.1109/ECCE-Asia.2013.6579115.
- [63] L. Yang, Y. Li, Z. Li, P. Wang, S. Xu, and R. Gou, “Loss Optimization of MMC by Second-Order Harmonic Circulating Current Injection”, *IEEE Transactions on Power Electronics*, vol. 33, no. 7, pp. 5739–5753, 2018. doi: 10.1109/TPEL.2017.2751068.
- [64] J. Wang, X. Han, H. Ma, and Z. Bai, “Analysis and Injection Control of Circulating Current for Modular Multilevel Converters”, *IEEE Transactions on Industrial Electronics*, vol. 66, no. 3, pp. 2280–2290, 2019. doi: 10.1109/TIE.2018.2808901.
- [65] D. Townsend, G. Mirzaeva, and G. C. Goodwin, “Capacitance minimization in modular multilevel converters: A reliable and computationally efficient algorithm to identify optimal circulating currents and zero-sequence voltages”, in *2017 IEEE 12th International Conference on Power Electronics and Drive Systems (PEDS)*, [S.l.]: IEEE, 2017, pp. 98–104. doi: 10.1109/PEDS.2017.8289183.
- [66] S. Fuchs, M. Jeong, and J. Biela, “Reducing the Energy Storage Requirements of Modular Multilevel Converters with Optimal Capacitor Voltage Trajectory Shaping”, in *2020 22nd European Conference on Power Electronics and Applications (EPE'20 ECCE Europe)*, IEEE, pp. 1–11.
- [67] M. H. Nehrir, C. Wang, K. Strunz, H. Aki, R. Ramakumar, J. Bing, Z. Miao, and Z. Salameh, “A Review of Hybrid Renewable/Alternative Energy Systems for Electric Power Generation: Configurations, Control, and Applications”, *IEEE Transactions on Sustainable Energy*, vol. 2, no. 4, pp. 392–403, 2011. doi: 10.1109/TSST.2011.2157540.

- [68] F. Blaabjerg, R. Teodorescu, M. Liserre, and A. V. Timbus, “Overview of Control and Grid Synchronization for Distributed Power Generation Systems”, *IEEE Transactions on Industrial Electronics*, vol. 53, no. 5, pp. 1398–1409, 2006. doi: 10.1109/TIE.2006.881997.
- [69] F. Tedesco, A. Casavola, and G. Fedele, “Discrete-time Frequency-Locked-Loop filters for parameters estimation of sinusoidal signals”, in *2013 IEEE 52nd Annual Conference on Decision and Control (CDC*, [Place of publication not identified]: IEEE, 2013, pp. 4399–4404. doi: 10.1109/CDC.2013.6760566.
- [70] F. Tedesco, A. Casavola, and G. Fedele, “Unbiased Estimation of Sinusoidal Signal Parameters via Discrete-Time Frequency-Locked-Loop Filters”, *IEEE Transactions on Automatic Control*, vol. 62, no. 3, pp. 1484–1490, 2017.
- [71] R. Teodorescu, M. Liserre, and P. Rodríguez, *Grid converters for photovoltaic and wind power systems*. Chichester, West Sussex: Wiley IEEE, 2011. doi: 10.1002/9780470667057.
- [72] S. Li, X. Wang, Z. Yao, T. Li, and Z. Peng, “Circulating Current Suppressing Strategy for MMC-HVDC Based on Nonideal Proportional Resonant Controllers Under Unbalanced Grid Conditions”, *IEEE Transactions on Power Electronics*, vol. 30, no. 1, pp. 387–397, 2015. doi: 10.1109/TPEL.2014.2329059.
- [73] D. Bernet and M. Hiller, “Grid-connected medium-voltage converters with parallel voltage-source active filters”, *IET Electric Power Applications*, vol. 13, no. 10, pp. 1507–1513, 2019. doi: <https://doi.org/10.1049/iet-epa.2019.0021>. eprint: <https://ietresearch.onlinelibrary.wiley.com/doi/pdf/10.1049/iet-epa.2019.0021>.
- [74] R. Krishna, S. K. Kottayil, and M. Leijon, “Direct predictive current control of grid connected neutral point clamped inverter for wave power extraction”, in *International Symposium on Power Electronics, Electrical Drives, Automation and Motion (SPEEDAM), 2010*, Piscataway, NJ: IEEE, 2010, pp. 175–179. doi: 10.1109/SPEEDAM.2010.5542184.
- [75] T. Geyer, “Model Predictive Direct Torque Control: Derivation and Analysis of the State-Feedback Control Law”, *IEEE Transactions on Industry Applications*, vol. 49, no. 5, pp. 2146–2157, 2013. doi: 10.1109/TIA.2013.2262255.

- [76] N. Panten, N. Hoffmann, and F. W. Fuchs, “Finite Control Set Model Predictive Current Control for Grid-Connected Voltage-Source Converters With *LCL* Filters: A Study Based on Different State Feedbacks”, *IEEE Transactions on Power Electronics*, vol. 31, no. 7, pp. 5189–5200, 2016. doi: 10.1109/TPEL.2015.2478862.
- [77] J. Hu, J. Zhu, and D. G. Dorrell, “Model Predictive Control of Grid-Connected Inverters for PV Systems With Flexible Power Regulation and Switching Frequency Reduction”, *IEEE Transactions on Industry Applications*, vol. 51, no. 1, pp. 587–594, 2015. doi: 10.1109/TIA.2014.2328785.
- [78] T. Geyer, *Model predictive control of high power converters and industrial drives*, First edition. Chichester, West Sussex, United Kingdom: Wiley, 2017.
- [79] W. Tian, X. Gao, and R. Kennel, “Model Predictive Control of Modular Multilevel Converters with Independent Arm-Balancing Control”, in *PRECEDE 2019*, [Piscataway, New Jersey]: IEEE, 2019, pp. 1–5. doi: 10.1109/PRECEDE.2019.8753360.
- [80] V. Spudic and T. Geyer, “Model Predictive Control Based on Optimized Pulse Patterns for Modular Multilevel Converter STATCOM”, *IEEE Transactions on Industry Applications*, vol. 55, no. 6, pp. 6137–6149, 2019. doi: 10.1109/TIA.2019.2936797.
- [81] P. Karamanakos and T. Geyer, “Guidelines for the Design of Finite Control Set Model Predictive Controllers”, *IEEE Transactions on Power Electronics*, vol. 35, no. 7, pp. 7434–7450, 2020. doi: 10.1109/TPEL.2019.2954357.
- [82] Energy Management Division, *HVDC – High-voltage direct current transmission: Unrivalled practical experience*, Siemens AG, Ed., 2017.
- [83] H. Akagi, “Classification, Terminology, and Application of the Modular Multilevel Cascade Converter (MMCC)”, *IEEE Transactions on Power Electronics*, vol. 26, no. 11, pp. 3119–3130, 2011. doi: 10.1109/TPEL.2011.2143431.
- [84] M. Guan and Z. Xu, “Modeling and Control of a Modular Multilevel Converter-Based HVDC System Under Unbalanced Grid Conditions”, *IEEE Transactions on Power Electronics*, vol. 27, no. 12, pp. 4858–4867, 2012. doi: 10.1109/TPEL.2012.2192752.

- [85] D. Karwatzki and A. Mertens, “Generalized Control Approach for a Class of Modular Multilevel Converter Topologies”, *IEEE Transactions on Power Electronics*, vol. 33, no. 4, pp. 2888–2900, 2018. doi: 10.1109/TPEL.2017.2703917.
- [86] H. Fehr, *Beiträge zur Modulation, Modellbildung und Energieregulung von modularen Mehrpunktstromrichtern (M2C)*, ser. Beiträge aus der Elektrotechnik. Dresden: Vogt, 2019.
- [87] R. Li, J. E. Fletcher, L. Xu, D. Holliday, and B. W. Williams, “A Hybrid Modular Multilevel Converter With Novel Three-Level Cells for DC Fault Blocking Capability”, *IEEE Transactions on Power Delivery*, vol. 30, no. 4, pp. 2017–2026, 2015.
- [88] A. J. Korn, M. Winkelnkemper, P. Steimer, and J. W. Kolar, “Capacitor voltage balancing in modular multilevel converters”, in *Power electronics, machines and drives*, Stevenage: IET, 2012, P119–P119. doi: 10.1049/cp.2012.0158.
- [89] P. Munch, D. Gorges, M. Izak, and S. Liu, “Integrated current control, energy control and energy balancing of Modular Multilevel Converters”, in *IECON 2010*, [Piscataway, N.J.]: IEEE, 2010, pp. 150–155. doi: 10.1109/IECON.2010.5675185.
- [90] R. A. Horn and C. R. Johnson, *Matrix analysis*, Second edition. New York, NY: Cambridge University Press, 2013.
- [91] L. Stefanski, D. Bernet, M. Schnarrenberger, C. Rollbühler, A. Liske, and M. Hiller, *Cascaded H-Bridge based Parallel Hybrid Converter - A novel Topology for perfectly sinusoidal high power Voltage Sources*, 2019. doi: 10.5445/IR/1000100736.
- [92] D. Bernet, L. Stefanski, and M. Hiller, “Integrating voltage-source active filters into grid-connected power converters modeling, control and experimental verification”, *IEEE Transactions on Power Electronics*, pp. 1–1, 2021. doi: 10.1109/TPEL.2021.3075068.
- [93] R. Penrose, “A generalized inverse for matrices”, *Mathematical Proceedings of the Cambridge Philosophical Society*, vol. 51, no. 3, pp. 406–413, 1955.
- [94] S. P. Engel and R. W. De Doncker, “Control of the Modular Multi-Level Converter for minimized cell capacitance”, in *Proceedings of the 2011 14th European Conference on Power Electronics and Applications*, 2011, pp. 1–10.

-
- [95] J. Pou, S. Ceballos, G. Konstantinou, V. G. Agelidis, R. Picas, and J. Zaragoza, "Circulating Current Injection Methods Based on Instantaneous Information for the Modular Multilevel Converter", *IEEE Transactions on Industrial Electronics*, vol. 62, no. 2, pp. 777–788, 2015. doi: 10.1109/TIE.2014.2336608.
- [96] S. Wang, G. P. Adam, A. M. Massoud, D. Holliday, and B. W. Williams, "Analysis and Assessment of Modular Multilevel Converter Internal Control Schemes", *IEEE Journal of Emerging and Selected Topics in Power Electronics*, p. 1, 2019. doi: 10.1109/JESTPE.2019.2899794.
- [97] M. Basic, S. Milovanovic, and D. Dujic, "Comparison of two modular multilevel converter internal energy balancing methods", *Proceedings of the 2019 20th International Symposium on Power Electronics (Ee)*, 2019.
- [98] C. Zhao, Z. Wang, Z. Li, P. Wang, and Y. Li, "Characteristics Analysis of Capacitor Voltage Ripples and Dimensioning of Full-Bridge MMC With Zero Sequence Voltage Injection", *IEEE Journal of Emerging and Selected Topics in Power Electronics*, vol. 7, no. 3, pp. 2106–2115, 2019. doi: 10.1109/JESTPE.2018.2878411.
- [99] J. Kennedy and R. Eberhart, "Particle swarm optimization", in *1995 IEEE International Conference on Neural Networks Proceedings*, [Place of publication not identified]: IEEE, 1995, pp. 1942–1948. doi: 10.1109/ICNN.1995.488968.
- [100] J. A. E. Andersson, J. Gillis, G. Horn, J. B. Rawlings, and M. Diehl, "CasADi – A software framework for nonlinear optimization and optimal control", *Mathematical Programming Computation*, 2018.
- [101] J. Bocker, B. Freudenberg, A. The, and S. Dieckerhoff, "Experimental Comparison of Model Predictive Control and Cascaded Control of the Modular Multilevel Converter", *IEEE Transactions on Power Electronics*, vol. 30, no. 1, pp. 422–430, 2015. doi: 10.1109/TPEL.2014.2309438.
- [102] B. Gutierrez and S.-S. Kwak, "Modular Multilevel Converters (MMCs) Controlled by Model Predictive Control With Reduced Calculation Burden", *IEEE Transactions on Power Electronics*, vol. 33, no. 11, pp. 9176–9187, 2018. doi: 10.1109/TPEL.2018.2789455.

- [103] J. Qin and M. Saeedifard, “Predictive Control of a Modular Multilevel Converter for a Back-to-Back HVDC System”, *IEEE Transactions on Power Delivery*, vol. 27, no. 3, pp. 1538–1547, 2012. doi: 10.1109/TPWRD.2012.2191577.
- [104] G. Darivianakis, T. Geyer, and W. van der Merwe, “Model predictive current control of modular multilevel converters”, in *Energy Conversion Congress and Exposition (ECCE), 2014 IEEE*, IEEE, 2014, pp. 5016–5023. doi: 10.1109/ECCE.2014.6954089.
- [105] M. Vatani, B. Bahrani, M. Saeedifard, and M. Hovd, “Indirect Finite Control Set Model Predictive Control of Modular Multilevel Converters”, *IEEE Transactions on Smart Grid*, vol. 6, no. 3, pp. 1520–1529, 2015. doi: 10.1109/TSG.2014.2377112.
- [106] A. Dekka, B. Wu, V. Yaramasu, R. L. Fuentes, and N. R. Zargari, “Model Predictive Control of High-Power Modular Multilevel Converters—An Overview”, *IEEE Journal of Emerging and Selected Topics in Power Electronics*, vol. 7, no. 1, pp. 168–183, 2019. doi: 10.1109/JESTPE.2018.2880137.
- [107] S. Fuchs, M. Jeong, and J. Biela, “Long Horizon, Quadratic Programming Based Model Predictive Control (MPC) for Grid Connected Modular Multilevel Converters (MMC)”, in *Proceedings, IECON 2019 - 45th Annual Conference of the IEEE Industrial Electronics Society*, Piscataway, NJ: IEEE, 2019, pp. 1805–1812. doi: 10.1109/IECON.2019.8927493.
- [108] *2018 20th European Conference on Power Electronics and Applications (EPE'18 ECCE Europe): 17-21 Sept. 2018*. Piscataway, NJ: IEEE, 2018.
- [109] J. E. Normey-Rico and E. F. Camacho, *Control of Dead-time Processes*, ser. Advanced Textbooks in Control and Signal Processing. London, Berlin, and Heidelberg: Springer, 2007. doi: 10.1007/978-1-84628-829-6.
- [110] D. Schröder, *Elektrische Antriebe - Regelung von Antriebssystemen*. Berlin, Heidelberg: Springer Berlin Heidelberg, 2015. doi: 10.1007/978-3-642-30096-7.
- [111] C. Ackermann, *Optimale Regelung der permanentmagneterregten Synchronmaschine unter Nutzung des Reluktanzmoments*, 2012. doi: 10.5445/IR/1000041168.

-
- [112] U. Nuß, *Hochdynamische Regelung elektrischer Antriebe*. Berlin: VDE-Verl., 2010.
- [113] T. Gemaßmer, *Effiziente und dynamische Drehmomenteinprägung in hoch ausgenutzten Synchronmaschinen mit eingebetteten Magneten*, 2015. DOI: 10.5445/KSP/1000046666.
- [114] J. Nocedal and S. J. Wright, *Numerical Optimization*, Second Edition, ser. Springer Series in Operations Research and Financial Engineering. New York, NY: Springer Science+Business Media LLC, 2006. DOI: 10.1007/978-0-387-40065-5.
- [115] S. Richter, “Computational complexity certification of gradient methods for real-time model predictive control”, PhD thesis, ETH Zurich, 2012. DOI: 10.3929/ETHZ-A-007587480.
- [116] F. Blaabjerg, M. P. Kazmierkowski, and R. Krishnan, *Control in power electronics: Selected problems*, ser. Academic Press series in engineering. Amsterdam and New York: Academic Press, 2002.
- [117] R. Schwendemann, S. Decker, M. Hiller, and M. Braun, *A Modular Converter- and Signal-Processing-Platform for Academic Research in the Field of Power Electronics*, 2018. DOI: 10.5445/IR/1000088519.
- [118] C. Axtmann, M. Boxriker, and M. Braun, *A custom, high-performance real time measurement and control system for arbitrary power electronic systems in academic research and education*, 2016. DOI: 10.5445/IR/1000063661.
- [119] S. Bernet, *Selbstgeführte Stromrichter am Gleichspannungszwischenkreis*. Berlin, Heidelberg: Springer Berlin Heidelberg, 2012. DOI: 10.1007/978-3-540-68861-7.
- [120] MATLAB, *Version 9.6.0.1114505 (R2019a) Update 2*. Natick, Massachusetts: The MathWorks Inc., 2019.
- [121] Q. Gui, J. L. Gnarig, H. Fehr, and A. Gensior, “Energy-Balancing of a Modular Multilevel Converter Using an Online Trajectory Planning Algorithm”, in *2020 22nd European Conference on Power Electronics and Applications (EPE’20 ECCE Europe)*, IEEE, pp. 1–11.
- [122] J. M. Carrasco, L. G. Franquelo, J. T. Bialasiewicz, E. Galvan, R. C. PortilloGuisado, M. Prats, J. I. Leon, and N. Moreno-Alfonso, “Power-Electronic Systems for the Grid Integration of Renewable Energy Sources: A Survey”, *IEEE Transactions on Industrial Electronics*, vol. 53, no. 4, pp. 1002–1016, 2006. DOI: 10.1109/TIE.2006.878356.

Datasheets and Application Notes

- [D1] VDE, *VDE-AR-N 4105 Erzeugungsanlagen am Niederspannungsnetz: Technische Mindestanforderungen für Anschluss und Parallelbetrieb von Erzeugungsanlagen am Niederspannungsnetz*, 11.2018.
- [D2] VDE, *VDE-AR-N 4120 Technische Regeln für den Anschluss von Kundenanlagen an das Hochspannungsnetz und deren Betrieb (TAR Hochspannung)*, 11.2018.
- [D3] VDE, *VDE-AR-N 4110 Technische Regeln für den Anschluss von Kundenanlagen an das Mittelspannungsnetz und deren Betrieb (TAR Mittelspannung)*, 11.2018.
- [D4] CENELEC: European Committee, *EN 50160 - Voltage Characteristics of Public Distribution System*, Brussels, Belgium, 1999.
- [D5] Infineon Technologies AG, *Datasheet FZ1200R45HL3 IHM-B module with Trench/Fieldstop IGBT3 and Emitter Controlled 3 diode*, 2019.
- [D6] Infineon Technologies AG, *Datasheet OptiMOSTM3 Power-Transistor*, 2011.
- [D7] Panasonic Corporation, *Aluminum Electrolytic Capacitors/ UQ Datasheet*, 2013.
- [D8] Intel Corporation, *Intel MAX 10 FPGA Device Datasheet*, 2018.
- [D9] Broadcom, Ed., *AFBR-16xxZ and AFBR-26x4Z/25x9Z Datasheet*, 2016.
- [D10] Intel Corporation, *Cyclone IV Device Datasheet*, 2016.
- [D11] Texas Instruments Incorporated, *12-BIT, 4 ANALOG INPUT, 6 MSPS, SIMULTANEOUS SAMPLINGANA-LOG-TO-DIGITAL CONVERTERS Datasheet*, 2003.
- [D12] LEM, *Current Transducer LAH 50-P Datasheet*, 2015.
- [D13] Keysight Technologies, *N2790A 100 MHz, N2791A 25 MHz and N2891A 70 MHz High-voltage Differential Probes Datasheet*, 2018.
- [D14] Keysight Technologies, *InfiniiVision 3000T X-Series Oscilloscopes Datasheet*, 2020.